Year : 2016

REMOTE SENSING METHODS FOR THE INVESTIGATION OF THE EVOLUTION AND DYNAMICS OF ALPINE LANDSCAPES

Natan Micheletti

UNIL | Université de Lausanne

Faculté des Géosciences et de l'Environnement
Institut des Dynamiques de la Surface Terrestre

REMOTE SENSING METHODS FOR THE INVESTIGATION OF THE EVOLUTION AND DYNAMICS OF ALPINE LANDSCAPES

Thèse de doctorat

présentée à la

Faculté des Géosciences et de l'Environnement de l'Université de Lausanne

par

NATAN MICHELETTI

B.Sc., M.Sc. Université de Lausanne, Suisse

JURY

Président du jury:	Prof. Michel Jaboyedoff
Directeur de thèse:	Prof. Stuart N. Lane
Co-directeur de thèse:	Dr. Christophe Lambiel
Expert:	Prof. Grégoire Mariéthoz
Expert:	Prof. Jim H. Chandler
Expert:	Prof. Tobias Heckmann

Lausanne, 2016

UNIL | Université de Lausanne
Décanat Géosciences et de l'Environnement
bâtiment Géopolis
CH-1015 Lausanne

IMPRIMATUR

Vu le rapport présenté par le jury d'examen, composé de

Président de la séance publique :	M. le Professeur Michel Jaboyedoff
Président du colloque :	M. le Professeur Michel Jaboyedoff
Directeur de thèse :	M. le Professeur Stuart Lane
Co-directeur de thèse :	M. le Docteur Christophe Lambiel
Expert interne:	M. le Professeur Grégoire Mariéthoz
Expert externe :	M. le Professeur Jim H. Chandler
Expert externe :	M. le Professeur Tobias Heckmann

Le Doyen de la Faculté des géosciences et de l'environnement autorise l'impression de la thèse de

Monsieur Natan MICHELETTI
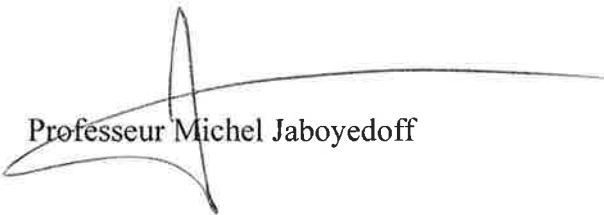
Titulaire d'une
Maîtrise ès Sciences en géosciences de l'environnement
de l'Université de Lausanne

intitulée

REMOTE SENSING METHODS FOR THE INVESTIGATION OF THE EVOLUTION AND DYNAMICS OF ALPINE LANDSCAPES

Lausanne, le 26 août 2016

Pour le Doyen de la Faculté des géosciences et de l'environnement

Professeur Michel Jaboyedoff

"The brutality of human wars is only one of the major hurdles we need to clear in order to achieve a satisfying shift in focus away from individual suffering towards that of true population stewardship. The other is the burgeoning environmental crisis we are busily creating for ourselves. [...] we should be able to create a global, sustainable environment for ourselves."

— Greg Graffin,
Population Wars: A New Perspective on Competition and Coexistence (2015), p. 240.

Acknowledgements

The accomplishment of this thesis would not have been possible without the invaluable help and support, whether scientific or not, received from many people.

First of all, I would like to thank my supervisor, Prof. Stuart Lane. Stuart believed in me and in this project from the very beginning, and his ever-present positive attitude has been priceless to me. In moments of doubt he was always there to motivate me and to push me forward, and his advices helped me to improve my skills in conducting research, writing papers and assisting students. I am very honoured to have had the opportunity to learn so much from him. I am very grateful to Dr. Christophe Lambiel for co-supervising my doctorate and always being kind and helpful. Christophe possesses a deep knowledge of Alpine environments, and having access to his suggestions and interpretation was a valuable resource for me. Some analyses employed in this thesis have been carried out during my research visit at the University of Loughborough. I am very thankful to Prof. Jim Chandler for having welcomed me there and for his "coaching" during that time. Jim took a great interest in my work and invested a lot of his time to assist me with my research. If the quality of the photogrammetric results in this thesis are any good, I must share a great deal of the credit with Jim. My sincere gratitude goes to Professors Grégoire Mariéthoz and Tobias Heckmann as well, for their interest in my research and for serving as experts to evaluate it.

During my doctorate, I had the chance to collaborate with many remarkable colleagues and we managed to produce and publish very interesting results together. I am very thankful to all of them for the research we shared. In particular, I want to thank Dr. Marj Tonini for having always been so kind to be during all these years in Lausanne and for the fruitful collaboration we had in the last few months.

Furthermore, I would like to thank all the colleagues and friends at the University of Lausanne for their help and for the good working atmosphere that they contribute to create. I had a long pathway across institutes during my stay in Lausanne (IGAR, IGUL, IGD, IDYST), but working (and having breaks or after-works at Zélig) with kind and friendly persons was a constant, and for that I am very grateful. In particular, I had a real pleasure in sharing my path (and offices) to the doctorate with Nico Bätz, whose positive outlook was simply infectious. A special thank goes to Nicola Deluigi, for having always been a friend more than a colleague during these

Acknowledgements

many, many years at the University.

I want to thank Les Tontons for being great friends and for having created such a pleasant atmosphere during our time together as students, it was *fresh*! Stepping outside the university domain, a big thank you goes to all my friends in Ticino (or from Ticino and now scattered around the country) for welcoming me with open arms every time I travel back to my home town. To all those friends that I hadn't seen much in the past years but that were always there for me: thank you for showing me how strong real friendship bonds are!

I simply couldn't have achieved this work without the constant and unconditional support and love of my family. Thank you all! In particular, I owe everything to my mother Gilda, for all the brave decisions that she took that made me who I am, and for I am seeing the world "*con i miei occhi, ma con i suoi occhiali*". Thank you to my brother Noa as well, for our shared childhoods and because no matter the distance between us, we will always have each other. A big hug to my uncle Sergio: my interest in geomorphology finds its roots in the wonderful and unforgettable expeditions in the Sahara desert he took me to! My thought goes to my grandparents Ivo and Lea as well, who were like a father and a mother to me and represented such a big part of my life. Thank you, I miss you so much.

Last but not least, I must express my profound gratitude to Antje for her unconditional support (and for always putting up with me!). Her encouragement through these years was invaluable. I treasure the wonderful moments we spent together and I hope to have her by my side as long as possible because she makes life so much easier just by taking me into her arms.

Finally, I want to thanks all those people that are indeed an important part of my life, but that I could not mention in these lines. From the bottom of my heart, **thank you!**

Lausanne, May 2016   N. M.

Financial support

Abstract

Whilst the effects of present-day climate change are apparent in many environmental systems, much less is known about its impact upon the geomorphic systems characteristic of Alpine environments. This is an important knowledge gap because of the potential vulnerability of Alpine landscapes. The gap exists for two primary reasons: (1) observing climate forcing is challenging because it is manifest over timescales of decades to centuries, over which timescale geomorphic data are commonly scarce; and (2) the geomorphic response of landscapes to climate change can be complex, reflecting both spatially differential sensitivities to climate forcing and the effects of landscape heritage associated with historical glacial activity. Nonetheless, there is a consensus in the scientific community about the potentially high sensitivity of Alpine regions to climate change, because of the vulnerability of permafrost, glacial and nival processes to changes in atmospheric temperature and precipitation and the large amount of sediment stored on the associated hillsides.

One approach to addressing this knowledge gap is to harness the power of remote sensing. A number of active and passive remote sensing methods could be employed for the reconstruction and monitoring of both whole landscapes and individual landforms. This Thesis aims to use such approaches to quantify the geomorphic dynamics of high mountain areas at the timescale of decades and so in the context of recent and rapid climate warming. It does so recognizing that both endogenous (landscape legacy) and exogenous (climatic forcing) processes may matter. To support this primary aim, a secondary aim arises: the evaluation of the potential of a number of remote sensing techniques for landscape and landform monitoring at multiple temporal and spatial scales. Thus this Thesis also tests in an Alpine setting the geomorphological potential of photogrammetric methods, using both aerial and hand-held sensors and both traditional and the innovative Structure-from-Motion processing approaches, and Terrestrial Laser Scanner techniques.

The Thesis shows that remote sensing approaches prove to be an advantageous approach for a number of scales of application. In particular, over large spatial extents and in the case of decadal scale climate forcing of Alpine landscapes, photogrammetry was found to be capable of quantifying process rates within the limits of detection determined by the resolution of historical imagery. The information unlocked from aerial archives reveals distinct geomorphic responses to cold and warm periods and to changes in rates of precipitation and snow cover. Nonetheless, whilst enhanced sediment production is observed locally, evidence suggest a weak propagation of climate change signals through the landscape due to impeded connection to the river system and/or sediment transport capacity limitation.

Résumé

Bien que les effets des changements climatiques actuels soient visibles dans de nombreux systèmes environnementaux, un manque de connaissances des impacts sur les paysages alpins persiste. Cette lacune existe pour deux raisons principales : (1) l'observation du forçage climatique représente un défi, car ses conséquences se manifestent sur des périodes de plusieurs décennies, voire des siècles, pour lesquels les données géomorphologiques sont généralement rares ; et (2) la réaction du paysage aux changements climatiques peut être complexe, reflétant à la fois des sensibilités différentes au niveau spatial et les effets du patrimoine paysager, comme par exemple son histoire glaciaire. Néanmoins, il existe un consensus dans la communauté scientifique à propos de la haute sensibilité potentielle des régions alpines au changement climatique, en raison de la vulnérabilité du pergélisol et des processus glaciaires et neigeux aux changements de température atmosphérique et des précipitations et en raison de la grande quantité de sédiments stockés sur les versants alpins.

Une stratégie pour aborder ces problématiques s'appuie sur le potentiel de la télédétection. Une série de méthodes de télédétection active et passive peuvent être utilisées pour reconstruire et surveiller le paysage entier et les éléments individuels qui le composent. Cette thèse vise l'application de ces approches pour quantifier les dynamiques géomorphologiques des paysages de haute montagne à l'échelle des décennies, et donc dans le contexte du réchauffement climatique récent et actuel. Cela est mis en pratique par la reconnaissance de l'importance des processus endogènes (héritage du paysage) et exogènes (forçage climatique). Le soutien à cet objectif en soulève un deuxième : l'évaluation du potentiel d'un certain nombre de techniques de télédétection pour le monitorage du relief et de ses formes géomorphologiques à plusieurs échelles temporelles et spatiales. Ainsi, cette thèse teste le potentiel des méthodes de photogrammétrie, en utilisant à la fois des senseurs aéroportés et portatifs et des approches de traitements traditionnels et innovants, et du balayage laser terrestre pour la recherche géomorphologique alpine.

Les résultats obtenus montrent que les approches de télédétection se révèlent avantageuses pour des nombreuses échelles d'application. En particulier, sur de grandes étendues spatiales et dans le contexte du forçage climatique du paysage alpin, la photogrammétrie aérienne d'archive se montre appropriée pour la quantification des taux des processus dans les limites de détection déterminées par la résolution des photographies historiques. Les résultats démontrent l'existence d'une réponse géomorphologique distincte pour des périodes froides ou chaudes, ainsi que selon les variations des taux de précipitations et de couverture de neige. Néanmoins, alors qu'une production accrue de sédiments est observée localement, des évidences suggèrent une faible propagation des signaux du changement climatique à travers le paysage. Les raisons semblent être une faible contribution des versants au réseau fluvial et/ou une capacité de transport des sédiments limitée.

Zusammenfassung

Obwohl die Auswirkungen des aktuellen Klimawandels in zahlreichen Umweltsystemen beobachtet wurden, sind die Kenntnisse dieser Auswirkungen auf alpine Landschaften immer noch ungenügend. Diese Lücke existiert aus folgenden Gründen: (1) Das Beobachten klimatischer Auswirkungen auf alpine geomorphologische Prozesse stellt eine grosse Herausforderung dar, da diese sich über eine Zeitspanne von mehreren Jahrzehnten bis Jahrhunderten bemerkbar machen können, für die meist nur wenige geomorphologische Daten zur Verfügung stehen. (2) Durch die unterschiedlichen Empfindlichkeiten verschiedener geomorphologischer Landschaftselemente sowie durch den grossen Einfluss des landschaftlichen Erbes, wie zum Beispiel der historischen Gletschertätigkeit, reagieren alpine Landschaftsentwicklungsprozesse sehr komplex auf Veränderungen des Klimas. Nichtsdestotrotz, aufgrund der hohen Empfindlichkeit des Permafrosts und der Gletscher- und Schneeprozesse gegenüber Veränderungen der atmosphärischen Temperatur und der Niederschlagsmenge sowie der grossen Menge an Sedimenten die an den Alpenhängen abgelagert werden und wurden, herrscht in der wissenschaftlichen Gemeinschaft ein breiter Konsens über die potentielle hohe Sensibilität der alpinen geomorphologischen Systeme in Bezug auf den zu erwartenden Klimawandel.

Fernerkundung bietet ein hohes Potential, um die geomorphologische Sensibilität zu erkunden. Aktive und passive Fernerkundungsmethoden können genutzt werden, um gesamte Landschaften sowie ihre einzelnen geomorphologischen Elemente historisch zu rekonstruieren und kontinuierlich zu überwachen. Die vorliegende Dissertation zielt auf die Anwendung dieser Ansätze, um die geomorphologische Dynamik der hochalpinen Landschaft über Jahrzehnte, und somit im Kontext der jüngsten Klimaerwärmung, zu quantifizieren. Der hier dargestellte Ansatz fokussiert vor allem auf die Bedeutung der endogenen (landschaftliches Erbe) und exogenen (klimatische Einflüsse) Prozesse. Die Umsetzung dieses primären Ziels zieht ein sekundäres Ziel mit sich: Die Bewertung des Potenzials einer Reihe von Fernerkundungsmethoden für das Monitoring von Landschaften und ihrer geomorphologischen Formen auf mehreren räumlichen und zeitlichen Skalen. Damit wird das Potenzial photogrammetrischer Methoden, insbesondere luftgestützter und tragbarer Sensoren in Kombination mit traditionellen und innovativen "Structure-from-Motion" Ansätzen, sowohl auch terrestrischen Laserscanning Techniken für die alpine geomorphologische Forschung getestet.

Die Ergebnisse zeigen, dass die hier dargestellten Fernerkundungsansätze für eine breite Reihe von Anwendungsskalen vorteilhaft sind. Die Archiv-Luftphotogrammmetrie ist besonders für die Quantifizierung der Auswirkungen des Klimawandels auf geomorphologische Prozesse in grossen Landschaftsausschnitten geeignet. Die Auflösung der historischen Luftbilder bestimmt die Detektionsgrenze dieser Prozesse. Die aus den Luftarchiven ermittelten Informationen zeigen, dass kalte und warme Klimaphasen, sowie Variationen der Niederschlagsmenge und der Schneedeckenmächtigkeit unterschiedliche Auswirkungen auf geomorphologische Prozesse haben. Obwohl ein lokaler Anstieg der Sedimentproduktion beobachtet werden konnte, konnten nur geringe Anzeichen einer Ausbreitung dieser Klimawandelsignale in der Landschaft beobachtet werden. Die Gründe hierfür scheinen der geringe Beitrag der untersuchten Berghänge zum Gesamtwasserabfluss und/oder die beschränkte Sedimenttransportfähigkeit zu sein.

Riassunto

Nonostante gli effetti del cambiamento climatico attuale siano evidenti in molti sistemi ambientali, una conoscenza deficitaria perdura riguardo il suo impatto sui paesaggi alpini. Tale lacuna esiste per due principali ragioni: (1) gli effetti del cambiamento climatico sono difficili da osservare, in quanto manifesti su scale temporali di decenni, o persino secoli, per le quali prevale una scarsità di dati geomorfologici esaustivi; e (2) la reazione del paesaggio a tali cambiamenti può essere complessa e riflettere al contempo delle sensibilità spaziali differenti e gli effetti del patrimonio paesaggistico, come ad esempio la cronistoria glaciale. Tuttavia, vi è un consenso nella comunità scientifica riguardo l'elevata sensibilità delle regioni alpine ai cambiamenti climatici, a causa della vulnerabilità di permafrost e processi glaciali e nevosi ai cambiamenti di temperatura atmosferica e di precipitazioni, oltre che all'ampio stoccaggio di sedimenti concentrato sui pendii alpini.

Una strategia per colmare questa lacuna di conoscenza può essere l'avvalersi del potenziale delle tecniche di telerilevamento. Vari metodi di telerilevamento attivo e passivo possono essere impiegati per ricostruire e monitorare il paesaggio ed i singoli elementi che lo compongono. Questa tesi si propone di utilizzare tali metodi per quantificare le dinamiche geomorfologiche nelle regioni di alta montagna a scala temporale decennale, e quindi nel contesto del riscaldamento climatico recente e attuale. In tale approccio viene riconosciuta l'importanza dei processi di tipo endogeno (di eredità paesaggistica) ed exogeno (climatici). A sostegno di questo obiettivo primario, una seconda finalità si pone: lo sviluppo e la valutazione di diverse tecniche di telerilevamento per il monitoraggio dei rilievi alpini e delle loro forme geomorfologiche, a più scale temporali e spaziali. Pertanto, questa tesi mette alla prova metodi di fotogrammetria, utilizzando al contempo sensori aeroportati e portatili ed approcci tradizionali ed innovativi (come l'emergente Structure-from-Motion), e tecniche di scansione laser per la ricerca geomorfologica in scenari alpini.

I risultati ottenuti dimostrano come gli approcci di telerilevamento rappresentino una risorsa efficace e vantaggiosa per una vasta gamma di applicazioni. In particolare, ad ampia scala spaziale e nel contesto di cambiamento climatico nelle regioni alpine, la fotogrammetria aerea d'archivio si è dimostrata appropriata per la quantificazione dei processi geomorfologici entro limiti di rilevamento determinati dalla risoluzione delle immagini storiche stesse. I risultati rivelano una reazione geomorfica distinta a periodi di caldo e freddo, oltre che a variazioni di precipitazioni e copertura nevosa. Ciononostante, malgrado un accrescimento della produzione sedimentaria sia presente a scala locale, la propagazione dei segnali di cambiamento climatico attraverso il paesaggio appare debole. La ragione risiede nello scarso contributo dei versanti al sistema fluviale e/o a limitate capacità di trasporto di sedimenti.

Contents

Contents

List of Figures

List of Tables

Acronyms

AF	Alluvial Fan
AGNES	Automated GNSS Network for Switzerland
ATE	Automated Terrain Extraction
a.s.l.	above sea level
BW	Black and White
CI	Connectivity Index
COP	Conference of the Parties
DBSCAN	Density-Based Scan Algorithm with Noise
DEM	Digital Elevation Model
dGPS	differential Geographic Positioning System
DoD	DEM of Difference
DTM	digital terrain model
eATE	enhanced Automated Terrain Extraction
e.g.	*exempli gratia*: for example
i.e.	*id est*: namely
FC	Focal Centre
FWM	Failure Warning Model
GCP	Ground Control Point
GIS	Geographic Information System
GSB	Grand St-Bernard
GSM-SOCONT	Glacier and SnowMelt-SOil CONTribution model

Acronyms

GNSS	Global Navigation Satellite System
ICP	Iterative Closest Point
InSAR	Interferometric Synthetic Aperture Radar
IPCC	Intergovernmental Panel on Climate Change
LDC	Limit of Detection of Change
LIA	Little Ice Age
LiDAR	Light Detection And Ranging
LPS	Leica Photogrammetry Suite
kNN	k-Nearest-Neighbours
MAAT	Mean Annual Air Temperature
MARST	Mean Annual Rock Surface Temperatur
ME	Mean Error
ML	Machine Learning
MSA	Multi-Station Adjustment
PM	MegaPixels
MS	Multi-Spectral
MVS	Multi-View Stereo
NIR	Near InfraRed
PAN	Panchromatic
PERMOS	Swiss Permafrost Monitoring Network
PM	PhotoModeler
PPS	Principal Point of Symmetry
RCM	Regional Climate Model
RGB	Red, Green, Blue
RMSE	Root Mean Square Error
ROI	Region Of Interest
RTK	Real Time Kinematic

SAR	Synthetic Aperture Radar
SCA	Sediment Contributing Area
SfM	Structure-from-Motion
SIFT	Scale Invariant Feature Transformation
SOP	Sensor's Orientation and Position
STD	Standard deviation of error
TIN	Triangulated Irregular Network
TIUW	Total Image Unit-Weight
TLS	Terrestrial Laser Scanner
UAV	Unmanned Aerial Vehicle
VAW	Laboratory of Hydraulics, Hydrology and Glaciology
w.e.	water equivalent
123D C.	123D Catch

Introduction Part I

1 Thesis overview

1.1 Motivation

In 1990, the Intergovernmental Panel for Climate Change (IPCC) published a pioneer report for the scientific assessment of the possible effects of human activities upon the world's climate. Since then, a series of studies have progressively refined our comprehension of the nature of climatic variability, its causes and what this might imply for the world's climates in the foreseeable future. Whilst the inevitability of future climate warming is now recognized, attempts to develop strategies and objectives to restrain it, e.g. as discussed in the context of the United Nation conference on climate change (COP21), held in Paris in December 2015, remain incomplete.

Concern over the topic has progressively expanded from the scientific community and governmental authorities, to be the subject of media coverage and concerns amongst the general public. One reason for this is that, and independently of the future, the consequences of climate changes are already among us. They may be challenging to observe, to identify and to limit, but they are indeed real. One more challenge naturally emerges for the scientific community, relating to the quantification of these consequences for the Earth system. Parry *et al.* [2007], for the IPCC, synthesise the state of impact studies but also make a critical observation: very little work has been conducted on the expected impacts of climate change on geomorphic dynamics in mountain watersheds, particularly regarding sediment production and transfer. Knight and Harrison [2013] argue that Earth surface system responses to climate change are generally poorly understood and critically omitted from policymakers in impact managing decisions. They also claim that decadal-scale datasets of instrumented basins are required to monitor the response of these systems to climate change, and specify that this requires a considerable international science effort as well as commitment from national governments. This doctoral thesis aims to contribute to this cause.

1.2 Objectives

This thesis attempts to deepen our understanding of the impacts of climate change on high mountain environments by investigating the directs effects on their geomorphic dynamics. These areas are likely to respond dramatically to climate change because of (1) the vulnerability of permafrost, glacial and nival processes to temperature and precipitation changes [Pelto and Hedlund, 2001; Kääb et al., 2007; Oliva and Ruiz-Fernandez, 2015]; (2) the ample availability of unconsolidated, potentially mobile sediments left after deglaciation [Ballantyne et al., 2014]; and (3) steep slopes, that potentially aid sediment mobilization [Brocklehurst and Whipple, 2002]. The implications of changes in geomorphic dynamics in mountainous regions are many. They may interfere directly with human activities and infrastructure and affect water resources, electric power production, tourism, ecology and biodiversity, geomorphological heritage, cause natural hazards, etc.

The geomorphological objective of this thesis requires efficient methods to measure and to quantify landscape morphology and its changes. The need to retrieve extensive spatial information at varying time-scales (from months to the century) arises. One approach to accomplish this is through remote sensing techniques i.e., methods allowing the acquisition of information about objects without physical contact. Thus, this thesis also seeks the evaluation of the potential of a number of remote sensing techniques for landscape and landform monitoring at multiple temporal and spatial scales.

Following the considerations above, the main objectives pursued in this thesis can be stated as follows:

1. Develop an integrated approach to better comprehend the impacts of recent climate change upon Alpine landscapes and the implied consequences in terms of mass downwasting and sediment flux.

2. Investigate of the potential of a number of remote sensing techniques for landscape and landform monitoring at multiple temporal and spatial scales.

The substantive geomorphological objective (1, above) includes some secondary aims. First, the detection of morphological changes and modifications in sediment transfer rates of different elements in the high mountains at annual to decadal scales. This could potentially unveil the impact of climate forcing upon the landforms of Alpine environments. Second, the dynamics of morphological changes need to be considered in a holistic, systemic approach by taking into account the coupling of different elements of the landscape. Effectively, a crucial control upon the propagation of climate signals through the landscape is exerted by sediment connectivity, thus a manner of formally characterizing the latter is deemed necessary.

The developments included in the methodological objective (2, above) sustain the geomorphic investigation. This thesis seeks to test in an Alpine setting the geomorphological potential of

photogrammetric methods, using both aerial and hand-held sensors; and both traditional and the innovative Structure-from-Motion processing approaches, and Terrestrial Laser Scanning techniques.

1.3 Contribution of the thesis

1.3.1 Key contributions

This thesis is based upon pieces of research published individually in international scientific journals after peer-review. Accordingly, these articles are reproduced with their original, published content, and this is clearly indicated at the beginning of the chapter. In the introductory section of every paper, a brief state-of-the-art explains the contribution of each article to the specific topic they address. It also provides a brief explanation of its role in the broader development of the thesis. The research manuscripts forming the basis on the thesis are:

- Micheletti, N., Tonini, M. and Lane, S.N. (2016). A 3-D clustering approach for feature detection from point clouds: application to a rock glacier front in the Swiss Alps, *Geomorphology*, under review.

- Micheletti, N. and Lane, S.N. (2016). Water yield and sediment export in small, partially glaciated Alpine watersheds in a warming climate, *Water Resources Research*, 52:4924-4943.

- Micheletti, N., Lambiel, C. and Lane, S.N. (2015). Investigating decadal-scale geomorphic dynamics in an alpine mountain setting, *Journal of Geophysical Research: Earth Surface*, 120(10):2155-2175.

- Micheletti, N., Lane, S.N. and Chandler, J.H. (2015). Application of archival aerial photogrammetry to quantify climate forcing of Alpine landscapes, *The Photogrammetric Record*, 30(150):143-165.

- Micheletti, N., Chandler, J.H. and Lane, S.N. (2015). Investigating the geomorphological potential of freely available and accessible structure-from-motion photogrammetry using a smartphone, *Earth Surface Processes and Landforms*, 40(4):473-486

In the remainder of Section 1.3, a set of other contributions of the wider thesis project is introduced, as these are not presented exhaustively in this thesis itself.

1.3.2 Remote sensing of an Alpine temperate glacier, from the scale of decades to hours

The remote sensing approaches tested in this thesis were also applied to an Alpine temperate glacier in the context of the Master project of Chrystelle Gabbud, for which the author provided

key support. The objective of this project was the employment of remote sensing methods for the understanding the advance and recession dynamics of an Alpine valley glacier at the timescales of decades, seasons, and a single day. At the decadal scale, archival imagery has been used to obtain photogrammetric restitution of the glacier surface, and retrieve its position in time. The latter has then been employed to explore the linkages between glacier retreat and climate forcing. At seasonal and daily scales, repeated geodetic measurements were obtained using a Terrestrial Laser Scanner with the intent of studying glacier surface ablation and glacial hydrodynamics. The findings of this project have been published in:

- Gabbud, C., Micheletti, N. and Lane, S.N. (2016). Response of a temperate Alpine valley glacier to climate change at the decadal scale, *Geografiska Annaler: Series A, Physical Geography*, 98(1):81-95.

- Gabbud, C., Micheletti, N. and Lane, S.N. (2015). Lidar measurement of surface melt for a temperate Alpine glacier at the seasonal and hourly scales, *Journal of Glaciology*, 61(229):963-974.

1.3.3 Decadal evolution of a very small heavily debris-covered glacier

The approach described in full detail in Chapter 3 of this thesis was employed to compute high-precision digital elevation models and orthorectified photographs for a whole mountainside. Results are used in Chapter 7, where the decadal-scale geomorphic dynamics of the landscape are investigated using archival aerial imagery. Of particular interest in the area of study is a small, heavily debris-covered glacier located in an Alpine permafrost environment. Therefore, the data generated in this thesis were further analysed and used to deepen our knowledge of this glacial system. The results have been published as a research paper in:

- Capt, M., Bosson, J.-B., Fischer, M., Micheletti, N. and Lambiel, C. (2016). Decadal evolution of a very small heavily debris-covered glacier in an Alpine permafrost environment, *Journal of Glaciology*, doi: 10.1017/jog.2016.56.

1.3.4 Sediment export and transient landscape response following Alpine glacier recession

Chapter 8 makes use of rare records of water yield and sediment export to explore decadal scale climate forcing upon small high mountain watersheds. The product presented in this thesis was achieved through a wider collaboration supported with the Swiss National Science Foundation and aided by collaboration with hydropower companies. The focus of the paper identified below is similar in approach but very different in focus, being concerned with an Alpine valley glacier rather than smaller glaciers on Alpine hillslopes:

- Lane, S.N., Bakker, M., Gabbud, C., Micheletti, N. and Saugy, J.-N. (2016). Sediment export, transient landscape response and catchment-scale connectivity following rapid climate warming and Alpine glacier recession, *Geomorphology*,
doi: 10.1016/j.geomorph.2016.02.015.

1.3.5 Structure-from-Motion (SfM) photogrammetry

Most topographic surveying techniques require relative expensive technologies or specialized user supervision. For that reason, it comes with no surprise that the advent of Structure-from-Motion photogrammetry was acclaimed with great interest by geomorphic researchers. Structure-from-Motion technology allows the use of consumer grade digital camera and highly automated data processing (often fee to use), as opposed to the traditional requirements of relatively expensive sensors and specialized user supervision. Chapter 4 consists of a research paper that investigates the geomorphological potential of freely available and accessible Structure-from-Motion photogrammetry using very basic image acquisition devices, in this case smartphones. The lesson learned from this research are reproduced in another publication, aspiring to guide potential new users in successfully applying this technique for a range of geomorphic studies:

- Micheletti, N., Chandler, J.H. and Lane, S.N. (2015). Structure from Motion (SfM) Photogrammetry, *Geomorphological Techniques*, Chap. 2, Sec. 2.2.

1.4 Organization of the manuscript

This thesis manuscript includes four distinct parts, structured as follows. This introductory part has provided a brief overview of the thesis, identified its motivation and objectives and summarised the key contributions of the project not presented herein. In the more technical Part II, Chapter 2 introduces remote sensing approaches as a resource for Alpine research. The remaining three chapters of Part II address developments of digital photogrammetry and laser scanning for the quantification both whole landscapes and individual landforms. Part III addresses the investigation of the impact of climate forcing upon high mountain environments. Each chapter includes a piece of research that employs, amongst others, the techniques described in Part II for the study of the evolving dynamics of Alpine landscapes. Finally, Part IV summarizes the main findings of this thesis, offers a brief reflection on the implications for understanding Alpine landscapes and discusses possible future research directions in the field.

Bibliography

Ballantyne, C. K., Wilson, P., Gheorghiu, D., and Rodés, A. (2014). Enhanced rock-slope failure following ice-sheet deglaciation: timing and causes. *Earth Surface Processes and Landforms*, 39(7):900–913.

Brocklehurst, S. H. and Whipple, K. X. (2002). Glacial erosion and relief production in the Eastern Sierra Nevada, California. *Geomorphology*, 42(1-2):1–24.

Houghton, J. T., Jenkins, G. J., and Ephraums, J. J., editors (1990). *Climate Change: The IPCC Scientific Assessment*. Cambridge University Press, Cambridge, Great Britain, New York, NY, USA and Melbourne, Australia.

Kääb, A., Frauenfelder, R., and Roer, I. (2007). On the response of rockglacier creep to surface temperature increase. *Global and Planetary Change*, 56:172–187.

Knight, J. and Harrison, S. (2013). The impacts of climate change on terrestrial Earth surface systems. *Nature Climate Change*, 3(1):24–29.

Oliva, M. and Ruiz-Fernandez, J. (2015). Coupling patterns between para-glacial and permafrost degradation responses in Antarctica. *Earth Surface Processes and Landforms*, 40(9):1227–1238.

Parry, M. L., Canziani, O. F., Palutikof, J. P., van der Linden, P. J., and Hanson, C. E., editors (2007). *Contribution of Working Group II to the Fourth Assessment Report of the Intergovernmental Panel on Climate Change*. Cambridge University Press, Cambridge, United Kingdom and New York, NY, USA.

Pelto, M. S. and Hedlund, C. (2001). Terminus behavior and response time of North Cascade glaciers, Washington, USA. *Journal of Glaciology*, 47:497–506.

Remote sensing methods for Alpine Part II research

2 Introduction to remote sensing

2.1 An overview of the science of remote sensing

From a general point of view, *remote sensing* is the science of obtaining information (*sensing*) about objects or surfaces from a distance (*remote*). In this regard, it represents an alternative to *in-situ* (on site) observations. The nature of the sensed signal may be very diverse: optical, acoustic, or microwave [Schowengerdt, 2007]. Depending on the type of interaction with the target, two categories of remote sensors can be distinguished, namely active and passive sensors. In active remote sensing, instruments are equipped with a source of radiation used to send signals towards the object of interest. Subsequently, the sensor registers the radiation that is scattered back by the target surface. The most common examples of active remote sensing acquisitions employed in environmental sciences include laser methods (Light Detection And Ranging - LiDAR, Vosselman and Maas [2010]) and radar systems (e.i. Synthetic Aperture Radar - SAR, Curlander and McDonough [1992]). In contrast, passive sensors merely record the solar electromagnetic radiation that is reflected or spontaneously emitted by the Earth's surface, without directly stimulating the object of interest. The most trivial example is a photograph, but of great relevance nowadays is multispectral and hyperspectral imagery obtained by Earth observation satellites [Richards and Jia, 1999]. Furthermore, remote sensing technologies may be distinguished by their mode of acquisition, which can be ground-based, airborne or satellite-borne.

The format of remotely acquired data may vary. The most common structure is the recording of the acquired information in a set of cells commonly called pixels, that are subsequently organized in a regular raster grid (an image). On the other hand, some technologies (e.g. LiDAR) produce a series of three-dimensional coordinates of varying spatial density, called point clouds. The interpolation of such clouds onto regular grids or triangulated irregular network for practical use is common (e.g. Alho et al. [2009]; Jaboyedoff et al. [2012]; Gabbud et al. [2015]). Frequently, and according to needs, the final outcome of the remote sensing acquisition can be spatially geo-referenced and integrated in a Geographic Information System (GIS) environment, where further analysis involving overlapping spatial layers can be performed.

2.2 Why sense Alpine environments remotely?

One of the major obstacles in high mountain geomorphological research is the remoteness of the sites of interest, which makes their direct access troublesome and consequently *in situ* measurements arduous to obtain. Furthermore, collecting evidence for most Alpine environments requires information over the (often vast) spatial extent at which geomorphologic processes are manifest. High mountain research can benefit from three-dimensional information to quantify topography and to characterize surface changes over time. Remote sensing is able to fulfil this by providing extensive information on terrain geometry and cover, significantly contributing to our understanding of dynamic processes, their sensitivities and of potential impacts on human and natural systems [Kääb, 2002].

In the field of geomorphology, Digital Elevation Models (DEMs) from remotely sensed data represent a prime tool for such morphometric analyses [Fischer et al., 2011], and have known substantial developments in their generation and use at high spatial resolution in the last 25 years [Lane et al., 2010]. A DEM is a quantitative model of the terrain in digital form. It can be created using direct survey data, but adopting remotely sensed data is usually preferable when spatial extension exceeds the very local scale. Varied remotely sensed data are exploitable for DEM generation, including optical images and LiDAR point clouds, tested in this thesis for Alpine research at multiple temporal and spatial scales. Photographic technology is employed in the context of digital photogrammetric approaches. In this regard, we engage with both aerial (archival and recently, specially flown) and hand-held sensors, and we deploy both traditional "stereo" photogrammetry and innovative Structure-from-Motion processing approaches. Further, we exploit the potential of the ground-based mode of LiDAR technology, namely Terrestrial Laser Scanning (TLS).

2.3 Analytical photogrammetry

Photogrammetry is the art, science, and technology of obtaining reliable information about physical objects and the environment through processes of recording, measuring, and interpreting photographic images and patterns of recorded radiant electromagnetic energy and other phenomena [Wolf et al., 2014]. Traditionally, photogrammetry was used to extract three-dimensional informations from two-dimensional images using optical and mechanical stereo-plotters [Slama, 1980]. With the developments of computerized numerical methods in the 1980s, new analytical photogrammetric techniques became practicable, reducing the several technical and physical constraints of the traditional photogrammetric approach, notably (i) camera position and orientation restrictions; and (ii) the requirement for metric cameras [Chandler and Moore, 1989]. Furthermore, and as characteristic of remote sensing approaches, a photograph is a "non-contact" measurement technique, thus adapted for collecting information about inaccessible or dangerous areas, which has commonly been problematic in Alpine environments. By virtue of these advantages, geomorphologists have extensively operated with analytical photogrammetry in recent decades (e.g. Kääb and Vollmer

[2000]; Lane et al. [2010]; Fischer et al. [2011]; Bennett et al. [2012]). For complete details on the foundational principles of photogrammetry, the reader can refer to Wolf et al. [2014]. The principles of photogrammetry application for geomorphological research are discussed in detail in Chandler and Moore [1989] and Lane et al. [1993, 1994]. A brief summary of the main concepts is presented here.

In the field of photogrammetry, a distinction is made between *photo-coordinate space* and the *object-coordinate space.* The former serves as a reference for positions in the image space, where the x and y axis are parallel to the photograph plan, the z axis perpendicular to it, and the origin is the camera lens (O also called *perspective centre*). The latter is defined as the three-dimensional real-world coordinates that could be employed to describe the object or area of interest. The relationship between two mutually associated coordinate systems is referred to as *projective transformation* and serves as the functional basis for the two *collinearity equations* (e.g. Chandler and Moore [1989]; Wolf et al. [2014]):

$$x = \frac{-c[r_{11}(X-X_0) + r_{21}(Y-Y_0) + r_{31}(Z-Z_0)]}{[r_{13}(X-X_0) + r_{23}(Y-Y_0) + r_{33}(Z-Z_0)]} \tag{2.1}$$

$$y = \frac{-c[r_{12}(X-X_0) + r_{22}(Y-Y_0) + r_{32}(Z-Z_0)]}{[r_{13}(X-X_0) + r_{23}(Y-Y_0) + r_{33}(Z-Z_0)]} \tag{2.2}$$

where X, Y and Z are real-world coordinates of one point in the object space, X_0, Y_0 and Z_0 are the coordinate of the perspective centre in the object space system, r_{11} to r_{33} are the elements of the *rotation matrix* which are functions of the orientation of the camera axis in the object space and c is the focal length of the camera. In other words, one point in the object space simultaneously have real-world coordinates $[X, Y, Z]$ and photo-coordinates $[x, y, -c]$, and the two systems are thus related. Whilst the image coordinates x and y are measured and the calibrated focal length c is a constant, these two equations have three unknowns, namely the coordinates of the object point X, Y and Z. Hence, it is necessary to use a second photograph for obtaining a unique solution and computing new object coordinates simply by measuring two conjugate points on the images. In Figure 2.1, the theoretical aspects of analytical photogrammetry are illustrated.

The collinearity model described above implies that real-world coordinates can be derived for each point that is identified in two images, but requires known image positions (X_0, Y_0 and Z_0 for each image). These are usually derived using a mathematical procedure, of which the most widely used and efficient is the *bundle adjustment* [Granshaw, 1980]. The latter requires at least three ground control points to be known in the object space, and their correspondence in the image spaces to be measured. From then on, camera parameters (position and rotation) can be obtained for each photograph using a least-squares estimation.

The advent of fully automated methods during the 1990s marked the transition from traditional photogrammetric procedures to digital photogrammetry using digital imagery (either obtained
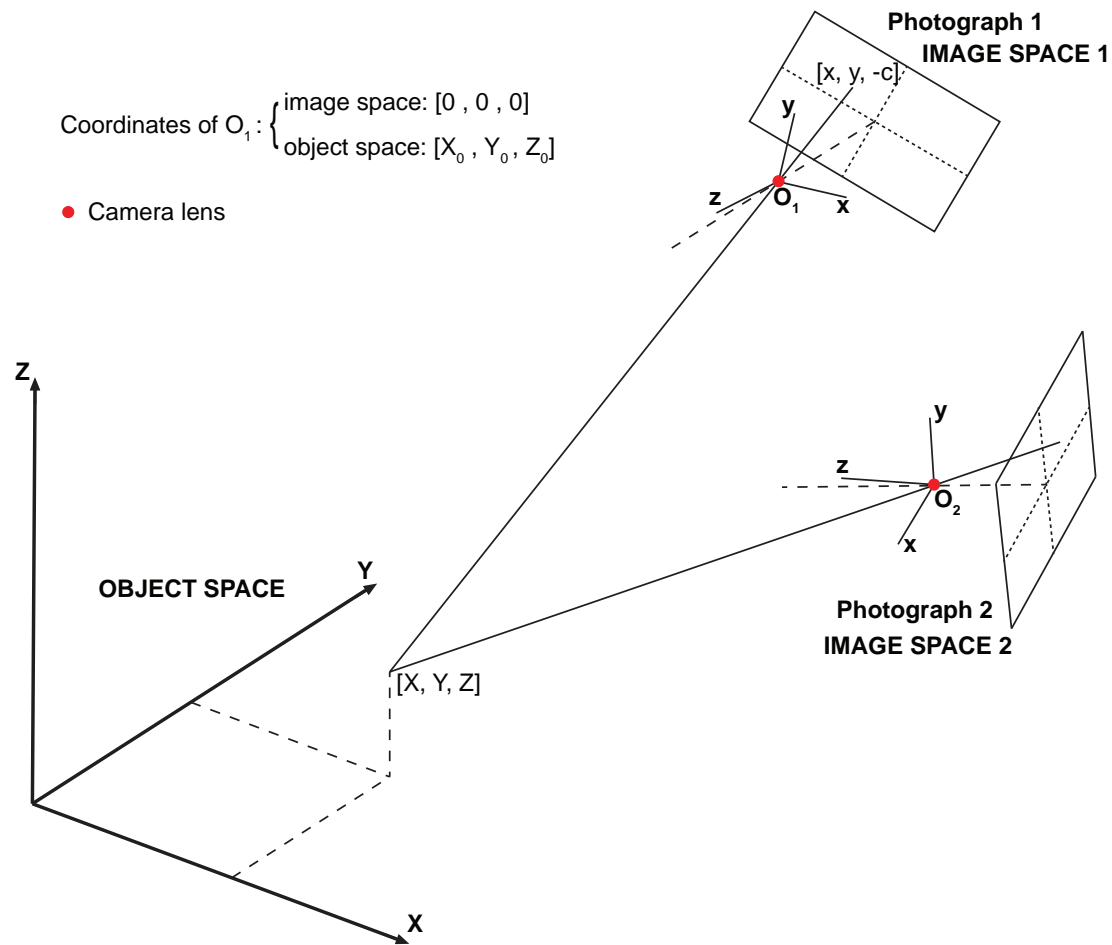
Figure 2.1 – Theoretical aspects of photogrammetry: the projective transformation between the object space and the image space (modified from Chandler and Moore [1989] and Lane et al. [1994]).

as such or digitised). One of the major advantages here has been the introduction of automatic stereomatching algorithms, able to identify large numbers of homologous point pairs in two or more images and to compute their ground coordinates using camera parameters [Dissart and Jamet, 1995]. Subsequently, photogrammetry became a widely used, cost- and time-effective approach for geoscience research [Lane et al., 2000], where remarkable new frontiers of development are still being crossed nowadays (e.g. by the advent of new methods like Structure-from-Motion (SfM) using Multi-View Stereo algorithms, see Smith et al. [2015]).

2.3.1 Aerial photogrammetry

The term "aerial photogrammetry" indicates the application of the principle illustrated above to aerial photographs (see Figure 2.2). This utilization of photogrammetry is particularly useful in the field of cartography or when the necessity to survey a large area exists. Crucially, aerial

photogrammetry represents a unique resource for deriving three-dimensional information on past landscapes using the extensive coverage of aerial imagery commonly collected by national agencies since the 1950s. These photographs are often digitised using appropriate photogrammetric scanners, and therefore we refer to the procedure as *archival aerial digital photogrammetry*. Whilst airborne-derived photographs are traditionally collected using frame cameras, today a wide use is made of digital devices. Nowadays, aerial imagery is often employed to obtain DEMs or orthorectified photographs over large spatial extents, allowing the detection of vertical changes, measuring terrain displacements or precise mapping.

airplane design: freepik.com
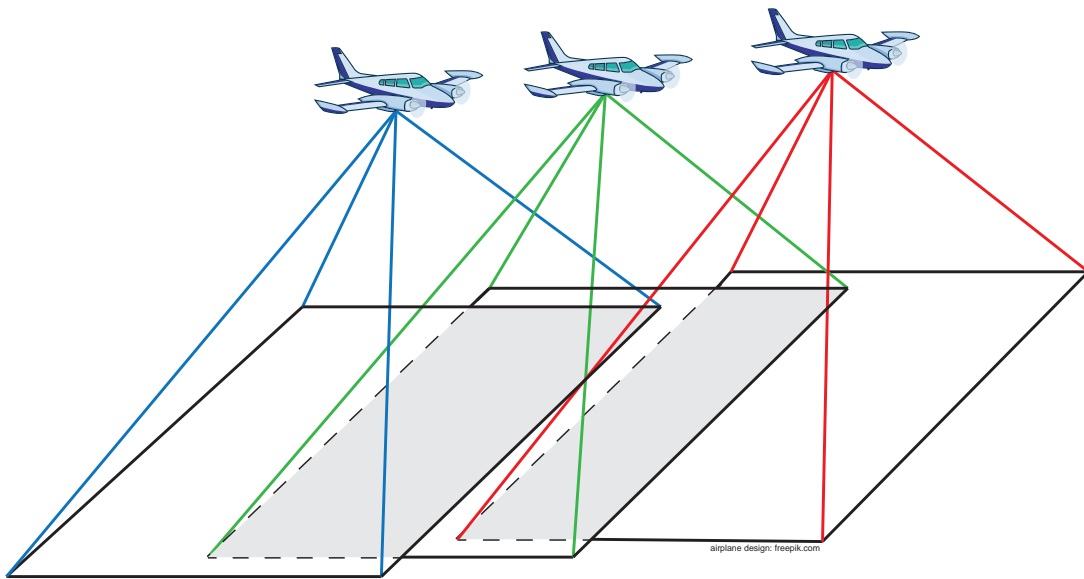
Figure 2.2 – Principle of aerial photograph acquisition; overlapping images of the landscape are acquired by collecting multiple photos in the course a single flight.

In contempt of its wide use, the application of aerial photogrammetry for geomorphological research still poses complications, in particular when exploiting archival imagery in Alpine regions. First, collecting enough good quality ground control data in Alpine landscapes can be challenging. These areas may be difficult to access, unstable (and hence unreliable as ground control) and devoid of easily identifiable spots, as infrastructure. Second, applications of aerial photogrammetry in zones of large elevation ranges can be problematic, by reason of occlusions and of the possible low densities of the acquired data in areas of complex or rough topography. Third, because archival aerial imagery may have been acquired at a large range of flying heights, its scale may be unsuitable for generating precise elevation data within small areas. Accordingly, the limits of detectable changes need to be carefully considered to ensure correct interpretation of results. Furthermore, the contrast and quality of old imagery may vary, and not always be optimal for this type of analysis. Finally, despite the ease with which elevation data can be extracted from photographs, conventional processing principles and controls upon photogrammetrically-derived data are still crucial and need careful consideration. These issues are approached and discussed in Chapter 3, where a workflow including caveats to

overcome these challenges is proposed.

2.3.2 Structure-from-Motion photogrammetry

Structure-from-Motion photogrammetry has its origins in the machine vision community, where it was used for the tracking of points across sequences of images occupied from different positions. This method has been developed and adapted for generating elevation data using potentially many images collected in sequence [Fonstad et al., 2013]. As in traditional photogrammetry, SfM employs overlapping images acquired from multiple viewpoints [Micheletti et al., 2015]. However, SfM photogrammetry differs from traditional photogrammetric approaches by determining internal camera geometry and camera position and orientation automatically using image-matching processes, without the need for a pre-defined set of ground control data [Westoby et al., 2012]. SfM approaches are often extended to include Multi-View Stereo (MVS) photogrammetry algorithms to increase the point density by several order of magnitude [Smith et al., 2015].

The exact implementation of Structure-from-Motion may vary from one software package to another. Smith et al. [2015] proposes a schematic representation of the typical workflow. Micheletti et al. [2015] summarized its general functioning as follows:

"Multiple views of an object are captured with a digital camera from a range of different positions. A scale invariant feature transform (SIFT) then identifies common feature points across the image set, sufficient to establish the spatial relationships between the original image locations in an arbitrary 3-D coordinate system. A sparse bundle adjustment (e.g. Snavely et al. [2008]), needed to transform measured image coordinates into 3-D points covering the area of interest, is used in this process. The result is three-dimensional locations of the feature points in the form of a sparse point cloud in the same, local three-dimensional coordinate system. The sparse point cloud is then intensified using Multi-View Stereo (MVS) techniques (e.g. Furukawa and Ponce [2010]). It is the ability of these techniques to generate very high resolution datasets, whilst isolating and removing gross errors, which is now allowing such visually impressive 3-D models to be generated so easily when compared to traditional stereo-based DEM generation methods involving stereomatching [Remondino et al., 2014]."

Recent developments in the field have two crucial components: first, because of the ease with which sensor distortion can be modelled, the range of sensors that can be used has increased; second, low-cost and fully automated platforms has opened the doors for non-specialized users. This progress, along with the rising popularity of smartphones and of Unmanned Aerial Vehicles (UAVs) or drones, has created a fertile ground for the spread of this technology in various disciplines. A detailed review of Structure-from-Motion photogrammetry and its application in physical geography is provided by Smith et al. [2015]. That said, its new found popularity has been at the expense of a number of issues, well-rehearsed in traditional photogrammetry, but often overlooked in the rapid adoption of SfM methods. The user is much less involved in data quality control, thus the origins of errors in the derived models may

not be easy to identify. Furthermore, image quality, scale and geometry still play a fundamental role in the delivery of high quality results. These controls are investigated in Chapter 4, where an examination of the potential of fully automated SfM photogrammetry in combination with consumer grade digital cameras is carried out.

2.4 Terrestrial laser scanning

Terrestrial Laser Scanning (TLS) is the ground-based application of Light Detection And Raging (LiDAR) technology, which consists of measuring the properties (principally the distance) of a target by illuminating it with a laser beam and analysing the back-scattered, returning signal. The acronym laser stands for light amplification by stimulated emission of radiation. Laser light has the unique properties of being monochromatic (single frequency and wavelight), coherent (all light waves in phase with each other) and directional (collimated: parallel waves) [Cameron, 2013]. A TLS device emits an ultraviolet, visible or near-infrared beam and employs the time of flight of the laser pulse to compute the distance between the target surface and itself. By virtue of mirrors or mechanics that orientate the laser beam in a well-defined direction, and by knowing the line of sight and the attitude of the device (its lateral axis "*pitch*", vertical axis "*yaw*" longitudinal axis "*roll*") it is possible to determine the three-dimensional position of the reflective surface relative to the device [Jaboyedoff et al., 2012]. Hence, back-scattered signals captured by the receiver are converted to $[\Delta X, \Delta Y, \Delta Z]$ coordinates relative to the scanner's position. A single laser beam may result in multiple back-scattered signals (e.g. if the beam hits dust in the air or vegetation but proceeds through, see Figure 2.3).
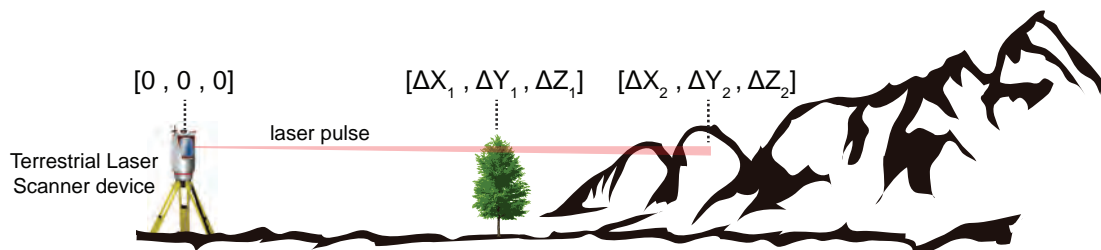
Figure 2.3 – Principle of Terrestrial Laser Scanning data acquisition, with two back-scattered signals for a laser beam.

TLS campaigns produce 3D point clouds (e.g. Figure 2.4), generally with high point density, and sequential acquisitions of the latter are regularly used for detecting and quantifying topographic change (e.g. Schürch et al. [2011]; Jaboyedoff et al. [2012]; Abellan et al. [2014]; Gabbud et al. [2015]). Since modern devices are able to collect many millions of points, working on the resulting dataset is often challenging in terms of computational efforts. In Chapter 5, a semi-automatic, cluster method to facilitate and improve the quality of point clouds analysis is proposed. For further details on the principles of LiDAR technology, see Shan and Toth [2008] and Vosselman and Maas [2010].

<div align="center">(a)</div>
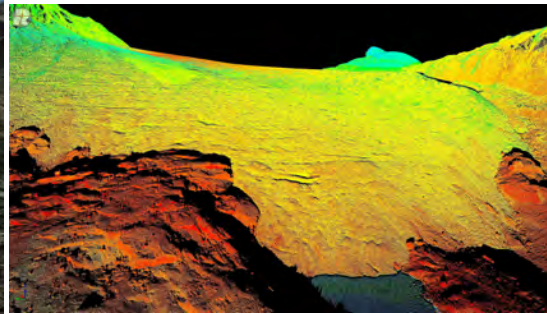
<div align="center">(b)</div>

Figure 2.4 – (a) RIEGL VZ-6000 Terrestrial Laser Scanner operating at the front of the Conejeras glacier, Colombia (b) Example of TLS-derived point cloud (laser reflectance as colours for visualization purposes).

Bibliography

Abellan, A., Oppikofer, T., Jaboyedoff, M., Rosser, N. J., Lim, M., and Lato, M. J. (2014). Terrestrial laser scanning of rock slope instabilities. *Earth Surface Processes and Landforms*, 39:80–97.

Alho, P., Kukko, A., Hyyppa, H., Kaartinen, H., Hyyppa, J., and Jaakkola, A. (2009). Application fo boat-based laser scanning for river survey. *Earth Surface Processes and Landforms*, 34:1831–1838.

Bennett, G. L., Molnar, P., Eisenbeiss, H., and McArdell, B. W. (2012). Erosional power in the Swiss Alps: characterization of slope failure in the Illgraben. *Earth Surface Processes and Landforms*, 37(15):1627–1640.

Cameron, M. H. (2013). *Physical Agents in Rehabilitation: From Research to Practice.* Elsevier/Saunders, St. Louis, Missouri, USA.

Chandler, J. H. and Moore, R. (1989). Analytical photogrammetry: a method for monitoring slope instability. *Quarterly Journal of Engineering Geology and Hydrogeology*, 22(2):97–110.

Curlander, J. C. and McDonough, R. N. (1992). *Synthetic Aperture Radar: Systems and Signal Processing.* Wiley, New York.

Dissart, O. and Jamet, O. (1995). 3D reconstruction of buildings from stereo images using both monocular analysis and stereo matching: an assessment within the context of cartographic production. *Proceedings of the Society of Photo-Optical Instrument Engineers*, 2486:255–266.

Fischer, L., Eisenbeiss, H., Kääb, A., Huggel, C., and Haeberli, W. (2011). Monitoring Topographic Changes in a Periglacial High-mountain Face using High-resolution DTMs, Monte Rosa East Face, Italian Alps. *Permafrost and Periglacial Processes*, 22(2):140–152.

Fonstad, M. A., Dietrich, J. T. Courville, B. C., L., J. J., and Carbonneau, P. E. (2013). Topographic structure from motion: a new development in photogrammetric measurement. *Earth Surface Processes and Landforms*, 38(4):421–430.

Furukawa, Y. and Ponce, J. (2010). Accurate, dense, and robust multiview stereopsis. *IEEE Transactions on Pattern Analysis and Machine Intelligence*, 32:1362–1376.

Gabbud, C., Micheletti, N., and Lane, S. N. (2015). Lidar measurement of surface melt for a temperate Alpine glacier at the seasonal and hourly scale. *Journal of Glaciology*, 61:963–974.

Granshaw, S. I. (1980). Bundle adjustment methods in engineering photogrammetry. *The Photogrammetric Record*, 10(56):181–207.

Jaboyedoff, M., Oppikofer, T., Abellan, A., Derron, M.-H., Loye, A., Metzger, R., and Pedrazzini, A. (2012). Use of LIDAR in landslide investigations: a review. *Natural Hazards*, 61:5–28.

Kääb, A. (2002). Monitoring high-mountain terrain deformation from repeated air- and space borne optical data: examples using digital aerial imagery and ASTER data. *ISPRS Journal of Photogrammetry & Remote Sensing*, 57:39–52.

Kääb, A. and Vollmer, M. (2000). Surface Geometry, Thickness Changes and Flow Fields on Creeping Mountain Permafrost: Automatic Extraction by Digital Image Analysis. *Permafrost and Periglacial Processes*, 11:315–326.

Lane, S. N., Chandler, J. H., and Richards, K. S. (1994). Developments in monitoring and modelling small-scale river bed topography. *Earth Surface Processes and Landforms*, 19(4):349–368.

Lane, S. N., James, T. D., and Crowell, M. D. (2000). Application of digital photogrammetry to complex topography for geomorphological research. *The Photogrammetric Record*, 16(95):793–821.

Lane, S. N., Richards, K. S., and Chandler, J. H. (1993). Developments in photogrammetry; the geomorphological potential. *Progress in Physical Geography*, 17(3):306–328.

Lane, S. N., Widdison, P. E., Thomas, R. E., Ashworth, P. J., Best, J. L., Lunt, I. A., Sambrook Smith, G. H., and J., S. C. (2010). Quantification of braided river channel change using archival digital image analysis. *Earth Surface Processes and Landforms*, 35(8):971–985.

Micheletti, N., Chandler, J. H., and Lane, S. N. (2015). Structure from Motion (SfM) Photogrammetry. *Geomorphological Techniques*, Chap. 2:Sec. 2.2.

Remondino, F., Spera, M. G., Nocerino, E., Menna, F., and Nex, F. (2014). State of the art in high density image matching. *The Photogrammetric Record*, 29(146):144–166.

Richards, J. A. and Jia, X. (1999). *Remote Sensing Digital Image Analysis: An Introduction*. Springer.

Schowengerdt, R. A. (2007). *Remote Sensing: Models and Methods for Image Processing*. Academic Press, Elsevier Inc.

Schürch, P., Densmore, A. L., Rosser, N. J., Lim, M., and McArdell, B. W. (2011). Detection of surface change in complex topography using terrestrial laser scanning: application to the Illgraben debris-flow channel. *Earth Surface Processes and Landforms*, 36(14):1847–1859.

Shan, J. and Toth, K. (2008). *Topographic laser ranging and scanning: principles and processing*. CRC Press, Taylor & Francis Group, LLC, UK.

Slama, C. C., editor (1980). *The Manual of Photogrammetry*. American Society of Photogrammetry.

Smith, M. W., Carrivick, J. L., and Quincey, D. J. (2015). Structure from motion photogrammetry in physical geography. *Progress in Physical Geography*, doi: 10.1177/0309133315615805.

Snavely, N., Seitz, S. M., and Szeliski, R. (2008). Modeling the World from Internet Photo Collections. *International Journal of Computer Vision*, 80(2):189–210.

Vosselman, G. and Maas, H.-G. (2010). *Airborne and Terrestrial Laser Scanning.* CRC: Boca Raton, FL, USA.

Westoby, M. J., Brasington, J., Glasser, N. F., Hambrey, M. J., and Reynolds, J. M. (2012). 'Structure-from-Motion photogrammetry': A low-cost, effective tool for geoscience applications. *Geomorphology*, 179:300–314.

Wolf, P. R., Dewitt, B. A., and Wilkinson, B. E. (2014). *Elements of Photogrammetry with Applications in GIS.* McGraw-Hill Education: New York, Chicago, San Francisco, Athens, London, Madrid, Mexico City, Milan, New Delhi, Singapore, Sydney, Toronto.

3 Application of archival aerial photogrammetry to quantify climate forcing of Alpine landscapes

Natan Micheletti, Stuart N. Lane, Jim H. Chandler

Context

With technological advance, digital photogrammetry has become increasingly automated and cost-effective. Nonetheless, terrain model generation remains complicated by the user needing to define critical parameters and choose appropriate algorithms, along with proper field data collection and handling of uncertainty. Furthermore, a number of complications might arise when working with archival imagery of low contrast or sub-optimal scale, or in areas of complex topography. As a consequence, good practice at different stages of data processing is not always well understood by non-expert users.

This chapter presents a possible workflow to overcome the challenges represented by topographic complexity (including occlusions and large elevation changes), variation in image texture and sub-optimal image scale that are often encountered by geomorphologists working with aerial photogrammetry in steep and complex terrains, especially when using archival imagery. Whilst of wider interest for expert users, this contribution primarily seeks to serve as a benchmark for geomorphological research undertaken by non-photogrammetrists in mountainous regions.

In the context of this thesis, the chapter represents the methodological foundation for the investigation of Alpine landscapes dynamics using archival aerial photogrammetry (Chapters 7 and 8).

Abstract

Recent and future climate change may lead to landscape changes in geomorphic processes and process rates. Such modifications are likely to be widely distributed, making their direct measurement difficult and there are almost no such measurements at decadal intervals. Aerial imagery has been acquired by many national agencies since the 1950s and significant archives remain. Unlocking the information from these data sources is important because their timescale may inform significant unresolved hypotheses regarding the impact of rapid climate change on Alpine environments. However, such photogrammetric applications are challenging because of topographic complexity (including occlusions and large elevation ranges) and variations in image texture. A complete workflow is described from raw data to the treatment and interpretation of results. This is applied to imagery of Val d'Héréns, Switzerland, a landscape containing an assemblage of glacial, periglacial, hillslope and fluvial landforms across a height range of 1800 to 3600 m from the 1960s to the present. These changes reveal important characteristics of landscape scale erosion and deposition at the decadal scale.

Keywords: aerial photogrammetry; archival imagery; climate forcing; digital elevation model; geomorphic changes; geomorphology;

3.1   Introduction

Geomorphological research is always in need of three-dimensional data to describe topographic surfaces and to monitor their change over time. The possibility of generating quantitative elevation data from stereo photography has played an important role in this regard, as demonstrated by pioneer applications of photogrammetry to geomorphological studies [Wickens and Barton, 1971; Welch and Jordan, 1983; Small et al., 1984; Chandler and Cooper, 1988; Chandler and Moore, 1989; Lane et al., 1994]. With the advent of fully automated methods and the transition from traditional to digital photogrammetry during the 1990s, photogrammetry became a widely used, cost- and time-effective approach for geoscience research [Lane et al., 2000]. Crucially, it represents a unique resource for deriving three-dimensional data of past landscapes using the extensive coverage of aerial imagery commonly available since the 1950s. This type of application, named archival aerial digital photogrammetry, has proved successful for a wide range of fields, including fluvial geomorphology [Lane et al., 2003, 2010], permafrost and periglacial processes [Kääb and Vollmer, 2000; Kneisel and Kääb, 2007; Fischer et al., 2011], and hillslope processes [Chandler and Brunsden, 1995; Walstra et al., 2007; Schwab et al., 2008; Bennett et al., 2013].

Despite the ease with which elevation data can be extracted from imagery, including new photogrammetric methods like structure from motion (SfM) (for example, Fonstad et al. [2013]), the application of digital photogrammetry for geomorphological research still poses the following complications:

1. The ease of automated data generation offered by digital photogrammetry may cause the user to underestimate data quality issues [Cooper, 1998; Lane et al., 2000] or to overlook key data quality controls [James and Robson, 2014]. This is problematic because in spite of the advanced algorithms and automated processes offered by digital and emerging forms of photogrammetry, conventional controls upon photogrammetrically derived data are still crucial and need careful consideration.

2. The application of aerial digital photogrammetry in areas of complex or rough topography and large elevation ranges can be problematic, particularly occlusions caused by sudden elevation changes or where the density of the acquired data is low in areas of complex topography.

3. Because archival aerial imagery may have been acquired at a large range of flying heights, its scale may be unsuitable for generating precise elevation data within small areas. Accordingly, the limits of detectable changes need to be carefully considered to ensure correct interpretation of results.

4. Older aerial photographs can be characterised by imagery of low contrast and varying quality, which improved with time as photogrammetric emulsions evolved; data processing and the quality of final results will inevitably be affected by this variability.

Sediment production and transfer together with glacial and periglacial processes in high mountain basins are potentially sensitive to the significant changes in climatic conditions that have affected the European Alps over the past century. Understanding the effects of such changing conditions upon landscapes is challenging because of the difficulty of investigating this climate forcing (the difference in insolation (sunlight) absorbed by the earth and energy radiated back into space) over decades to centuries, despite this being the timescale over which significant hypotheses are raised over human impacts upon climate change and consequently geomorphic systems [Reynard et al., 2012; Knight and Harrison, 2013]. Archival aerial imagery offers a unique opportunity to address this scientific topic [Schwab et al., 2008; Bennett et al., 2013]. The research described in this paper seeks to describe the complete workflow adopted for the application of archival aerial photogrammetry in the Swiss Alps to assess the extent to which geomorphological changes associated with climate forcing can be quantified in high mountain landscapes.

A sequence of aerial imagery from the 1960s to the present day has been used to compute digital elevation models for Val Héréns, Switzerland (Figure 3.1). The case study consists of a steep deglaciated zone, ranging from about 1800 to 3600 m above mean sea level (a.s.l.). The area is comprised of an actively changing, and hence locally dynamic, assemblage of glacial, periglacial, hillslope and fluvial landforms. It is likely to be sensitive to climate forcing, by virtue of landforms highly sensitive to temperature changes (glaciers and permafrost) and because of the presence of unconsolidated, historically weathered and glacially derived material, representing high potential for significant sediment mobilisation.
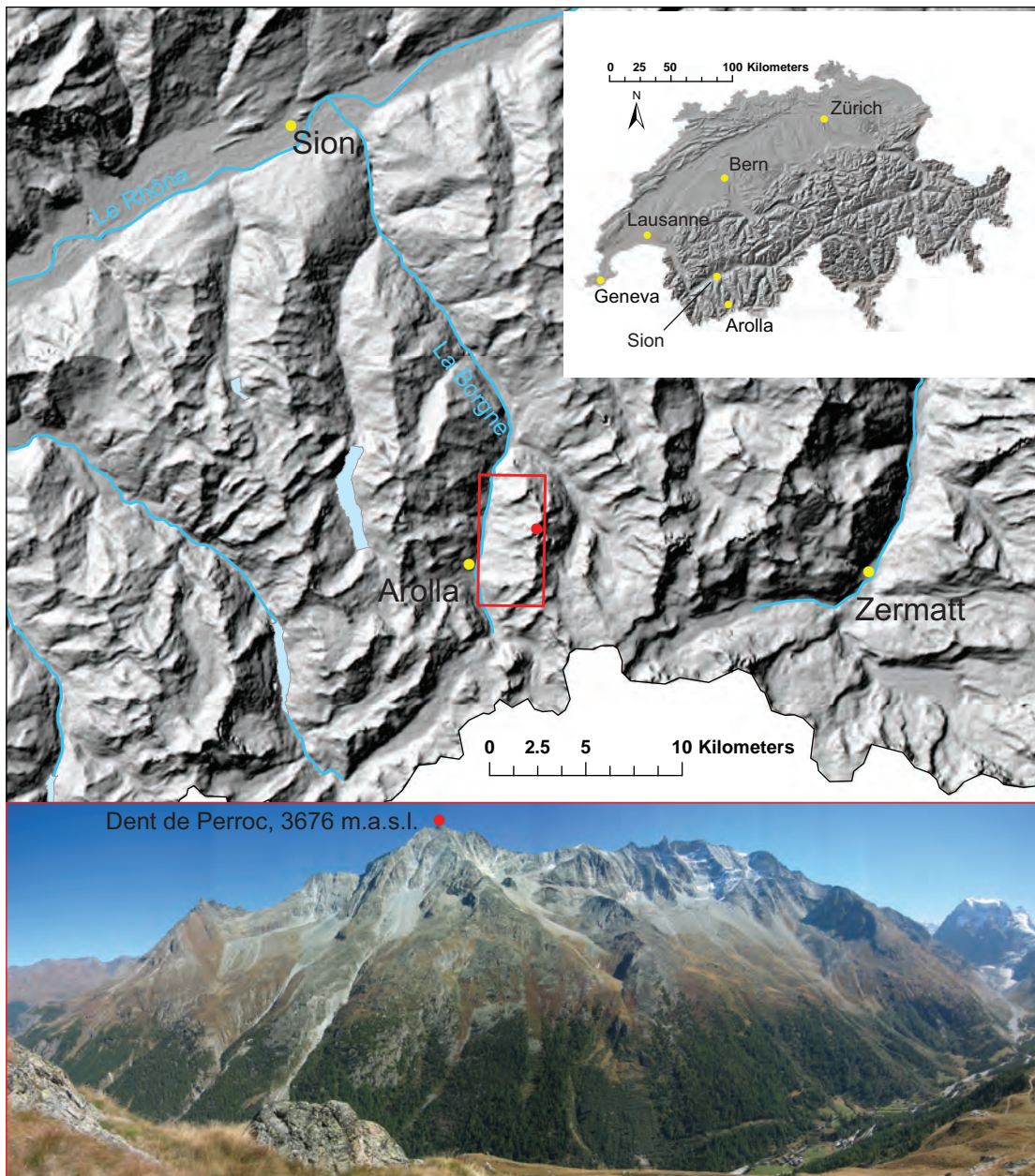
Figure 3.1 – Case study area near Arolla, Héréns Valley, Switzerland, indicated by the red rectangle. The peak of Dent de Perroc is indicated by the red dot on both the map and photograph. Relief shading and river data: Swisstopo. Photography by C. Lambiel, 2004.

In presenting the workflow, the issues that arise at different stages of the data processing are identified and solutions are proposed which are applicable even with limited ground control data. Thus, guidance, advice and caveats are offered for the potential geomorphological applications of archival aerial photogrammetry in high mountain environments. All photogrammetric data processing has been performed using ERDAS IMAGINE Leica Photogrammetry Suite (LPS) 2010, released in November 2009, while post-processing operations and results analysis have been implemented using Matlab and ArcGIS.

Table 3.1 – Characteristics of the aerial imagery available from Swisstopo and Flotron in 2012.

Date	Scale	Lens type	Emulsion	Calibrated focal length [mm]
(1) 28th September 1967	1:15700	Leica 15 UAG 120	BW	152.87
(2) 8th September 1977	1:20900	Leica 3008 15 UAG II	BW	153.02
(3) 19th July 1983	1:19000	Leica 15/4 UAG	BW	153.37
(3) 7th September 1983	1:20900	Leica 15/4 UAG	BW	153.37
(4) 10th August 1988	1:20900	Leica 15/4 UAG	BW	153.37
(4) 10th August 1988	1:23500	Leica 15/4 UAG	BW	153.37
(5) 7th October 1995	1:26800	Leica 15/4 UAG-S	BW	152.52
(6) 2nd September 1999	1:26000	Leica 15/4 UAG-S	RGB	152.52
(6) 2nd September 1999	1:28000	Leica 15/4 UAG-S	RGB	152.52
(7) 17th August 2005	1:24600	Leica 15/4 UAG-S	RGB	153.51
(7) 17th August 2005	1:24800	Leica 15/4 UAG-S	RGB	153.51
(8) 20th September 2012	1:5200	UltraCam-X lenses (4 PAN; 4 MS)	RGB-NIR	100.50

BW = black and white; RGB = red, green, blue (colour); NIR = near infrared; PAN = panchromatic; MS = multi-spectral.

3.2 Aerial imagery and interior orientation

The archival aerial images used in the study were acquired by the Swiss Federal Office of Topography (Swisstopo) using a range of different analogue cameras. These include a number of 23 cm x 23 cm images for seven distinct epochs, all collected at similar periods of the year (end of summer–beginning of autumn) with flying heights varying between 5000 and 7000 m a.s.l. These have been scanned by Swisstopo at a resolution of 14 μm (1814 dpi) using a photogrammetric-quality scanner and vary in scale between 1:15700 and 1:28000. The fore-and-aft (forward) overlap between two consecutive frames in a flight line is about 80%, which is a routine Swisstopo policy because of the high relief displacement in such mountainous areas.

An eighth set of aerial photographs was acquired in 2012 by Flotron using an UltraCam-X digital camera, which represents the most recent dataset of the study. The UltraCam-X camera is equipped with four panchromatic and four multispectral lenses. The images are composed of 14430 x 9420 pixels of 7.2 μm (about 10.39 cm x 6.78 cm frame size) and have a scale of 1:5200. The lateral overlap (sidelap) specification was also 80%; therefore, 12 images were used to cover the whole area of interest. The list of images used for the study and their characteristics are presented in Table 3.1.

A block file representing each epoch was created in ERDAS LPS, using either frame or digital camera geometric models for Swisstopo and Flotron imagery, respectively, and employing the Swiss coordinate system with the geodetic datum CH1903. Calibration certificates were

available at www.swisstopo.admin.ch. This resource provided: (a) the calibrated focal length (principal distance); (b) radial distortions referenced to the principal point of symmetry (PPS); (c) PPS displacement with respect to the focal centre (FC); and (d) fiducial mark coordinates referred to the FC. To complete the definition of the internal geometry of the camera, the fiducial marks were manually measured on the images and a 2D affine transformation established to determine the origin of the photo coordinate system [Intergraph Corporation, 2014]. This transformation was achieved with a sub-pixel root mean square error (RMSE), typical for this type of imagery.

The Flotron digital imagery was provided with a calibration file for the digital camera. This provided the calibrated focal length (100.50 mm) and the PPS offsets. Imagery was corrected by Flotron to show no significant radial distortions. Calibrated fiducial marks and associated management were not necessary because the photo coordinate system can be defined simply by indicating the pixel dimensions (7.2 μm x 7.2 μm) in ERDAS LPS.

3.3   Field data and exterior orientation

Considerable fieldwork was required to establish an appropriate number of ground control points (GCPs) necessary for photogrammetric restitution where the unstable high mountain environment creates significant challenges. The GCPs need to satisfy two requirements: (a) stable over time (that is, not moving or changing in appearance during the period of study); and (b) easily and precisely identifiable on the images. Finding sufficient points with these characteristics can be problematic in an active landscape where some areas are typically: (a) difficult to access; (b) may or may not be experiencing movement over a 50-year period; and (c) may be devoid of infrastructure. Ideal candidates for this kind of study are the corners of roofs of traditional and un-renovated buildings, but use had to be made of the centre of isolated, medium-sized, round-shaped boulders (approximately 2 m in diameter was appropriate given the scale and resolution of the imagery) located in clearly stable areas. Such boulders were preferred because they can be easily identified on images and the uncertainty when measuring their apparent centre is limited. It is also fundamental that the points provide adequate coverage across the site, including a wide elevation range.

Two Leica System 500 differential global positioning system (dGPS) units were used to obtain the required control for the case study, the field campaign being carried out in July 2012. A total of 169 GCPs were measured along the valley bottom and mountainsides, across an area of approximately 20 km^2 (3 km x 6.5 km) and with an elevation range of more than 1000m (1808 to 2828 m a.s.l.) (Figure 3.2). A dGPS base station was established early in the field programme and 6 h of static observations obtained. Data were subsequently downloaded from the nearest available Automated GNSS Network for Switzerland (AGNES) located in Martigny, 30 km away in the Rhône valley. These were post-processed in Leica Geo Office to correct coordinates to the Swiss national coordinate system CH1903. Visual inspection of the horizontal displacements derived by the correction using Swisstopo orthophotos is
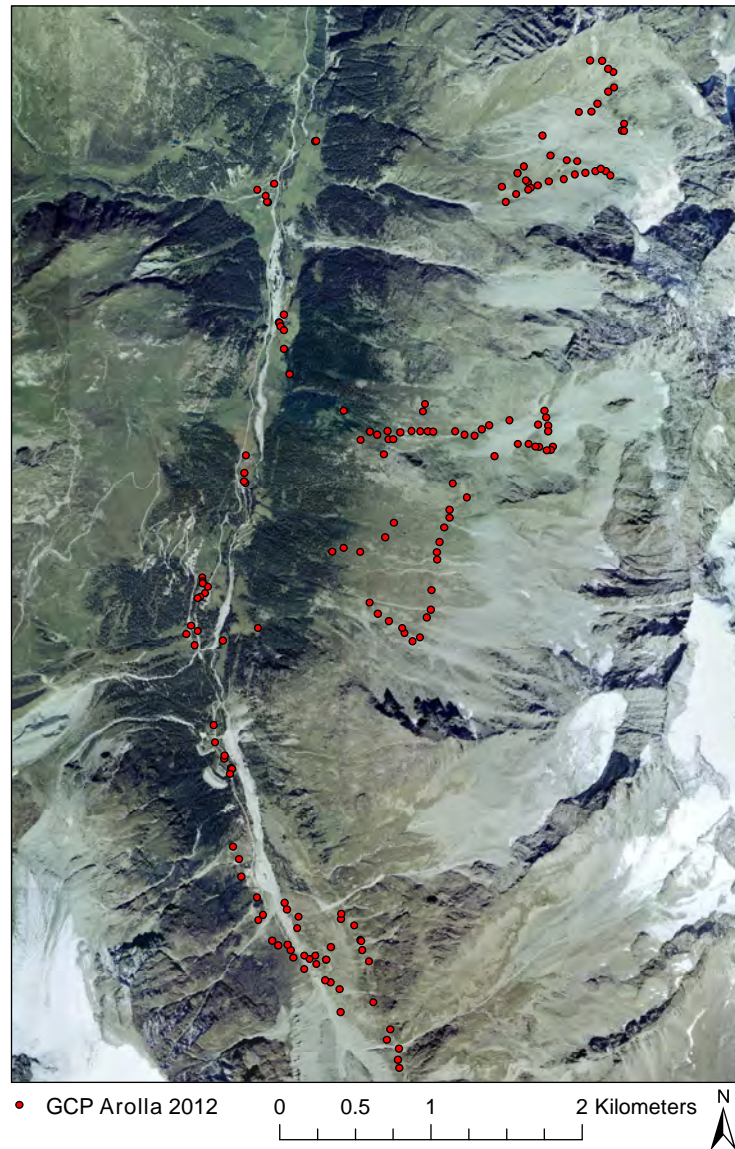
Figure 3.2 – Ground control point distribution in the Arolla Valley, Switzerland, shown by red dots.

shown in Figure 3.3. It was not possible to survey all the points using a single base station because of limitations in radio communication, either because of the base-to-rover distance or due to topographic screening. Three further base stations were established in the valley, all linked directly to the initial base station. Subsequent post-processing of the original real time kinematic (RTK) data allowed the determination of the coordinates of all GCPs in the CH1903 system. All GCP coordinates were estimated with a precision better than ±0.05 m.

To estimate initial exterior orientation parameters associated with each image, the GCPs were manually measured and assigned to the corresponding point on the images. It was not
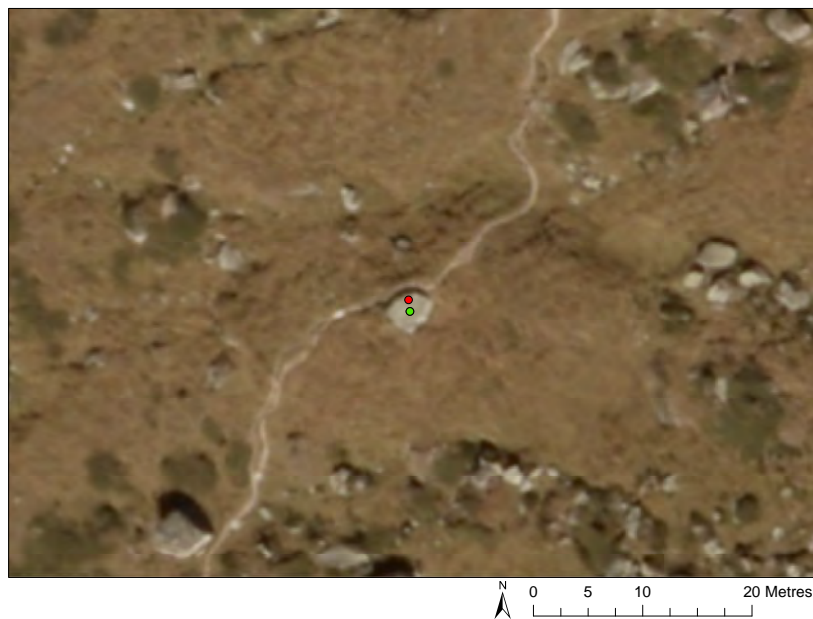
Figure 3.3 – Ground control points before (red) and after (green) applying the post-processing correction using Swiss Automated GNSS Network data. The point, located in a stable area near a path, was measured at the centre of the boulder, but it was necessary to correct the newly established dGPS base position to derive correct coordinates.

necessary to measure all GCPs, and neither could every GCP be found or identified precisely. The availability of a large dataset of GCPs reduced the reliance upon individually measured points, hence improving the quality of the solution. After having identified a sufficient number of control points, well distributed in space and with a large elevation range, a proportion were reclassified as check points. Check points are not used to estimate the exterior orientation parameters but to provide a direct estimate of the accuracy of the restitution. This is done in terms of discrepancy between the photogrammetrically derived position and the GCP coordinates.

After solving the initial bundle adjustment using just GCP measurements, it was possible to perform automatic tie-point extraction. However, and as mentioned in similar studies (for example, Fischer et al. [2011]), this procedure is not efficient for areas including extremely steep terrain and exhibiting many shadows. Therefore, either automatically generated tie points needed to be checked manually or the tie points should be measured manually. An additional problem arose during the processing of the Flotron 2012 imagery. GCPs could not be surveyed on all parts of the mountainside because of dangerous and difficult access in regions of cliffs. This was problematic since, given the large scale of the 2012 images, there were an insufficient number of control points for some frames and LPS (and traditional photogrammetric packages) requires a sufficient number of GCPs for successful solution of the bundle adjustment. To address this issue, a well-established GCP transfer procedure was adopted (see Lane et al. [2010]). First, a bundle adjustment was obtained for those images

where sufficient GCPs were available. Second, on these images, clearly identifiable features were found and marked as common tie points where they were also visible on images without sufficient GCPs. Third, these tie points were relabelled as GCPs and were measured on the images without sufficient GCPs; the measurements were used to obtain a bundle adjustment for all of the imagery. As explained in Lane et al. [2010], it is important to note that these new GCPs have a poorer precision than those surveyed directly in the field using dGPS. However, this approach provided a viable and satisfying solution for images with insufficient GCPs.

ERDAS LPS uses a conventional bundle adjustment to perform the aerial triangulation and to estimate exterior orientation parameters for each image used [Intergraph Corporation, 2014]. In this procedure, image point and GCP standard deviations are crucial and need to be commensurate with the expected precision of both image measurements and object control. This allows for more flexibility during the bundle adjustment and leads to a better solution. Image point standard deviations can be indicated in pixel units and should be related to the measurement precision and image quality/resolution. These values were changed to 0.5 for the scanned Swisstopo imagery, whilst the default value of 0.3 was used for the digital Flotron 2012 imagery. GCPs were constrained to an object precision of 0.5 m in plan and 0.3 m in height. These globally applied values were chosen to account for the following uncertainty sources: (a) imprecision in measuring the centres of boulders or in surveying non-horizontal boulders in steep zones; and (b) uncertainty in dGPS measurements themselves, including post-processing with AGNES data.

ERDAS LPS offers a number of indicators to estimate the quality of the exterior orientation solution. The total image unit-weight (TIUW) RMSE is a global precision indicator describing the quality of the entire solution in the image space [Intergraph Corporation, 2014]. Root mean square errors for both control and check points are also provided, and for both ground coordinates (X, Y, Z) and stereo intersection accuracy in image coordinates (x, y) [Fischer et al., 2011; Intergraph Corporation, 2014]. The aerial triangulation summary for each epoch is presented in Table 3.2. Overall, the bundle adjustment yielded very satisfying results and in accordance with what was expected assuming the known data quality. This is of fundamental importance because it has been shown that random error in a bundle adjustment can translate into systematic error in the stereomatching derived data (for example, Lane et al. [2004]), and so effort is required to minimise them. These data also give a preliminary indication of the possible precision of data points extracted from the imagery although, as discussed below, this may be downgraded according to the success of the stereomatching process.

3.4 Automatic stereomatching

In digital photogrammetry, automatic stereomatching algorithms are used to identify homologous point pairs and to compute their ground coordinates using exterior orientation parameters [Dissart and Jamet, 1995]. These algorithms are based upon detecting similar image intensity patterns within either small image "areas" or located around distinct "features".

Table 3.2 – Exterior orientation performances

Date	TUIW RMSE	Control point RMSE					Check point RMSE				
		X	Y	Z	x	y	X	Y	Z	x	y
1967	0.41	0.46	0.43	0.15	0.31	0.31	0.42	0.23	0.26	0.07	0.11
1977	0.30	0.28	0.28	0.14	0.29	0.30	0.41	0.07	0.18	0.32	0.01
1983 (July)	0.32	0.23	0.29	0.14	0.41	0.33	0.15	0.45	0.44	0.24	0.09
1983 (Sept)	0.31	0.30	0.27	0.10	0.29	0.30	0.45	0.15	0.43	0.21	0.08
1988	0.33	0.41	0.45	0.26	0.44	0.35	0.36	0.30	0.45	0.21	0.39
1995	0.29	0.29	0.37	0.19	0.32	0.25	0.09	0.29	0.56	0.28	0.18
1999	0.36	0.30	0.31	0.22	0.35	0.30	0.38	0.33	0.38	0.25	0.20
2005	0.34	0.22	0.28	0.17	0.28	0.33	0.25	0.27	0.38	0.26	0.21
2012	0.17	0.12	0.13	0.14	0.17	0.19	0.28	0.24	0.18	0.14	0.22

TIUW = total image unit-weight; X, Y, Z ground coordinates are in metres; x, y photo coordinates are in pixels.

This distinction is the basis of classifying the approaches into either featurebased or area-based [Remondino et al., 2014]. Feature-based approaches achieve correspondence between interest points. These are locations which exhibit "distinctness" and identified using an interest operator, generally attributed to Förstner [1986]. On the other hand, area-based methods correlate small windows of pixels on two images to perform the matching. Accordingly, crucial to the matching process is sufficient texture or variations in pixel intensity in the images [Lane et al., 2000; Remondino et al., 2014]. In ERDAS LPS, two area-based stereomatching algorithms are now available, Automated Terrain Extraction (ATE) and enhanced Automated Terrain Extraction (eATE), the latter being capable of classifying points. Both eATE and ATE were evaluated and considered but ATE required more modest computing resources and was more rapid, easier to use and hence more effective. In addition, ATE has been successfully used in the past on a range of projects [Walstra et al., 2007; Lane et al., 2010] and was therefore adopted for this study. ATE exploits the epipolar constraint to improve the image-matching process and offers customisable strategy parameters for optimising results, along with suggested parameter sets for a number of terrain types (such as high mountains, rolling hills, urban areas and so on). These parameters may strongly influence coordinate determination in mountainous regions [Lane et al., 2000]. Among the parameters available, the correlation coefficient limit, the correlation window size and the search window size on the epipolar line are indicated as the most important [Leica Geosystems Geospatial Imaging, 2006]. The correlation coefficient limit indicates the minimum acceptable correlation for two matched pixels for the point to be accepted. A high coefficient threshold inevitably identifies only high-quality matches [Lane et al., 2000]. It is obvious that a trade-off is necessary for this parameter; keeping only high-quality matched points means that the total number matched is smaller, which can be a problem in mountainous topography where the relief can be complex. On the other hand, accepting low-correlation matches can allow false matches to be included in the dataset and

hence produce poorer quality data. The default value for this parameter for high mountains is 0.8 [Intergraph Corporation, 2014]. The correlation window size is the size (in pixels) of the area used for computing the correlation coefficient between sets of pixels on different images. This usually needs to be smaller for areas containing large variations in topographic relief, grey level or colour intensity; the default value proposed by ERDAS LPS [Intergraph Corporation, 2014] for high mountain regions is 7 x 7 pixels. The search window size across the epipolar line can be adapted to help point matching in cases where the exterior orientation is of low quality; that is, to permit the matching of points further away from the epipolar line. Finally, the user needs to indicate the output cell size, which determines the resolution of the rasterised digital elevation model (DEM). In this research, for reasons explained below, point clouds of ground coordinates generated from matched points and exterior orientation parameters are preferred as output instead of an already rasterised or triangulated DEM.

The strategy parameters would be expected to affect different surface characteristics in different ways, not least because surface cover influences image texture. Thus, to assess strategy parameter effects, a very high density of check data is needed, and certainly beyond what could be acquired practicably during a normal field campaign [Lane et al., 2004]. The alternative is to use sensitivity analysis where key parameters are varied one at a time to quantify their effects on estimated elevations (for example, Lane et al. [2000]; Gooch and Chandler [2001]). Consequently, the effect of varying the correlation coefficient limits (from 0.7 to 0.9) and correlation window sizes (from 5 x 5 to 11 x 11 pixels) was quantified. The comparison of results is performed at the level of point clouds (X, Y, Z coordinates), by associating points within a Euclidean distance of 0.5 m in X and Y, and comparing their elevation in order to assess the sensitivity of the extracted data to strategy parameters. For this detailed sensitivity analysis, two pairs of images from the 1988 epoch were used. Three regions of interest (ROIs) with contrasting terrain characteristics and image texture were identified for the analysis (Figure 3.4a): (a) a field of large boulders; (b) a zone of fine sediments and texture; and (c) a steep area with abrupt elevation changes. Changing the correlation window or the search window sizes did not produce any change for any of the three ROIs, an outcome that can be explained by the robustness of the exterior orientation solution and the presence of sufficient texture in the images. However, modifying the correlation coefficient limit has important consequences. Increasing the coefficient from 0.7 to 0.8 causes a reduction of about 10% in the number of extracted points, while an increase from 0.8 to 0.9 only produces a further 3% reduction. This is satisfying since it indicates that using the suggested value for high mountain environments (0.8) provides good-quality output. Furthermore, changing the correlation coefficient also causes elevation changes to some points (Table 3.3). These differences have an expectation μ and a median Q_{50} of zero for each ROI, although, the degree of spread varies. To help interpret the distribution of elevation differences, the cumulated distribution of the absolute elevation discrepancies is shown in Figure 3.4b. The latter demonstrate that the majority of points are not sensitive to the strategy parameters, as confirmed by the low value containing two-thirds of absolute residuals (the 66% quantile (0.66) in Figure 3.4b corresponding to 0.17 m elevation difference for the fine texture zone and 0.34 m for the other two).

(a)

(b)
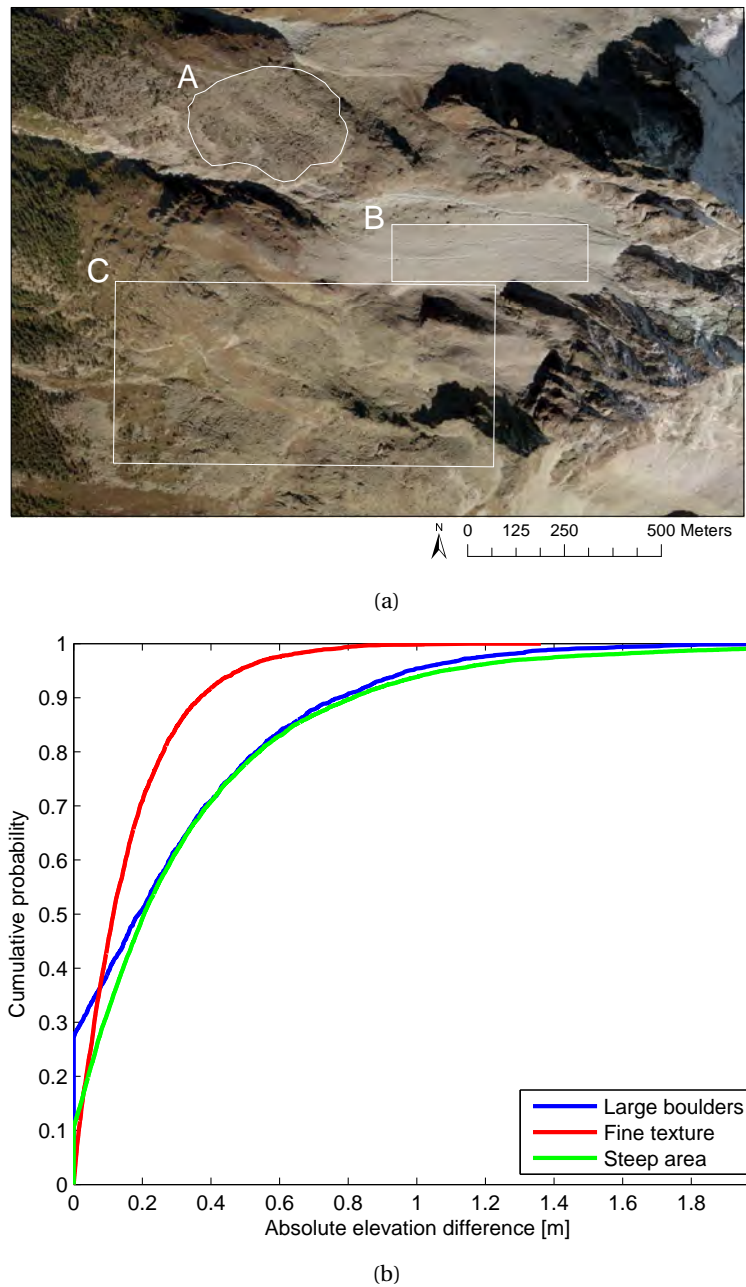
Figure 3.4 – (a) Zones of different morphology and texture (A, large boulders; B, fine texture; C, steep area). (b) Effect of correlation coefficient parameter change (from 0.8 to 0.9) on single points for zones of different morphology and texture shown in (a).

Changes in stereomatching strategies appear to affect only some points in the generated DEM. This justified further use of the failure warning model (FWM) developed by Gooch and Chandler [2001], who employed it to demonstrate that changing strategy parameters affect only less robust points in steep, low-texture or shadowed areas, whilst elevation estimations for the remainder of the derived points are almost unaffected. In this study, FWM was used

Table 3.3 – Distribution statistics of elevation difference caused by changing the correlation coefficient parameter from 0.8 to 0.9 on single points.

Zone	μ	σ	Q_{50}	$\mu(abs(\text{dZ}))$	Q_{50} of abs	Q_{66} of abs
Boulders	0	0.45	0	0.29	0.19	0.34
Fine texture	0	0.23	0	0.16	0.12	0.17
Steep area	0	0.62	0	0.34	0.20	0.34

μ is the expectation; σ is the standard deviation; Q_{50} *of abs* is the median and Q_{66} *of abs* the 66% quantile of the absolute height differences $abs(\text{dZ})$.

as an informative tool to define automatically areas that are susceptible to changes in the strategy parameters and thus where elevation data are unreliable. This approach is used to justify the use of the strategy parameters employed and provides an alternative to the lengthy and demanding parameter optimisation process, which requires independent data.

The principle of the FWM is that the sensitivity of strategy parameters can be used to identify areas where elevation data quality is likely to be poorer and thus provide a caveat for further DEM use. The FWM algorithm includes two parts:

1. The slope in an area around interpolated points is investigated to identify unreliable interpolation estimates, which is particularly critical in complex or steep topographic zones.

2. The identification of areas susceptible to changes in the strategy parameters using DEMs of difference (DoD). In this stage, the value of each point in the difference image is examined individually. If that value is greater than the standard deviation σ of all points in the model multiplied by a user definable parameter A (here $A = 1$), the point is tagged as sensitive:

$$\left| \text{DoD}_{x,y} \right| > A \cdot \sigma(\text{DoD}). \tag{3.1}$$

To continue the investigation of the effect of varying the strategy parameters on the stereomatching procedure, phase (2) of the FWM was applied here for the 1959 and 1988 epochs (Figure 3.5). Results are consistent between the two years, with similar zones sensitive to strategy parameters highlighted by the model. These correspond mostly to steep, low-texture or shadowed areas. In contrast, the rest of the area does not seem to be affected by changes in the strategy parameters. On this basis, the final data were processed using the suggested parameters for high mountain areas for every epoch, and the observation regarding the lower confidence of data points in relatively steep, low-texture or shadowed areas was noted. A masking procedure is necessary to address issues in these areas, as explained later.

(a) 1988   (b) 1959
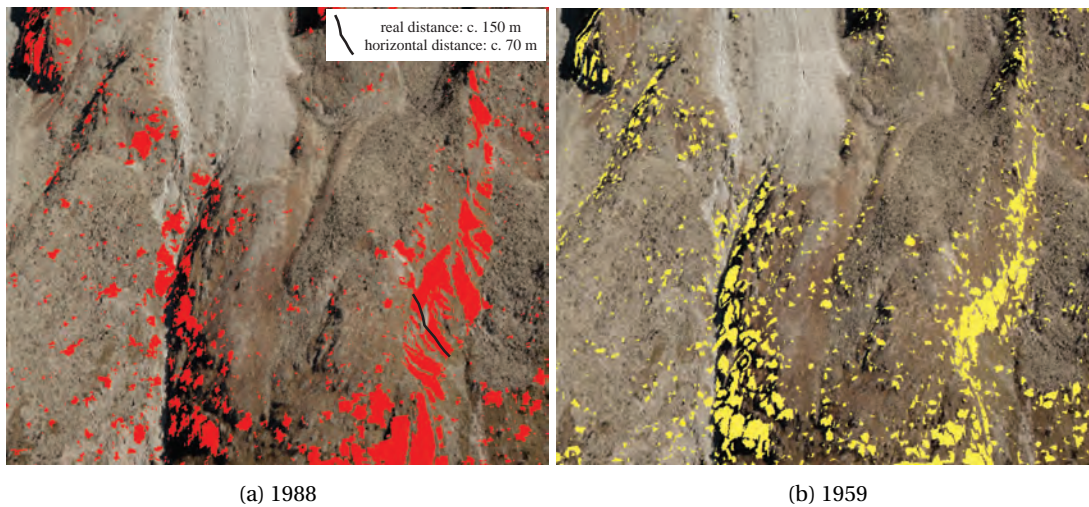
Figure 3.5 – Example of 3D visualisation of failure warming model (FWM) output for: (a) 1988 (red); and (b) 1959 (yellow) imagery, generating similar results in highlighting very steep or low-textured areas.

3.5 Data post-processing

For each image used in this research, raw point clouds of ground coordinates generated from matched points were extracted using the ATE DEM extraction module in LPS. Despite a robust bundle adjustment and stereomatching parameters adapted to mountain regions, the derived elevation data can still present errors in the form of mismatched points that generate either negative or positive spikes. A common practice to address these issues is the application of a filter over the rasterised DEM, typically a low-pass filter, but this is known to cause loss of detail and possible propagation of error into good points [Lane et al., 2004; Milledge et al., 2009]. Hence, it is preferred to adopt an approach able to identify and remove elevations that are probably incorrect. To perform this operation, the following two filtering methods were adopted:

1. The first employs a statistical Chauvenet-type criterion using reliable external elevation data in the form of a coarse registration DEM (25m resolution Swisstopo DEM from 2005). Each derived elevation Z_p is evaluated as follows:

$$\left| Z_p - Z_c \right| > 1.96 \cdot \textit{stdfilt}\,(\text{coarse DEM}) \tag{3.2}$$

where Z_p is the elevation of a stereomatching derived point, Z_c is the pixel value of the coarse DEM where the point falls and *stdfilt* (coarse DEM) is the standard deviation of the elevation in the 3 x 3 neighbourhood around this pixel. This condition identifies elevations that significantly differ from the coarse DEM. By using a locally derived standard deviation, the algorithm allows for large differences in steep zones but is less permissive in flatter areas. Since it relied on a 2005 DEM in this study, it is clear that the

filter is not reliable where local rates of elevation change over time are high. Therefore, a geomorphological map [Lambiel et al., 2016] was used to identify zones matching this condition, such as glaciers, debris-covered glaciers, push moraines or rock glaciers. The filter was not applied in such regions.

2. The second method is a topographic criterion using localised slope data to detect spikes. A triangulated irregular network (TIN) was generated from the point cloud and slopes steeper than 50°were highlighted. Points responsible for these slopes were removed and the TIN updated to deal with clusters of erroneous points. The iteration was completed three times. This method is clearly not reliable for very steep slope zones or cliffs, hence these areas were identified and removed from the analysis.

The combined outcome for both methods was used to decide whether to retain or remove points, and the geomorphological map [Lambiel et al., 2016] was employed to use the filter more appropriately to the local land surface. DEM error is supposed to vary with the type of surface and hence error-handling procedures should be sensitive to surface type and be adaptable to ensure retention of good-quality points. Further, this procedure was applied only in cases where the derived data seemed to contain erroneous points in order to avoid the unnecessary elimination of high-quality points.

An interpolation in the geographical information system (GIS) environment ArcGIS was performed to generate the final 1 m resolution raster DEMs using ordinary kriging, with polynomial trend removal of order 3 and a stable variogram model. Since the derived datasets generally have a high density of points, the effect of the interpolation on the result is expected to be considerably reduced. However, areas with lower densities are indeed present and are very sensitive to the choice of the interpolator and its parameters. In this regard, comparative analysis of interpolators is discussed in the literature such as Aguilar et al. [2005] and Arun [2013]. Where more than one image pair was necessary to cover the ROI, mosaicking was performed in ERDAS 2010 using the overlapping function "feather". Examples of hill shading for 2012 data and for archival Swisstopo imagery are presented in Figure 3.6.

3.6 Quality assessment and error propagation

The final DEMs should be evaluated to establish their quality. This may be achieved by taking datasets from different dates and comparing individual data points for zones where it is absolutely certain that no changes have occurred [Dewez et al., 2013]. In this research it could not be assumed that there were zones of no change and so it was necessary to focus upon high-resolution and high-quality independent data points. However, such data are not typically available in this kind of study and, therefore, it can be challenging to obtain a reliable estimation of the quality of a derived DEM. In this case there were a number of high-quality spot measurements in the form of unused GCPs, and these were available for quality assessment. In this analysis, only points on the hillslope were used to assess the final

(a) 2012
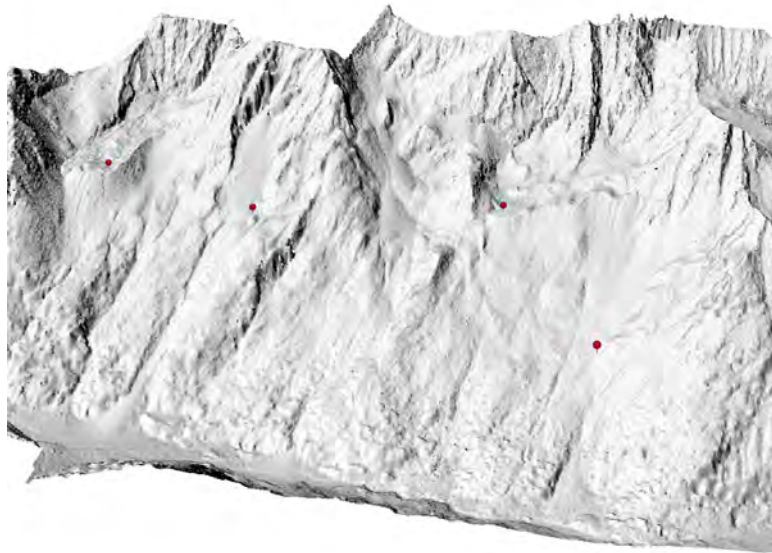
(b) 1988

Figure 3.6 – Examples of hill shading with examples of four common points in red: (a) recent Flotron imagery from 2012; (b) archival Swisstopo data from 1988.

DEMs. As in Lane et al. [2000], the error was defined as the difference in elevation between the dGPS measurement and the DEM value at that location, and the error value is used to compute accuracy in the form of the mean error (ME) and precision in the form of the standard deviation of error (STD) as follows:

$$\textbf{STD} = \sqrt{\frac{\sum_{i=1}^{n}((p_i - s_i) - (\overline{p-s}))^2}{n}} \tag{3.3}$$

where p_i and s_i are the associated photogrammetric DEM and dGPS survey elevations, respectively. Use of the ME and the STD in this way requires the errors to be Gaussian, which is

Figure 3.7 – Q–Q plot (left) and cumulative distribution function (right) of error data versus a standard normal distribution: (a) oldest (1967) DEM; (b) most recent (2012) DEM.

often not the case in digital photogrammetric applications [Höhle and Höhle, 2009]. Gaussian error allows a probabilistic confidence approach to the propagation of error (see below). If the errors are not Gaussian, alternative approaches are needed to estimate random error. Höhle and Höhle [2009] proposed guidelines for robust accuracy measures suited to a non-normal error distribution based on quantile descriptors.

To investigate the normality of the error distribution, measured quantiles (Q) were plotted against the quantiles of a normal distribution having the same mean and standard deviation, in a Q–Q plot, and the two cumulative distribution functions were compared (Figure 3.7). Additionally, the Lillifors test was used to evaluate the null hypothesis that DEM errors are normally distributed. In every case the hypothesis was accepted at the 5% significance level. The outcome verified that all DEM error distributions follow a normal distribution.

Table 3.4 summarises the quality of DEMs for each year. The MEs are not null, indicating a small bias in the DEMs. Effectively, dGPS elevations are generally higher than their DEM

equivalents and there is no spatial structure in this bias. To provide a better estimation of absolute elevation changes between the years, these biases have been removed by adding the ME to each DEM.

Table 3.4 – DEM precision and accuracy assessment using dGPS survey data

DEM date	1967	1977	1983	1988	1995	1999	2005	2012
ME	0.315	0.504	0.281	0.296	0.541	0.493	0.453	0.356
STD	0.765	0.820	0.953	0.644	0.751	0.827	0.998	0.462

ME = mean error; STD = standard deviation of error.

This study is concerned with quantifying climate forcing of Alpine landscapes, that is, investigating the possible link between climatic conditions and morphological changes in the landscape. The identification of patterns of erosion and deposition from DoD is a fundamental aspect in this regard. Moreover, it is necessary to adopt a framework to quantify the confidence that apparent erosion and deposition patterns are real changes and not noise associated with random errors in surfaces computed using digital photogrammetry. On the basis of the framework for error analysis proposed by Taylor [1997], Lane et al. [2003] applied an error propagation methodology where the uncertainty in the magnitude of change σ_c in the DoD is determined by the root of the sum in quadrature of the uncertainties σ_1 and σ_2 associated with the two individual DEMs:

$$\sigma_c = \sqrt{\sigma_1^2 + \sigma_2^2} \tag{3.4}$$

The STD is used here as a measure of uncertainty, but it can be employed to formulate statistical testing of the significance of each elevation difference $Z_1 - Z_2$ using a t test [Lane et al., 2003]:

$$t = \frac{Z_1 - Z_2}{\sqrt{\sigma_1^2 + \sigma_2^2}} \tag{3.5}$$

This equation can be used to threshold the DoD, hence labelling elevation differences within the threshold as noise. With $t = 1$, the confidence limit for detection of change is 68%. In the research described here, the minimum level of detection was set with a confidence limit of 90% ($t = 1.64$). This was selected to have greater confidence that a discrepancy is indeed significant and represents real geomorphological change, whilst maintaining enough informative signals in the DoD. Table 3.5 summarises the limit of detection of change (LDC) at this confidence limit for DoDs computed between different epochs. The change detection that can be achieved corresponds to ±1 to ±3 parts per 10000 of the flying height.

The last operation that was necessary prior to DoD analysis required an irresolvable aerial

Table 3.5 – Limit of detection of change (LDC) with confidence limits of 68% and 90% computed using the error propagation methods explained in the text.

Year pair	68% confidence limit [m]	90% confidence limit [m]
2012-2005	1.100	1.804
2005-1999	1.296	2.126
1999-1995	1.118	1.833
1995-1988	0.990	1.623
1988-1983	1.135	1.862
1983-1977	1.244	2.040
1977-1967	1.121	1.839
2012-1988	0.793	1.300
1983-1967	1.208	1.981
2012-1967	0.894	1.466

photogrammetric issue to be addressed: DEM comparisons in near-vertical rockwalls or forested areas. Steep rock faces and trees can create significant occlusions because of the differences in position of the cameras associated with a particular stereopair. This problem is more apparent towards the edge of any particular image in the pair and stereomatching processes can be very ineffective in such areas. Only a few matched points representing topographic high points are derived, and interpolation between isolated data points is very unreliable because topographic low points are not present. Accordingly, DoDs will always feature extensive and unrealistic elevation differences in these areas (see the example in Figure 3.8). A precise reconstruction of these areas is beyond the scope of archival digital applications unless more images of the same date are available; hence a masking procedure was applied here. With the help of orthorectified images, hill-shaded representations, point clouds and DoDs, limits of rockwalls and forest boundaries were manually identified and excluded from the datasets.

3.7 Climate forcing and geomorphic changes in Alpine landscapes: an illustration

Following the methodology presented above, a DEM has been generated for each available year from the 1960s to the present day. What this yields in terms of our understanding of climate forcing in Alpine landscapes is now illustrated. Reference to the climatic conditions that affect the landscape is also necessary for this purpose; this is provided by the mean annual air temperature (MAAT) data for Switzerland (such measurements began in 1864 and are provided by the Swiss Federal Office of Meteorology and Climatology [MeteoSwiss, 2014]). Figure 3.9 displays the deviation of each MAAT from a reference mean during the period 1961 to 1990. Such temperature data illustrate that the period 1967 to 1983 was a period of relative climate stability but from 1983 to 2012 relative climate warming occurred.

(a)

(b)
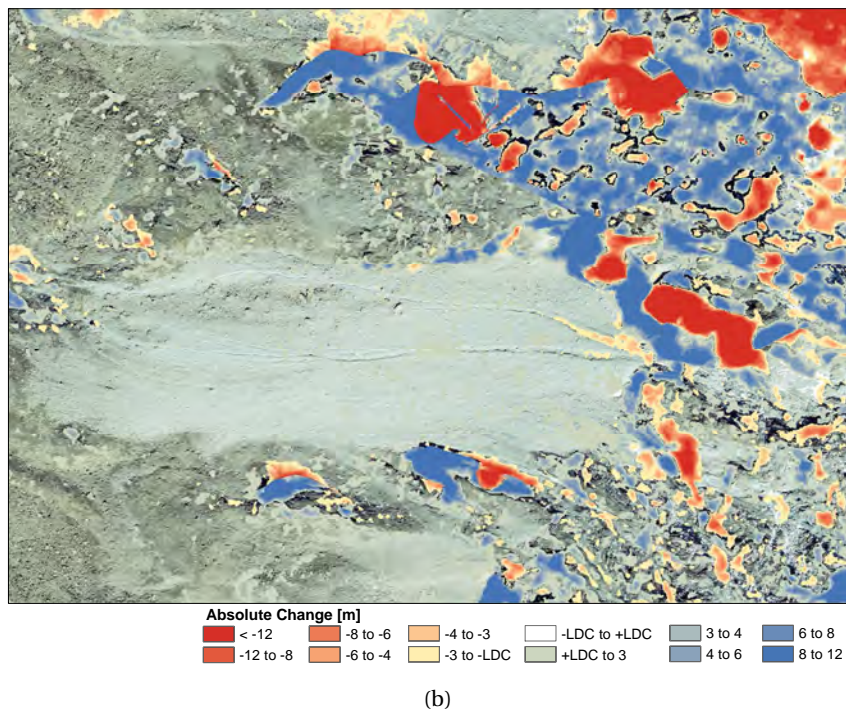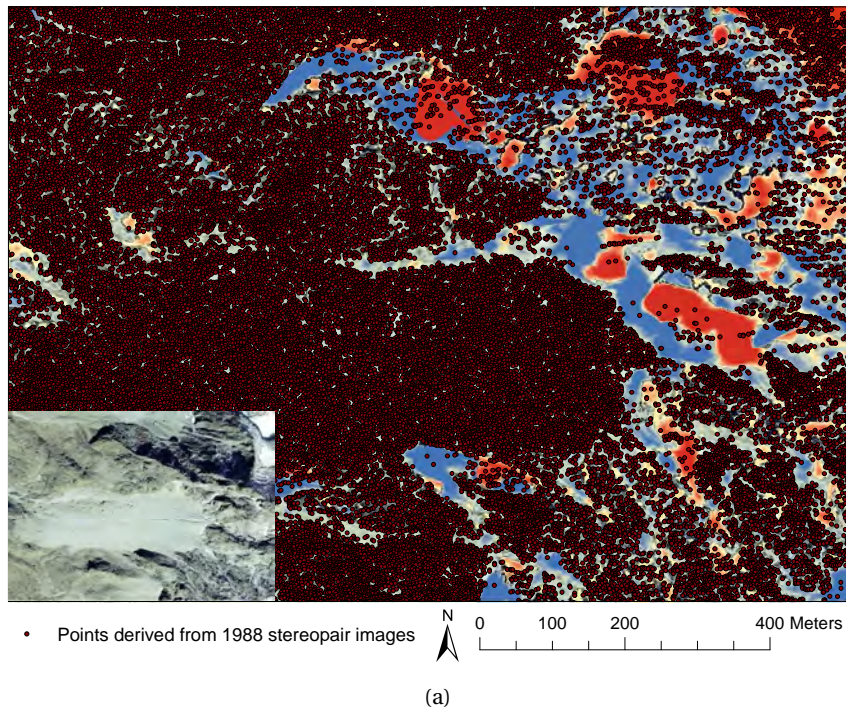
Figure 3.8 – (a) Ineffective stereomatching in rockwalls for a 1988 stereopair shown by data gaps. (b) Consequent unrealistic elevation changes featured in the 2012–1988 DoD (LDC = 1.30 m). Blues represent absolute changes greater than +6 m. Reds represent absolute changes greater than -8 m.

Figure 3.9 – Mean annual air temperatures in Switzerland between 1864 and 2013 as deviation from a reference mean established between 1961 and 1990. The black line indicates the 20-year weighted average (low-pass Gaussian filter). The numbers 1 to 8 indicate the year of available aerial imagery (see also Table 3.1). Data from the Swiss Federal Office of Meteorology and Climatology [MeteoSwiss, 2014].

The interpretation of results is helped by a reference to the spatial assemblage of landforms present; a geomorphological map of the region provided by Lambiel et al. [2016] was used for this purpose (Figure 3.10, right), allowing the identification of which components of the landscape are most sensitive to both climate cooling and climate warming. The comparison between 1983 to 1967 and 2012 to 1988 DoDs is presented in Figure 3.10 (left and centre, where absolute changes and LDC have been normalised by year) and illustrates a distinct response to warming and stable periods. During the stable/cold period the landscape is also very stable, except for glaciers and debris-covered glacier systems that experience a noticeable gain in volume in their upper part; this can be explained by a process of cryogenesis (very low temperatures and their effects). On the other hand, the period from the mid-1980s to 2012 features enhanced hillslope activity, particularly in rock glaciers, rockslides and debris flow channels. It is apparent that warming climatic conditions caused extensive shrinking of glacial systems, especially in the accumulation area and the glacier front zone. Yet, ice ablation is compensated by cold-period ice supply in the central part of the Tsarmine glacier (northern areas in Figure 3.10) and at the front of the Tsa glacier (southeast on the geomorphological map in Figure 3.10). These changes aside, perhaps one of the most interesting elements of Figure 3.10 is the relative stability of this landscape despite recent climate changes.
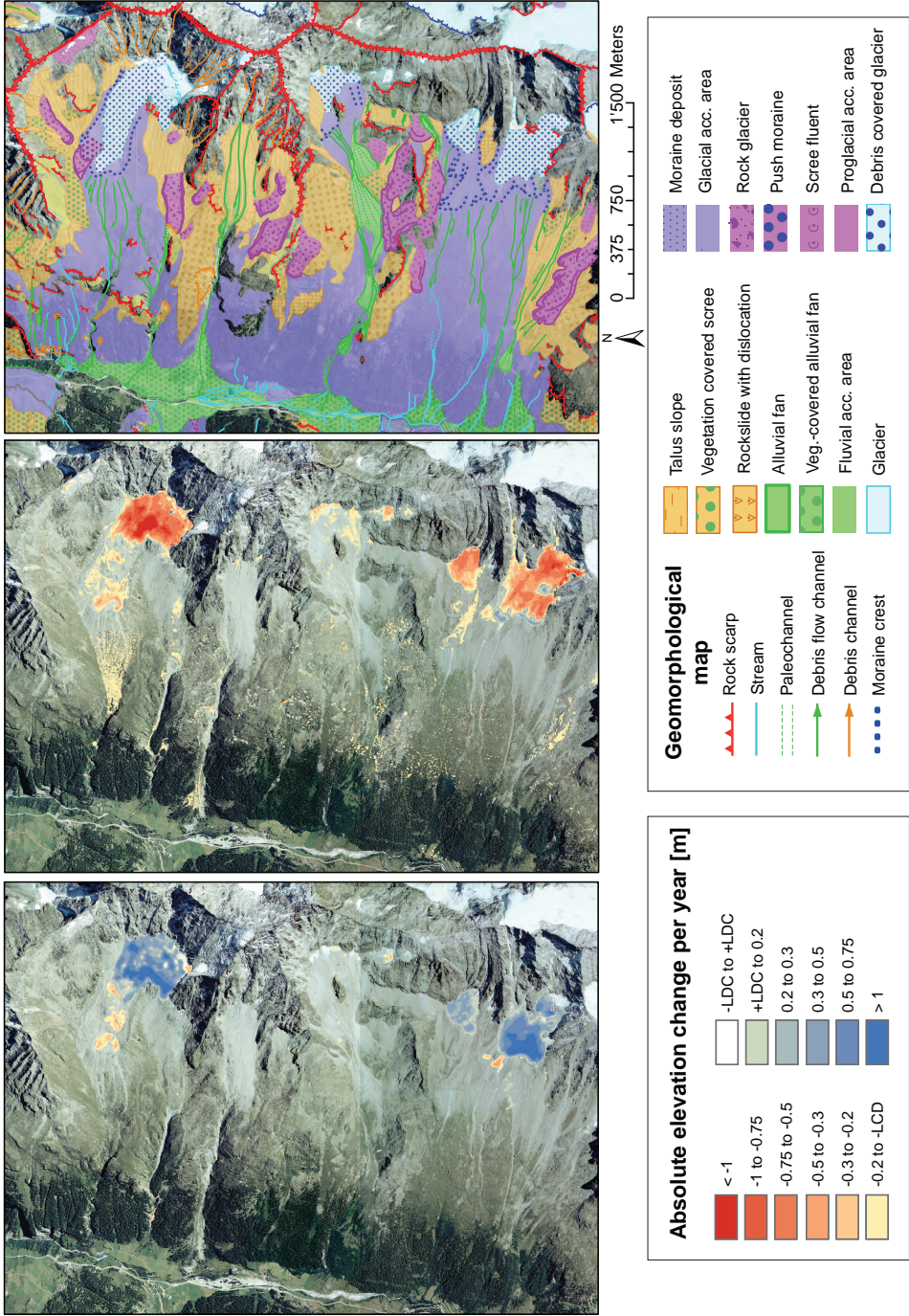
Figure 3.10 – DEMs of difference comparison between the cold period (left, 1983–1967, yearly LDC = 0.054m), and warming period (centre, 2012–1988, yearly LDC = 0.124m). The geomorphological map (right) acts as a reference to the underlying spatial assemblage of landforms present [Lambiel et al., 2016]. A distinct landscape response to both the warming and cooling periods is found. The most evident examples include: cryogenesis in glacier accumulation areas versus glacier retreat and increase in activity of rock glaciers under warming conditions.

3.8 Conclusion

In the present research, a complete workflow for the application of archival aerial photogram-metry to quantify geomorphological changes and climate forcing of high mountain landscapes has been proposed. Archival aerial photogrammetry applications remain challenging in Alpine environments for various reasons, including wide elevation differences, sub-optimal quality and varying scale of imagery, and the difficulties of establishing ground control. The approach articulated in this study and lessons learned are intended to help geomorphologists work with archival aerial imagery for other sites. Ways to overcome these challenges have been presented, including techniques to establish appropriate control, conducting careful analysis outcomes at every step and using a conservative approach for error propagation. Accordingly, this paper demonstrates that it is possible to employ archival imagery to obtain high-quality DEM data suitable for geomorphological research. Results are encouraging and suggest that, even for complex and steep topography, the information locked in archival aerial photogrammetry represents a valuable and exploitable resource. It should be stressed that this technique can only observe changes in elevation greater than 1 to 1.5 m when using imagery of the scale used here (approximately 1:20000). This figure equates well with the expected height accuracy of ± 1 to ± 3 parts per 10000 of the flying height at a single epoch, cited in previous work [Fryer et al., 1994]. Erosion and deposition patterns that create a vertical signal smaller than this cannot be detected reliably using archival aerial imagery of this scale and historical quality.

Acknowledgements

Bibliography

Aguilar, F. J., Agüera, F., Aguilar, M. A., and Carvajal, F. (2005). Effects of terrain morphology, sampling density, and interpolation methods on grid DEM accuracy. *Photogrammetric Engineering & Remote Sensing*, 71(7):805–816.

Arun, P. V. (2013). A comparative analysis of different DEM interpolation methods. *The Egyptian Journal of Remote Sensing and Space Science*, 16(2):133–139.

Bennett, G., Molnar, P., McArdell, B., Schlunegger, F., and Burlando, P. (2013). Patterns and controls of sediment production, transfer and yield in the Illgraben. *Geomorphology*, 188:68–82.

Chandler, J. H. and Brunsden, D. (1995). Steady state behaviour of the Black Ven mudslide: the application of archival analytical photogrammetry to studies of landform change. *Earth Surface Processes and Landforms*, 20(3):255–275.

Chandler, J. H. and Cooper, M. (1988). Monitoring the development of landslides using archival photography and analytical photogrammetry. *Land and Minerals Surveying*, 6(11):576–584.

Chandler, J. H. and Moore, R. (1989). Analytical photogrammetry: a method for monitoring slope instability. *Quarterly Journal of Engineering Geology and Hydrogeology*, 22(2):97–110.

Cooper, M. A. R. (1998). Datums, coordinates and differences. In Lane, S. N., Richards, K. S., and Chandler, J. H., editors, *Landforms Monitoring, Modelling and Analysis*, pages 21–36. Wiley, Chichester, UK.

Dewez, T. J. B., Rohmer, J., Regard, V., and Cnudde, C. (2013). Probabilistic coastal cliff collapse hazard from repeated terrestrial laser surveys: case study from Mesnil Val (Normandy, northern France). *Journal of Coastal Research, Special Issue*, 65:702–707.

Dissart, O. and Jamet, O. (1995). 3D reconstruction of buildings from stereo-images using both monocular analysis and stereomatching: an assessment within the context of cartographic production. *Proceedings of the Society of Photo-Optical Instrument Engineers*, 2486:255–266.

Fischer, L., Eisenbeiss, H., Kääb, A., Huggel, C., and Haeberli, W. (2011). Monitoring topographic changes in a periglacial high-mountain face using high-resolution DTMs, Monte Rosa East Face. *Italian Alps. Permafrost and Periglacial Processes*, 22(2):140–152.

Fonstad, M. A., Dietrich, J. T., Courville, B. C., Jensen, J. L., and Carbonneau, P. E. (2013). Topographic structure from motion: a new development in photogrammetric measurement. *Earth Surface Processes and Landforms*, 38(4):421–430.

Förstner, W. (1986). A feature-based correspondence algorithm for image matching. *International Archives of Photogrammetry and Remote Sensing*, 26(3/3):150–166.

Fryer, J. G., Chandler, J. H., and Cooper, M. A. R. (1994). On the accuracy of heighting from aerial photographs and maps: implications to process modellers. *Earth Surface Processes and Landforms*, 19(6):577–583.

Gooch, M. J. and Chandler, J. H. (2001). Failure prediction in automatically generated digital elevation models. *Computers & Geosciences*, 27(8):913–920.

Höhle, J. and Höhle, M. (2009). Accuracy assessment of digital elevation models by means of robust statistical methods. *ISPRS Journal of Photogrammetry and Remote Sensing*, 64(4):398–406.

Intergraph Corporation (2014). ERDAS IMAGINE Help. Technical report, Huntsville, Alabama, USA. http://www.hexagongeospatial.com [Accessed; 5th December 2014].

James, M. R. and Robson, S. (2014). Mitigating systematic error in topographic models derived from UAV and ground-based image networks. *Earth Surface Processes and Landforms*, 39(10):1413–1420.

Kääb, A. and Vollmer, M. (2000). Surface geometry, thickness changes and flow fields on creeping mountain permafrost: automatic extraction by digital image analysis. *Permafrost and Periglacial Processes*, 11(4):315–326.

Kneisel, C. and Kääb, A. (2007). Mountain permafrost dynamics within a recently exposed glacier forefield inferred by a combined geomorphological geophysical and photogrammetrical approach. *Earth Surface Processes and Landforms*, 32(12):1797–1810.

Knight, J. and Harrison, S. (2013). The impacts of climate change on terrestrial Earth surface systems. *Nature Climate Change*, 3(1):24–29.

Lambiel, C., Maillard, B., Kummert, M., and Reynard, E. (2016). Geomorphological Map of the Hérens Valley (Swiss Alps). *Journal of Maps*, 12(1):160–172.

Lane, S. N., Chandler, J. H., and Richards, K. S. (1994). Developments in monitoring and modelling small-scale river bed topography. *Earth Surface Processes and Landforms*, 19(4):349–368.

Lane, S. N., James, T. D., and Crowell, M. D. (2000). Appication of digital photogrammetry to complex topography for geomorphological research. *The Photogrammetric Record*, 16(95):793–821.

Lane, S. N., Reid, S. C., Westaway, R. M., and Hicks, D. M. (2004). Remotely sensed topographic data for river channel research: the identification, explanation and management of error. In Kelly, R. E. J., Drake, N. A., and Barr, S. L., editors, *Spatial Modelling of the Terrestrial Environment*, pages 113–136. Wiley, Chichester, UK.

Lane, S. N., Westaway, R. M., and Murray Hicks, D. (2003). Estimation of erosion and deposition volumes in a large, gravel-bed, braided river using synoptic remote sensing. *Earth Surface Processes and Landforms*, 28:249–271.

Chapter 3. Application of archival aerial photogrammetry to quantify climate forcing of Alpine landscapes

Lane, S. N., Widdison, P. E., Thomas, R. E., Ashworth, P. J., L., B. J., Lunt, I. A., S., S. G. H., and Simpson, C. J. (2010). Quantification of braided river channel change using archival digital image analysis. *Earth Surface Processes and Landforms*, 35(8):971–985.

Leica Geosystems Geospatial Imaging (2006). Leica Photogrammetry Suite Automatic Terrain Extraction User's Guide. Technical report, Norcross, Georgia, USA. 154 pages.

MeteoSwiss (2014). Climate Today: Trends in Switzerland. Technical report, Federal Office of Meteorology and Climatology Meteoswiss, Zürich http://www.meteoswiss.admin.ch/home/climate/present-day/climate-trends.html [Accessed; 1st December 2014].

Milledge, D. G., Lane, S. N., and Warburton, J. (2009). The potential of digital filtering of generic topographic data for geomorphological research. *Earth Surface Processes and Landforms*, 34(1):63–74.

Remondino, F., Spera, M. G., Nocerino, E., Menna, F., and Nex, F. (2014). State of the art in high density image matching. *The Photogrammetric Record*, 29(146):144–166.

Reynard, E., Lambiel, C., and Lane, S. N. (2012). Climate change and integrated analysis of mountain geomorphological systems. *Geographica Helvetica*, 67(1-2):5–14.

Schwab, M., Rieke-Zapp, D., Schneider, H., Liniger, M., and Schlunegger, F. (2008). Landsliding and sediment flux in the Central Swiss Alps: a case study from the Schimbrig landslide, Entlebuch. *Geomorphology*, 97(3-4):392–406.

Small, R. J., Beecroft, I. R., and Stirling, D. M. (1984). Rates of deposition on lateral moraine embankments, Glacier de Tsidjiore Nouve, Valais, Switzerland. *Journal of Glaciology*, 30(106):275–281.

Taylor, J. R. (1997). *An Introduction to Error Analysis: The Study of Uncertainties in Physical Measurements*. University Science Books, Sausalito, California, USA.

Walstra, J., Dixon, N., and Chandler, J. H. (2007). Historical aerial photographs for landslide assessment: two case histories. *Quarterly Journal of Engineering Geology and Hydrogeology*, 40(4):315–332.

Welch, R. and Jordan, T. R. (1983). Analytical non-metric close-range photogrammetry for monitoring stream channel erosion. *Photogrammetric Engineering & Remote Sensing*, 49(3):367–374.

Wickens, E. and Barton, N. R. (1971). The application of photogrammetry to the stability of excavated rock slopes. *The Photogrammetric Record*, 7(37):46–54.

Natan Micheletti, Jim H. Chandler, Stuart N. Lane

Context

The advent of Structure-from-Motion photogrammetry in physical geography has already had a major impact through its ability to generate three-dimensional data rapidly with minimal financial costs and expertise. Since sensor distortions can be easily modelled, all consumer grade digital cameras can be employed to acquire valuable geomorphic data. Moreover, the technology is available even to non-specialized users by virtue of low-cost (sometimes free), fully automated and even internet-based processing platforms. Taken together, these developments go as far as to make near instantaneous production of digital terrain models in the field using the ubiquitous smartphone technology possible.

This paper investigates what can be acquired using hand-held smartphone sensors and free, internet-based processing systems, using terrestrial laser scanning point clouds as benchmark data and comparing both devices and software packages to traditional approaches.

In the context of this thesis, the chapter represents an examination of the potential of new remote sensing approaches (SfM photogrammetry in combination with smartphone sensors) for applied geomorphological research.

Abstract

We test the acquisition of high-resolution topographic and terrain data using hand-held smartphone technology, where the acquired images can be processed using technology freely available to the research community. This is achieved by evaluating the quality of digital terrain models (DTM) of a river bank and an Alpine alluvial fan generated with a fully automated, free-to-use, structure-from-motion package and a smartphone integrated camera (5 megapixels) with terrestrial laser scanning (TLS) data used to provide a benchmark. To evaluate this approach a 16.2-megapixel digital camera and an established, commercial, close-range and semi-automated software are also employed, and the product of the four combinations of the two types of cameras and software are compared. Results for the river bank survey demonstrate that centimetre-precision DTMs can be achieved at close range (10 m or less), using a smartphone camera and a fully automated package. Results improve to sub-centimetre precision with either higher-resolution images or by applying specific post-processing techniques to the smartphone DTMs. Application to an entire Alpine alluvial fan system shows the degradation of precision scales linearly with image scale, but that (i) the expected level of precision remains and (ii) difficulties in separating vegetation and sediment cover within the results are similar to those typically found when using other photo-based techniques and laser scanning systems.

Keywords: structure-from-motion (SfM); close-range photogrammetry; digital terrain model (DTM); terrestrial laser-scanning (TLS);

4.1   Introduction

The last two decades has seen a revolution in topographic data measurement for geomorphic research, with both a substantial increase in the rate at which it is possible to acquire precise, three-dimensional terrain data and the ease with which associated methods can be applied. Initially, these developments focused upon constructing digital elevation models (DEMs) or digital terrain models (DTMs) using both photogrammetric (e.g. Lane et al. [1994]; Barker et al. [1997]; Lane [2000]; Westaway et al. [2000]) and differential global positioning system (dGPS) (e.g. Fix and Burt [1995]; Brasington et al. [2000]) data. While these approaches allowed users to generate DEM data themselves and so to control the data acquisition process (e.g. through ground-based surveys), they remained highly dependent upon both expensive equipment and expertise to manage and improve data quality [Lane et al., 2004]. Over the last decade, terrestrial laser scanners proved capable of generating very high-quality DEM data [Heritage and Hetherington, 2007; Alho et al., 2009; Hodge et al., 2009a,b; Schaefer and Inkpen, 2010] and have almost become routine in some DEM collection strategies. However, they remain relatively expensive items of technology and have only recently become truly portable. Thus much interest remains in acquiring DEM data using much less expensive technologies and the last few years have seen a series of innovative adaptation of imaging systems for geomorphic research, including range imaging [Nitsche et al., 2013] and applications of the

Kinect sensor [Mankoff and Russo, 2013]. Such methods have proved capable of measuring topographic surfaces with a precision in the millimetre to centimetre range as the basis of DEM construction.

Photogrammetric developments have been fundamental in allowing the development of DEM-based methods in geomorphology. Approaches to photogrammetric DEM collection required access to expensive hardware and software, even when the traditional constraints imposed by aerial (or analogue) photogrammetric methods were relaxed through use of analytical methods [Chandler and Moore, 1989]. They also required correct handling of geometrical distortions associated with image acquisition, notably when using non-metric cameras (e.g. Chandler et al. [1990]; Butler et al. [1998, 2002]; Brasington and Smart [2003]). Most recently, many of these constraints have been surpassed or have become more automated through the development of structure-from-motion (SfM) methods (e.g. James and Robson [2012]; Westoby et al. [2012]; Fonstad et al. [2013]). SfM has its origins in the machine vision community, particularly the tracking of points across sequences of images occupied from different positions. It has been developed and adapted for generating DEM data using potentially many images in a sequence [Fonstad et al., 2013]. In traditional photogrammetry, only two images of the same surface are required. After an estimation of image orientation, stereo matching is then used, as it is in SfM approaches, to identify conjugate point pairs in the images and these can be used to determine 3D coordinates of points in the images, provided ground control data are available to determine sensor position and orientation, and sensor internal geometrical distortions are known. SfM differs by starting with the image-matching process, of multiple images of unknown position, orientation and distortion, to produce many matched points. By doing this for multiple images of the same surface, it becomes possible through iteration to determine relative sensor position, orientation and distortion. The resulting model can be transformed into a 3D object system after processing if ground control points are available (e.g. Westoby et al. [2012]; Fonstad et al. [2013]). As with conventional close-range photogrammetry and laser-scanning techniques, SfM is a truly 3D measurement technique in that by measuring the same surface from multiple perspectives the result is a 3D point cloud rather than a 2.5D surface (i.e. a set of x, y locations each with a single z value).

SfM-based techniques have been recently employed for a number of geoscience applications, including coastal erosion [James and Robson, 2012], fluvial environments [Fonstad et al., 2013; Woodget et al., 2015] and gully headcut retreat [Gomez-Gutierrez et al., 2014]. The aim of this paper is not to repeat a demonstration of the potential of the SfM approach for geoscience applications (see Westoby et al. [2012]; Chandler and Fryer [2013]; Fonstad et al. [2013]; James et al. [2013]). Rather, it is to assess two developments. First, because of the ease with which sensor distortion can be modelled, the range of potential sensors has increased. Even ubiquitous imaging technologies, such as smartphone sensors, might be used to acquire valuable geomorphic data. Second, alongside these new SfM approaches has been the development of low-cost, sometimes free, Internet-based processing systems: images can be uploaded, processed and the derived 3D data downloaded, sometimes only a few minutes after submission. Taken together, these two developments offer the possibility of very fast,

fully automated and low-cost acquisition of 3D data, based upon the analysis of smartphone-acquired images submitted to a processing service. Thus the aim of this paper is to assess the quality that can be achieved using a freely available and instantly accessible SfM resource with smartphone imagery, a combination that can enable exceptionally low cost, rapid and easy 3D object capture and DTM acquisition in geomorphology. There is a range of options currently available for the acquisition of high-resolution topographic data using a hand-held camera (Table 4.1), and 1a: smartphone and Internet-based SfM system represents the lowest approach in terms of cost, expert supervision needs and possibly processing time. To assess the quality of such approach, we take a highly constrained photogrammetric approach, using a high-quality sensor and subscription-based software capable of generating DEMs using two images (Table 4.1, approach 2c). We then compare this with three progressively less stringent elements of data acquisition: (i) the use of smartphone sensors (Table 4.1, approach 1c); (ii) the use of a non-subscription Internet processing service (Table 4.1, approach 2a); and (iii) processing involving almost no ground control data. Two developments are not tested here: traditional, non-Internet-based processing SfM-MVS (multi-view stereo) (Table 4.1, image processing approach b) and the SfM-MVS approach integrated into subscription-based photogrammetry software (Table 4.1, image processing approach d, notably PhotoModeler release 2014).

Table 4.1 – Examples of sensor and image processing alternatives for image-based high-resolution topographic data acquisition at close and intermediate scale with a hand-held camera.

Sensor	Smartphone[1] High-quality sensor[2]
Image processing approach	Internet-based SfM system[a] Locally-based SfM-MVS software[b] Close-range (oblique) photogrammetry[c] SfM-MVS photogrammetry[d]

Superscript numbers and letters are referred to in the text.

In all cases, our benchmark comparison is with data acquired using terrestrial laser scanning (TLS) technologies and we focus upon one close-range measurement application (a 10 m long by 1.20 m high river bank) and one intermediate measurement-scale application (an Alpine alluvial fan of approximately 87000 m^2). In addition, we perform a specific laboratory experiment to investigate the relation between the number of frames and quality of the derived DTMs.

4.2 Methodology

4.2.1 Close-range measurement scale

Figure 4.1 shows the workflow adopted in this research.
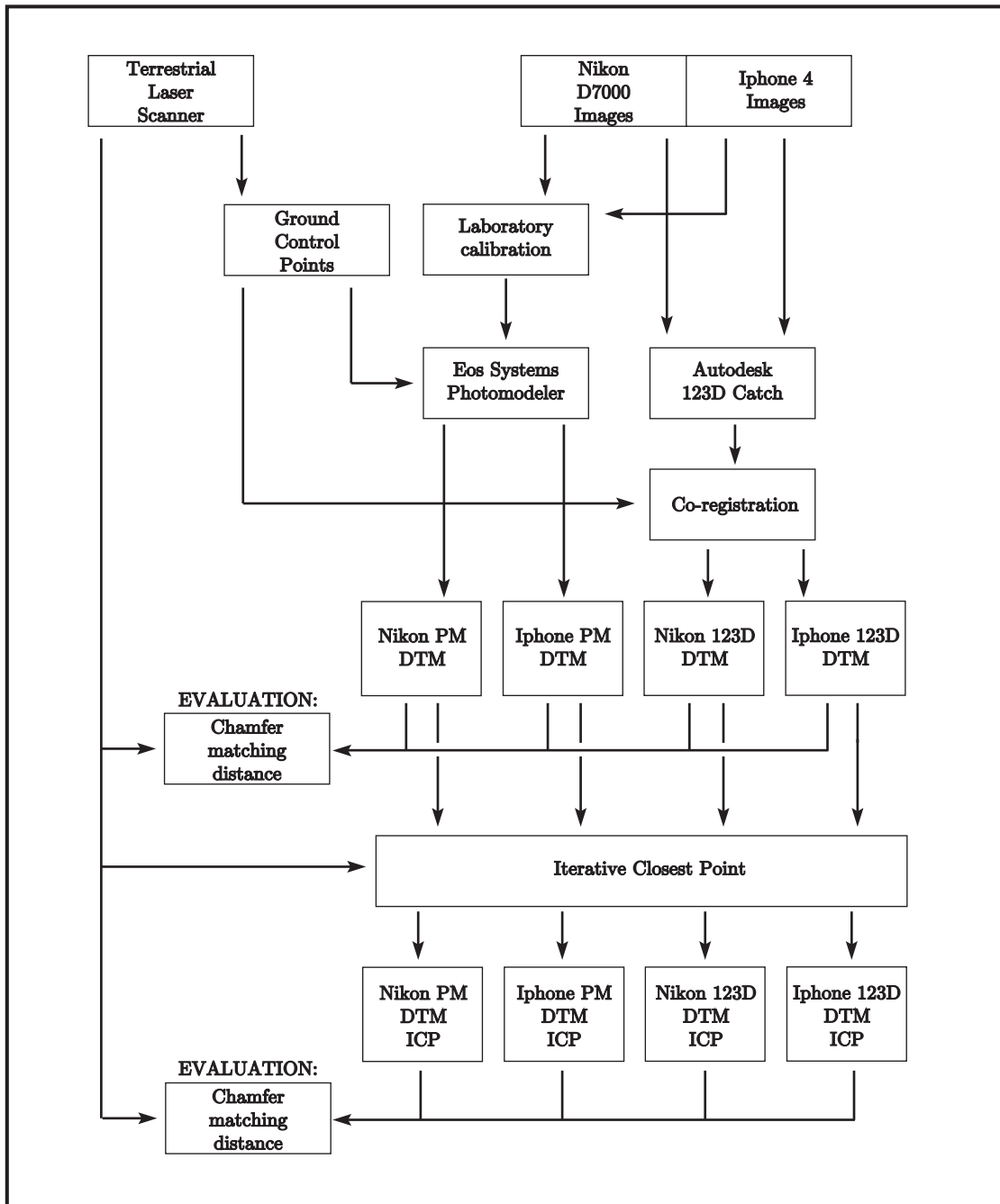
Figure 4.1 – Methodology scheme: the comparison with benchmark (TLS) data is performed using the Chamfer distance twice (prior to and after the application of the ICP algorithm).

Data acquisition

The close-range case study chosen for the experiment is a 10 m long by 1.20 m high length of riverbank, in the Borgne d'Arolla, Val d'Hérens, Switzerland (Figure 4.2). The riverbank texture is heterogeneous, with grains ranging in size from a few centimetres to half a metre set in a coarse-sand and fine-gravel matrix. Ten photogrammetric "coded" targets were distributed along the riverbank and used as tie points for image orientation and for the computation of an appropriate transformation between the coordinate systems associated with the differing processing approaches examined. However, coordinates of the control points were not established using a conventional control survey involving a total station. Instead, TLS coordinates of the same coded targets were extracted and used for co-registration purposes.

Figure 4.2 – Riverbank of the Borgne d'Arolla, Valais, Switzerland. 10 targets printed on regular paper are disposed along it for referencing purposes.

To assess the accuracies of the generated DTMs, TLS data were used as a benchmark. The riverbank was scanned from a distance of approximately 13 m using an Optech ILRIS 3D scanner, with a point spacing of approximately 2 mm. In the absence of an absolute coordinate system, TLS coordinates are used to provide a reference. 3D coordinates of targets in the TLS system were identified manually using the point cloud data management software Cloud Compare [EDF R&D, 2012], freely available at www.danielgm.net/cc.

The first device used for image acquisition was a Nikon D7000 model: a 16.2-megapixel digital single-lens reflex camera. Thirteen photographs were acquired from a short distance (8–12 m) with a fixed-focus 35 mm lens, attempting to obtain a uniform coverage of the feature and to maximize overlap. The same procedure was adopted using a smartphone – an Apple Iphone 4 device – equipped with a 5-megapixel camera, also used to collect 13 photographs.

3D scene reconstruction using PhotoModeler and 123D Catch

Photographs collected using the Nikon D7000 and Iphone 4 devices were processed using both Eos Systems Inc. PhotoModeler software (Version 2012) and Autodesk 123D Catch. A fundamental difference exists between the two software packages used. PhotoModeler provides more comprehensive facilities and control to the user at the expense of requiring greater understanding, making it more challenging for non-photogrammetrists. Effectively, it requires the user to know at least the basic concept of photogrammetry and technical terms, and to be able to correctly sustain the software in performing interior and exterior orientation and to understand the controls on output quality. In contrast, 123D Catch is a fully automated, black-box tool and expert supervision is unnecessary. The potential expert input offered by PhotoModeler should generate better results, but 123D Catch has the distinct value of being freely available to all, particularly non-specialized users.

PhotoModeler is a subscription software which provides tools for image analysis to generate 3D clouds of points. Its cost varies depending on options selected and whether the usage is commercial or academic. Prices and details of PhotoModeler are available at www.photomodeler. com.

To generate accurate spatial data using conventional photogrammetry it is essential to determine the geometrical characteristics of the imaging sensor [Chandler, 1999]. This can be achieved using a targeted field and well-established camera calibration methods involving a self-calibrating bundle adjustment. With modern software and appropriate coded targets this has become a routine and fully automated procedure [Sanz-Ablanedo et al., 2012]. Thus the two devices were used to capture different photographs of similar targets to those used on the riverbank but located on a planar surface (a wall). These images were used in PhotoModeler to estimate camera calibration models for the two sensors. These interior orientation models were then used for PhotoModeler analysis of the riverbank imagery.

A bundle adjustment was used to estimate camera positions and orientations and to extract final point clouds, with a user control on point density. TLS target coordinates were imported into PhotoModeler and associated with their corresponding targets in the images. The use of these tie points allowed transformation of point clouds in PhotoModeler directly to the TLS coordinate system.

The software 123D Catch, developed by Autodesk, implements an SfM-based approach. It is freely available at www.123dapp.com/catch as PC software, smartphone app or web app, all providing the same services in generating the 3D models and differing only in the post-processing options. It requires the user to supply a minimum of three images of objects, to generate 3D meshes automatically. Images are resampled down to a 3 MP resolution currently, so a high-resolution sensor is not required. Moreover, images do not need to be from the same distance or have the same scale. The software does not pose restrictions upon camera type or focus settings; a camera calibration model is derived directly and automatically from each photograph provided by the user. Nevertheless, 123D Catch provides an output file (in

FBX format) where some basic calibration data are provided, such as estimated focal length, exterior orientation parameters, sensor size and scale factors. All photographs obtained using the Nikon D7000 and the Iphone 4 devices were uploaded to the Autodesk server in distinct projects, and automatically processed to generate 3D meshes. The maximum mesh density option was selected in 123D Catch. These meshes were exported in LAS-format files to allow further analysis in the Cloud Compare software. For practical reasons, the PC interface of 123D Catch was employed.

In both software systems, image-covered polygonal meshes were generated for visualisation purposes, by connecting the derived points in 3D space by line segments (Figure 3). The point clouds (mesh vertices) were used for the analysis.
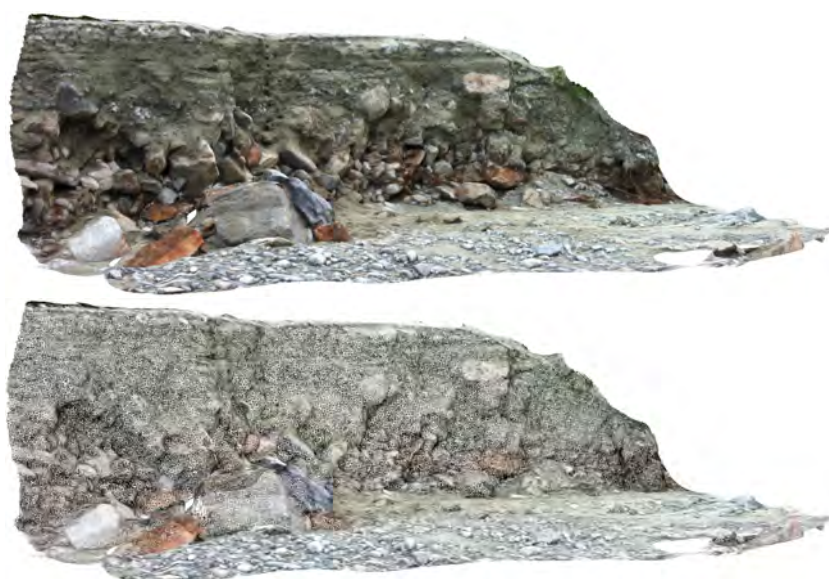
Figure 4.3 – Examples of image-covered polygonal mesh (above) and its wireframe (below), generated using Iphone 4 images and 123D Catch.

Post-processing and comparison with terrestial laser scanning

The Nikon D7000 and Iphone 4 photographs processed using the PhotoModeler and Autodesk 123D Catch software resulted in four point clouds. However, the 123D Catch models required a further post-processing operation after the DTMs had been generated to transform the DTMs to the TLS system. In our case, we used Horn's absolute orientation algorithm (Horn, 1987) implemented in Matlab. A manual identification of targets across multiple images is performed in 123D Catch, and the corresponding coordinates are extracted from the FBX output file. Afterwards, a rotation, translation and scaling transformation is used to compute 123D Catch coordinates in the TLS system. The accuracy of this transformation is demonstrated by the root mean square of the residuals shown in Table 4.2.

To simplify the comparison process, points not in the area of interest were eliminated in all

Table 4.2 – Root mean squared error of targets position transformation for Autodesk 123D Catch models [m].

Device	X	Y	Z
Nikon D7000	0.0043	0.0122	0.0035
Iphone 4	0.0146	0.0305	0.0018

point clouds. The resulting point clouds include a number of points varying from 200000 to 600000 (Figure 4.4). The TLS data include more than 3 million points.

The comparison between SfM models and TLS data is performed using the distance tool in Cloud Compare. The tool uses a chamfer matching algorithm [Barrow et al., 1977] to compute the chamfer distance, i.e. a value of dissimilarity between two point clouds. This value is computed by associating each point in the compared dataset with its closest point in the reference dataset and calculating the three-dimensional distance. These are the reported error values, referred to as "errors" or "distance errors". To improve visualization of the results, a maximum distance of 0.1 m was set to isolate outliers.

A further comparison was made after the application of an iterative closest point (ICP) algorithm. The algorithm iteratively revises a transformation solution in order to minimize the spatial difference between the two point clouds [Zhang, 1994]. It optimizes a rotation matrix and a translation vector to fit the compared point cloud to the reference one. ICP has previously been used in both SfM [James and Robson, 2012] and close-range photogrammetry [Eos Systems Inc., 2012] quality assessment to ensure that the coordinate system alignment is as tight as possible. This is also a logical step as the aim is to compare two methods used to generate data in the same coordinate system requiring any alignment problems to be removed.

4.2.2 Intermediate measurement scale

Data acquisition and 3D scene reconstruction

An Alpine alluvial fan located near the village of Satarma, Val d'Hérens, Switzerland (Figure 4.5) provided an intermediate-range case study. The area of the alluvial fan is approximately 87000 m^2. As in the previous case study, TLS data were used to provide a benchmark for comparison. The TLS data have a point density of approximately 15 cm in the middle-upper part of the fan, where vegetation is absent and the surface is grass and sediment covered, and are registered in the Swisstopo LV95 coordinate system using dGPS measured targets. The focus of the intermediate-range study is on the performance of the use of smartphone sensors and Internet processing services over a larger area. Hence the analysis was performed using an Autodesk 123D Catch model (see "Close range measurement scale", above) obtained from 13 photographs captured with an Apple Iphone 4 device only. Images were taken upfan, from approximately 350 to 450 m from the channel turn visible in the middle of the alluvial fan in Figure 4.5.

(a) Nikon D7000 Photomodeler

(b) Nikon D7000 123D Catch

(c) Iphone 4 Photomodeler

(d) Iphone 4 123D Catch

(e) Terrestrial Laser Scanner
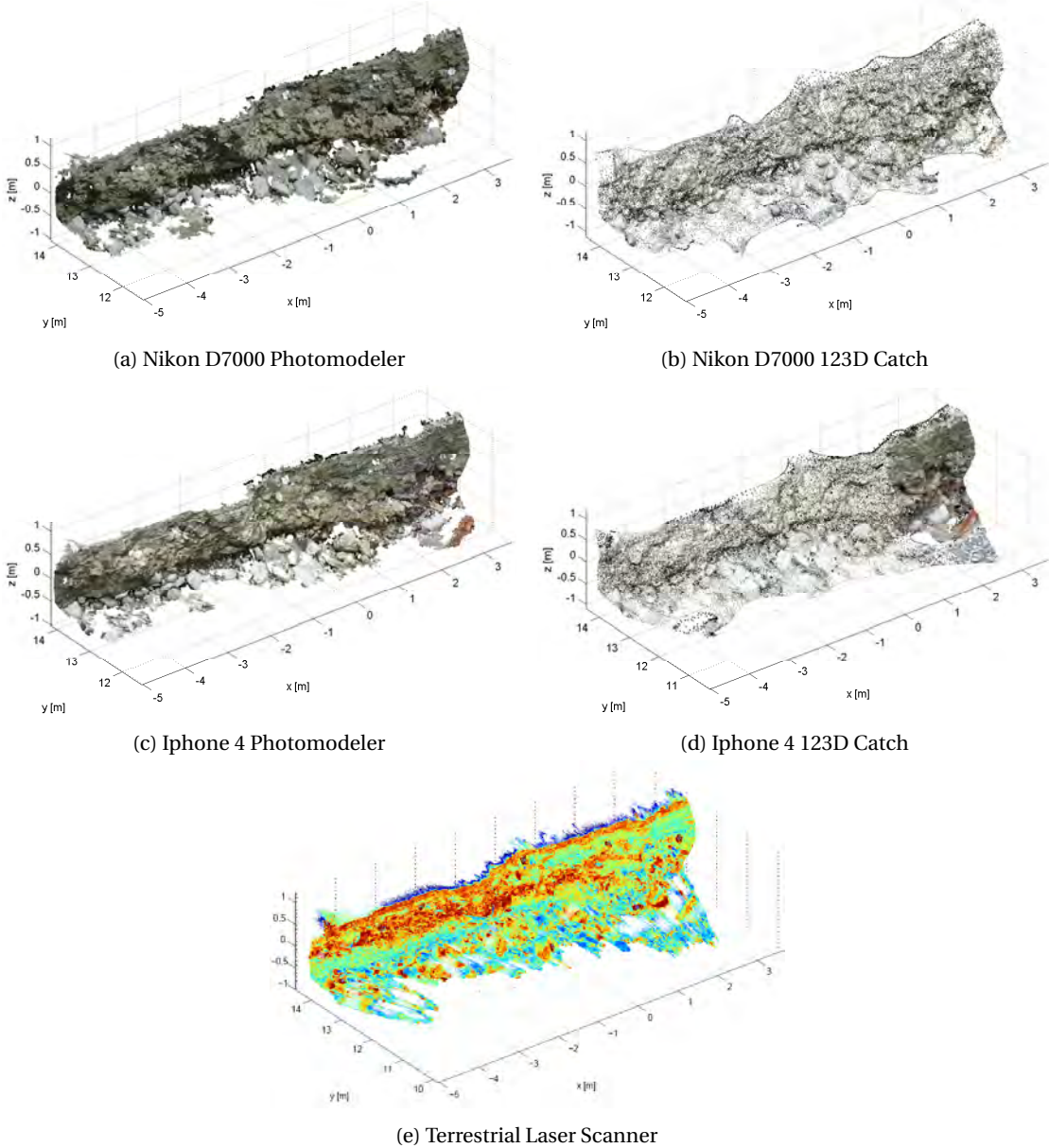
Figure 4.4 – Riverbank point clouds generated using different devices and software: (a) Nikon D7000 Photomodeler; (b) Nikon D7000 123D Catch; (c) Iphone 4 Photomodeler; (d) Iphone 4 123D Catch; (e) terrestrial laser scanner. Part (d) presents a heterogeneous point density because of better image coverage in some zones, as discussed further in the text. Part (e) is presented with laser reflectance as colours for visualization purposes.

This case study is more challenging compared to the close-range one and includes a number of complications. First, and as expected, the acquisition of an appropriate set of images for the analysis is more difficult given the size of the object of study. In particular, very well-defined structures on the fan might not have a sufficient representation from different angles and available positions from the imaging survey. Second, the alluvial fan is partially covered by vegetation and this represents a major problem for multiple reasons. At this scale, the occlusion caused by vegetation cannot be recovered by the acquisition of images from different angles, as data collection from the ground allows limited positions for the camera. Further, comparison with TLS data would be problematic because of the well-known characteristics of laser surveys in vegetated zones (i.e. points on leaves versus points passing through the vegetation and hitting the ground). Finally, in this case, the increased distance between the camera and the alluvial fan is not optimal for obtaining the necessary image texture, causing the 3D reconstruction to be more difficult and of varying quality.

Figure 4.5 – Satarma alluvial fan, Valais, Switzerland.

Post-processing and comparison with terrestrial laser scanning

Similar to the close-range experiment (see above), Horn's absolute orientation algorithm [Horn, 1987] was used to transform the alluvial fan 123D Catch model coordinates into the official Swiss coordinate system LV95, used for the TLS data. Since the scale of this experiment is too large for the use of coded targets, eight well-defined points were manually identified and used as tie points between the two sources of data to perform an approximate transformation. A Monte Carlo simulation to refine the transformation was then executed. The resulting 123D Catch model is presented in Figure 4.6. Owing to the presence of vegetation and related shading effects and point cloud density differences between the 123D Catch model and the TLS

data, the sampling of points for the comparison process proved challenging. To overcome this issue and to obtain reliable results, the point clouds were clipped so that the comparison was performed on the exposed main fan channel zone, where vegetation effects can be neglected (red perimeter in Figure 4.6). The calculation of error is performed as in the close-range case study, by using the Chamfer algorithm to calculate distance errors and the ICP algorithm to reduce co-registration errors (see "Post-processing and comparison with terrestial laser scanning", above).
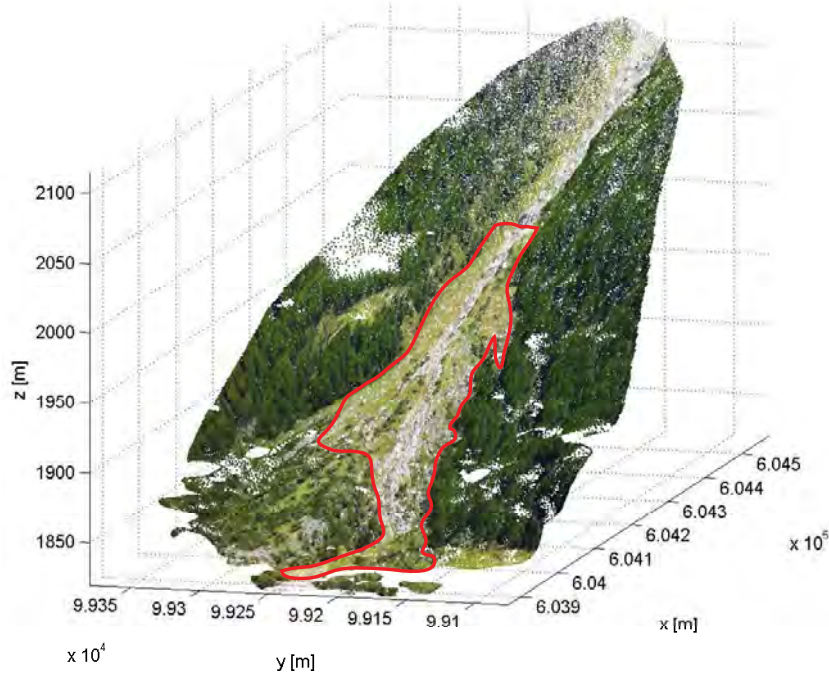
Figure 4.6 – Satarma alluvial fan point cloud generated using an Iphone 4 and Autodesk 123D Catch. The highlighted zone is where the quantitative analysis is performed.

4.2.3 Laboratory experiment using a flat surface

One of the potential main controls on the successful application of SfM methods in geoscience is likely to be the number of images. It is reasonable to suppose that an increase in the number of images can generate a more dense mesh, potentially enhancing the quality of derived models. Very large datasets of more than 100 images were employed in similar studies [James and Robson, 2012; Westoby et al., 2012; Fonstad et al., 2013], but these authors show how this lengthens processing times due to the computationally demanding nature of keypoint descriptor extraction, matching and reconstruction algorithms. The Iphone 123D Catch software currently allows a maximum upload of 70 images, while the PC interface allows more (note: generated meshes can be transferred between both interfaces).

The optimal or sufficient number of images required to maximize the quality of the derived models is likely to vary according to the complexity of the surface being measured as well as

the exact sensor (and hence frame coverage) being used. In order to investigate the impact of the number and distribution of images on the quality of the computed models in a generic way, we have undertaken an additional experiment using a simple methodology the authors had used previously [Chandler et al., 2005]. We took the hypothesis that the number and distribution of the frames should be fundamental for controlling the quality and specifically the accuracy of the model. When a reduced number of frames are employed, the generated model could be deformed and/or successful only for a part of the scene. This suggests the need to consider (i) an appropriate distribution of photo locations to capture the scene, and (ii) significant overlap between as many frames as possible. In a laboratory experiment, a simple A3 (29.7 cm x 42 cm) high-quality print of a highly textured image (a pebble surface) was pasted on to a flat wooden board, which can be assumed to be planar. This enables a very large number of checkpoints to be determined in the object space and allows the accuracy of the measurement system to be quantified (Figure 4.7). A total of 53 convergent and oblique frames were collected using the Iphone 4 device. Given the reduced scale and simplicity of this extreme test setting, it was possible to acquire all frames with significant overlapping areas between them, while maintaining a good coverage of possible image capturing positions. We then focus on the 123D Catch software, reflecting this paper's emphasis on low-cost processing options. A number of Autodesk 123D Catch projects were generated by varying the number of images and view angles.

Figure 4.7 – Set up for the experiment: high quality print pasted on a wooded plank to be as flat as possible.

The relation between the number of frames and the quality of derived DTMs was tested using the following method: after generating a 123D Catch model using all images available, groups of frames were progressively removed while maintaining a good scene covering and overlapping area. Hence models are generated using 53, 40, 30, 20, 13, 10, 8 and 7 frames. Although 123D Catch can be used with only three images, projects with fever than seven frames

failed to provide satisfying results, probably because the iterative process for the exterior orientation could not converge with few images in this case and need more redundancy to be successful. To allow direct comparison, all meshes were scaled directly in 123D Catch using a measured distance.

Since the object surface is flat (topography is completely absent), model accuracy can be determined without the need for coordinate manipulation, which provides a major benefit of this particular methodology. A best-fit plane is computed by minimizing the perpendicular distances between the plane and the points in the point clouds. Then, the distance between the plane and each 3D point is determined to estimate model accuracy.

4.3 Results

4.3.1 Close-range measurement scale results

The error analysis for the SfM data and TLS for both direct registration and iterative closest point algorithm for the initial riverbank test is presented in Table 4.3. The histograms of distance error (Figure 4.8) have log-normal distributions, with a positive skew, and hence we focus on the median rather than the mean error in the results analysis. Optimum results with direct registration were obtained using the Nikon D7000 frames in PhotoModeler software, with a median error of 0.0038 m. In contrast, the application of Autodesk 123D Catch to Nikon D7000 photographs has a median error of 0.0044 m compared to TLS data. As expected, Iphone 4 images using PhotoModeler degrade to a median error of 0.0053 m. The application of Iphone 4 data to Autodesk 123D Catch degrades further to a 0.0148 m median error. For every approach, the error median is lower than the mean error, because of the positive skew of error distributions. Generally, all models provide very low median values, with the exception of the Iphone 4 123D Catch approach.

Table 4.3 – Distance errors between the riverbank SfM models and the TLS data for both direct registration and ICP algorithm [m].

DTM	Median $(Q_{.50})$	$Q_{.75}$	$Q_{.90}$	$Q_{.95}$	$Q_{.99}$	Mean	Mode
N. D7000 - PM	0.0038	0.0070	0.0123	0.0170	0.0323	0.0061	0.0027
N. D7000 - PM - ICP	0.0031	0.0047	0.0089	0.0162	0.0717	0.0056	0.0027
N. D7000 - 123D C.	0.0044	0.0086	0.0159	0.0297	> 0.1	0.0090	0.0023
N. D7000 - 123D C. - ICP	0.0034	0.0059	0.0104	0.0141	0.0249	0.0053	0.0023
Iphone4 - PM	0.0053	0.0114	0.0203	0.0274	0.0455	0.0089	0.0028
Iphone4 - PM - ICP	0.0032	0.0051	0.0102	0.0152	0.0539	0.0054	0.0023
Iphone4 - 123D C.	0.0148	0.0274	0.0449	0.0615	> 0.1	0.0207	0.0044
Iphone4 - 123D C. - ICP	0.0079	0.0149	0.0225	0.0271	0.0382	0.0105	0.0030

(a) Nikon D7000 Photomodeler

(b) Nikon D7000 123D Catch

(c) Iphone 4 Photomodeler

(d) Iphone 4 123D Catch
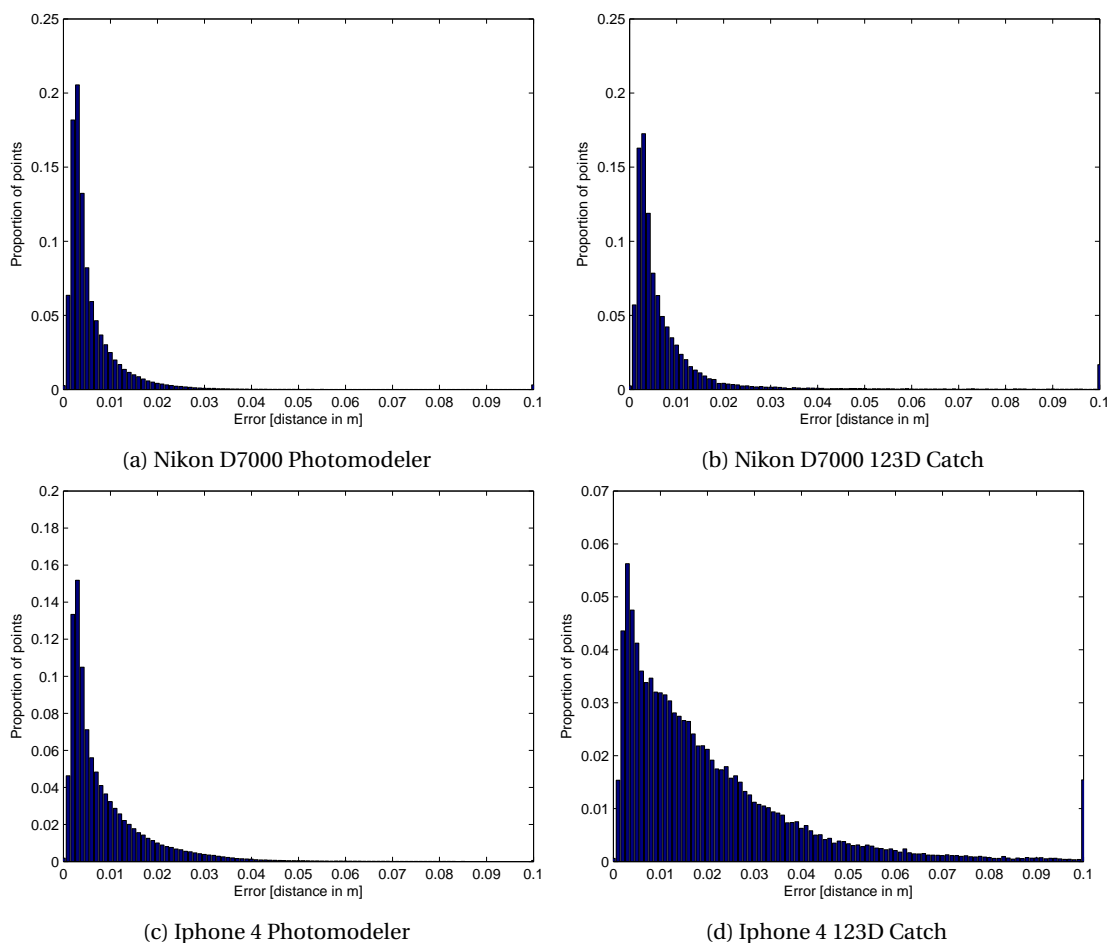
Figure 4.8 – Histograms of distance errors distributions for the Borgne d'Arolla riverbank for each approach compared to TLS data: (a) Nikon D7000 Photomodeler; (b) Nikon D7000 123D Catch; (c) Iphone 4 Photomodeler; (d) Iphone 4 123D Catch.

With the exception of Iphone 4 123D Catch, all experiments achieve 95% of distance errors below 0.03 m. There is a high level of similarity between the two Nikon D7000 distributions (Figures 4.8a and 4.8b), which differ only in the number of outliers (more important for 123D Catch, as confirmed by the 99th centile in Table 4.3), and slightly in the proportion of errors between 0.01 and 0.02 m. The Iphone 4 Photomodeler approach (Figure 4.8c) has a similar distribution to Nikon D7000 approaches, but with a slightly greater proportion of points with a 0.02 to 0.03 m error (confirmed by higher quantiles values). Finally, whilst Iphone 4 images processed in 123D Catch presented in Figure 4.8d have an error distribution which peaks at a similar error to other approaches (i.e. below 0.005 mm, with a slightly higher mode of 0.0044 m), its right tail is much more important, featuring higher errors than the others methods as demonstrated by the 75th centile, respectively 0.013, 0.0188 and 0.0204 m greater and more importantly by the 0.0615 value of the 95th centile, greater by more than 0.03 m.

The ICP algorithm was applied to help separate out registration and random errors. The

application of the ICP algorithm did not improve the Nikon D7000 PhotoModeler result significantly; the median error decreases by only 0.0007 m, while the mean error drops only by 0.0005 m. On the other hand, the Iphone 4 PhotoModeler and the Nikon 123D Catch models benefit greatly from the refined coordinate system alignment by ICP. After the ICP application, mean errors between these models and the TLS data are approximately 0.005 m, with median values of 0.0032 and 0.0034 m – a performance that could be considered comparable to the Nikon D7000 PhotoModeler results. The Iphone 4 123D Catch result also improves considerably; the mean error decreases by one half and is now approximately 0.01 m. The median also decreases by one half (from 0.0148 to 0.0079 m).

Figure 4.9 shows the distribution of errors after the ICP application. These distributions are consistent with the error statistics observed in Table 4.3: both Nikon D7000 applications and Iphone 4 PhotoModeler results are comparable (Figure 4.9a and 4.9b), achieving very satisfying performances. On the other hand, while Iphone 4 123D Catch errors reduce considerably, its error distribution demonstrates how performances are still inferior to the three aforementioned approaches (Figure 4.9d). Nonetheless, the model benefits greatly from the correction, as demonstrated also by important reduction in errors centiles.

For an additional visualization of the benefits of the ICP algorithms, nine DEMs on a regular grid with 0.005 m spacing were generated (four direct registration models, four post-ICP models and one using the TLS data). Given the high density of points, a simple triangle-based linear interpolation was sufficient to generate DEMs at the chosen resolution. For visualization, the grid was generated on the $X-Z$ coordinate axis, with elevation provided by the Y axis, and on a rectangular zone of the riverbank. DEMs of difference (DoD) were generated by subtracting the eight SfM and PhotoModeler surfaces from the TLS surface, which is used again as benchmark (the smaller the value of the DoD, the more accurate the model). Figure 4.10 illustrates the direct registration DoD compared with the ICP one, for the four SfM and PhotoModeler approaches. Results are broadly as expected with differences reduced following use of the ICP algorithm. The Nikon sensor appears to generate the smallest differences but optimum accuracies appear to be achieved with 123D Catch. Table 4.4 illustrates the root mean squared error (RMSE) of each DEM compared to the TLS one. These values confirm the visual observations, as PhotoModeler models benefit less from ICP (from 0.0381 to 0.0197 m using the Nikon sensor and from 0.0213 to 0.0174 m using the Iphone 4 sensor) than the 123D Catch outputs (0.0647–0.0168 m for the Nikon-PM approach). We attribute the high differences still remaining in the Iphone 4-123D Catch model after the ICP application to a systematic error introduced by the tilting clearly visible in Figure 4.10. The improvement inducted by the ICP for this model is approximately 0.02 m but could be greater if the model were not tilted.

Figure 4.11 shows the distance errors between the four SfM and PhotoModeler models and the reference TLS data as point clouds. Generally, the largest errors are concentrated around the edges of the riverbank, either on the top of it or on the blocks at its base. Secondly, a difference in point density between the PhotoModeler and 123D Catch models is visible;

(a) Nikon D7000 Photomodeler - ICP

(b) Nikon D7000 123D Catch - ICP

(c) Iphone 4 Photomodeler - ICP

(d) Iphone 4 123D Catch - ICP
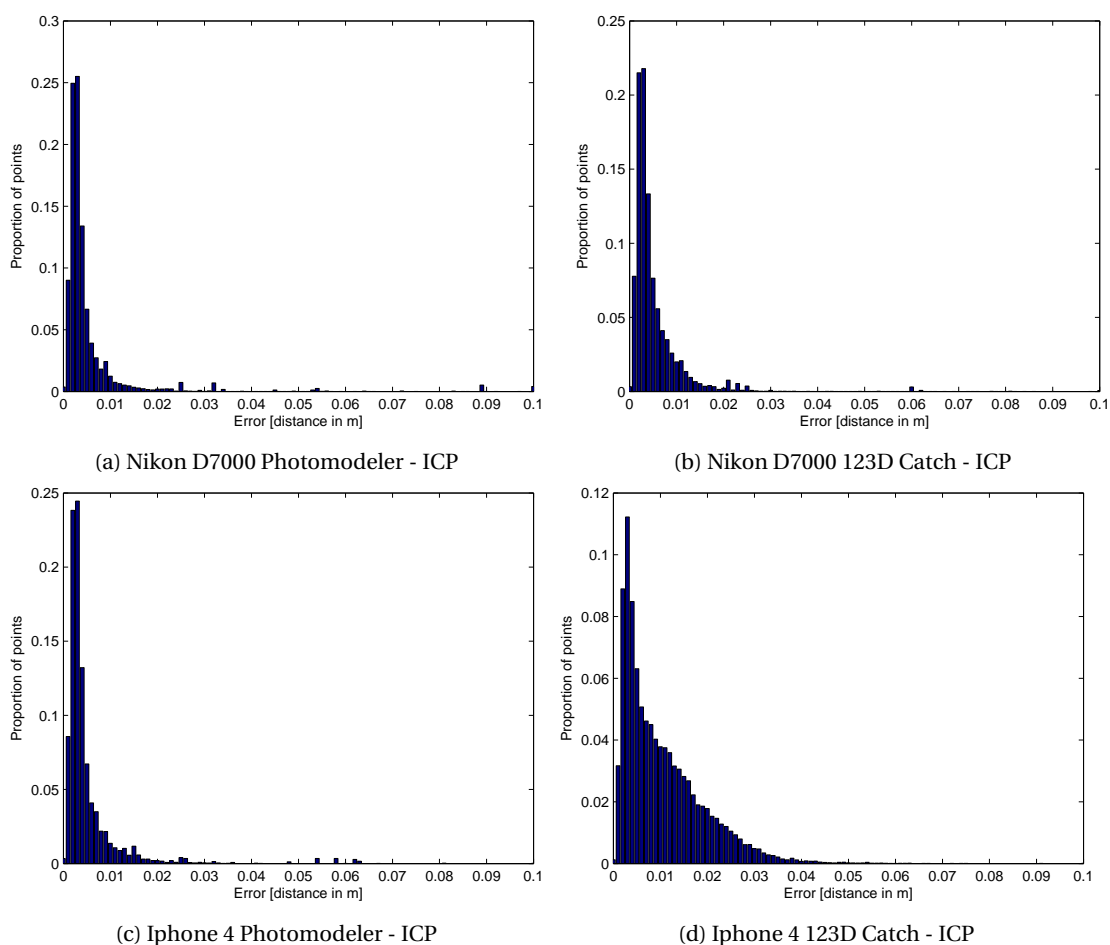
Figure 4.9 – Histograms of distance error distributions for the Borgne d'Arolla riverbank for each approach compared to TLS data after the application of the ICP algorithm: (a) Nikon D7000 Photomodeler – ICP; (b) Nikon D7000 123D Catch – ICP; (c) Iphone 4 Photomodeler – ICP; (d) Iphone 4 123D Catch – ICP.

Table 4.4 – Root mean squared error between the riverbank and the TLS interpolated DEMs for both direct registration and ICP algorithm [m].

DEM	RMSE
N. D7000 - PM	0.0381
N. D7000 - PM - ICP	0.0197
N. D7000 - 123D C.	0.0647
N. D7000 - 123D C. - ICP	0.0168
Iphone4 - PM	0.0213
Iphone4 - PM - ICP	0.0174
Iphone4 - 123D C.	0.0502
Iphone4 - 123D C. - ICP	0.0306

Nikon D7000 PhotoModeler

Nikon D7000 123D Catch

Iphone 4 PhotoModeler

Iphone 4 123D Catch

Z

X

0   0.5   1   2 Meters   Difference to TLS [m]

0.10

0

−0.10
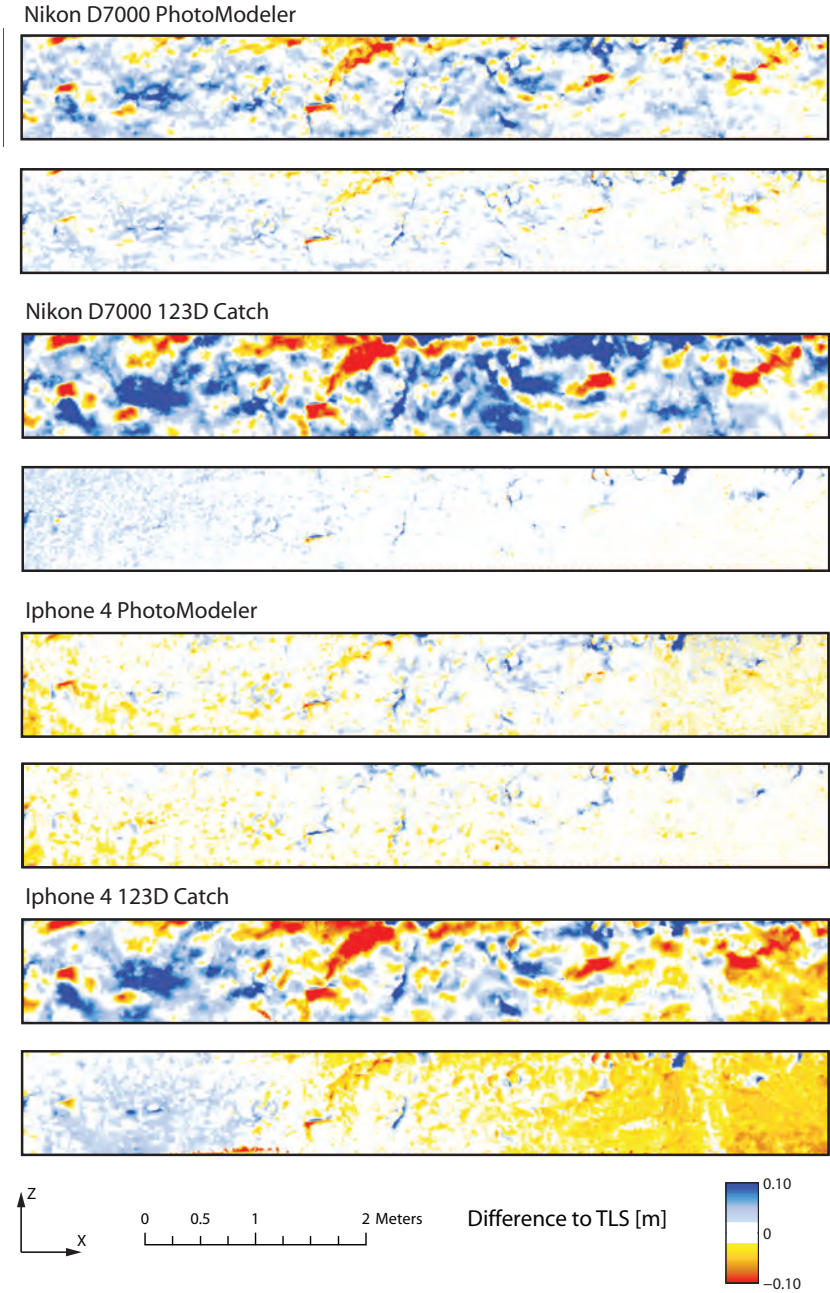
Figure 4.10 – DEMs of differences between SfM and PhotoModeler models and TLS, prior (above) and post (below) ICP application (0.005 m grid resolution).

PhotoModeler-derived point clouds have a point spacing of approximately 0.007 m, while the distance between two neighbouring points in 123D Catch is approximately 0.02 m. Third, it is possible to identify individual stones or other structures where errors are larger. Effectively, major errors are located in shaded spots, surrounding stones or in small crevices. Finally, Iphone models have larger point densities on the right edge of the riverbank, although these zones correspond to higher errors. We attribute the larger point density to the fact that more

(a) Nikon D7000 Photomodeler

(b) Nikon D7000 123D Catch

(c) Iphone 4 Photomodeler

(d) Iphone 4 123D Catch
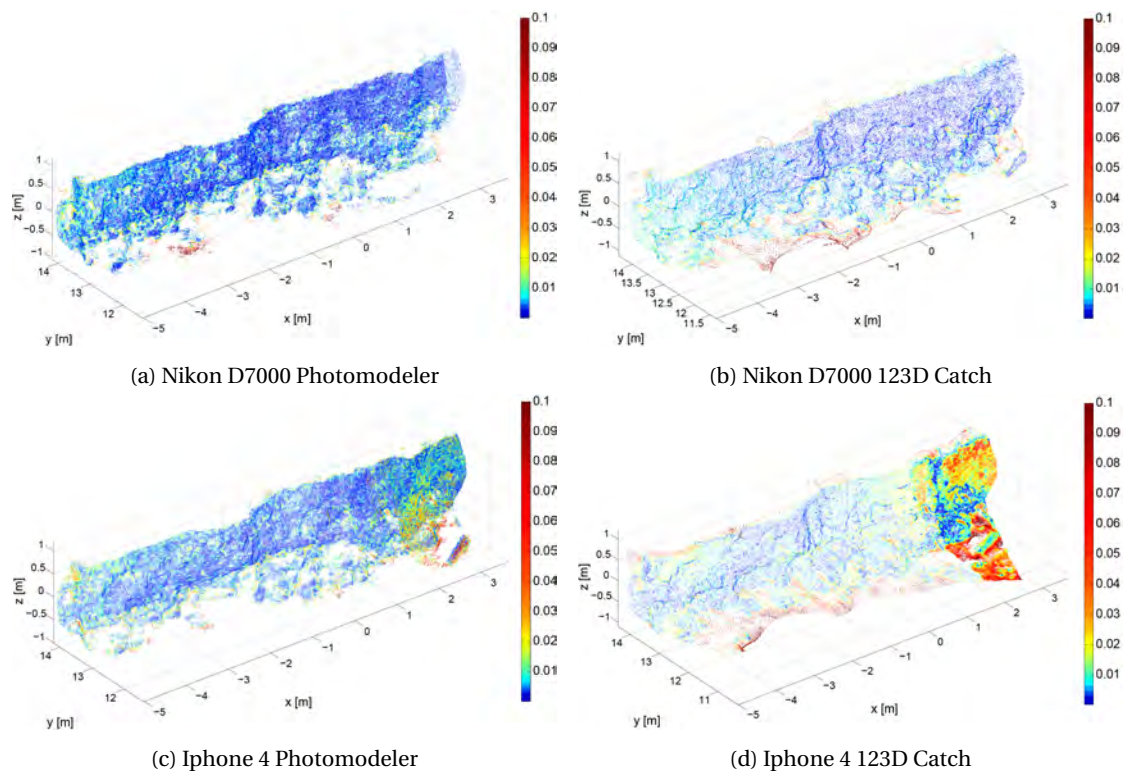
Figure 4.11 – Point cloud errors for the SfM and PhotoModeler models and TLS comparison for the Borgne d'Arolla riverbank (m): (a) Nikon D7000 Photomodeler; (b) Nikon D7000 123D Catch; (c) Iphone 4 Photomodeler; (d) Iphone 4 123D Catch.

images seem to contribute to matched points in this zone. Nevertheless, because of photo position and orientation, the baseline does not seem optimal for depth precision.

4.3.2 Intermediate measurement scale results

Distance errors between the Iphone 4, 123D Catch model and TLS data are shown in Table 4.5 for the alluvial fan. A median error of approximately 0.600 m is obtained. The error distribution for the alluvial fan–TLS comparison (Figure 4.12a) is log-normal, similar to the close-range experiment distributions (Figure 4.8). The frequency peak corresponds to an error of approximately 0.5 m (with a 0.44 m mode), and more than 75% of distances are less than 1 m (the 75th quantile is 0.9493 m).

As expected, the application of the ICP algorithm improves the results significantly: the aligned cloud points have a median error of 0.4226 m, with a mean of 0.5263 m. The error distribution histogram in Figure 4.12b and Table 4.5 show this improvement, with now more than 86% of errors less than 1 m.

Figure 4.13 visualizes these errors. The largest distance errors are concentrated on the flanks of the main channel, and discrepancies between the cloud points seem to increase upstream

Table 4.5 – Distance errors between the alluvial fan 123D Catch model and the TLS for both direct registration and after application of the ICP algorithm [m].

DTM	Median (Q.50)	Q.75	Q.90	Q.95	Q.99	Mean	Mode
Iphone4 - 123D C.	0.5998	0.9493	1.1333	1.5637	1.8882	0.6892	0.44
Iphone4 - 123D C. - ICP	0.4226	0.7282	1.0740	1.2912	1.7320	0.5263	0.15

(a) Iphone 4 123D Catch   (b) Iphone 4 123D Catch - ICP
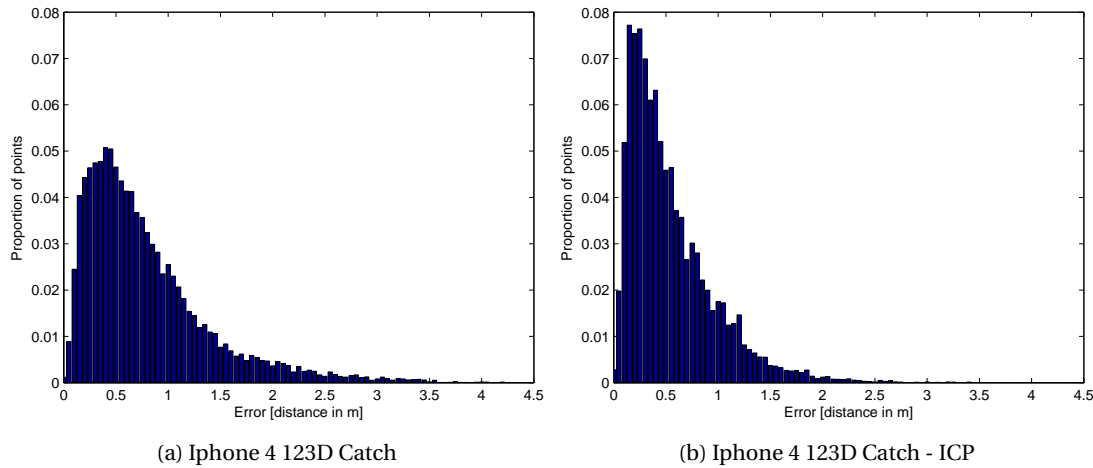
Figure 4.12 – Histograms of distances distributions for Satarma alluvial fan SfM models compared to TLS data: (a) Iphone 4 123D Catch; (b) Iphone 4 123D Catch – ICP.

in that area. This may be explained by an insufficient coverage of the channel flanks in the pictures for a solid reconstruction of their shape. The camera positions are too few and too low to allow an optimal orientation to reconstruct channel flanks. In addition, the increase in pixel size with distance up the fan translates into an increasing distance between the sensor and the observed surface and this also could be responsible for less accurate reconstructions. This also, reduces the density of derived samples in the point cloud and, as a consequence, the precision of the model. To verify this assumption, a subset of points has been extracted representing a narrow strip in the direction of slope. A scatterplot of the discrepancy of the sampled points between 123D Catch and TLS data, as a function of distance to one camera position, is presented in Figure 4.14a. This demonstrates a trend of increasing error with enhancement of distance between camera and object, with the channel flanks errors superimposed on this. Figure 4.14 also illustrates the error vector components for the same narrow strip (4.14b, 4.14c and 4.14d). The error does not feature a particular trend in the X and Y dimensions. On the other hand, the elevation dimension Z error features a positive trend. This could be because of (i) the strict correlation between elevation and distance from camera position given the positions from where images where collected (i.e. around the alluvial fan, but always at its front), or (ii) uncertainties in the co-registration of data in this dimension (plausible given the steepness of the fan).
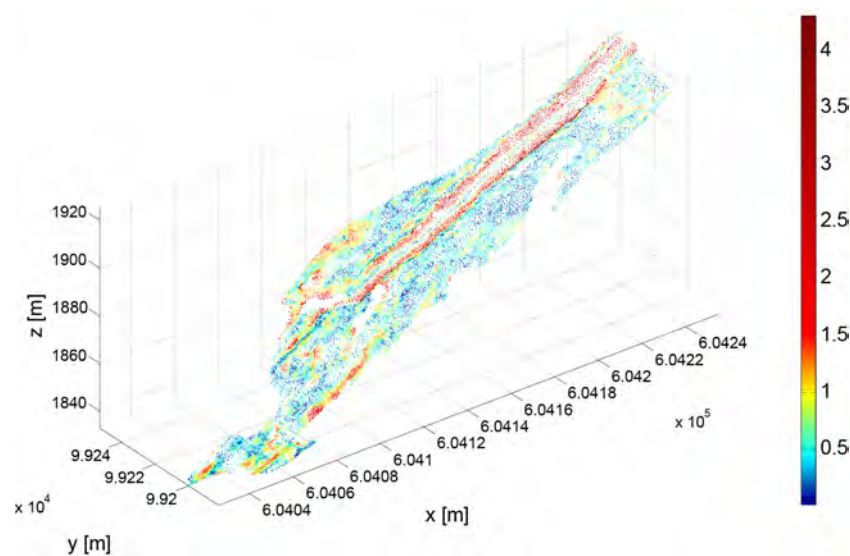
Figure 4.13 – Point clouds errors for the Iphone 4 123D Catch model and TLS comparison for the main channel area of the Satarma alluvial fan [m].

4.3.3 Laboratory experiment results

Table 4.6 presents the results of the flat surface laboratory experiment. The median distance error for a seven-frame model is 0.171 mm, while for the use of all frames it is almost one half (0.091 mm). Thus the accuracy of the results directly depends on the number of frames provided to the software; that is, using more images translates into more accurate models. However, this pattern is nonlinear. The addition of one frame considerably increases the model quality when using a reduced number of images, as demonstrated by the median distance errors of models with seven and eight frames (0.171 and 0.114 mm respectively). However, changing from eight to ten frames leads to almost identical median errors (0.114–0.115 mm). However, it would appear that outliers affect these results (e.g. the quantile 0.95 error reduces from 0.528 to 0.498 mm; Table 4.6). This tendency is also observed when moving from 10 to 13 to 20 images, where improvements are evident for outliers only (error reductions of 0.498 to 0.423 to 0.394 mm).

4.4 Discussion

At close range, the application of SfM approaches provided very satisfying results in comparison to benchmark TLS data, as has been shown in previous studies (e.g. James and Robson [2012]; Westoby et al. [2012]; Fonstad et al. [2013]). Our results show that this approach can be extended to acquire centimetre precision DTMs using smartphone imagery captured from a distance of up to 10 m and a fully automated online analytical service. This precision is improved to a sub-centimetre scale by either: (i) the use of a higher-quality sensor or, possibly more importantly, higher-resolution images; or (ii) the use of more specific, commercial close-

(a) Distance value

(b) *X* component

(c) *Y* component
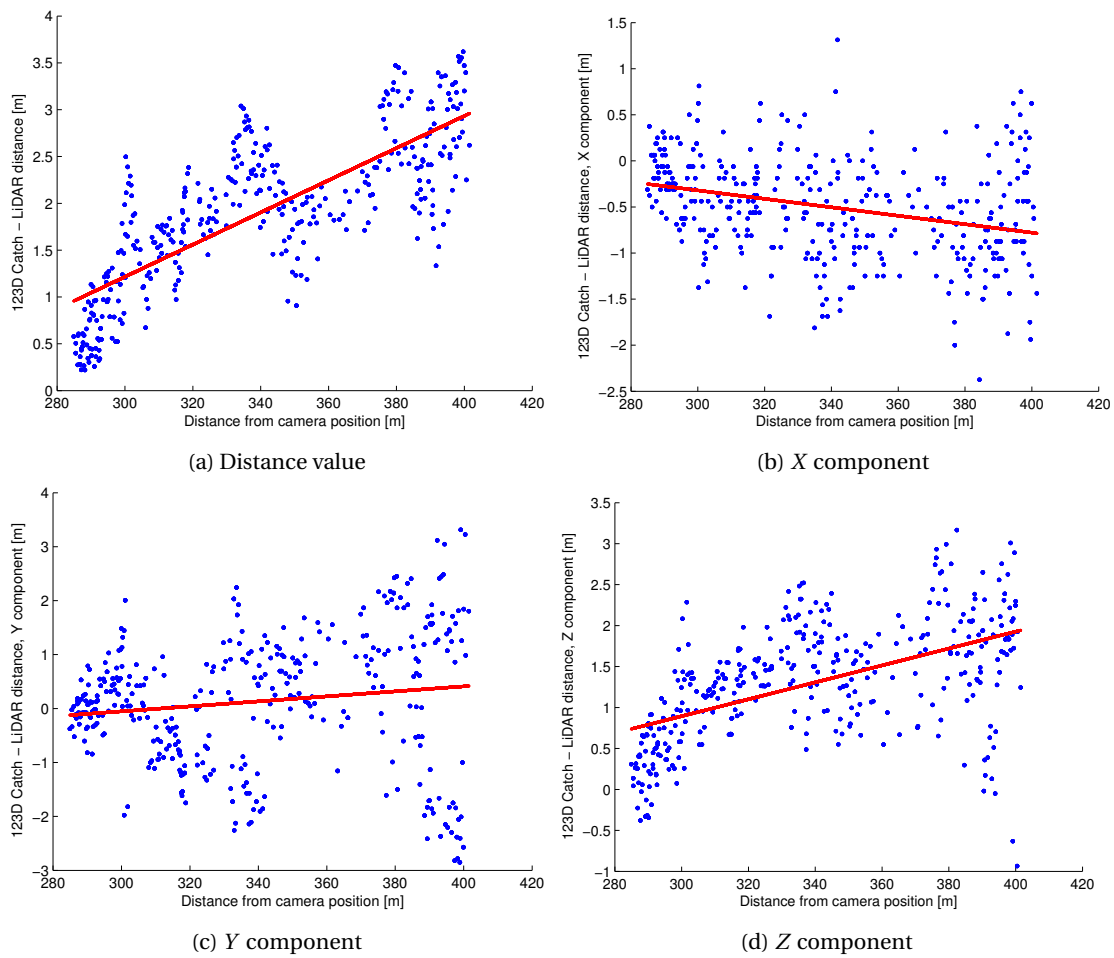
(d) *Z* component

Figure 4.14 – Distance errors between the 123D Catch model and the TLS data as a function of distance from the camera on the main channel flanks area of the Satarma alluvial fan: (a) distance value; (b) X component; (c) Y component; (d) Z component.

Table 4.6 – Distance errors between the flat surface models and best fitting plane [mm].

Number of images	*Median (Q.50)*	*Q.75*	*Q.95*	*Mean*
7	0.171	0.279	0.529	0.207
8	0.114	0.193	0.528	0.168
10	0.115	0.211	0.498	0.166
13	0.128	0.215	0.423	0.161
20	0.117	0.203	0.394	0.149
30	0.090	0.176	0.415	0.136
40	0.095	0.181	0.397	0.134
53	0.091	0.167	0.392	0.137

range photogrammetry software for data generation. The approach here has three advantages over traditional photogrammetry and laser scanning techniques. First, and as with other SfM applications, images can be acquired with a reduction in the sensor, position and geometry constraints as compared with traditional photogrammetric methods. The result is more rapid data acquisition than both traditional photogrammetry and laser scanning methods, and the possibility of using a wider range of devices, including smartphones. The second is represented by the rapid data processing and very fast point cloud generation, using Internet communication systems and fully automated services. This implies that digital elevation data as well as 3D images (e.g. Figure 4.3) can be generated in only a few minutes, without the need for post-processing of laser measurements or expert supervision. Finally, financial costs are close to zero, while laser scanning devices remain expensive pieces of equipment.

There is a co-registration uncertainty linked to the rotation, translation and scaling transformation (estimated using targets positions in Table 4.2) used to transform 123D Catch data into the TLS coordinate system. This was reflected in the change in distance errors after application of the ICP algorithm and is comparable to findings in similar studies (e.g. James and Robson [2012]; Westoby et al. [2012]; Fonstad et al. [2013]), where is it indicated as an important source of uncertainty. In particular, Westoby et al. [2012] indicate how errors in the co-registration procedure can be linked to the manual identification of ground control points in both point cloud datasets and consequently impact upon the accuracy of the transformation matrix applied to the data. Unfortunately, contrariwise to other approaches, to compare 123D Catch and TLS data this manual identification is a necessity. Accordingly, the error estimated between the 123D Catch point clouds and the TLS data can be reduced with more precise coordinate transformation. The use of the iterative closest point (ICP) algorithm (as demonstrated by James and Robson [2012]) confirmed this assumption. The ICP algorithm is expected to minimize the transformation error (but without changing the scale), so that distances between SfM and TSL data can be interpreted as approach-dependent errors. In that sense, the ICP is used to determine the source of the errors, e.g. registration issues versus random errors, by minimizing the effect of the former. Nevertheless, ICP can only be effective if there is an even distribution of data points. In fact, a surface with large voids would itself introduce errors in the surface matching and well-defined tie points can be useful. In the absence of a second dataset for comparison the ICP cannot be applied, but if the model needs to be geo-referenced anyway the use of GCPs (and targets) is advantageous and can provide a sufficiently precise registration for many geoscience applications. As mentioned previously, the ICP proved very efficient in the present study. However, there is a formal distinction between SfM approaches. In PhotoModeler, TLS targets were used as ground control points, so that the registration errors are expected to be dominantly dependent on the bundle adjustment quality. Hence 123D Catch surfaces are expected to benefit most from the ICP application. This is visually confirmed by the DEMs of difference in Figure 4.10: as expected, 123D Catch models benefit greatly from the ICP application, confirming that a non-negligible part of the error could be linked to registration uncertainty possibly arising from the lower image resolution. ICP-induced improvements are lower for PhotoModeler models. These

results are consistent with values in Table 4.3, particularly when observing mean distance errors.

A fundamental control over DTM quality is exerted by the texture of the imagery. Areas of low image texture will yield lower-density point clouds as well as more uncertain point qualities, because the image-matching algorithm relies strictly on image texture. However, image texture is not only dependent upon surface characteristics but also image quality and resolution, particularly image scale. Autodesk currently limits image sizes to 3 MP, which can mean either increasing the image scale or the number of images to achieve an acceptable model resolution. The practicality and speed of data generation associated with using a smartphone–123D Catch approach comes at the price of slightly poorer precision in the resulting surface data. However, the Autodesk 123D Catch smartphone "app" offers the possibility of near-instantaneous acquisition of 3D data, based upon the analysis of smartphone-acquired images submitted to the free Internet-based processing systems using wireless communication. This implies that a first indication on results can be made in near-real time while still in the field. This is hugely beneficial as additional images can be acquired rapidly if either coverage or point density is inappropriate. However, this could only be done if good data network coverage is available, which could not always be the case in field applications.

Extension to an Alpine alluvial fan system demonstrated a linear degradation of precision with image scale, which is logical for a photograph-based approach and also observed in other studies (e.g. James and Robson [2012]). As explained by Fonstad et al. [2013], this is once again due to image texture; as viewing distances increase, the textural features required to calculate a point in that area could become insufficient. For that reason, and as with any photograph-based technique, Fonstad et al. [2013] affirms that SfM is most effective in small study areas, where moderate-quality cameras have sufficient resolution to capture detailed texture. However, this is strictly dependent on the scale that provides the dominant texture in the images, as when capturing larger surface features point matching could be more successful from longer distances than at a closer range. Nevertheless, we found that if the median errors for the riverbank and alluvial fan studies are scaled by the mean distance between generated points and the sensor, accuracies are approximately 1:625. Thus, despite precision degradation, intermediate-scale models maintain the expected level of precision for their scale, as defined by image resolution. Improvements in alluvial fan models could be achieved by taking imagery at a range of distances. Such a "multiscale" imaging solution suggests great promise. Fonstad et al. [2013] suggest that this procedure would reduce systematic distortions over large distances and still produce dense point clouds. However, this has not been verified and would require a more sophisticated strategy for data collection, involving advanced technology such as camera-equipped drones or kites for the alluvial fan case.

The flat surface experiment contributed to understanding the impact of varying the number of frames used by Autodesk 123D Catch. Additional frames generally increase model accuracy compared to a reduced number of images. Nevertheless, their benefit seems to affect outliers only when the number of images is already sufficient for a good representation of the surface

of interest. This suggests that adding groups of images reduces the number of poorer-quality points, a reasonable hypothesis given that point-matching precision is dependent on image location. It appears that although mesh density increases and errors stabilize with increasing number of frames, denser meshes are not necessarily of better quality in terms of accuracies. Smaller image sets can still provide acceptable accuracies, provided their spatial distribution is adequate. The experiment featured an idealized case where (i) a frame can cover 100% of area of interest and (ii) topography is completely absent. Nevertheless, the analysis proved useful in showing that, unlike other traditional forms of photogrammetry, the number of images in an SfM application is absolutely critical. Nonetheless, as anticipated, the relation between results quality and number of frames is likely to differ from case to case.

SfM models are influenced equally by the difficulties of occlusion and separating vegetation and sediment cover typical of laser scanning systems. In SfM approaches, vegetation is important not only for occlusion effects but also for degradation in the quality of surface reconstruction. This has been largely discussed by Westoby et al. [2012], with evidence of errors introduced by the presence of vegetation.

The investigation presented in this paper discussed a number of technical aspects. The mentioned approaches have advantages and disadvantages and their use depends on the specific application. Table VII summarizes these technical approaches. The list is not exhaustive: other approaches and solutions exist.

Table 4.7 – Technical aspects and some possible alternatives for the acquisition of high-resolution topographic and terrain data.

Technical aspect	Options	Main characteristics
Survey	Smartphone	Low cost, portable, potential wireless internet access, low quality
	High-quality sensor	High quality, portable, moderate cost, no internet access
	TLS	High precision, expensive, less portable
Image Processing	Internet-based SfM	Free, near real time, fully automatic, lower quality
	Local software SfM	Mostly free and automatic, better quality expected
	Traditional "stereo" photogrammetry	High quality, subscription cost, expert knowledge
	SfM-MVS photogrammetry	As above but also greater automation and reliability
Co-registration	Scaling	Fast and easy, comparison with other datasets not possible
	Tie points	Comparison with other datasets only, average precision
	Targets + GCP	Any coordinate system, high precision, not always possible
	ICP	Refinement of alignment, needs two co-registered datasets

Since 123D Catch is a process that automatically finds and matches common features between images, it is critical to capture imagery with the right characteristics. Autodesk provides useful guidelines and tutorials for potential users that can be found at http://www.123dapp.com/. Our recommendations would involve acquiring a multiscale image set which initially captures the whole site with a few frames at low resolution before obtaining a greater number of images at closer range to capture the required detail. It is important to collect images from varying directions, and for each 3D point to be identifiable in at least two or preferably three frames. The optimal angle between each image will depend on the subject of interest. Since the features are extracted from the whole photographs, it is fundamental that (i) the whole scene is static, (ii) light between the frames is consistent (no flash), and (iii) images are not overexposed or underexposed as this can often confuse the feature-matching process. If occlusions are present, increasing the number of photos is essential to ensure adequate image coverage. Moreover, increasing the number of photos may produce denser meshes and can improve model accuracy. The adequate number of images required is likely to vary between case studies and cameras used and it is encouraged to investigate whether or not the derived data are sensitive to the number of images acquired and ensure that redundant frames are sufficient. It is advisable not to use zoom lenses, as it could be difficult to obtain an accurate reconstruction with them. Finally, measuring transparent, reflective or homogeneous surfaces should be avoided because the features in this type of subjects are very difficult to match by the automatic feature-matching process. If the generated model needs to be computed in real-world coordinates or co-registered with existing or future datasets, the use of coded and referenced targets can be advantageous. The marked objects need to be clearly identifiable and well represented on the images. Since 123D Catch operates with a fully automatic procedure, it is not possible to insert GCPs to directly compute the mesh in a real-world coordinate system. Hence, in order to minimize error introduced by the registration procedure, the manual identification of the targets needs to be eased by ensuring a high density of points in target zones. If the size of the object is so large as to prevent the use of targets, easily identifiable natural features can be used. If a second dataset is available, after an approximative registration using common points or targets the application of the ICP algorithm can be employed in an attempt to minimize registration errors. If the aim is to monitor changes in an area or an object through time, it is suggested to isolate stable zones for the ICP application and further apply the transformation to the whole dataset. Finally, if a simply scaled model is desired, a known distance can be inserted as a reference in 123D Catch to scale the mesh. To summarize:

1. Plan camera survey, registration or method to introduce scale in advance.

2. Capture the whole subject first, then the details.

3. Ensure coverage is appropriate. Basic principle: ensure that every point on the object appears on at least three images, which are acquired from spatially different locations.

4. Static scene.

5. Consistent light

6. Avoid overexposed and underexposed images.

7. Consider occlusions (see 3, above).

8. Avoid transparent, reflective or homogeneous surfaces.

The uploading of the images to Autodesk servers depends on their number and on the internet connection, but can be as rapid as a few minutes. The processing time is dependent not only on the number of images but also on their texture, and varies from 5 to 30 min for an initial result. It is then possible to generate a maximum-density mesh, which increases the processing time slightly. Overall, the generation of 3D data from raw data is considerably fast. Autodesk 123D Catch therefore provides an invaluable tool for geomorphologists, particularly in terms of cost, speed and ease of use.

4.5 Conclusion

In this contribution, the potential of a straightforward SfM approach using basic smartphone imaging technology and partial and fully automated data-processing resources has been investigated. Two case studies have been chosen for the analysis, namely a riverbank as a close-range example, and an Alpine alluvial fan as an intermediate-distance case. With the use of TLS data to produce a benchmark, the quality of DTMs generated using different sensors and processing methods has been assessed. Efforts were made to reduce the co-registration uncertainty in order to verify model accuracy. The quality of SfM results has proven to be related to image quality and photo scale. Nevertheless, the use of smartphone sensors allows practical and rapid geomorphic data collection and processing. Also, fully automated processing systems proved to be a valid resource for generating a spatial record of objects and DTM generation, especially at close range. These characteristics make fully automated SfM processing systems an appealing and promising approach for geoscience applications, deserving further efforts to investigate system performance in a wide range of environmental settings and terrain types.

Acknowledgements

Bibliography

Alho, P., Kukko, A., Hyyppa, H., Kaartinen, H., Hyyppa, J., and Jaakkola, A. (2009). Application fo boat-based laser scanning for river survey. *Earth Surface Processes and Landforms*, 34(13):1831–1838.

Barker, R., Dixon, L., and Hooke, J. (1997). Use of terrestrial photogrammetry for monitoring and measuring bank erosion. *Earth Surface Processes and Landforms*, 22(13):1217–1227.

Barrow, D. H., Tenenbaum, J. M., Bolles, R. C., and Wolf, H. C. (1977). Parametric correspondence and chamfer matching: two new techniques for image matching. In *Proc. 5th Int. Joint Conf. Artificial Intelligence, Cambridge, MA, 659-663.*

Brasington, J., Rumsby, B. T., and McVey, R. A. (2000). Monitoring and modelling morphological change in a braided gravel-bed river using high resolution GPS-based survey. *Earth Surface Processes and Landforms*, 25(9):973–990.

Brasington, J. and Smart, R. M. A. (2003). Close range digital photogrammetric analysis of experimental drainage basin evolution. *Earth Surface Processes and Landforms*, 28(3):231–247.

Butler, J., Lane, S. N., Chandler, J. H., and Porfiri, E. (2002). Through-water close range digital photogrammetry in flume and field environments. *The Photogrammetric Record*, 17(99):419–439.

Butler, J. B., Lane, S. N., and Chandler, J. H. (1998). Assessment of DEM quality for characterizing surface roughness using close range digital photogrammetry. *The Photogrammetric Record*, 16(92):271–291.

Chandler, J. H. (1999). Effective application of automated digital photogrammetry for geomorphological research. *Earth Surface Processes and Landforms*, 24(1):51–63.

Chandler, J. H., Cooper, M. A. R., and Robson, S. (1990). Analytical aspects of small format surveys using oblique aerial surveys. *Journal of Photographic Science*, 37(6):235–240.

Chandler, J. H. and Fryer, J. (2013). Autodesk 123D Catch: how accurate it is? *Geomatics World*, 2(21):28–30.

Chandler, J. H., Fryer, J., and Jack, A. (2005). Metric capabilities of low-cost digital cameras for close range surface measurement. *The Photogrammetric Record*, 20(109):12–26.

Chandler, J. H. and Moore, R. (1989). Analytical photogrammetry: a method for monitoring slope instability. *Quarterly Journal of Engineering Geology and Hydrogeology*, 22(2):97–110.

EDF R&D (2012). Cloudcompare (version 2.4) [gpl software]. Technical report, Telecom ParisTech.

Eos Systems Inc. (2012). Quantifying the accuracy of dense surface modeling within Photo-Modeler Scanner. Technical report.

Fix, R. E. and Burt, T. P. (1995). Global positioning system: an effective way to map a small area or catchment. *Earth Surface Processes and Landforms*, 20(9):817–827.

Fonstad, M. A., Dietrich, J. T., Courville, B. C., and Carbonneau, P. E. (2013). Topographic structure from motion: a new development in photogrammetric measurements. *Earth Surface Processes and Landforms*, 38(4):421–430.

Gomez-Gutierrez, A., Schnabel, S., Berenguer-Sempere, F., Lavado-Contador, F., and Rubio-Delgado, J. (2014). Using 3D photo-reconstruction methods to estimate gully headcut erosion. *Catena*, 120:91–101.

Heritage, G. and Hetherington, D. (2007). Towards a protocol for laser scanning in fluvial geomorphology. *Earth Surface Processes and Landforms*, 32(1):66–74.

Hodge, R., Brasington, J., and Richards, K. S. (2009a). Analysing laser-scanned digital terrain models of gravel bed surfaces: linking morphology to sediment transport processes and hydraulics. *Sedimentology*, 56(7):2024–2043.

Hodge, R., Brasington, J., and Richards, K. S. (2009b). In situ characterization of grain-scale fluvial morphology using terrestrial laser scanning. *Earth Surface Processes and Landforms*, 34(7):954–968.

Horn, B. K. P. (1987). Closed-form solution of absolute orientation using unit quaterions. *Journal of the Optical Society of America*, 4(4):629–642.

James, M. R., Ilic, S., and Ruzic, I. (2013). Measuring 3D coastal change with a digital camera. In *Proceedings of Coastal Dynamics*.

James, M. R. and Robson, S. (2012). Straightforward reconstruction of 3D surfaces and topography with a camera: Accuracy and geoscience application. *Journal of Geophysical Research*, 117(F3):F03017.

Lane, S. N. (2000). The measurement of river channel morphology using digital photogrammetry. *The Photogrammetric Record*, 16(96):937–961.

Lane, S. N., Reid, S. C., Westaway, R. M., and Hicks, D. M. (2004). Remotely sensed topographic data for river channel research: the identification, explanation and management of error. In Kelly, R., Drake, N., and Barr, S., editors, *Spatial Modelling of the Terrestrial Environment*, pages 157–174. Wiley, Chichester.

Lane, S. N., Richards, K. S., and Chandler, J. H. (1994). Developments in monitoring and modelling small-scale river bed topography. *Earth Surface Processes and Landforms*, 19(4):349–368.

Mankoff, K. D. and Russo, T. A. (2013). The Kinect: a low-cost, high-resolution, short-range 3D camera. *Earth Surface Processes and Landforms*, 38(9):926–936.

Nitsche, M., Turowski, M. J., Badoux, A., Rickenmann, D., Kohoutek, T. K., Pauli, M., and Kirchner, J. W. (2013). Range imaging: a new method for high-resolution topographic measurements in small- and medium-scale field sites. *Earth Surface Processes and Landforms*, 38(8):810–825.

Sanz-Ablanedo, E., Chandler, J. H., and Wackrow, R. (2012). Parametrising internal camera geometry with focusing distance. *The Photogrammetric Record*, 27(138):210–226.

Schaefer, M. and Inkpen, R. (2010). Towards a protocol for laser scanning of rock surfaces. *Earth Surface Processes and Landforms*, 35(4):417–423.

Westaway, R. M., Lane, S. N., and Hicks, D. M. (2000). The development of an automated correction procedure for digital photogrammetry for the study of wide, shallow, gravel-bed rivers. *Earth Surface Processes and Landforms*, 25(2):209–226.

Westoby, M., Brasington, J., Glasser, N. F., Hambrey, M. J., and Reyonds, M. J. (2012). 'Structure-from-Motion' photogrammetry: A low-cost, effective tool for geoscience applications. *Geomorphology*, 179:300–314.

Woodget, A. S., Carbonneau, P. E., Visser, F., and Maddock, I. (2015). Quantifying submerged fluvial topography using hyperspatial resolution UAS imagery and structure from motion photogrammetry. *Earth Surface Processes and Landforms*, 40(1):47–64.

Zhang, Z. (1994). Iterative point matching for registration of free-form curves and surfaces. *International Journal of Computer Vision*, 13:119–152.

5 Geomorphological activity at a rock glacier front detected with a 3D density-based clustering algorithm

Natan Micheletti, Marj Tonini, Stuart N. Lane

Context

Terrestrial Laser Scanners (TLS) are extensively used in geomorphology for remotely sensing and to derive digital elevation models (DEMs). Modern devices are able to collect many millions of points per minute. Working on the resulting dataset is often troublesome in terms of computational effort. Indeed, it is not unusual that raw point clouds are filtered prior to DEM creation, such that only a subset of points is retained and the interpolation process becomes less of a burden. Whilst this procedure is in many cases necessary, it leads to a considerable loss of valuable information. Because of the reasons above, being able to perform geomorphological research directly on point clouds would be profitable.

This paper proposes an approach to isolate erosion and deposition features semi-automatically in 3-D point clouds. A clustering method, namely the Density-Based Scan Algorithm with Noise (DBSCAN), is applied to identify mass movements at the front of a very active Alpine rock glacier. The methodology allows detection of volumetric features with higher accuracy with respect to traditional, raster or TIN based, approaches.

In the context of this thesis, the chapter represents an attempt to process dense point clouds more efficiently for change detection purposes in geomorphology. This contribution also offers insights into the geomorphologic activity of an active rock glacier during a summer characterized by a heat wave.

Abstract

Acquisition of high density point clouds using Structure from Motion photogrammetry and terrestrial laser scanners (TLS) has become commonplace in geomorphic science. However, the derived point clouds are often filtered and/or interpolated onto regular grids and the grids compared so as to detect changes (erosion/deposition). This procedure is necessary for some applications (e.g. digital terrain analysis) but it leads to a considerable loss of potentially valuable information contained within the point clouds. In the present study, a semi-automatic methodology for geomorphological analysis and feature detection from point clouds is developed. It rests on the use of the Density-Based Spatial Clustering of Applications with Noise (DBSCAN), applied to TLS data for a rock glacier front in the Swiss Alps. The proposed methods allowed the isolation of clusters of erosion and deposition directly from point clouds without the prior need for interpolation or data reduction and with an accuracy that depends only on the actual sampling resolution. The results are illustrated for the summer of 2015, a season of enhanced geomorphic activity associated with exceptionally high temperatures.

Keywords: DBSCAN; terrestrial laser-scanning (TLS); point clouds; feature detection; rock glacier;

5.1   Introduction

The rapid development of new remote sensing methods for topographic measurement has revolutionized geoscience research over the last two decades. Central to many of these methods is the production of point clouds, often with an exceptionally high, but spatially variable point density. For instance, terrestrial laser scanning (TLS) has been one of the most successful method for 3D data collection [Bauer et al., 2003; Glenn et al., 2006; Heritage and Hetherington, 2007; Alho et al., 2009; Schaefer and Inkpen, 2010; Deems et al., 2013; Gabbud et al., 2015] and sequential acquisition can be used to detect and quantify surface change [Abellan et al., 2014; Gabbud et al., 2015; Neugirg et al., 2016].

Whilst the developments of terrestrial scanners and ground-based Structure from Motion photogrammetry have made data collection more cost effective as compared with airborne methods, three challenges arise. First, the large number of points acquired is computationally challenging, and datasets have to be filtered such that only a subset of points is finally retained for the analysis (e.g. Abellan et al. [2006]). The consequences of this dataset reduction are dependent on the spatial scales of variability in the surfaces being considered and the questions being asked with those data. It is possible to reduce data density significantly without statistically altering the terrain proprieties at certain (coarser) scales [Gessler et al., 2000; Chaplot et al., 2001]. However, representation of more detailed micro-scale topographic characteristics will need to retain a higher density of data points [Florinsky and Kuryakova, 2000; Anderson et al., 2006]. If the questions being asked of a dataset relate to change detection

(i.e. determination of erosion and deposition), the scale chosen for the analysis will affect directly the estimations of changes obtained [Lane et al., 1994]. Second, whilst unmanned airborne vehicles increasingly allow for low cost aerial survey, terrestrial data collection methods remain important but suffer from perspective effects, which can lead to either zones of occlusion (shadow effect) or spatially-variable point densities. For change detection, such zones need to be treated carefully. Third, in the vast majority of contributions (e.g. Alho et al. [2009]; Jaboyedoff et al. [2012]; Gabbud et al. [2015]) 3D point clouds are interpolated to digital elevation models (DEMs), either as regular raster grids or triangulated irregular networks (TINs). These are effectively 2.5D representations of the topography [Jaboyedoff et al., 2012] because they assign a single Z elevation to a point (defined by X, Y coordinates), excluding the possibility that the point has multiple Z values. Furthermore, rasterized DEMs will require very high grid densities to capture the detail available in the original point data, but DEMs created at high resolution will have areas highly dependent upon point interpolation processes, where the point cloud densities are lower. TINs have similar problems where large triangles are created in zones of low point density.

For these reasons, it may be appropriate to develop change detection methods based upon the direct analysis of the point clouds using semi-automatic or automatic methods to detect and extract individual features. The latter have been proposed recently, notably for rockfall detection and rock mass structure analysis [Gigli and Casagli, 2011; Brodu and Lague, 2012; Riquelme et al., 2014; Tonini and Abellan, 2014; Rohmer and Dewez, 2015]and they tend to be based upon the identification of clusters of points that share the same characteristics. There are fewer examples of the application of cluster-based methods for volume calculation (e.g. Olsen et al. [2015]), especially where there has been no prior interpolation.

The aim of this paper is to develop and to apply a semi-automated method for isolating and identifying erosion and deposition features directly from point cloud data using a 3D clustering algorithm. Specifically, we tested the Density-Based Spatial Clustering of Applications with Noise (DBSCAN, Ester et al. [1996]) for isolating single erosion and deposition features from a TLS-generated point cloud. This approach has been previously employed to quantification of rockfalls and detection of mass joints [Riquelme et al., 2014; Tonini and Abellan, 2014]. The novelty of the proposed approach consists in the implementation of the DBSCAN 3D-module for the direct detection and quantification of erosion and deposition from point clouds, without the need for interpolation and so avoiding the creation of associated artefacts. The only factor that then influences the change estimations is the density of the original TLS data. We developed the method for a classic example of a geomorphic system that has been studied using TLS (e.g. Bauer et al. [2003]; Bodin and Schoeneich [2008]; Avian et al. [2009]): rock glaciers.

5.2 Case study: the Tsarmine rock glacier

The proposed methodology was developed for a very active rock glacier front located in the Swiss Alps: the Tsarmine rock glacier. Generally speaking, active rock glaciers act as sediment conveyors able to transfer large quantities of rock debris downward by permafrost-related creep [Delaloye et al., 2010; Gärtner-Roer, 2012]. Their velocities may vary from a few centimeters to several meters per year [Lambiel et al., 2008; Barboux et al., 2014]. Alpine rock glaciers are widely recognized as a primary agent in gravitational processes, including rockfalls and debris flows, as a result of their steep and unstable fronts [Kääb et al., 2007; Harris et al., 2009; Lugon and Stoffel, 2010]. As a consequence, monitoring and quantifying their dynamics is of great interest, particularly in the face of climate change that could potentially enhance downslope displacement rates (e.g. Kääb et al. [2007]; Lugon and Stoffel [2010]; Micheletti et al. [2015]).

The Tsarmine rock glacier is located in the Hérens Valley, in the Western Swiss Alps (Figure 5.1). Its front is located at 2480 m a.s.l. (near the regional lower limit of permafrost, Lambiel and Reynard [2001]) and it is steep, devoid of vegetation and unstable. From the front, there is the regular detachment of debris, with delivery to a steep corridor containing a small stream, where deposits of boulders are visible for several hundred meters downstream.
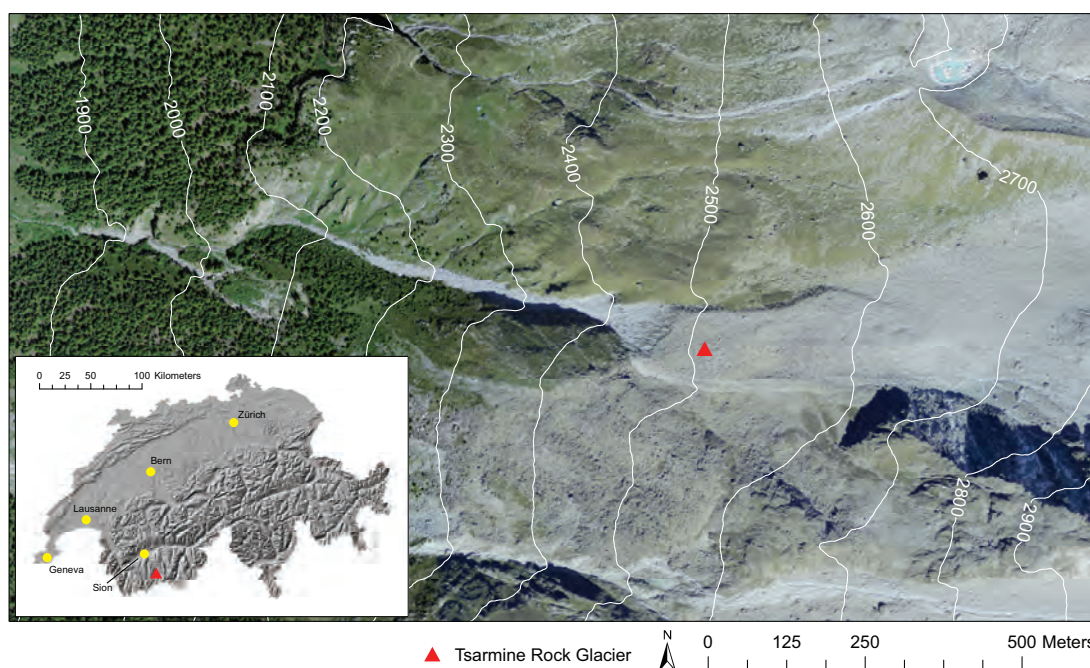
Figure 5.1 – The Tsarmine rock glacier, located in the Hérens Valley, in the Western Swiss Alps (aerial photograph and relief shaded: Swisstopo).

The kinematics of the Tsarmine rock glacier have been investigated using archival aerial photogrammetry, differential SAR interferometry (DInSAR), differential GPS and fixed GPS measurements [Lambiel et al., 2008; Delaloye et al., 2010; Barboux et al., 2014; Micheletti et al.,

2015]. Rapid creep, of the order of 1 to 2 m yr^{-1}, was measured during the years 1990s and 2000s [Barboux et al., 2014; Micheletti et al., 2015]. Following the rock glacier classification proposed by Lambiel et al. [2008], the Tsarmine rock glacier might be considered very rapid and susceptible to very frequent destabilization. Recent GPS data suggest an apparent acceleration since the summer of 2012 and the body of the rock glaciers advanced at velocities of c. 4 m yr^{-1} in the last years, with peaks up to 6 m yr^{-1} in 2015 (unpublished data, Universities of Lausanne and Fribourg). Because of this exceptionally high displacement rate, the Tsarmine rock glacier is likely to be associated with considerable geomorphic change at its front even over short time-scales. As a consequence, it represents an ideal candidate for developing our method.

5.3 Methodology

Figure 5.2 gives an overview of the methodology, from data acquisition through to computation of the volume of change associated with each detected movement units (i.e. erosion and deposition). In summary: (1) point clouds were generated using a TLS on a number of dates (see Section 5.3.2); (2) these clouds were co-registered using stable zones within the surveyed area (bedrock outcrops); (3) the precision of the co-registration of the target dataset onto the datum was used to define points where there may have been some change, expressed as a minimum Euclidean distance; (4) points that are retained were subjected to a clustering algorithm, DBSCAN, which aimed to group points into single features; (5) these features were then labeled as clusters of erosion or of deposition according to the elevation assignment of the change; and (6) the volume of change was finally calculated for each cluster.

5.3.1 DBSCAN: 3-D density based clustering method

The clustering algorithm DBSCAN (Density-Based Spatial Clustering of Applications with Noise, Ester et al. [1996]; Campello et al. [2013]) was used to classify points within the clouds into single cluster features. The computational environment to perform the analysis was the open source R programming language [R Core Team, 2015], using the *dbscan package* [Hahsler et al., 2016]. This procedure allows identification of clusters of arbitrary shape in 2D or 3D space on the base of the local density of points. Essentially, points that are close together are grouped into the same cluster, while points isolated or in very low-density regions are labelled as noise. Only two parameters are required to perform this classification (Figure 5.3): the neighbourhood size epsilon (*eps*) and the minimum number of points necessary to form a cluster (*MinPts*). On the basis of these two parameters, the algorithm explores each point in the cloud, counting the number of the neighbouring points falling within a circle (for the 2D model) or a sphere (for the 3D model) of radius equal to the *eps*-value: if this number is equal to or greater than *MinPts*, the group of points is labelled as a cluster; otherwise points are classified as noise (see Figure 5.3). The central point of each identified cluster is called *core*-point. Then, as some points in the pattern can be density-reachable
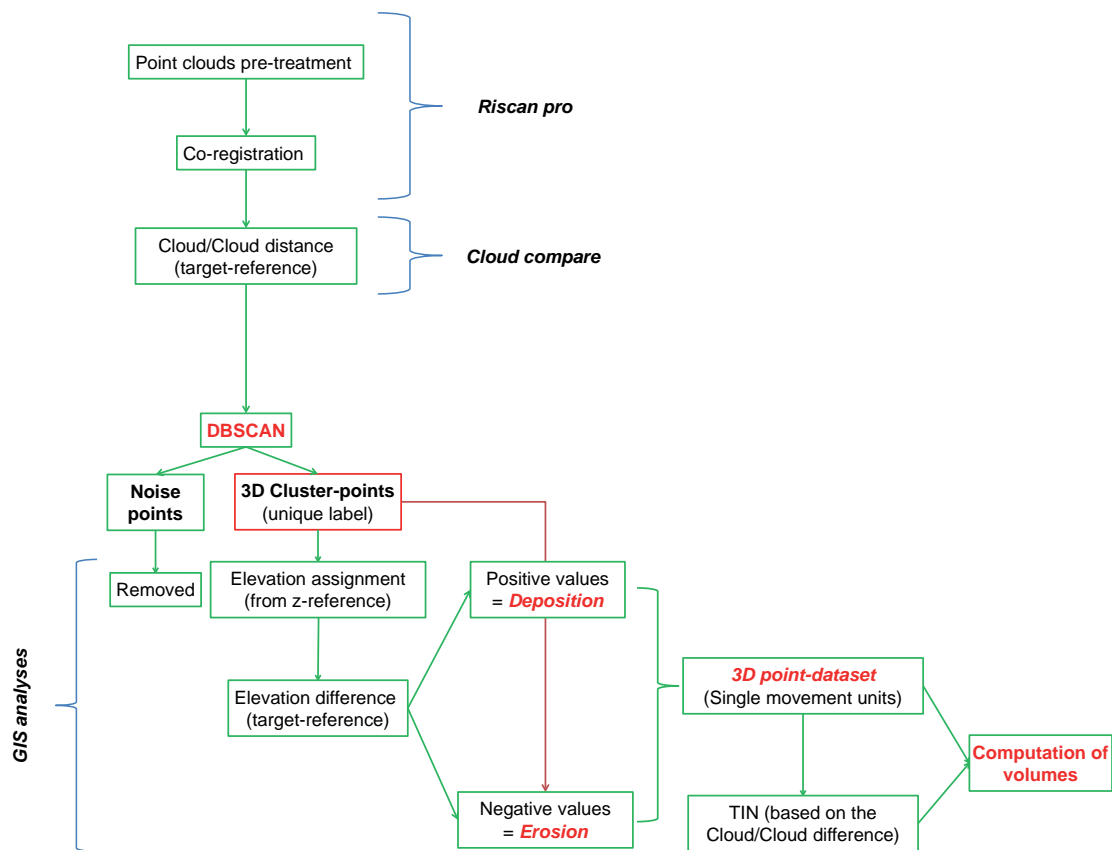
Figure 5.2 – The workflow of the stepwise analysis for a single time-step. For each time-step analysed, the target and reference point clouds are defined as explained in Section 5.3.3.

by more than one *core*-point, they belong to more than one cluster. These are called *seed*-points. The corresponding *core*-points of clusters connected by *seed*-points are said to be density-connected to each other and their clusters blended together to form a unique cluster of arbitrary shape.

The two parameters *eps* and *MinPts* greatly affect the shape, size and number of clusters detected by the algorithm. Their choice mainly relies on a decision that has to be taken as to whether the aim is to identify a large number of small clusters or a small number of large clusters within the original dataset. The default value for *MinPts* in the used package is 5 [Campello et al., 2013]. The actual value used should reflect: (1) dataset size, as when working with very high density datasets, higher values may need to be set to remove noise; and (2) the surface being considered which will determine the spatial scale of erosion and deposition units, and hence the point density that should be needed for a group of points to be coherent. Once that the *MinPts* parameter has been fixed, a suitable value for the *eps* neighbourhood size can be deducted using a k-nearest neighbours (k-NN) distance graph, that is plotting the distance to the k-nearest neighbour and imposing *k* as equal to *MinPts*. The optimal *eps*-value should coincide with strong curvature in the plot: smaller values should give rise to a strong
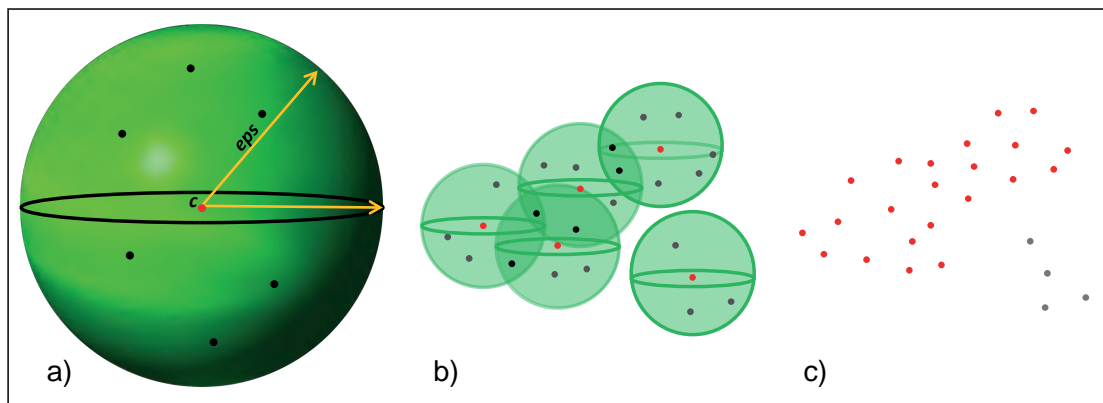
Figure 5.3 – (a) The minimum number of points (*MinPts*) at a maximum distance (*eps*) around the *core*-point (*c*, red dots) defines a cluster. (b) The *core*-points are density-connected by the chain of intermediate *seed*-points (black dots) and (c) their clusters blended together to form a unique cluster of arbitrary shape (red point cloud).

fragmentation and small isolated clusters dispersed among noise-points; for larger values, the majority of the detected clusters will blend together to make bigger clusters.

5.3.2 Field Campaign

An ultra-long range LiDAR RIEGL VZ-6000 scanner was employed to acquire sequential 3D datasets of the rock glacier front. This high speed (up to 222,000 measurements per second), high precision (10 mm at 150 m range) device has proven very efficient for geomorphological research (e.g. Gabbud et al. [2015]; Fischer et al. [2016]). By means of its long-range capability (up to 6000 m), the use of this device allowed the scan position to be set on the opposite side of the valley facing the rock glacier (c. 2800 m of flying distance, see Figure 5.4). TLS scans were performed on four different dates over two consecutive summers: a first survey was carried out on the 23th of September 2014, whilst three more were completed on the 29th of June, the 20th of July and the 22th of September 2015. As it is routine in TLS surveys, the laser device was placed on a tripod over stable ground. The same approximate instrument position was used for each survey. The laser pulse repetition frequency was reduced to its minimal value (30 kHz) to prevent range ambiguity. Vertical and horizontal angle increments were both set to 0.004°, except for the 2014 survey where a value of 0.0045° was chosen (resulting in slightly lower expected point densities). For registration purposes, a very large area containing extensive stable zones in addition to the rock glacier was scanned. The RIEGL VZ-6000 is equipped with on-board inclination sensors, meaning that even when not geo-referenced, resulting data Z dimension represents the elevation above the X-Y plane. An example of the point cloud appearance at the rock glacier front is shown in the detail of Figure 5.4.
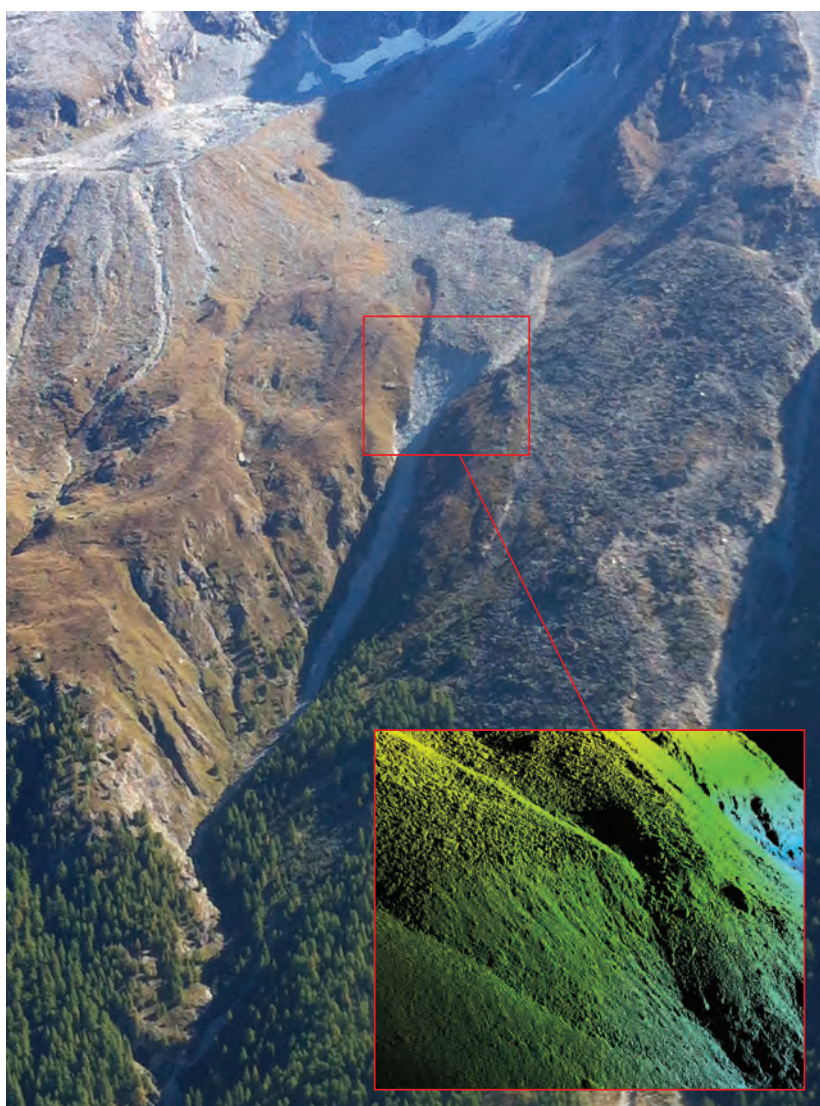
Figure 5.4 – The Tsarmine rock glacier and the steep corridor below its front, as visible from the scanning site on the opposite valley side. The detail shows the point cloud of the rock glacier front (survey: 22/09/2015); the front width is c. 100 m.

5.3.3 Point cloud pre-treatment and co-registration

TLS data were imported and processed initially using the software RiSCAN PRO. The first step was the manual removal of non-ground surface points, caused by atmospheric reflections due to dust or moisture. Afterwards, a relative registration of point clouds was necessary to co-register the four surveys into a common coordinate system. The most recent data (the 22th of September 2015) were treated as the datum. Surfaces prone to considerable topographic change (including the rock glacier) were identified and excluded from the co-registration procedure. A coarse, approximate registration was achieved by manually identifying corresponding points between the datum and each point cloud and shifting the latter by modifying

the SOP (Sensor Orientation and Position) matrix. Subsequently, the co-registration was refined using the Multi-Station Adjustment (MSA) RiSCAN PRO function. The latter uses an Iterative Closest Point (ICP) method [Zhang, 1994]. In the ICP, the orientation and the position of scan positions is modified using least-squares minimization of residuals in order to calculate the best overall fit in respect to the datum. Each residual is defined as the distance between each data point in the cloud being co-registered and its closest point in the datum. After the best fit is determined, the residual distances were calculated and used to assess the quality of co-registration. For all co-registered scans, the residual distances have a Gaussian distribution with mean of zero. Thus, the precision of the co-registration procedure could evaluated by the standard deviation of the residual distances (σMSA): in our case it ranged from ± 0.0598 to ± 0.0987 m.

After co-registration, a mask was used to restrict point clouds to the area of interest: the front of the rock glacier and the corridor below. The point density in the area of interest was c. 24 p m^{-2} for 2015 surveys and 12 p m^{-2} for the 2014 one. The clustering algorithm (DBSCAN) requires as input a 3D dataset, which in our case consists in the point cloud of displacement distance, the latter measured as a Euclidean distance. For any two co-registered datasets, we set the sequentially first dataset as the target and the more recent dataset as the reference. For each point in the target cloud it is necessary to identify its corresponding nearest point in the reference cloud, referred to as the Cloud/Cloud difference (Table 5.1). Consequently, datasets were compared using the distance tool in the point cloud data management software Cloud Compare [EDF R&D, 2012], freely available at www.danielgm.net/cc. This tool exploits a chamfer matching algorithm [Barrow et al., 1977] to obtain the three-dimensional (Euclidean) distance between each point in the target dataset with its closest point in the reference dataset.

Table 5.1 – LiDAR scans and their use as target and reference datasets in the analyses.

Target	Reference	Time-step
29/06/2015	20/07/2015	1 month
20/07/2015	22/09/2015	2 months
29/06/2015	22/09/2015	3 months
23/09/2014	22/09/2015	1 year

These distances comprise two components: (1) real erosion/deposition signals; and (2) noise associated with the fact that points are not exactly co-located in zones of no change, due to sampling or co-registration errors. In practice, as the MSA used zones of no change, the residual distances for these zones are a measure of the noise in the data (i.e. σMSA). The question then becomes what multiple of σMSA to use. One option is to apply some kind of statistical confidence to the distances determined (e.g. in only one dimension $\pm 1.96\sigma$MSA gives a 95% confidence that the distance is a signal and not noise, Lane et al. [2003]). However, if densities are spatially variable within the zone of interest, or between the zones used for the MSA and the zone of interest, such precision may be misleading. One alternative is to take a process-based definition. Here, we note from field observations that the size of displaced

boulders is typically >0.30 m and we use this as a change criteria: that is a boulder must move through its own volume to be considered a change. For comparison, 0.30 m is approximately 3σMSA, approximately a 99.5% confidence level.

5.3.4   Choice of DBSCAN parameters

In the present study, the minimum number of points to constitute a cluster was fixed first, and then the plot of the k-nearest neighbor (k-NN) distance was used to find a suitable value for the *eps* neighbourhood size. To test the influence of DBSCAN parameters on cluster identification, the one month scan (Table 5.1) was used. First, we applied increasing values of *MinPts* (the default of 5, and 10, 15 and 20) to determine the value more appropriate to our case study. We determined k-NN plots for each *MinPts* value, using the plot curvature to identify the optimal *eps*-distance to the kth nearest neighbour. Secondly, to evaluate if the value corresponding to the strong curvature of the k-NN plot is effectively the best choice, we kept *MinPts* equal to the value judged more appropriate (in our case 10) in terms of number of clusters and percentage of noise, and we explored the effects caused by different *eps*-values.

5.3.5   Determination of erosion and deposition volumes

The DBSCAN algorithm provides a dataset containing the following components: the x,y,z-coordinates of each point plus an integer vector assigning it to either a particular clusters or, for the value 0, as a noise point. Then a stepwise GIS analysis was performed to discriminate between single movement units of erosion and deposition, and for the determination of their volumes. This was achieved by using single, rasterized DEMs of the reference dataset (computed here at 0.5 m resolution) and assigning the sign of the elevation difference, designating erosion or deposition, to each cluster-point (allowing to split clusters). Finally, the computation of the volumes of each single movement units was achieved by creating a TIN surface based on the value of the Cloud/Cloud difference (the distance of the closest point in the reference dataset).

5.3.6   Comparison with traditional DEM-to-DEM approaches

In a final stage, the results of the cluster-based volume estimates were compared with ones obtained by the traditional, rasterized, DEM comparison approach, focusing on the one month time lapse. The target (June 2015) and reference (July 2015) co-registered point clouds were interpolated to a 0.3 m regular grid. Given the high point density, a natural neighbour interpolation was deemed sufficient for that purpose. The subtraction between two raster DEMs is traditionally used to detect elevation changes. To isolate real change from noise induced by the data or the interpolation procedure, we could follow the error propagation proposed by Lane et al. [2003]. A 95% confidence limit would provide a detection limit of ±0.27 m, very close to the 0.3 m value used for the DBSCAN analysis. Hence the detection limit used was rounded up to use the same value.
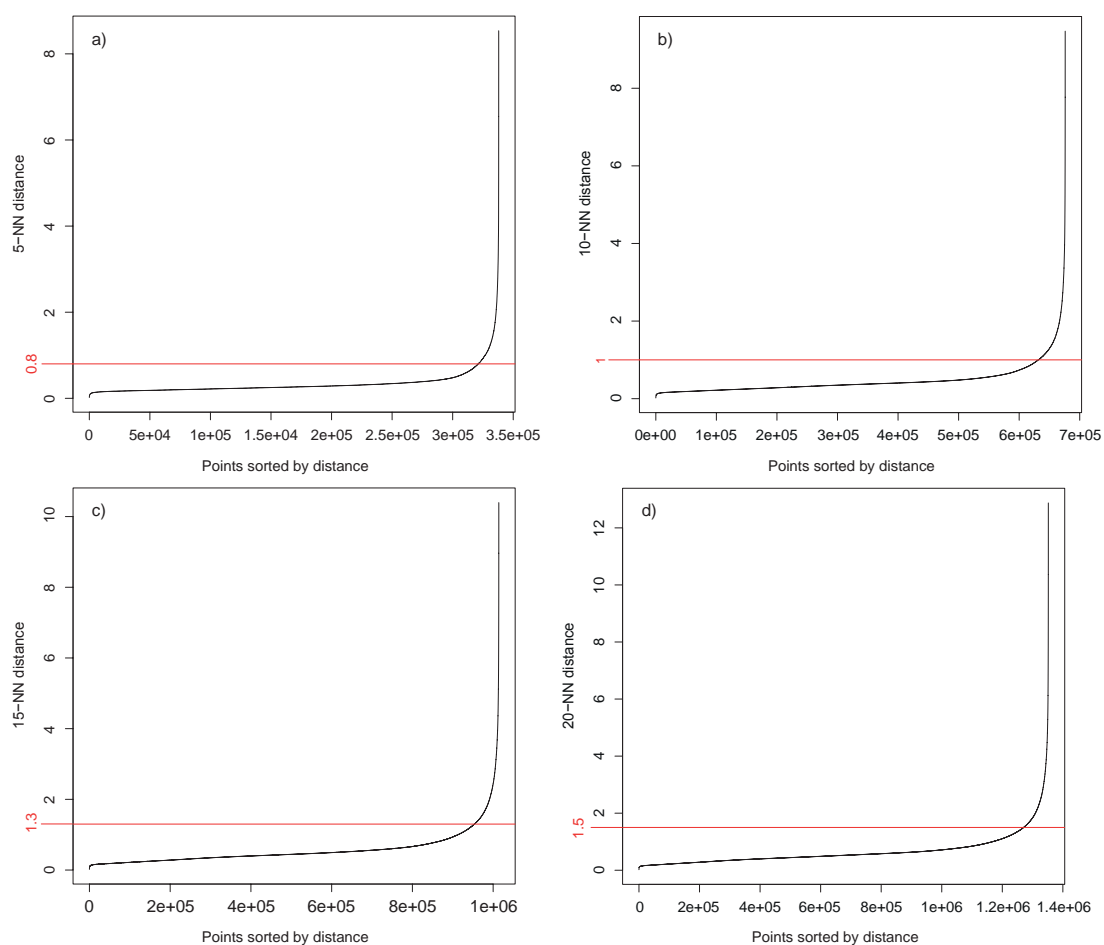
Figure 5.5 – Optimal *eps* value retrieved using k-NN plots for *MinPts* equal to 5 (a), 10 (b), 15 (c) and 20 (d).

5.4 Results

5.4.1 Effects of DBSCAN parameters

The k-distance graphs obtained by applying *MinPts* equal to 5, 10, 15 and 20 (Figure 5.5) shows that the related optimal *eps*-values, coinciding with the strong curvature of the plot, also increase from 0.8 up to 1.5 m, approximately linearly. By fixing *MinPts* as equal to 10, values of 0.5, 1.5 and 2 meter for *eps* were tested against the allegedly best one of 1 meter (Figure 5.5b). Table 5.2 shows the results obtained by applying these DBSCAN parameters on the number of clusters identified, the percentage of points labelled as noise, the number of movement units detected and the volume of change that results.

Table 5.2 illustrates that volumetric estimations do not seem to be particularly sensitive to the tested DBSCAN parameters. This is notably the case for the *MinPts* parameter and whilst the number of identified clusters changes substantially, the percentage points classified as

Table 5.2 – Sensitivity of the resulting number of clusters and volumes of erosion and deposition to changes in the DBSCAN parameters (The effect of parameter settings on aggregation and disaggregation of clusters is shown in Figure 5.6).

Param. setting	MinPts	Eps [m]	Cluster features	Noise points [%]	Movement units	V_{TOT} [m^3]	V_E [m^3]	V_D [m^3]
	increasing							
(a) 1	5	0.8	695	5.0	913	761	320	441
(a) 2	**10**	**1**	**327**	**6.8**	**484**	**738**	**313**	**425**
(a) 3	15	1.3	159	6.3	261	748	316	432
(a) 4	20	1.5	108	6.5	185	747	315	432
	constant							
(b) 1	10	0.5	751	22.7	814	658	290	368
(b) 2	**10**	**1**	**327**	**6.8**	**484**	**738**	**313**	**425**
(b) 3	10	1.5	149	2.7	241	788	330	458
(b) 4	10	2	86	1.3	148	808	338	470

noise changes much less. Thus, the effect of *MinPts* is primarily upon the number of clusters identified and not the number of points that belong to a cluster. This number then is likely to be a key control on the global volume estimates. When the *MinPts* is set to 10 and the *eps* parameter is varied, the number of clusters changes dramatically, and so does the percentage of points identified as noise. Thus, the *eps* parameter not only controls the number of clusters identified but also whether seed-point are shared among several clusters, which blend together. It is then not surprising that the volumes of change are more sensitive to different values of *eps* than when the *MinPts* parameter is varied (Table 5.2). However, the range of variability of the volume changes is proportionately lower than the range of variability of either the number of clusters or the percentage noise points. That is, a certain number of key points are retained in all analyses, and these have a dominant effect on estimates of volumes of change. It is perhaps interesting that it is the volumes of deposition that are more sensitive to the *eps* parameter and the percentage of points that are noise. This may reflect the fact that the deposition signature is less spatially coherent than the erosion signature, with erosion concentrated on key areas (e.g. the rock glacier terminus) but the deposition reflecting local micro-topography (filling of lows).

The question that then arises is what values, notably of *eps*, should be used? Unfortunately, this analysis gives no clear rule as to what should be chosen, and it does not appear to matter too much for the estimation of erosion on this surface. For deposition, the only means of providing a justification is to consider the spatial scale of the kinds of depositional process that has been observed in this kind of environment. Deposition appears to be micro-topography controlled, with a length scale of about 1 m, suggesting a 1 m value of *eps*. More generally, the use of this kind of approach needs additional field observations to help to choose the most suitable value of the *eps* parameter according to the expected scales of erosion and deposition.
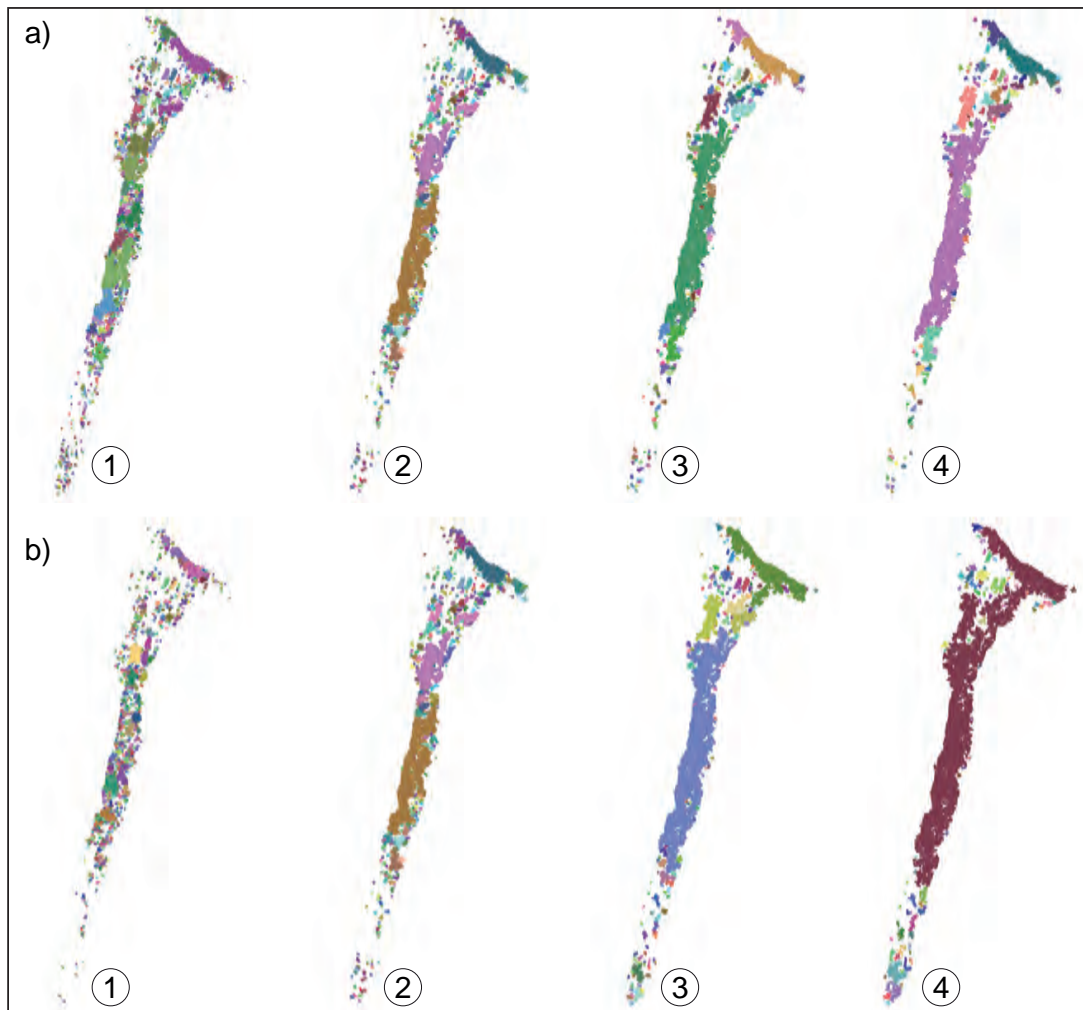
Figure 5.6 – Sensitivity of the clusters aggregation/disaggregation to changes in the DBSCAN parameters (see Table 5.2).

5.4.2 Comparison with traditional DEM comparison

Figure 5.7 compares the maps of erosion and deposition units obtained by applying DBSCAN with the results generated using a traditional, rasterized, DEM comparison. At one level, the patterns are very similar. The same areas are highlighted as erosion and deposition, although the rasterized DEM of difference has more scattered, isolated changed as the comparison makes no reference to the extent to which the data are coherently organized. However, volumetric estimations with DEM comparison are three times higher than with the 3D-clustering approach (see Table 5.3 below), with values for one month close to what would be expected to be observed in one year. These volumetric changes appear unrealistic at the timescale of one month for the presented case study. We attribute this to the effect of artificial surface differences associated with point density effects. Point interpolation assigns an elevation to
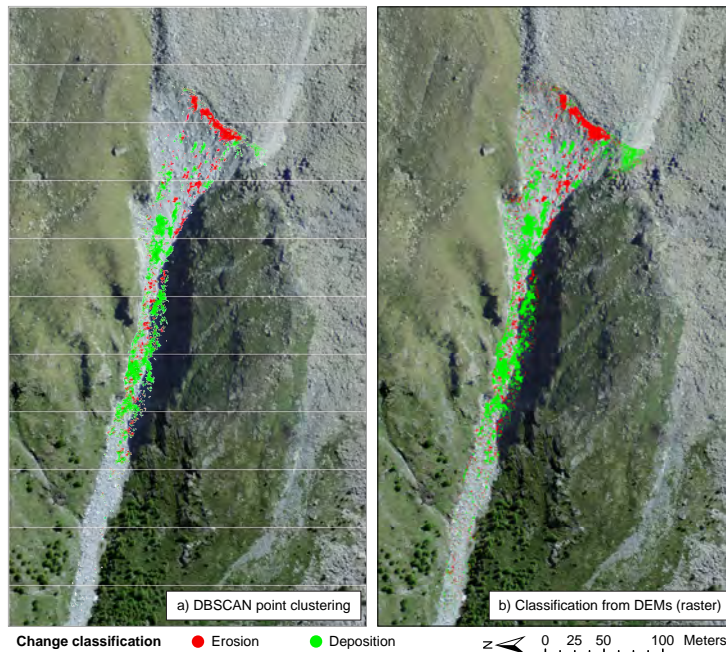
Figure 5.7 – Comparison for one month data between a) DBSCAN point clusters and b) erosion and deposition patters classified from rasterized DEMs comparison.

every grid point and then every grid point is compared, giving a change if it is greater than the 0.3 m detection limit used here. No reference is made to the coherence of changes by association to adjacent points. Given the complex surface variability, interpolation to grids may cause isolated elevation changes that are a result of the chance inclusion of topographic highs and lows in the interpolation surface, rather than any actual geomorphic change. More generally, whether or not a clustering algorithm is used, meaningful detection of surface change should consider the spatial coherence of the change, with respect to the known spatial variability within the surface.

5.5   Discussion

5.5.1   Merits of a 3D-clustering approach

Remote sensing techniques for data acquisition have developed rapidly in recent years. The output of these procedures (i.e. 3D point clouds) are widely used in the geosciences [Abellan et al., 2016] and developing new and fast algorithms for feature extraction is mandatory in this context. Our approach, based on a density clustering method, proved to be very useful for detecting movement units (i.e. erosion and deposition features) at a rock glacier front, allowing extracting and quantifying volumetric changes. The same procedure can be applied to extract 3D features related to any geomorphologic process such as rockfall, debris flows, landslide, etc. As with similar methodologies based upon using point clouds for feature detection [Riquelme
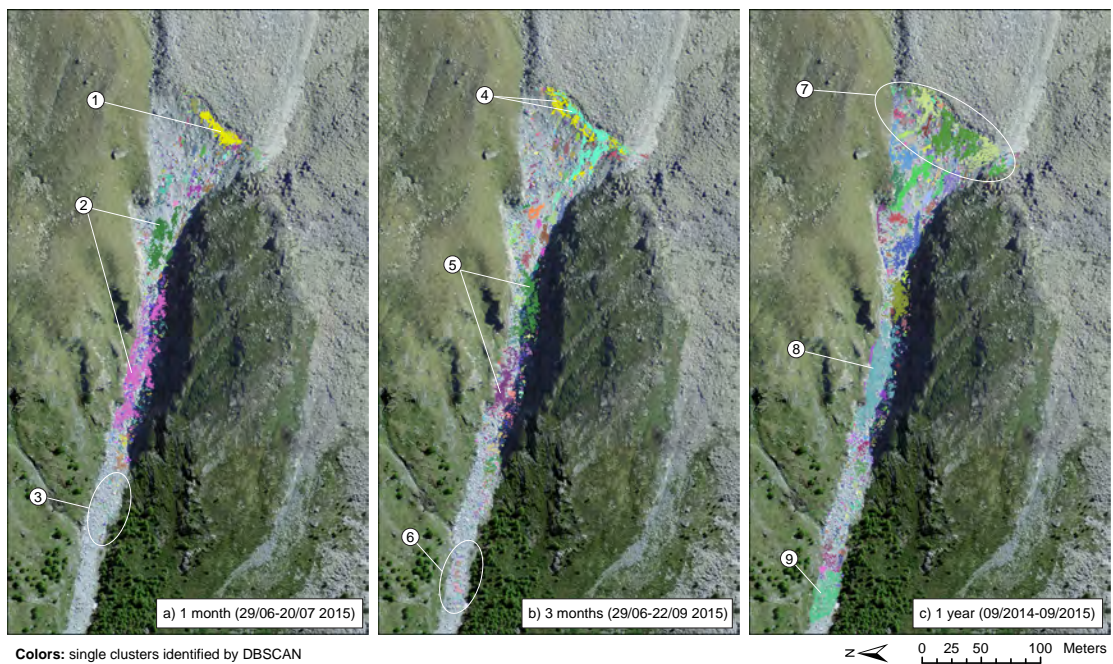
Figure 5.8 – Three-dimensional geomorphological changes identified using DBSCAN for a) one and b) three months and c) one year time lapses. The colour of the dots represents single erosion or deposition features. Numbers are referred to in the text.

et al., 2014; Tonini and Abellan, 2014; Olsen et al., 2015], our approach leads to a reduction in noise and to clustering of points into individual features. Nonetheless, compared with existing applications there are some advantages. First, it is very fast, notably the most recent version of the dbscan package [Hahsler et al., 2016]. Second, by adopting a 3D approach, the method can be applied to any surface regardless of local topographic slope. On steep mountain sides, lateral point displacement might be reduced, with vertical point displacement becoming important, emphasizing the need for a 3D rather than a 2D approach. Third, the proposed methods allowed the isolation of clusters directly from point clouds without the prior need for interpolation or data reduction and with an accuracy that depends only on the actual sampling resolution.

5.5.2 Geomorphological activity at the rock glacier front

Figure 5.8 illustrates the clusters identified by DBSCAN, where each color corresponds to a unit of morphological change. The geomorphological activity during a time-step of one month in the summer 2015 highlights a major cluster with diverse smaller ones at the rock glacier front (Figure 5.8a, 1). From 100 m downslope, an area of deposition is characterized by the presence of two particularly large clusters (Figure 5.8a, 2). In the lower part of the area of study, very small clusters are observed (Figure 5.8a, 3). These are likely to be single boulders that were able to move farther downslope in the channel.

Clusters identified over a time-step of three months (Figure 5.8b) appear larger at the rock
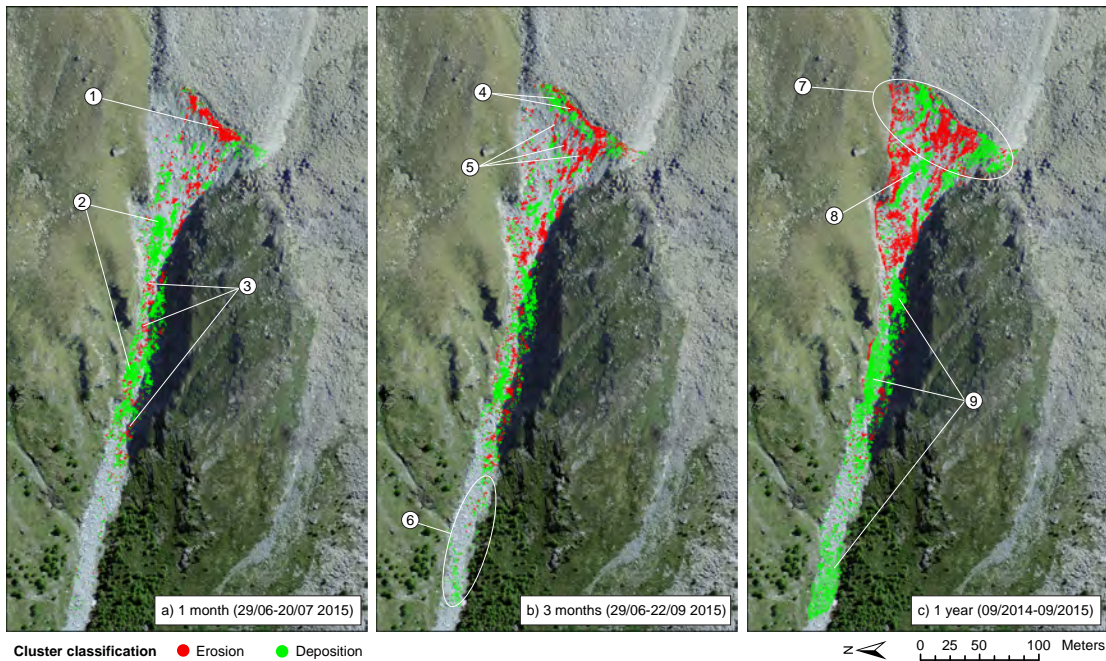
Figure 5.9 – Deposition and erosion features for the field campaigns corresponding to a) one and b) three months and c) one year time lapses. Numbers are referred to in the text.

glacier front, although they do not seem to be more numerous. Despite their proximity, the two major clusters are not unified (Figure 5.8b, 4). The central part of the slope seems slightly more fragmented, although two very large clusters are once again visible (Figure 5.8b, 5). Larger clusters are featured in the lower part of the study area in comparison with the shorter timescale analysis, indicating that several boulders reached that zone (Figure 5.8b, 6).

One-year clusters are shown in Figure 5.8c. Almost the whole front surface has undergone change, as indicated by various large clusters (Figure 5.8c, 7). The middle part of the area of interest has almost completely changed as well, as testified by the presence of many clusters including a very large one (Figure 5.8c, 8). In the lower part, small clusters precede another very large one, depicted in green (Figure 5.8c, 9).

The clusters presented in Figure 5.8 are then classified as erosional or depositional following the procedure discussed in Section 5.3.5 (Figure 5.9). This demonstrates that the largest cluster visible at the front at the one-month time-step is due to a rockfall event which occurred in July 2015 (Figure 5.9a, 1). The remaining features in this zone are a mixture of erosion and deposition, probably caused by detached material blocked by other boulders and unable to travel farther. As expected, the vast majority of clusters in the channel are depositional (Figure 5.9a, 2). Erosional footprints in that zone are scattered but exist (e.g. Figure 5.9a, 3), indicating potential remobilization of material or incision.

Figure 5.9b shows that the two major and separated front clusters at the three month time-scale are opposite in nature (Figure 5.9b, 4). The fact that the erosional cluster is located

Table 5.3 – Synthesis of the geomorphological activity (deposition (D) and erosion (E) movements) at the Tsarmine rock glacier during the summer 2015 and between Sept. 2014 and Sept. 2015. Volumes (V) in m^3.

Time-step	Number of clusters	V_{TOT} [m^3]	V_E[m^3]	V_D [m^3]
1 month	484	738	313	425
2 months	543	826	410	416
3 months	410	1376	536	840
1 year	538	2056	724	1332
1 month*	-	2079	1014	1065

*Traditional DEM comparison

above the deposition area allows two hypotheses. On the one hand the eroded material could have simply slid from the upper part of the detachment niche without leaving the rock glacier front. On the other hand, the two clusters could be unrelated; in that case the eroded material has likely left the front area, and the depositional pattern could be due to the front advance caused by deformation-related creep in the rock glacier body. Given the scale of the analysis (three months) and the seasonal conditions (summer, affected by a heat wave), this second scenario appears more realistic. The front is also characterized by the presence of many erosional clusters with elongated shapes (e.g. Figure 5.9b, 5), very likely caused by collapse and consequent transit of material downstream. Spatial patterns in the channel are similar to the one-month application, but material is deposited further downstream in this case (Figure 5.9b, 6).

The geomorphological activity at the rock glacier front over one year is almost equally divided into erosion and deposition (Figure 5.9c, 7). Whilst erosional patterns are proof of material detaching as permafrost thaws, the green features in Figure 7c are probably due to the rock glacier advancing. In that sense, deposition in these clusters is only apparent, as it is merely a displacement forward. Starting from only 50 m below the crowning of the front, depositional patterns could also be caused by material trapped after a collapse by cause of surface roughness; the elongated cluster in the centre could be an example (Figure 5.9c, 8). Throughout the course of the channel, large clusters of deposition are visible (Figure 5.9c, 9).

Table 5.3 summarizes the geomorphological activity at the Tsarmine rock glacier during the summer 2015 (one, two and three month time-steps) and during one entire year (September 2014 to September 2015). The number of clusters identified by the DBSCAN analysis oscillates between 410 and 543 and does not seem to be related to the duration considered. On the other hand, the total volume of geomorphological change (V_{TOT}) consistently increases as time intervals increase. This implies that over the longer term bigger clusters of geomorphological activity are being identified, which is the expected outcome, also reflected in no real evolution in the number of clusters. Generally, estimates of eroded and accumulated volumes are

balanced at short time scales (one and two months), as one would expect. However, deposition volumes dominate at the longer time span. A possible explanation lies in the fact that the front invariably advances under the influence of creep-related deformation in the rock glacier body. The process is slow and continual, and permafrost thaw and rock fall at the front mitigates it, but at longer timescales it is possible that a part of the front has not yet collapsed, and the advance become visible as an apparent gain of material. On the other hand, another consequence is the reduction or suppression of the volumes of collapsed material that can be observed, as the void might be masked by front advance. Consequently, results should tend to slightly overestimate the total accumulation and underestimate eroded volumes. These processes are likely to be relevant at intermediate and long timescales (e.g. three months and one year, Figure 5.8b and 5.8c), and explain (i) the unbalance between V_E and V_D at these timescales, and (ii) the disagreement between the combination of eroded volumes (V_E) for one and two months and three months erosion.

MeteoSwiss [2016], in their annual climatic report, indicated that year 2015 was once again a record-year for measured air temperature. In particular, the summer 2015 was characterized by an extreme heat wave, and it is classified as the second warmest summer in Switzerland since the beginning of measurements, 152 years ago. Beaten only by the extreme summer of 2003, it registered between 2 and 2.5 °C more than the norm 1981-2010 [MeteoSwiss, 2016]. As a permafrost-related process, rock glacier creep is supposedly very sensitive, amongst others controlling factors, to temperature forcing (e.g. Kellerer-Pirklbauer and Kaufmann [2012]).

The results achieved in this study offer detailed information on the dynamics of the Tsarmine rock glacier front during the hot summer of 2015. During only about one month, 313 m^3 of erosion occurred in the investigated zone. The following two months display slightly higher values: 410 m^3. For both periods, little more than 400 m^3 of accumulated material are estimated. The superior geomorphological activity in the shorter, earlier time span could be an indication of the crucial role of snowmelt, which generally occurs around May for this elevation and orientation, in eroding and mobilizing boulders at the rock glacier front. Another reason could be a strong capacity of thawing at the front that manifests at the beginning of the summer season.

Analysis of the June and September 2015 LiDAR datasets resulted in an estimated 536 m^3 of erosion. It could be argued with confidence that this result is an underestimation. GPS measurements indicate that the rock glacier surface moved at a velocity of almost 5 m yr^{-1} during that period, which correspond to a net advance of 1.25 m. This process partially conceals collapse events by causing the front to advance and occupy the space left empty. The volume of eroded material should be at least a few hundred cubic meters more. The same is true for volumetric estimations for one year (September to September). We argue that erosion quantities (724 m^3) are strongly underestimated for the same reason, as confirmed by accumulation volumes that are almost double of them (1332 m^3, excluding material that travelled further downstream). Whilst an accurate estimation could not be formulated, it is realistic to assume that the rock glacier front delivers sediments downstream in the order of c.

$1500 \, \text{m}^3 \, \text{yr}^{-1}$.

The mass transfer occurred at the Tsarmine rock glacier front during the hot summer 2015 appears extremely high, a fact that could be attributed to the exceptionally high mean velocities observed in the last couple of years (c. $4 \, \text{m} \, \text{yr}^{-1}$). These are considerably higher than the kinematics estimated for the beginning of the 2000s (1 to $2 \, \text{m} \, \text{yr}^{-1}$, Barboux et al. [2014]; Micheletti et al. [2015]), which nonetheless included the 2003 heat wave, suggesting that sediment delivery rates might be much higher nowadays in comparison with 10-15 years ago. In this regard, Gärtner-Roer [2012] observed, for a very active rock glacier located in an adjacent valley (the Turtmann Valley), maximum velocities of $2.59 \, \text{m} \, \text{yr}^{-1}$ during the heat wave of the summer 2003, with a corresponding peak of sediment transfer rate of $1.1 \, \text{Mt} \, \text{yr}^{-1}$ (corresponding to c. $415 \, \text{m}^3 \, \text{yr}^{-1}$ if a specific weight of $2.65 \, \text{t} \, \text{m}^{-3}$ is considered, Barsch [1977]). For a similar case study in the Mattertal Valley, Lugon and Stoffel [2010] encountered much slower kinematics at the beginning of the years 2000s, with maximum movement rates of $0.88 \, \text{m} \, \text{yr}^{-1}$. They estimated a mass flux of $500\text{-}700 \, \text{m}^3 \, \text{yr}^{-1}$, but corrected sediment delivery to $300\text{-}400 \, \text{m}^3 \, \text{yr}^{-1}$ due to the considerable amount of voids and ice contained in the rock glacier. Following these indication, it would be plausible to assume that erosion volumes at the Tsarmine rock glacier have almost doubled in the last decade. Comparing our results to the behaviour of other rock glaciers during the hot summer of 2015 could provide insights in this sense.

The maps of erosion and deposition clusters (Figures 5.8 and 5.9) illustrate the high geomorphological activity at the front of the rock glacier during the period of study. Nonetheless, boulders detaching from the front do not appear to travel far. Large clusters of deposition are identified a few hundred meters below the front, and with a few exceptions at longer time spans where traces of material extend farther downstream, boulders are exclusively stocked in the first 200 m of the channel. Hence, despite evidence of significant sediment production at the rock glacier front, impacts at the valley bottom are absent for the time being. A further remobilization of this material (e.g. by debris flows events) is not to be excluded, but the diameter of rocks is quite substantial and thus the risk quite mitigated.

5.6 Conclusions

The application of the DBSCAN 3D-module using TLS point clouds permitted detection of erosion and deposition features, their mapping and derivation of detailed volumetric change estimations for a rock glacier front located in the Swiss Alps. Single clusters of erosion and deposition were extracted directly from point clouds without the necessity of reduce or interpolate the 3-D original data. The proposed approach is semi-automatic and allows detecting realistic volumetric features, depending only on the actual data available. This methodology represents an alternative to traditional point cloud processing techniques for applications in geomorphology.

Remarkable geomorphological activity was observed at a rock glacier front during the sum-

mer of 2015, likely under the influence of the very rapid permafrost creep suggested by GPS measurements. To determine if the influence of the exceptionally high temperatures observed that season plays a driving role in these processes, TLS surveys for the following summers would be necessary, and the proposed approach would be ideal to efficiently process the resulting datasets. Moreover, a more detailed coupling between meteorological events, climatic data and morphological changes were beyond the focus of this study, but would need to be performed to infer the effects of external forcing on sediment production at a rock glacier front.

Acknowledgements

Bibliography

Abellan, A., M.-H., D., and Jaboyedoff, M. (2016). "Use of 3D Point Clouds in Geohazard" Special Issue: Current Challenges and Future Trends. *Remote Sensing*, 8(130):doi:10.3390/rs8020130.

Abellan, A., Oppikofer, T., Jaboyedoff, M., Rosser, N. J., Lim, M., and Lato, M. J. (2014). Terrestrial laser scanning of rock slope instabilities. *Earth Surface Processes and Landforms*, 39(1):80–97.

Abellan, A., Vilaplana, J. M., and Martinez, J. (2006). Application of a long-range Terrestrial Laser Scanner to a detailed rockfall study at Vall de Núria (Eastern Pyrenees, Spain). *Engineering Geology*, 88(3-4):136–148.

Alho, P., Kukko, A., Hyyppa, H., Kaartinen, H., Hyyppa, J., and Jaakkola, A. (2009). Application fo boat-based laser scanning for river survey. *Earth Surface Processes and Landforms*, 34(13):1831–1838.

Anderson, E. S., Thompson, J. A., Crouse, D. A., and Austin, R. E. (2006). Horizontal resolution and data density effects on remotely sensed LIDAR-based DEM. *Geoderma*, 132(3-4):406–415.

Avian, M., Kellerer-Pirklbauer, A., and Bauer, A. (2009). LiDAR for monitoring mass movements in permafrost environments at the cirque Hinteres Langtal, Austria, between 2000 and 2008. *Natural Hazards and Earth System Sciences*, 9:1087–1094.

Barboux, C., Delaloye, R., and Lambiel, C. (2014). Inventorying slope movements in an Alpine environment using DInSAR. *Earth Surface Processes and Landforms*, 39(15):2087–2099.

Barrow, D. H., Tenenbaum, J. M., Bolles, R. C., and Wolf, H. C. (1977). Parametric correspondence and chamfer matching: two new techniques for image matching. In *Proc. 5th Int. Joint Conf. Artificial Intelligence, Cambridge, MA, 659-663*.

Barsch, D. (1977). Nature and importance of mass-wasting by rock glaciers in alpine permafrost environment. *Earth Surface Processes*, 2(2-3):231–245.

Bauer, A., Paar, G., and Kaufmann, V. (2003). *Permafrost*, chapter Terrestrial laser scanning for rock glacier monitoring, pages 55–60. Taylor and Francis, London.

Bodin, X. and Schoeneich, P. (2008). High-resolution DEM extraction from terrestrial LIDAR topometry and surface kinematics of the creeping alpine permafrost: The Laurichard rock glacier case study (Southern French Alps). In *Proceedings of the Ninth International Conference on Permafrost*.

Brodu, N. and Lague, D. (2012). 3D terrestrial lidar data classification of complex natural scenes using a multi-scale dimensionality criterion: Applications in geomorphology. *ISPRS Journal of Photogrammetry and Remote Sensing*, 68:121–134.

Campello, R. J. G. B., Moulavi, D., and Sander, J. (2013). Density-Based Clustering Based on Hierarchival Density Estimates. In *Proceedings of the 17th Pacific-Asia Conference on Knowledge Discovery in Databases, PAKDD 2013.*

Chaplot, V., Bernoux, M., Walter, C., Curmi, P., and Herpin, U. (2001). Soil carbon storage prediction in temperate hydromorphic soils using a morphologic index and digital elevation model. *Soil Science*, 166(1):48–60.

Deems, J., Painter, T., and Finnegan, D. (2013). LiDAR measurement of snow depth: a review. *Journal of Glaciology*, 59(215):467–479.

Delaloye, R., Lambiel, C., and Gärtner-Roer, I. (2010). Overview of rock glacier kinematics research in the Swiss Alps. Seasonal rhythm, interannual variations and trands over several decades. *Geographica Helvetica*, 65:135–145.

EDF R&D (2012). Cloudcompare (version 2.4) [gpl software]. Technical report, Telecom ParisTech.

Ester, M., Kriegel, H.-P., Sander, J., and Xu, X. (1996). A Density-Based Algorithm for Discovering Clusters in Large Spatial Databases with Noise. In *Proc. 2nd Int. Conf. on Knowledge Discovery and Data Mining, Portland, OR, AAAI Press*, pages 226–231.

Fischer, M., Huss, M., Kummert, M., and Hoelzle, M. (2016). Use of an ultra-long-range terrestrial laser scanner to monitor the mass balance of very small glaciers in the Swiss Alps. *The Cryosphere Discussions*, doi:10.5194/tc-10-1279-2016.

Florinsky, I. V. and Kuryakova, G. A. (2000). Determination of grid size for digital terrain modeling in landscape investigations-exemplified by soil moisture distribution at a micro-scale. *International Journal of Geographical Information Science*, 14(8):815–832.

Gabbud, C., Micheletti, N., and Lane, S. N. (2015). Lidar measurement of surface melt for a temperate Alpine glacier at the seasonal and hourly scale. *Journal of Glaciology*, 61(229):963–974.

Gärtner-Roer, I. (2012). Sediment transfer rates of two active rock glaciers in the Swiss Alps. *Geomorphology*, 167-168:45–50.

Gessler, P. E., Chadwick, O. A., Chamran, F., Althouse, L. D., and Holmes, K. W. (2000). Modeling soil-landscape and ecosystem properties using terrain attributes. *Soil Science Society of America Journal*, 64(6):2046–2056.

Gigli, G. and Casagli, N. (2011). Semi-automatic extraction of rock mass structural data from high resolution LIDAR point clouds. *International Journal of Rock Mechanics & Mining Sciences*, 48(2):187–198.

Glenn, N. F., Streutker, D. R., Chadwick, D. J., Thackray, G. D., and Dorsch, S. J. (2006). Analysis of LiDAR-derived topographic information for characterizing and differentiating landslide morphology and activity. *Geomorphology*, 73(1-2):131–148.

Hahsler, M., Piekenbrock, M., Arya, S., and Mount, D. (2016). Density Based Clustering of Applications with Noise (DBSCAN) and Related Algorithms. Technical report, Package dbscan for R.

Harris, C., Arenson, L. U., and others, . (2009). Permafrost and climate in Europe: Monitoring and modelling thermal, geomorphological and geotechnical responses. *Earth-Science Reviews*, 92(3-4):117–171.

Heritage, G. and Hetherington, D. (2007). Towards a protocol for laser scanning in fluvial geomorphology. *Earth Surface Processes and Landforms*, 32(1):66–74.

Jaboyedoff, M., Oppikofer, T., Abellan, A., Derron, M.-H., Loye, A., Metzger, R., and Pedrazzini, A. (2012). Use of LIDAR in landslide investigations: a review. *Natural Hazards*, 61:5–28.

Kääb, A., Frauenfelder, R., and Roer, I. (2007). On the response of rockglacier creep to surface temperature increase. *Global and Planetary Change*, 56:172–187.

Kellerer-Pirklbauer, A. and Kaufmann, V. (2012). About the relationship between rock glacier velocity and climate parameters in Central Austria. *Austrian Journal of Earth Sciences*, 105(2):94–112.

Lambiel, C., Delaloye, R., Strozzi, T., Lugon, R., and Raetzo, H. (2008). ERS InSAR for assessing rock glacier activity. In *Proceedings of the Ninth International Conference on Permafrost*.

Lambiel, C. and Reynard, E. (2001). Regional modelling of present, past and future potential distribution of discontinuous permafrost based on a rock glacier inventory in the Bagnes-Hérémence area (Western Swiss Alps). *Norwegian Journal of Geography*, 55(4):219–223.

Lane, S. N., Chandler, J. H., and Richards, K. S. (1994). Developments in monitoring and modelling small-scale river bed topography. *Earth Surface Processes and Landforms*, 19(4):349–368.

Lane, S. N., Westaway, R. M., and Murray Hicks, D. (2003). Estimation of erosion and deposition volumes in a large, gravel-bed, braided river using synoptic remote sensing. *Earth Surface Processes and Landforms*, 28(3):249–271.

Lugon, R. and Stoffel, M. (2010). Rock-glacier dynamics and magnitude-frequency relations of debris flows in a high-elevation watershed: Ritigraben, Swiss Alps. *Global and Planetary Change*, 73:202–210.

MeteoSwiss (2016). Climatic report, year 2015. Technical report, Zürich.

Micheletti, N., Lambiel, C., and Lane, S. N. (2015). Investigating decadal-scale geomorphic dynamics in an alpine mountain setting. *Journal of Geophysical Research: Earth Surface*, 120:2155–2175.

Neugirg, F., Stark, M., Kaiser, A., Vlacilova, M., Della Seta, M., Vergari, F., Schmidt, J., Becht, M., and Haas, F. (2016). Erosion processes in calanchi in the Upper Orcia Valley, Southern Tuscany, Italy based on multitemporal high-resolution terrestrial LiDAR and UAV surveys. *Geomorphology*, 269:8–22.

Olsen, M. J., Wartman, J., McAlister, M., Mahmoudabadi, H., O'Banion, M. S., Dunham, L., and Cunningham, K. (2015). To Fill or Not to Fill: Sensitivity Analysis of the Influence of Resolution and Hole Filling on Point Cloud Surface Modeling and Individual Rockfall Event Detection. *Remote Sensing*, 7:12103–12134.

R Core Team (2015). *R: A Language and Environment for Statistical Computing*. R Foundation for Statistical Computing, Vienna, Austria.

Riquelme, A. J., Abellan, A., Tomas, M., and Jaboyedoff, M. (2014). A new approach for semi-automatic rock mass joints recognition from 3D point clouds. *Computers & Geosciences*, 68:38–52.

Rohmer, J. and Dewez, T. (2015). Analysing the spatial patterns of erosion scars using point process theory at the coastal chalk cliff of Mesnil-Val, Normandy, northern France. *Natural Hazards and Earth System Sciences*, 15:349–362.

Schaefer, M. and Inkpen, R. (2010). Towards a protocol for laser scanning of rock surfaces. *Earth Surface Processes and Landforms*, 35(4):417–423.

Tonini, M. and Abellan, A. (2014). Rockfall detection from terrestrial LiDAR point clouds: A clustering approach using R. *Journal of Spatial Information Science*, 8:95–110.

Zhang, Z. (1994). Iterative point matching for registration of free-form curves and surfaces. *International Journal of Computer Vision*, 13:119–152.

Insights into the recent evolution of Alpine landscapes

6 Studying the evolving dynamics of Alpine environments

6.1 The forcing of Alpine landscapes

Generally speaking, external drivers and interactions amongst internal processes control the development of landforms in natural environments. In other words, the evolution of a landscape is determined by the coupling of *endogenous* processes (interior regulation and interaction between elements of the system) and *exogenous* (external) forces. Of course, what is endogenous and what is exogenous is scale dependent. However, this distinction provides a valuable conceptual framework for geomorphic change in Alpine landscapes. One of the most influential contribution to this reflection was provided by Schumm and Lichty [1965]; they argued that the distinction between cause and effect in the development of landforms (and hence landscape evolution) is a function of time and space. The choices made by the observer determine the kinds of causal relations identified and hence what is exogenous and what is endogenous. From a general point of view, every cause is an effect and every effect a cause [Mackin, 1963]. The boundaries set by the researcher for a given study arbitrates which elements are the driving (independent) factors, and which ones the dependent processes or forms that act accordingly to the conditions of the former. For example, how relief evolves is dictated by time, climate and geology (lithology and structure) at geological timescales; in turn, at shorter temporal scales, relief is deemed a relevant factor in driving hillslope processes. Therefore, it is necessary to define the limits of the system that is considered, both temporally and spatially, in order to define the roles and processes at play [Schumm and Lichty, 1965].

In this conceptual formulation of causality, high mountain environments are no exception. In the context of the evolution and dynamics of Alpine landscapes in the 20th and 21st centuries, a primary concern of this thesis, it is imperative to define the scales of interest and hence the direction of causal relations. Through the identification of agents and processes relevant at these temporal (decadal) and spatial (mountain environment) scales, boundaries conditions can be set and a holistic approach can be developed. Only then can the interdependence of the elements of the landscape be considered in the context of driving, independent forces, and the evolving dynamics of Alpine environment retraced. Such an approach is valuable for

deepening our understanding of Alpine systems in the face of climate change because it helps to tease out precisely what is causal.

At the scale of the 20th and 21st centuries, an essential role is likely to be played by climate. Recent considerations suggest that, irrespective of future greenhouse-gas emissions, a mean surface temperature increase of 2°C over 1990 levels is inevitable, and an increase of 4°C by the end of the century is not unlikely [Knight and Harrison, 2013; IPCC, 2014]. High sensitivity to this forcing is expected for glaciated areas at low- and mid-latitudes ([Knight and Harrison, 2009], see also Chapter 1). In addition to the obvious impacts on thermal properties of permafrost and nival processes (e.g. Pelto and Hedlund [2001]; Kääb et al. [2007]; Carturan et al. [2013]), global warming and heavy precipitation are likely to strongly affect the frequency and magnitude of mass movement by their capacity to enhance debris production and to sustain sediment mobilization and transfer (e.g. Stoffel and Huggel [2012]). Hence, recent climate change represent an exogenous, independent force that is likely to affect Alpine dynamics at the timescale of decades to centuries, with dramatic consequences on both endogenous processes and the landforms they produce, as extensively demonstrated in recent scientific literature (see Lane [2013] for more considerations and examples).

Another independent variable is represented by landscape heritage. The steep, glacially-inherited topography visible nowadays in high mountain environments is the dependent product of the climate-landform legacy. This endogenous aspect of the landscape acts as independent variable at the decadal-scale. First, it provides a high potential for sediment mobilization through the steepness of the slopes caused by past glaciation [Brocklehurst and Whipple, 2002]. Second, it is responsible for the significant amounts of historically weathered and glacially derived material available in these areas [Ballantyne et al., 2014]. Third, landscape legacy has a major role in the development of sediment connectivity, which might strongly influence how effective the sediment cascade is [Harvey, 2001; Burt and Allison, 2010; Heckmann and Schwanghard, 2013]. In other words, past glaciation determines how the elements of the system (landforms) are coupled together. The history of the landscape (i.e. its legacy) may be very influential in controlling geomorphological dynamics in mountainous areas.

Lastly, anthropogenic impact may strongly affect Alpine valleys, notably following exploitation for hydropower production. Here, we do not focus directly on anthropological forcing of climate change. Instead, we invoke human intervention for its potential capacity to alter the natural, geomorphic dynamics of the landscape. However, in contrast to the two previous factors, human forcing is not always present in Alpine environments, nor does it systematically constrain their dynamics; many watersheds are devoid from human infrastructure, or affected only partially (e.g. downstream of a water retention structure).

6.2 Mountain geomorphic systems

Landforms are the structural elements that compose a landscape. From a systemic point of view, these landforms are related by a network of processes belonging to different domains. In the context of Alpine environments, we commonly refer to six process domains (e.g. Otto and Dikau [2004]):

1. Gravitational domain

2. Glacial and nival domain

3. Cryogenic and periglacial domain

4. Fluvial, fluvioglacial and torrential domain

5. Anthropogenic domain

6. Unspecified domain (i.e. organic and organo-mineral sphere)

Climate and landscape legacy (and often anthropogenic actions) exert an independent control on erosion, transfer and accumulation of matter. By activating geomorphological processes, they create and modify landforms, thus potentially generating feedback-effects. This systemic conception is frequently referred as *geomorphic system* (e.g. Schrott et al. [2003]).

An elegant, yet simple conceptualization of mountain geomorphic systems can be formulated with the notion of the *sediment cascade*. Based upon the reflections of Chorley and Kennedy [1971] and Caine [1974], this conceptual model recasts the notion of sediment flux as the recurrence of erosion/transport/deposition cycles, through which sediments move from one element of the geomorphic system to the other. This conception suggests that sediments rarely reach the valley bottom (or sediment sinks as lacustrine or coastal deposits) with a single transport vector. Contrariwise, material mobilized within a landform is usually transferred and deposited in another geomorphological feature, where it could be transported further downstream afterwards. In this chain of geomorphological processes, an essential role of energy-provider is played by water and gravity. To better delineate this concept, one could refer to the comprehensive illustration of the sediment cascade of paraglacial processes (i.e. non-glacial processes conditioned by glaciation, Slaymaker [2009]) proposed by Ballantyne [2002] (Figure 6.1). The conceptualization describes how material moves from sediment sources to valley bottoms or terminal sinks by mean of various transfer processes and through different stores. A key research question in this topic concerns the extent of Alpine sediment cascade [Wichmann et al., 2009].

The perception of a sediment cascade implies a spatial relation between landforms, often referred with the term *connectivity* (e.g. Caine and Swanson [1989]; Harvey [2002]; Heckmann and Schwanghard [2013]). The functioning of the sediment flux system in cascading
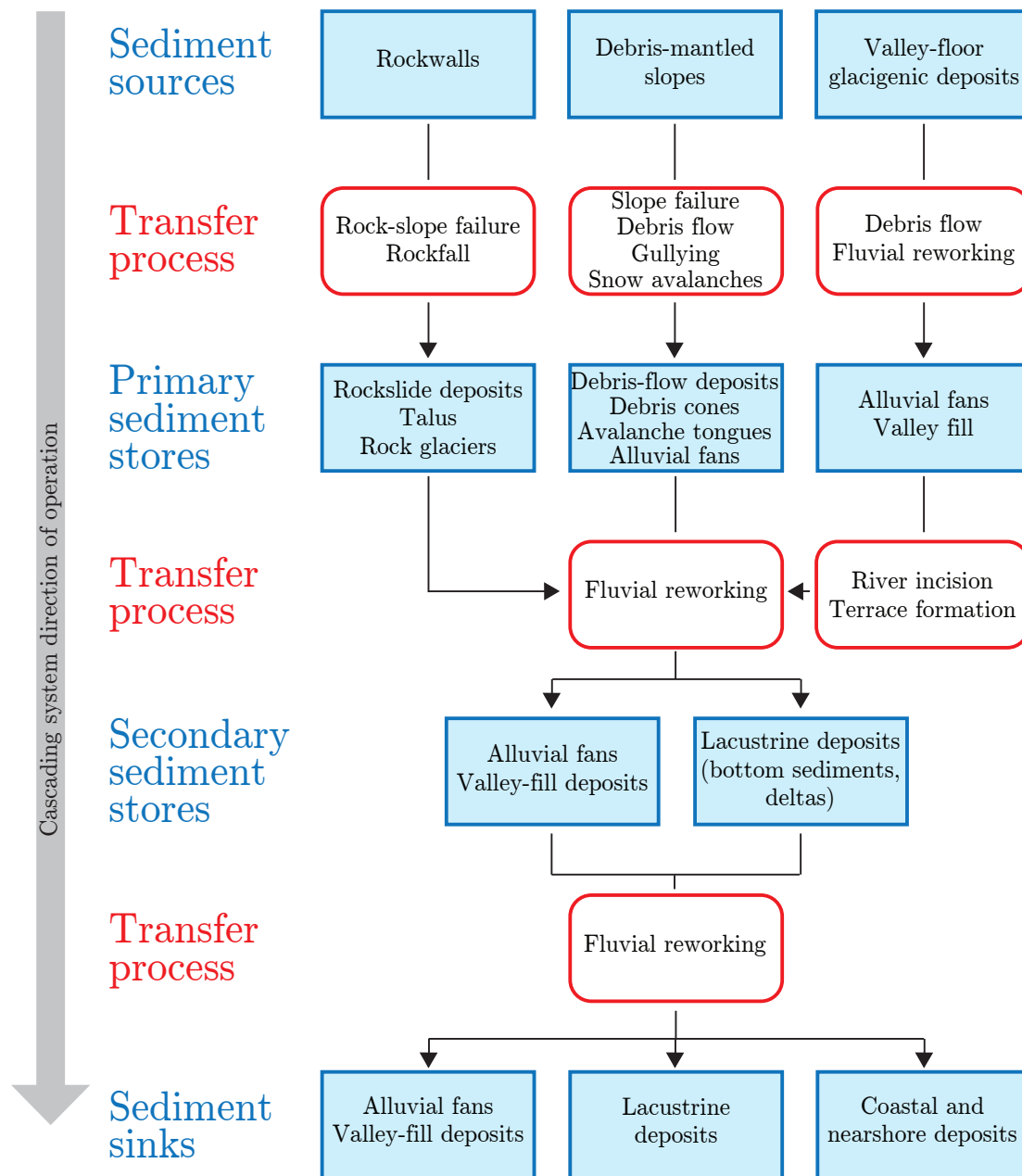
Figure 6.1 – Simplified paraglacial sediment cascade proposed by Ballantyne [2002] (modified). The scheme shows the principal primary and secondary sediment stores and the main sediment transfer processes.

mode requires an active sediment transfer (*functional connectivity*) and two landforms to be "connected" (*structural connectivity*) to ensure material flux. Otherwise, the cascade is interrupted, and material accumulates at an intermediate stage without continuing its journey downstream. When trying to understand how sediment cascades operate and how well it is coupled, these relations are usually described in a conceptual framework (e.g. Heckmann and

Schwanghard [2013]; Heckmann et al. [2015]) Connectivity is not merely present or absent; topographic complexity or surface roughness might impede sediment transfer and as a result reduce it, without damping it completely. Or a connection might be functional only under certain circumstances, as in the case of specific events. Moreover, an absolute disconnection may exist only within a given temporal scale, waiting for an event or transformation of the landscape able to establish connectivity. As sediment connectivity plays a fundamental control on the functioning of geomorphic systems, studying the evolving dynamics of Alpine environments must consider its state and the potential buffering effect it might have on the sediment cascade.

Not only connectivity, but also other concepts define sediment transfer in geomorphic system: *sediment availability* (the actual production and/or presence of material to mobilize), and *transport capacity* (the presence and efficiency of the engines necessary for the transport, Hickin [1995]). When the sediment balance is not in equilibrium, the system can be either *supply-limited* or *transport-limited*. Whilst mountain areas could be expected to be well suited in both factors by means of their legacy of sediment and the energy provided by their steep slopes, this may actually not always be the case. The reason lies once again in the heterogeneity of the geomorphic system in both its process domains and spatial dimension.

On the grounds of these consideration, recent climate change, landscape legacy and human activities impact, at the scale of decades and within an area of study, the hydrological system, the cryospheric and periglacial processes, the state of permafrost, the development of soil, etc. In turn, these mechanisms drive the geomorphic dynamics of the landscape, including landform modification and mass wasting. In particular, they co-exist and cooperate in controlling sediment mobilization and flux [Heckmann et al., 2015]. For these reasons, investigating climate change impact on Alpine landscapes requires a holistic and systemic approach, capable of discerning the role of the elements, which are inevitably bound together. In this part we attempt to do so through the reconstruction of geomorphic changes and sediment transfer, by considering not only single landforms or processes, but also the systemic nature of alpine geomorphology. Accordingly, whilst changes of surface and process rates are often retraced for individual landforms, a more entwined, holistic nature of mountain geomorphic system is observed. In Chapter 7, we attempt to identify where relevant elevation changes and surface displacement are located, how they relate to climate, and what does that imply for the geomorphic system in general. In Chapter 8, a step forward is made by also considering the actual sediment export from Alpine watersheds. These observations are coupled with climatic data, reconstructed geomorphic change, modelled sediment connectivity and changing stream transport capacity to hypothesis the causality and dynamics driving material downwasting in the context of recent and actual climate change.

6.3   Research applications in the Hérens Valley, Switzerland

To deepen our understanding of Alpine landscape dynamics in the face of climate change, we require a case study satisfying a certain number of criteria. First, it has to be relatively easily accessible to allow us to collect the required data in the field. Second, the landscape should encompass a large heterogeneity of landforms and a complete range of primary sediment transfer mechanisms typical of alpine environments. Third, having access to existent data and information on the landscape, as archives of historical photographs, geomorphological maps, measurements from meteorological stations, etc. would clearly be optimal. Finally, it would be excellent to have at disposal a significant scientific publication record.

In this thesis, we concentrated on some of the high mountain geomorphic systems of the Hérens Valley, located in Valais in the Western Swiss Alps (Figure 6.2). This Alpine valley expands from 470 m a.s.l. to its highest peak at 4357 m a.s.l., the Dent Blanche (literally "White Tooth"). It accommodates the Borgne river, which enters the Rhone river nearby Sion. Given its location in the central part of the Alps, the Hérens valley is in some way sheltered from the main atmospheric disturbances and rain-bearing systems [Lambiel et al., 2016]. Mean annual precipitation at the Evolène-Villa climatic station (1826 m a.s.l.) is of 730 mm (mean 1987-2014, MeteoSwiss measurements). The geology of the valley includes different main alpine tectonic units; from the Middle Penninic in its lower part, through the Upper Penninic in its centre and the Austro-alpine in its southern, higher sector [Steck et al., 2001]. The high elevation ranges create a strong geomorphic diversity, in which the main processes active in mountain areas (i.e. glacial, periglacial, gravitational and fluvial processes) are all well represented [Lambiel et al., 2016]. Geological and geomorphological maps of the Hérens valley are provided by Steck et al. [2001] and Lambiel et al. [2016] respectively.
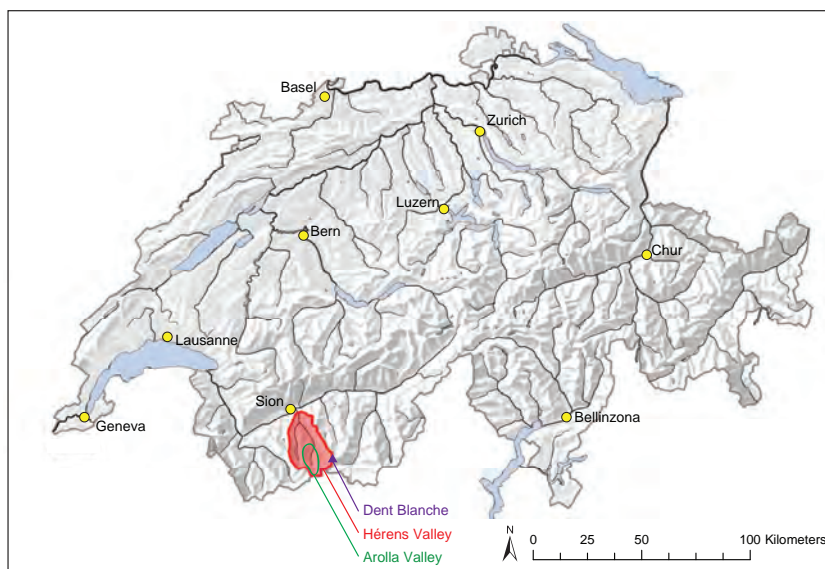
Figure 6.2 – Location of the Hérens Valley, the Arolla Valley and the Dent Blanche summit in the Western Swiss Alps (background image: Federal Office of Topography Swisstopo).

The geomorphic systems investigated in the next chapters are located in the Arolla valley, a branch of the Hérens that originates in Les Haudères (1420 m a.s.l.). This sector belongs to the Dent Blanche nappe of the Austro-alpine unit and is mainly composed of granite gneisses. The valley is characterized by steep slopes and high rockwalls and a very diverse geomorphological setting in terms of landforms and sediment transfer mechanisms. The Arolla valley has an ancient touristic tradition and the access to its glaciers is easy; this has attracted many researchers, and in particular the Haut Glacier d'Arolla has been widely studies (e.g. Sharp et al. [1993]; Mair et al. [2001]; Willis et al. [2003]; Gabbud et al. [2015, 2016]). Not merely glaciologists, the vast range of the geomorphic processes in motion attracted researchers in various geosciences domains. A very rich (and quite exhaustive) collection of scientific literature related to surface processes and other geographical topics in the Arolla valley is represented by EBIBALPIN (ebibalpin.unil.ch). Developed by the Faculty of Geosciences and Environment of the University of Lausanne, EBIBALPIN accommodates almost 200 scientific publications, various freely available data (including some related to this thesis itself) and an extensive amount of historical and recent photographs. Hence, it represents a very helpful resource for the reader interested in the geography of the valley. By reason of its geomorphological setting and tradition, in addition to a vast record of historical photographs, the Arolla valley satisfy the criteria mentioned above and represent an ideal case study for this thesis.

The sector examined in the following chapters corresponds to almost the whole East side of the Arolla valley (Figure 6.3), and ranges from 1800 to 3676 m a.s.l. (Dent de Perroc). The Haut Glacier d'Arolla and its surrounding area were investigated in the context of collaborations with colleagues and the related findings are not reported here (instead, refer to Gabbud et al. [2015, 2016]; Lane et al. [2016]). In this area of about 20 km^2 five small glacial systems are present, namely (from North to South) Tsarmine, Genevois, La Tsa, Douve Blanche and Bertol (see A, F, H, J and K in Figures 6.3 and 6.4). Furthermore, the mountainside displays an extremely diverse set of landforms and processes associated with all the domains discussed in Chapter 6.2 (see geomorphological map in Figure 6.4, reproduced from Lambiel et al. [2016]). Further images and details on the elements of the landscape are introduced in the appropriate parts of the following chapters.
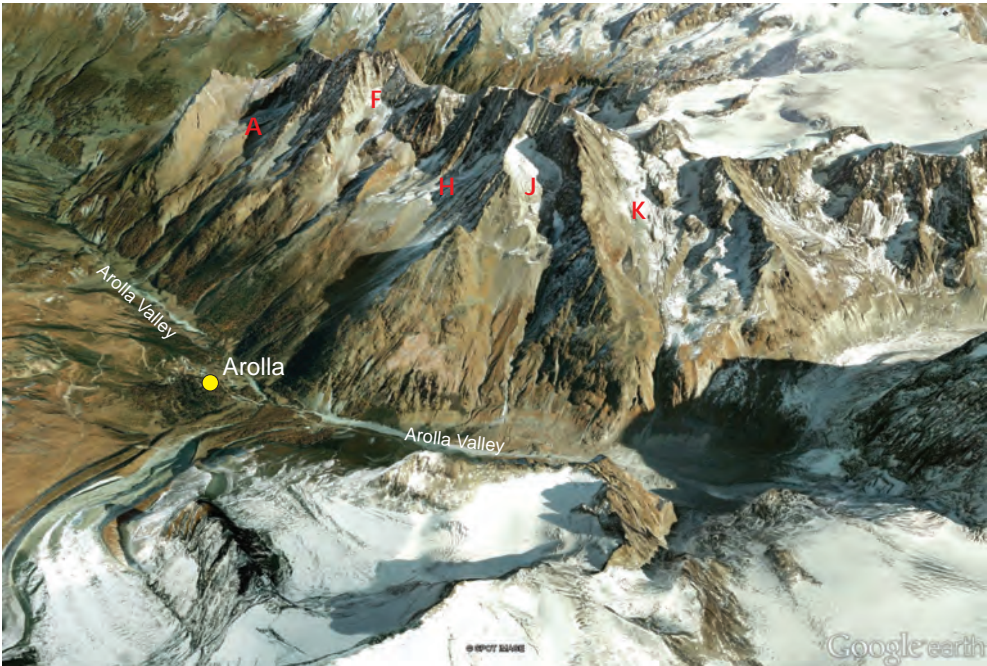
(a)
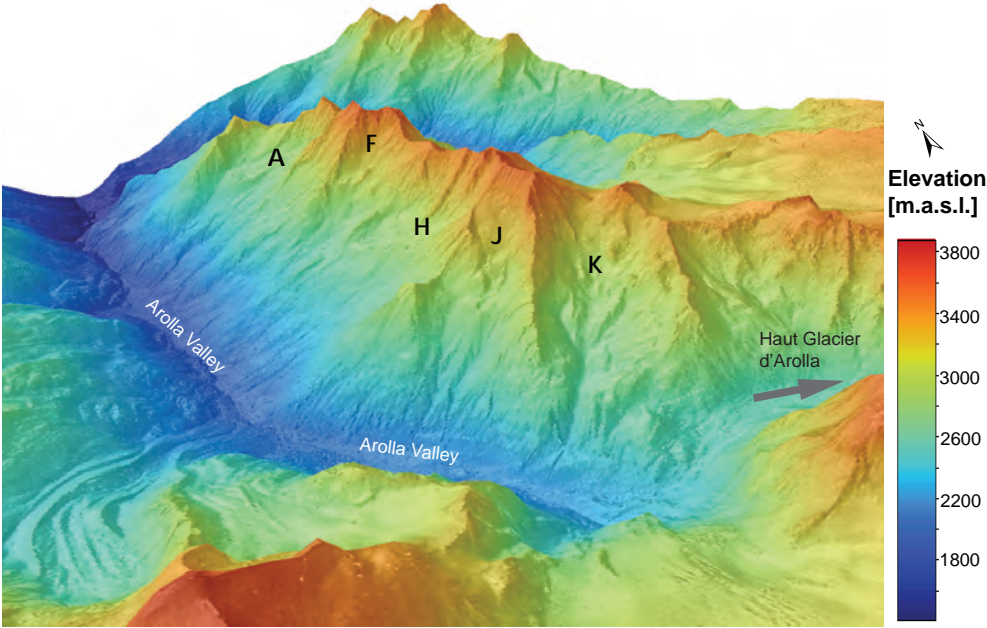
(b)

Figure 6.3 – 3D view of the Arolla Valley: Google Earth$^{\copyright}$ view (a) and hill shade map (b, relief data: Federal Office of Topography Swisstopo), with letters indicating the five glacial systems in the research area (see also Figure 6.4).
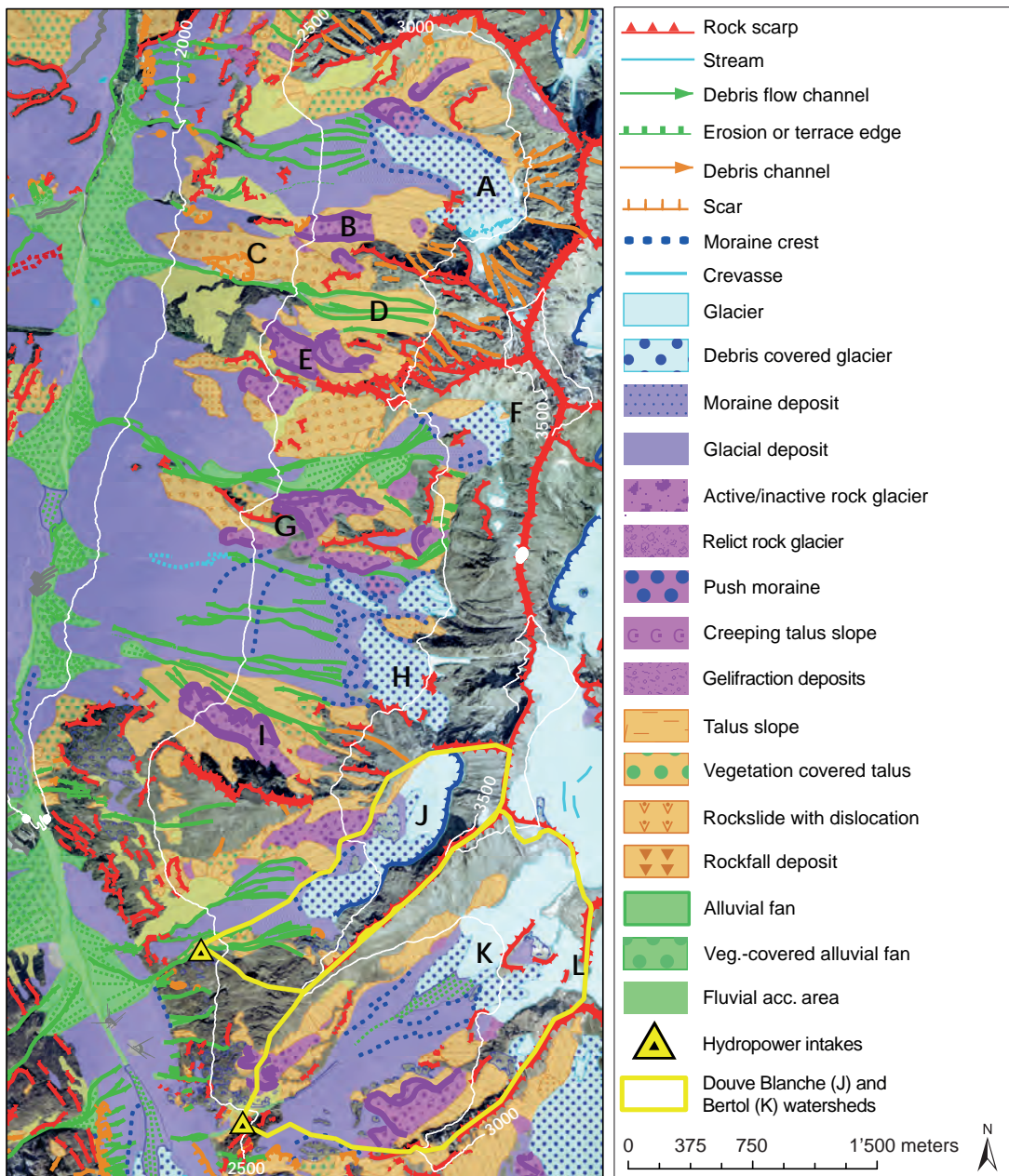
Figure 6.4 – Geomorphological map of the East side of the Arolla Valley [Lambiel et al., 2016]. Sites of interest: Tsarmine glacier (A), Tsarmine rock glacier (B), Perroc rockslide (C), Perroc talus slope (D), Lé Blâva rock glacier (E), Genevois Glacier (F), La Tsa hut (G), La Tsa glacier (H), La Roussette rock glacier (I), Douve Blanche glacier (J), Bertol glacier (K), Bertol hut (L).

Bibliography

Ballantyne, C. K. (2002). Paraglacial geomorphology. *Quaternary Science Reviews*, 21:1935–2017.

Ballantyne, C. K., Wilson, P., Gheorghiu, D., and Rodés, A. (2014). Enhanced rock-slope failure following ice-sheet deglaciation: timing and causes. *Earth Surface Processes and Landforms*, 39(7):900–913.

Brocklehurst, S. H. and Whipple, K. X. (2002). Glacial erosion and relief production in the Eastern Sierra Nevada, California. *Geomorphology*, 42(1-2):1–24.

Burt, T. and Allison, R. J. (2010). *Sediment Cascades: An Integrated Approach*. John Wiley & Sons, Chichester, UK.

Caine, N. and Swanson, S. (1989). Geomorphic coupling of hillslope and channel systems in two small mountain basins. *Zeitschrift für Geomorphologie*, 33(2):189–203.

Caine, T. N. (1974). *Arctic and Alpine Environments*, chapter The Geomorphic Processes of the Alpine Environment, pages 721–740. Methuen, London.

Carturan, L., Baldassi, G. A., Bondesan, A., Calligaro, S., and others, . (2013). Current Behaviour and Dynamics of the Lowermost Italian Glacier (Montasio Occidentale, Julian Alps). *Geografiska Annaler: Series A, Physical Geography*, 95(1):79–96.

Chorley, R. and Kennedy, B. (1971). *Physical Geography: a systemic approach*. Prentice-Hall.

Gabbud, C., Micheletti, N., and Lane, S. N. (2015). Lidar measurement of surface melt for a temperate Alpine glacier at the seasonal and hourly scale. *Journal of Glaciology*, 61(229):963–974.

Gabbud, C., Micheletti, N., and Lane, S. N. (2016). Response of a temperate Alpine valley glacier to climate change at the decadal scale. *Geografiska Annaler: Series A, Physical Geography*, 98(1):81–95.

Harvey, A. M. (2001). Coupling between hillslopes and channels in upland fluvial systems: implications for landscape sensitivity, illustrated from the Howgill Fells, northwest England. *Catena*, 42(2-4):225–250.

Harvey, A. M. (2002). Effective timescales of coupling within fluvial systems. *Geomorphology*, 44(3-4):175–201.

Heckmann, T. and Schwanghard, W. (2013). Geomorphic coupling and sediment connectivity in an alpine catchment - Exploring sediment cascades using graph theory. *Geomorphology*, 182:89–103.

Heckmann, T., Schwanghard, W., and Phillips, J. D. (2015). Graph theory - Recent developments of its application in geomorphology. *Geomorphology*, 243:130–146.

Hickin, E. J. (1995). *River geomorphology*. Wiley.

IPCC (2014). *Climate Change 2014: Synthesis Report. Contribution of Working Groups I, II and III to the Fifth Assessment Report of the Intergovernmental Panel on Climate Change*. IPCC, Geneva, Switzerland.

Kääb, A., Frauenfelder, R., and Roer, I. (2007). On the response of rockglacier creep to surface temperature increase. *Global and Planetary Change*, 56:172–187.

Knight, J. and Harrison, S. (2009). Sediment and future climate. *Nature Geoscience*, 2:230.

Knight, J. and Harrison, S. (2013). The impacts of climate change on terrestrial Earth surface systems. *Nature Climate Change*, 3(1):24–29.

Lambiel, C., Maillard, B., Kummert, M., and Reynard, E. (2016). Geomorphological Map of the Hérens Valley (Swiss Alps). *Journal of Maps*, 12(1):160–172.

Lane, S. N. (2013). 21st century climate change: where has all the geomorphology gone? *Earth Surface Processes and Landforms*, 38(1):106–110.

Lane, S. N., Bakker, M., Gabbud, C., Micheletti, N., and J.-N., S. (2016). Sediment export, transient landscape response and catchment-scale connectivity following rapid climate warming and Alpine glacier recession. *Geomorphology*, doi:10.1016/j.geomorph.2016.02.015.

Mackin, J. H. (1963). Rational and empirical methods of investigation in geology. In *The fabric of geology*. Addison-Wesley Publishing Co., Reading, Massachussetts.

Mair, D., Nienow, P., Willis, I., and Sharp, M. (2001). Spatial patterns of glacier motion during a high-velocity event: Haut Glacier d'Arolla, Switzerland. *Journal of Glaciology*, 47(156):9–20.

Otto, J.-H. and Dikau, R. (2004). Geomorphologic system analysis of a high mountain valley in the Swiss Alps. *Zeitschrift für Geomorphologie*, 48(3):323–341.

Pelto, M. S. and Hedlund, C. (2001). Terminus behavior and response time of North Cascade glaciers, Washington, USA. *Journal of Glaciology*, 47:497–506.

Schrott, L., Hufschmidt, G., Hankammer, M., Hoffmann, T., and Dikau, R. (2003). Spatial distribution of sediment storage types and quantification of valley fill deposits in an alpine basin, Reintal, Bavarian Alps, Germany. *Geomorphology*, 55(1-4):45–63.

Schumm, S. A. and Lichty, R. W. (1965). Time, Space, and Causality in Geomorphology. *American Journal of Science*, 263(2):110–119.

Sharp, M., RIchards, K., Willis, I., Arnold, N., Nienow, P., Lawson, W., and Tison, J.-L. (1993). Geometry, bed topography and drainage system structure of the haut glacier d'Arolla, Switzerland. *Earth Surface Processes and Landforms*, 18(6):557–571.

Slaymaker, O. (2009). *Periglacial and Paraglacial Processes and Environments*, chapter Proglacial, periglacial or paraglacial?, pages 71–84. Geological Society of London.

Steck, A., Epart, J.-L., Escher, A., Gouffon, Y., and Masson, H. (2001). Carte tectonique des Alpes de Suisse occidentale. Technical report, Federal Office for Water and Geology, Bern.

Stoffel, M. and Huggel, C. (2012). Effects of climate change on mass movements in mountain environments. *Progress in Physical Geography*, 36(3):421–439.

Wichmann, V., Heckmann, T., Haas, F., and Becht, M. (2009). A new modelling approach to delineate the spatial extent of alpine sediment cascades. *Geomorphology*, 111(1-2):70–78.

Willis, I., Mair, D., Hubbard, B., Nienow, P., Fischer, U., and Hubbard, A. (2003). Seasonal variations in ice deformation and basal motion across the tongue of Haut Glacier d'Arolla, Switzerland. *Annals of Glaciology*, 36(1):157–167.

7 Investigating decadal-scale geomorphic dynamics in an alpine mountain setting

Natan Micheletti, Christophe Lambiel, Stuart N. Lane

Context

This chapter inspects the geomorphic evolution of a steep alpine mountainside in the last decades in the face of recent climate change. The area of study includes an assemblage of glacial, periglacial, hillslope, and fluvial landforms and a complete range of primary sediment transfer mechanisms, typical of alpine environments. The workflow elucidated in Chapter 3 is applied to obtain maps of elevation changes and surface displacements, and volumetric differences. Results are coupled with climate data to show how the landscape responds to climate forcing and to geomorphological maps to understand how this response varies between both landscape elements and their spatial organization.

Of particular interest in the area of study is a small, heavily debris-covered glacier located in an Alpine permafrost environment. Therefore, results were further analysed and used to deepen our knowledge of this glacial system, and the findings have been published in Capt et al. [2016].

In the framework of the thesis, the chapter is a pillar for the primary objective: the comprehension of the sensitivity of Alpine landscapes to climate forcing, and the implied consequences in terms of mass displacements.

Abstract

We know little about the effect of recent climate variability upon landscapes at the timescale of decades because of (1) the complex, nonlinear, and path-dependent nature of the response of a landscape to climate forcing and (2) the difficulty of quantifying spatially distributed impacts at the timescale of decades to centuries, despite this being the timescale over which significant hypotheses have been raised over human impacts upon climate change and hence geomorphic systems. A unique resource to investigate the linkages between climatic variability and geomorphic response is provided by the extensive coverage of aerial imagery commonly available since the 1950s. Here we use archival digital photogrammetry to produce high-precision digital elevation models over large spatial scales, and so to reconstruct the quantitative history of surface downwasting and sediment flux in a high mountain alpine system, over the timescales of decades. Propagation of error methods is used to identify locations of significant landscape response and to compute volumes of significant surface change. Orthorectified aerial images are used in an image correlation framework to detect horizontal and vertical displacements of components of the landscape. Results are coupled to extant climate data and modeled snow cover to show how the landscape responds to climate forcing and to geomorphological maps to understand how this response varies between landscape elements. The results show distinct landscape response to both warming and cooling periods and a tendency for the acceleration of surface displacement under warming conditions. Precipitation and snow cover are critical in controlling glacier dynamics and rock glacier displacement velocities. However, while some landforms might lead to locally high sediment flux, landscape heritage can disconnect zones of high change rates from the valley bottom. Hence, the landscape response to climate forcing is not necessarily reflected in valley system processes or sediment deposits.

Keywords: archival aerial imagery to investigate decadal-scale changes; distinct response to different climatic forcing periods; geomorphic change investigation

7.1   Introduction

A progressive refinement of our understanding of climate change patterns has followed from the first and subsequent state-of-the-art syntheses of human impact on climate provided by the Intergovernmental Panel on Climate Change IPCC [1990], contributing fundamentally to our knowledge about how climate might change in the future. Despite this, quantification of climate change impacts upon the Earth system is underdeveloped [Kundzewicz et al., 2007] not least because of the complex, nonlinear response of geomorphic systems to perturbations [Phillips, 2003, 2009] and the difficulties of quantifying this response over large spatial and long temporal scales. While this is generally valid, it is especially true for polar, glacial, and periglacial regions which are potentially more vulnerable to climate change [Committee on Challenges and Opportunities in Earth Surface Processes, 2010]. The high climatic sensitivity of high mountain environments follows from four points. First, the glaciers, permafrost, and

nival processes that are widely present in these landscapes are highly sensitive to changes in atmospheric temperature [Pelto and Hedlund, 2001; Kääb et al., 2007; Carturan et al., 2013; Oliva and Ruiz-Fernandez, 2015; Staines et al., 2015]. Second, glaciated environments typically have increased relief, the steep slopes potentially aiding sediment mobilization [Brocklehurst and Whipple, 2002]. Third, deglaciated mountain environments commonly have significant amounts of historically weathered and glacially derived material, and so a legacy of high sediment availability [Ballantyne et al., 2014]. Finally, sediment dynamics are strongly dependent upon the thermal state of the subsurface, in terms of both sediment stabilization and production [Davies et al., 2001; Hales and Roering, 2007] and surface runoff generation because of the presence/absence of impeded drainage [Ford and Bedford, 1987; Bayard et al., 2005].

Understanding how climate change affects sediment production, transfer, and delivery in mountain landscapes is a fundamental focus of current geomorphic research [Montgomery and Stover, 2001; Hunt, 2002; Jomelli et al., 2004; Korup, 2004; Lane et al., 2007]. Scientific observations suggest that high mountain environments could be very sensitive to climate change, and an acceleration in sediment production and transport rates has been reported for some landforms in mountain sedimentary systems [Warner, 1987; Rumsby and Macklin, 1994; Dollar and Rowntree, 1995; Knox, 1999; Jomelli et al., 2004; Roer et al., 2008; Huggel et al., 2010, 2012; Bennett et al., 2013]. However, increased sediment delivery and transport for single landforms does not necessarily imply a climatic response at the landscape scale as (1) a landscape may contain a range of different landforms each with different climate sensitivities [Brunsden and Thornes, 1979] and (2) connection between these elements will be the ultimate control on sediment delivery. Effectively, a lack of sediment flux between landforms and sediment storage zones may lead to disconnections in parts of the sediment cascade [Brunsden and Thornes, 1979; Fryirs, 2013]. This may slow, or even halt, the diffusion of climate impacts through hillslopes. A large number of studies have considered climate forcing of single-landform types [Hölzle and Haeberli, 1995; Jomelli et al., 2004; Huggel et al., 2010, 2012]. Yet, it is the connections between them that determine whether or not sediment transfer rates will respond to climate change [Reynard et al., 2012].

This contribution addresses two research questions that follow from the above. First, are there coincidences between changes in climate forcing and modifications in alpine geomorphic process patterns and rates? Second, as the diffusion of the effects of such forcing may depend on the connections between individual landforms, can we see any evidence of the propagation of climate signals through the landscape? In order to respond to these questions we investigate the behavior of high mountain environments at a timescale of years to decades. A unique resource for such investigation is the extensive coverage of aerial imagery commonly available since the 1950s, which can be employed to produce high-precision digital elevation models (DEMs) over large spatial scales using digital photogrammetry. Research has demonstrated the potential of this approach for geomorphological studies including fluvial geomorphology [Lane et al., 2003, 2010; Hughes et al., 2006], mountain geomorphology [Kääb and Vollmer, 2000; Kääb, 2002; Roer et al., 2005; Wangensteen et al., 2006; Kneisel and Kääb, 2007; Fischer

et al., 2011, 2012] and studies of hillslope processes and sediment production, transfer, and yield [Chandler and Cooper, 1988; Walstra et al., 2007; Schwab et al., 2008; Bennett et al., 2012, 2013]. Our focus is upon a case study in the Swiss Alps, typical of many alpine mountain regions, where there is a range of landforms juxtaposed within the landscape. Aerial imagery from the 1960s to present is used to compute high-precision and fine-resolution digital elevation models. A quantitative comparison of successive DEMs employing propagation of error methods is implemented to identify locations of significant elevation change and geomorphic response and to estimate volumes of erosion and deposition and of glacier growth and retreat. To identify mass displacement, the derived orthorectified images are used in an image correlation framework to visualize and quantify surface displacements and their velocities over time. Results are coupled to extant climate data and modeled snow depth to show how the landscape responds to climate forcing and to geomorphological maps to understand how this response varies between both landforms and their spatial organization. Finally, given the possibly important role of sediment supply and connectivity in propagating the climatic signal through the hillslope, an attempt to identify how connectivity might impact fluxes to the valley bottom is undertaken.

7.2   Study site

The focus of this investigation is the Veisivi-Tsa ridge in the Hérens Valley, Switzerland (Figure 7.1). This steep alpine mountainside has an elevation range from 1800 m above sea level (a.s.l.) to 3676 m a.s.l. and an average slope of ~35°. The basin extends for ~5 km north-south, between the Petit Dent de Veisivi (3184 m a.s.l.) and La Maya (3042 m a.s.l.). The region is relatively dry because of the topographic barrier effect of the southern alpine divide, with annual precipitation between 900 and 1300 mm and mean annual air temperature at 2000 m a.s.l. of 3.4°C based upon the period 1991 to 2014 [MeteoSwiss, 2014]. The geomorphological setting of the landscape comprises an assemblage of glacial, periglacial, hillslope, and fluvial landforms and a complete range of primary sediment transfer mechanisms, typical of alpine environments. The area has been the subject of previous geomorphological investigations, especially regarding permafrost distribution and quantification of slope movement using interferometric synthetic aperture radar (InSAR) [Lambiel et al., 2004, 2008; Delaloye et al., 2007, 2008, 2010; Barboux et al., 2014].

7.3   Methodology

The methods used to generate the DEMs and orthophotographs used in this study are presented in an accompanying methods paper [Micheletti et al., 2015], and only a summary is provided here.
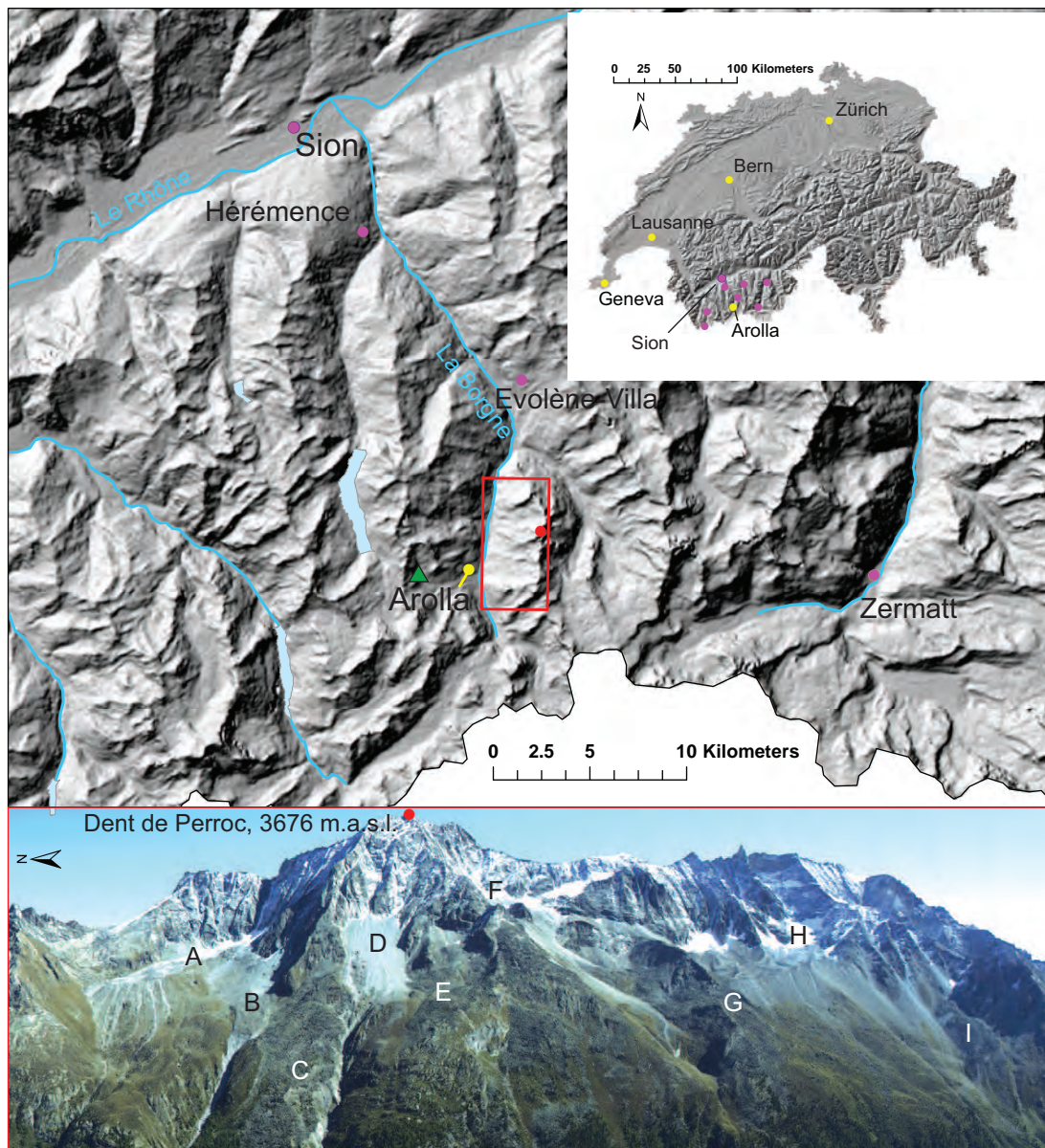
Figure 7.1 – The Veisivi-La Tsa ridge case study in Arolla, Hérens Valley, Switzerland (Relief shaded and river data: Swisstopo) with sites of interest: Tsarmine glacier (A), Tsarmine rock glacier (B), large rockslide (C), Perroc talus slope (D), Lé Blâva rock glacier (E), Genevois glacier (F), La Tsa hut (G), La Tsa glacier (H), La Roussette rock glacier (I).

7.3.1 Digital elevation models and interpretation

The archival aerial imagery employed in this study was acquired by the Swiss Federal Office of Topography (Swisstopo, www.swisstopo.admin.ch) and by Flotron AG (www.flotron.ch). Swisstopo imagery includes a number of 23 x 23 cm images for seven distinct epochs between 1967 and 2005 all collected at similar periods of the year (end of summer or beginning of

autumn) at altitudes varying between 5000 and 7000 m a.s.l. and using a range of analogue cameras. A photogrammetric quality scanner was used to scan these images at 14 μm (1814 dpi). These images vary in scale between 1:15,700 and 1:28,000. Calibration certificates for analogue cameras were available at www.swisstopo.admin.ch. It should be noted that the 1977 imagery was collected during partially snow-covered conditions, and hence the derived data quality are lower for that year. Flotron AG images were collected in September 2012 using an UltraCam-X camera, and they represent the most recent data set of the study. They are composed of 14,430 x 9420 pixels of 7.2 μm and have a scale of 1:5200. Multiple images were required to cover the whole area of interest. The Flotron AG digital imagery was provided with a calibration file for the digital camera.

In order to obtain the required ground control points (GCPs) necessary for photogrammetric restitution, a field campaign was carried out in July 2012 using two Leica System 500 differential GPS units. A total of 169 GCPs were identified, stable in time and easily and precisely identifiable on images (Figure 7.2), across an area of approximately 20 km^2 (3 x 6.5 km) and with an elevation range of more than 1000 m (1808 to 2828 m a.s.l.). Original RTK data processing and correction using Automated GNSS Network for Switzerland (AGNES) data allowed the determination of coordinates of all GCPs in the Swiss coordinate system to the geodetic datum CH1903 with a precision better than ±0.05 m.

The detailed methodology is presented in full in Micheletti et al. [2015]. All photogrammetric data processing was performed using ERDAS IMAGINE Leica Photogrammetry Suite (LPS) 2010, while postprocessing operations and results analysis were implemented using Matlab 2013 and ArcGIS 10. Calibration certificates and GCPs were used to estimate interior and exterior orientation parameters, respectively. Afterward, as is routine in digital photogrammetry [Dissart and Jamet, 1995], an automatic stereomatching algorithm was used to match points in image pairs and to compute their ground coordinates using exterior orientation parameters. Finally, the data were interpolated to generate 1 m resolution raster DEMs for every year. The quality assessment of individual DEMs was carried out using unused GCPs. As in Lane et al. [2000], errors were defined as the differences in elevation between dGPS measurements and the DEM values at corresponding dGPS locations and were used to compute accuracy in the form of mean error (ME) and precision in the form of standard deviation of error (STD) (Table 1). The shape of these error distributions was investigated and confirmed to be Gaussian at the 5% significance level [Micheletti et al., 2015].

Table 7.1 – DEM precision and accuracy assessment using dGPS survey data [m].

DEM	1967	1977	1983	1988	1995	1999	2005	2012
ME	0.315	0.504	0.281	0.296	0.541	0.493	0.453	0.356
STD	±0.765	±0.820	±0.953	±0.644	±0.751	±0.827	±0.998	±0.462

DEMs of difference (DoD) were computed by differencing DEMs for different years. This allows identification of changes between dates and hence patterns of erosion and deposition.

Figure 7.2 – Ground Control Point distribution in the Arolla Valley, Switzerland (Contour line spacing: 100 m, Orthophoto: Swisstopo 2005).

However, it was necessary to quantify the confidence that apparent changes between two epochs are real and not produced by random error. Following the error propagation methodology proposed in Lane et al. [2003] for Gaussian error distributions, the uncertainty in the magnitude of change in the DoD was determined by the root of the sum in quadrature of the uncertainties associated with individual DEMs:

$$\sigma_c = \sqrt{\sigma_1^2 + \sigma_2^2} \tag{7.1}$$

125

In this instance, the standard deviation of error is used as a measure of uncertainty, but it can be employed to formulate a statistical testing of the significance of each elevation difference $Z_1 - Z_2$ using a t test [Lane et al., 2003]:

$$t = \frac{Z_1 - Z_2}{\sqrt{\sigma_1^2 + \sigma_2^2}} \qquad (7.2)$$

Equation 7.2 can be used to threshold the DoD at a certain confidence limit and to attribute differences within this threshold to noise. In this study, the minimum level of detection was set with a confidence limit of 90% ($t = 1.96$). For the data set used in this study, Table 7.2 shows the associate limits of detection.

Table 7.2 – Limit of Detection of Change (LDC) with confidence limits of 68% and 90% computed using the error propagation methods explained in the text.

Year pair	68%	90%
2012-2005	1.100	1.804
2005-1999	1.296	2.126
1999-1995	1.118	1.833
1995-1988	0.990	1.623
1988-1983	1.135	1.862
1983-1977	1.244	2.040
1977-1967	1.121	1.839
2012-1988	0.793	1.300
1983-1967	1.208	1.981
2012-1967	0.894	1.466

Volumes of significant change were computed for every time step and geomorphological class for significant elevation changes at the 90% of confidence level. In order to compare landform types with different spatial extent, volumes were normalized by surface extent. To compare time periods, volumes were also normalized by the time between images. Accordingly, all results are provided in $m^3 m^{-2} yr^{-1}$. These statistics represent the rate of surface downwasting/deposition for each landform. If we follow Thomas [2001], these rates describe the sensitivity of the surface change of each landform to climate forcing, given that we can assume that all landforms have been subject to the same temperature or precipitation change. However, these are actually *absolute* measures of sensitivity as they make no reference to the magnitude of the rates of change expected under constant climate conditions, that is, the *relative* sensitivity. It is quite possible that climate forcing could cause a substantial increase in the rate of surface change for some landforms as compared with what would be expected under constant climate conditions, even though when compared with other landforms their absolute sensitivities remain small. One solution to this problem would be to calculate the change in rates of change between the periods with different climate forcing, but this characteristic is complicated by the fact that the process responses may be very different between

landforms in response to climate warming and cooling. For this reason, we avoid using the term sensitivity overly in the interpretation, notably when comparing different landforms. Rather, we use the terms rates of elevation change or downwasting.

Finally, DEMs were used to orthorectify aerial imagery in ERDAS LPS. The derived orthophotos were used to estimate surface displacements using the image correlation software 7D [Vacher et al., 1999]. Displacements could then be computed in pixels and converted to distances in meters. Image correlation analysis was performed for 15 x 15 pixel windows. Results were filtered to eliminate erroneous matches and unrealistic displacements induced by image deformation resulting from the orthorectification process in very steep areas or cliffs where the quality of the DEMs is low. Horizontal movements were extracted as vectors of displacement at a defined window resolution. Given the 0.35 m resolution of most orthophotos, a 15 x 15 pixel window corresponds to a 5.25 m x 5.25 m cellsize. Since horizontal displacement accounts only for XY dimensions, it is by definition an underestimation of the real displacement. Hence, outputs were divided by the cosine of the local slope to obtain the three-dimensional displacement distance. Finally, results were normalized by year in order to compare outputs obtained with imagery for different dates.

Displacement detection depends strictly on the quality and contrast of the input imagery. The latter is also dependent on the quality of the DEM, as uncertainty in elevation data can undermine the quality of the orthorectification process. Very large displacements at the surface (both vertical and horizontal deformations) may also generate decorrelation that causes the algorithm to fail to retrieve the displacement. Accordingly, not every pair of images provided results for the whole study area. To differentiate areas where information could not be derived from areas with no distinguishable displacement, a no movement and/or noise class (results inferior to 0.2 m/yr) is defined and displayed as transparent. The most complete and detailed outputs were obtained using the 1967–1977, 1977–1983, 1988–1999, and 1999–2005 pairs of imagery and are employed to investigate the response of surface displacement to climate forcing.

The interpretation of catchment-scale erosion and deposition patterns required reference to the spatial assemblage of landforms present in the study area. A geomorphological map of the region [Lambiel et al., 2016] was used for this purpose and permitted derived data to be linked to specific landforms. This is crucial for the identification of the landforms most active under recent climate change and their spatial organization.

7.3.2   Data interpretation: climatic context

The interpretation of mass movement in alpine environments at the decadal scale also requires reference to the climatic conditions that affected such systems. However, long-duration climatic data series are rarely available. Early climate monitoring tended to be focused on centers of population, and so climate data are often remote from many mountain study sites. In this study, the closest reliable data are available for Evolène-Villa (9 km from Arolla at an

elevation of 1826 m a.s.l.), but data are available only from 1987 and so are not sufficient to characterize our period of study. Hence, it was necessary to transfer data collected from more distant locations, which may lead to uncertainties in the associated climate data because of altitude and topographic effects. Accordingly, it is important to have access to multiple data series and, if possible, under similar geographic and topographic conditions to the area of interest, to transfer them to the locality under interest and to test them on more locally available but shorter records.

In Switzerland, the Swiss National Basic Climatological Network includes 29 climatic and 46 rainfall measurement stations, some of which started in 1864. Homogenized monthly data (i.e., historic measured values adjusted to current measuring conditions) from the nineteenth century are available for 14 stations and can be used to reconstruct climatic change for the last 150 years [MeteoSwiss, 2014]. To set a climate context and to sustain interpretations in the present study, data series from seven measurement stations were used (see purple dots in Figure 7.1 and Table 7.3). Two of these have long-term homogenized data: Col du Grand St-Bernard (GSB) at an altitude of 2461 m a.s.l. and 30 km to the southwest of Arolla and Sion, 482 m a.s.l., located 24 km north. The available climatic parameters are mean annual air temperature (MAAT), annual rainfall, and snowfall and snow depth. Data are provided by the Swiss Federal Office of Meteorology and Climatology MeteoSwiss (further information and data available at www.meteoswiss.admin.ch).

Table 7.3 – MeteoSwiss measurement stations employed.

Location	Elevation (m a.s.l.)	Data	Period	Km from (Arolla)	Direction
GSB	2461	Temp.	1864-present	30	South-West
Sion	482	Temp.	1864-present	24	North
Evolène-Villa	1826	Temp., Prec.	1987-present	9	North
Grächen	1550	Temp., Prec.	1960-present	34	North-East
Hérémence	1,238	Prec.	1960-present	18	North
Zermatt	1638	Prec.	1960-present	21	East
Bourg St-Pierre	1664	Prec.	1960-present	23	West
Grimentz	1512	Prec.	1960-present	19	North-East

Temp: temperature; Prec: precipitation.

Long time series of snowfall and snowdepth are scarce. The only data available for Arolla are daily snowdepth measurements from 1998 to 2011 for Fontanesses, located at 2850 m a.s.l. above the village of Arolla (green triangle in Figure 7.1). Snowfall and snowdepth will be strongly influenced by altitude as well as other local factors, such that relying on measurements in other sites is not optimal for reconstructing a decadal history of snowfall in the area of study. Hence, the GSM-SOCONT (Glacier and SnowMelt - SOil CONTribution model) modeling approach developed by Schaefli et al. [2005] was adopted. This is a well-established glaciohydrological model (e.g., Schaefli and Huss [2011]; Tobin et al. [2011]; Godon

et al. [2013]) which was used with available temperature and precipitation time series from proximate measurement stations (Sion and Hérémence, respectively) to extrapolate values of snow depth for elevation bands across the mountainside in Arolla. There are more complex modeling options, but these would demand additional data (e.g., measured incoming solar radiation) that are not available. The GSM-SOCONT model is detailed in Schaefli et al. [2005]. The model was set to run with a daily resolution, and empirical lapse rates were employed [Bouët, 1985]. The degree-day factor for snow and the effect of elevation on precipitation were optimized using the available Fontanesses data. Calibration using the daily snow depth data available provided a mean error of 8.6 cm with a precision of ±38.2 cm at the 90% confidence level, which is very satisfying given the simplicity of the model. Accordingly, the model is considered of sufficient quality to characterize the interannual snow cover trends for the site. To analyze the evolution of snow cover during the period of study, the model was used to estimate snow depth at the typical end of the accumulation period (31 March) and the typical end of the glacier ablation period (30 September) for every year from 1960 to the present at varying altitude bands but excluding the rockwalls (thus from 2100 to 2900 m a.s.l., Figure 7.5a).

7.4 Results: a quantitative history of surface changes in an Alpine system

7.4.1 Climatic Evolution

Figure 7.3 shows the evolution of mean annual air temperature (MAAT) from1864 to present as a deviation from the mean of the 1961–1990 reference period for Col du Grand St-Bernard (GSB). Comparison of the GSB 5 year moving mean with the national moving mean suggests a similar evolution of MAAT at the scale of decades. The correlation between MAAT data for Evolène-Villa and the GSB is 0.978, suggesting that the study site experienced a similar decadal-scale evolution to other regions of Switzerland. Figure 3 suggests that between the 1960s and the early 1980s there was a climatically cooler period. A very rapid warming followed fromthe mid-1980s to the 1990s. This trend continued, albeit more slowly, until present. With only two exceptions, the MAATs in the warming period are always higher than the reference mean, demonstrating the presence of strong temperature forcing during the last three decades.

Figure 7.4 presents annual rainfall data for measurement stations with similar conditions and close to Arolla. Measurements at the Col du Grand St-Bernard are not well suited for description of the Hérens valley patterns because Grand St-Bernard is located on an alpine col on the main southern alpine drainage divide and impacted by both southern and northern rain-bearing systems. Arolla is some way north of this divide and sheltered from southerly rain-bearing systems. Instead, we focus upon comparison of Evolène with five more characteristic (altitude and geographical position) locations (Figure 7.4). Five year moving means are similar for the five stations. Between the end of the 1960s and the beginning of the 1970s precipitation decreased slightly before increasing considerably in the second part of the 1970s. Then, a
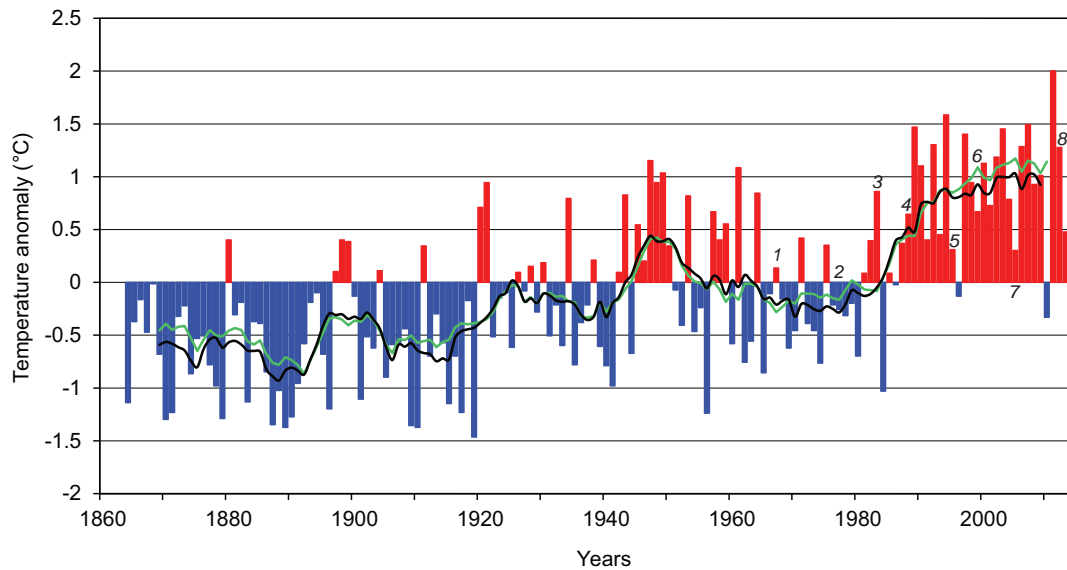
Figure 7.3 – Mean Annual Air Temperature at the Col du Grand St-Bernard between 1864 and 2013 as deviation from the reference mean established between 1961 and 1990. Trend lines indicate the 5 years moving average for that site (black) and Swiss mean (green). The numbers indicate the dates of available aerial imagery. Data: Swiss Federal Office of Meteorology and Climatology MeteoSwiss (www.meteoswiss.admin.ch).

modest decrease preceded the relative stability observed from the mid-1980s. Of particular interest are Hérémence and Evolène-Villa stations (1238 and 1826 m a.s.l., 18 and 9 km north of Arolla, respectively), as both are located in the Hérens valley. The Hérémence data are the most complete and feature a considerable decrease in annual precipitation before a substantial increase from the mid-1970s, with a peak at the beginning of the 1980s. Afterward, precipitation was stable at around 800 mm/yr, before decreasing considerably in the 2000s. The representativeness of these data as a proxy for the Arolla case study is sustained by the strong correlation between the longer term data series and the shorter Evolène-Villa series, available from the end of the 1980s, with similar trends apparent (Figure 7.4).

Results produced using the GSM-SOCONT model illustrate relatively lower March snow depths in the 1960s and mid-1970s (Figure 5a). Considerable increases in snow depth are then found for the following decade, reflecting the period of greater precipitation shown in Figure 4. From1985, end of winter snowdepth appears to have decreased steadily, albeit with high variability. Snow depths at the end of the summer (Figure 5b) show how the combination of high winter snow accumulation (Figure 7.5a) with low temperatures translated into considerable unmelted snow at the end of the summer at the altitudes of the glacial accumulation zones for the 1977–1985 period. On the other hand, snowcover appears to completely disappear at the altitudes of interest during every summer in the 2000s. While interannual variations are very
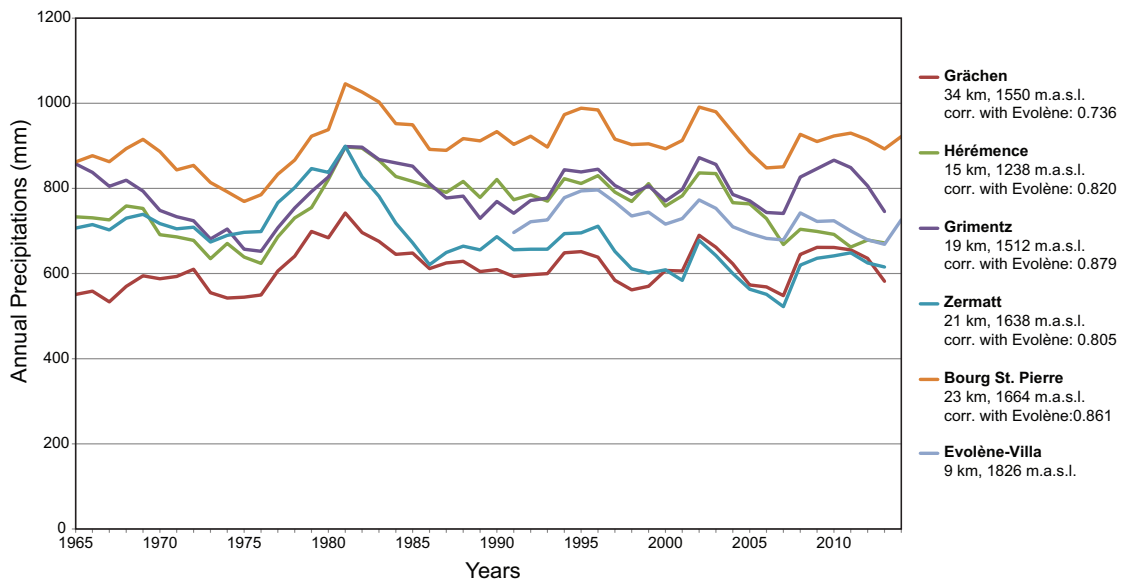
Figure 7.4 – Annual precipitation for meteorological stations located nearby Arolla (5 years moving average). The legend indicates the altitude and distance for each station from Arolla, as well as the correlation 1987-2014 with Evolène-Villa precipitation. Data: Swiss Federal Office of Meteorology and Climatology MeteoSwiss (www.meteoswiss.admin.ch).
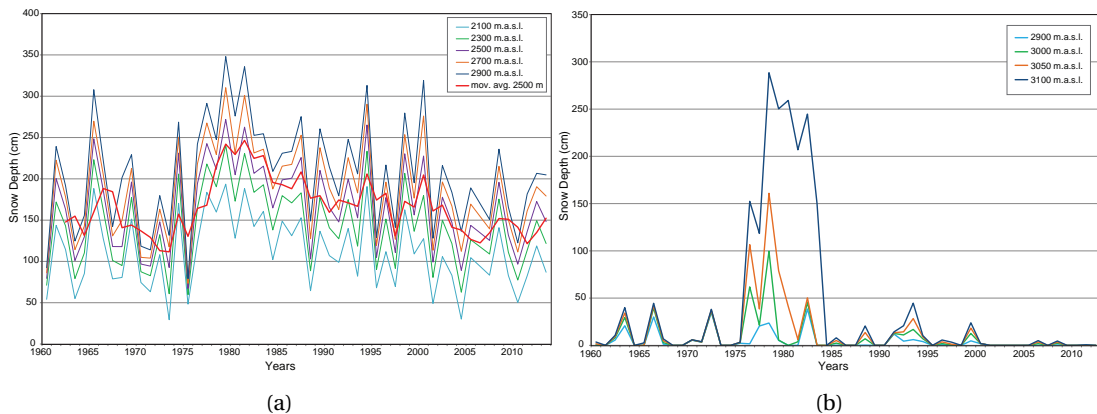
Figure 7.5 – Arolla snow depths modelled at various altitudes (a) 31 March and (b) 30 September, using the GSM-SOCONT model. In Figure 7.5a, the red line represents the 3 years moving average for the 2500 m.a.s.l. limit.

high, these results are consistent with other observations in Switzerland [Meteosuisse, 2014]. The considerable increase in snow depth observed from the mid-1970s to 1985 coincides with widespread glacial advance in the region in the early 1980s [VAW Laboratory of Hydraulics and Glaciology, 2013].

By considering the temperature, precipitation, and modeled snow cover depths together, we can consider the aerial imagery as relating to two distinct climate forcing stages: a relatively cooler and climatically more stable period (1960s to 1983) and a warming period (1983 to

131

present). The relatively cooler and stable period is characterized by a decrease in annual rainfall at first (mid-1960s to mid-1970s) but then greater precipitation at the end of the 1970s and beginning of the 1980s. Snow cover reflected this shift, only increasing with the start of the wetter period in the second half of the 1970s and 1980s. This emphasizes the importance of interannual precipitation variability in the study site for interannual variability in snow accumulation. Precipitation decreased as the climate warmed from the early 1980s, but this trend stopped from 1990, although examples of both wetter and drier years remain. Thus, the transition to the warming period also saw a net decrease in snowfall (after the high rates of the period 1975–1983), which then stabilized until the year 2000. In the 2000s, accumulated snow in March returned to levels characteristic of the 1960s but with lower snow cover in September because of warming effects.

7.4.2 DEMs of difference

Figure 7.6a shows the geomorphological map produced by Lambiel et al. [2016]. The two large glacial systems of Tsarmine and La Tsa are mainly debris-covered glaciers (A and H in Figures 7.1 and 7.6b). La Tsa comprises two smaller glaciers divided by a rockfall deposit zone and a detached, small area of debris-covered dead ice. The contexts of Tsarmine and La Tsa are similar. Both sites are relatively flat, and in addition to glacier and debris-covered glacier there are also small proglacial forefields, the latter delimited by Little Ice Age (LIA) moraines. These systems are each more than 400,000 m^2 in area, with the glacier and debris-covered glacier parts occupying ~284,000 and 227,000 m^2, respectively. The remainder of the area is mainly morainic deposits. The Genevois glacier (~65,000 m^2), where ice is no l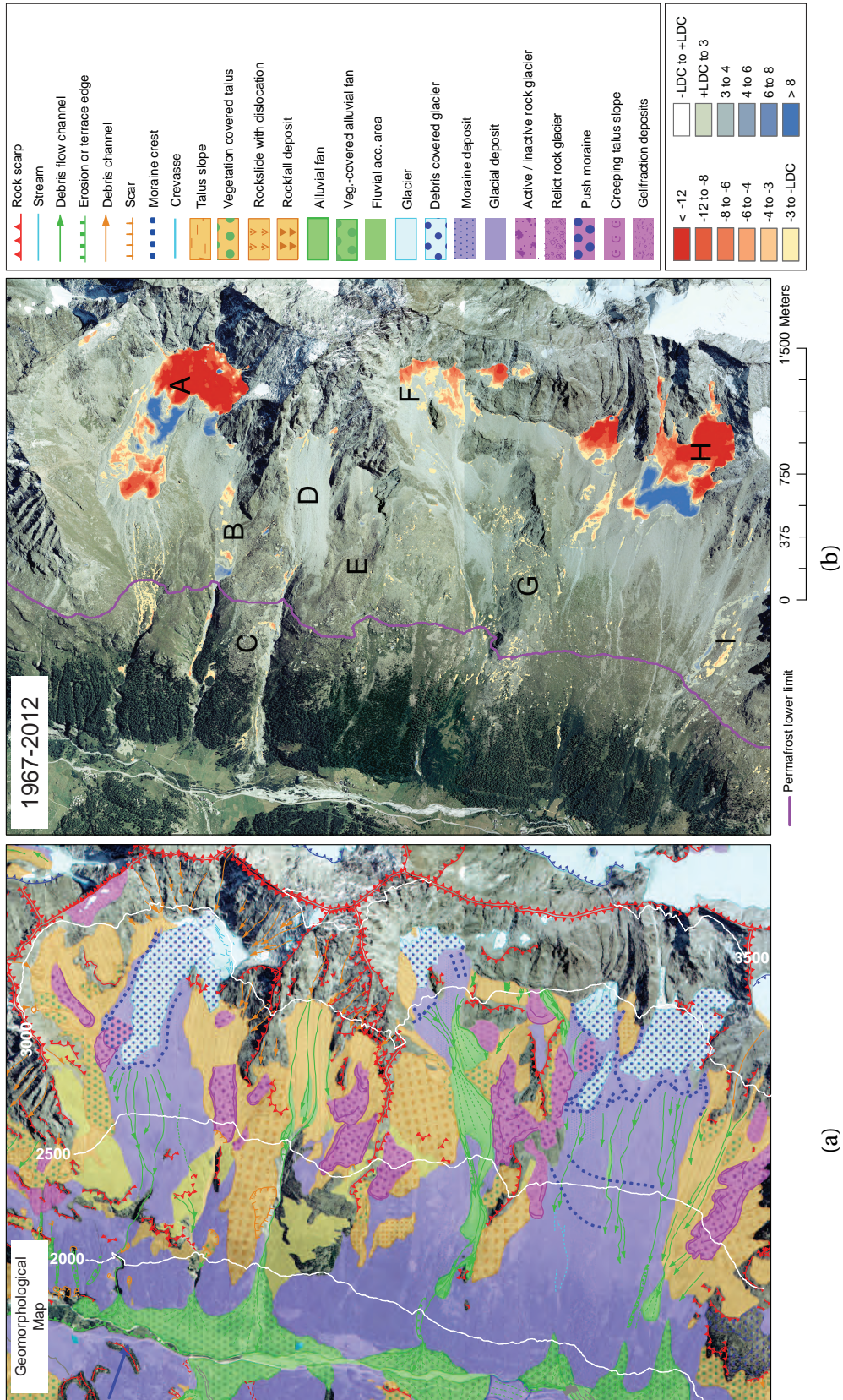onger visible, is located between these two larger glacial systems (F in Figures 7.1 and 7.6b), in a very steep location. A considerable number of active rock glaciers, mass movement processes (especially active rockslides), and fluvial process-related landforms are also mapped across the mountainside (see also Delaloye et al. [2007]; Barboux et al. [2014] for further details). Thus, the geomorphological map illustrates the presence of an assemblage of glacial, periglacial, hillslope, and fluvial landforms distributed over the area, and so a complex geomorphological setting.

Figure 7.6b shows the elevation changes between 1967 and 2012. Despite the substantial presence of unconsolidated material, the mountainside has been generally relatively stable at the limits of detection associated with our analysis over the last four and a half decades. Effectively, detectable surface downwasting is local. The largest magnitudes of change are found on glaciers and debris-covered glaciers. In the upper part of the Tsarmine and La Tsa systems, vertical loss is generally greater than 12 m, with peaks of more than 20 m. In their middle parts, increases in elevation of between 10 and 20 m are observed. It is probable that ice loss in the central part of these systems was mitigated by thickening caused by ice flux from upstream, with a possible legacy from glacier growth in the 1960s–1980s (see below). In Tsarmine, the lower part of the glacier suggests considerable downwasting. This is somewhat more limited in the Tsa system. In both cases, it suggests zones of elevation loss due to glacier

Figure 7.6 – (a) Geomorphological map [Lambiel et al., 2016] and (b) DEM of difference of 1967–2012, LDC 90% = 1.47 m, with regional lower limit of permafrost (∼2400 m a.s.l, Lambiel and Reynard [2001]) and sites of interest presented in Figure 7.1 (orthophoto: Swisstopo 2005).

marginal ablation. The Genevois glacier experienced only elevation loss and in reduced proportions as compared with the other glacier systems, a fact that could be explained by its smaller size.

Only the activity of two rock glaciers is clearly identifiable in the DEMs of difference: the Tsarmine rock glacier, located southwest of Tsarmine glacier (B in Figures 7.1 and 7.6b), and La Roussette, the most southern of all the area of study (I in Figures 7.1 and 7.6b). For both rock glaciers, an advancing front is evident, confirmed by an increase in elevation in their lower parts. The other rock glaciers in the mountainside show very little substantial downwasting over the 45 year period considered here. However, to conclude that these landforms are less active or inactive, it is also necessary to consider horizontal displacements especially as there may be lateral fluxes without elevation changes or ones that cannot be detected by the DoDs given their precision.

Gravity-related processes have vertical changes of a magnitude smaller than glacial and periglacial landforms. Nevertheless, rockslide activity produced significant downwasting in some locations over the 45 years considered. The most evident example is the Perroc rockslide located next to the Tsarmine rock glacier (C in Figures 7.1 and 7.6b), with traces of sliding toward the debris flow channel that connects the Perroc talus slope (D in Figures 7.1 and 7.6b) to the valley bottom. Traces of rockslide activity, although less marked, are also visible for the rockslide situated west of the La Tsa hut (G in Figures 7.1 and 7.6b). Detectable elevation changes were not encountered in talus slopes. Erosion and deposition on the mountainside by fluvial processes also appear to be limited given the precision of our data. Channel excavation is limited to a few cases. Notably, it can be seen in the debris flowchannels beneath Tsarmine, at the top and at the base of the Perroc talus slope, and in the debris flow channels extending from the Genevois glacier toward the valley bottom.

Figure 7.7 compares the DoDs for two distinct climatic periods: the cooler period that ended with some snow accumulation (a) and a rapid warming period (b). A distinct landscape response is shown for both periods. The mountainside appears to be very stable during the cooler period; the only significant elevation changes are associated with the glaciers with gains of several meters. Downwasting is very low and visible only in a few patches especially on the lower part of the Tsarmine and La Tsa glacier systems (A and H in Figure 7.1). The patterns observed during the rapid warming period of the 1980s are in the opposite direction. The glaciers experienced a loss in elevation of 4 to 10 m in their upper part. The elevation gain in their middle part, already visible in Figure 7.6b, is observed here but is of lower magnitude (3 to 6 m) and of smaller extent. More isolated but significant elevation changes, which were completely absent during the cooler period, are found across the hillslope. These changes relate mostly to gully erosion on terminal moraines, shallow excavation of debris flow channels, slight signs of activity at rock glacier fronts, or rockslide activity.
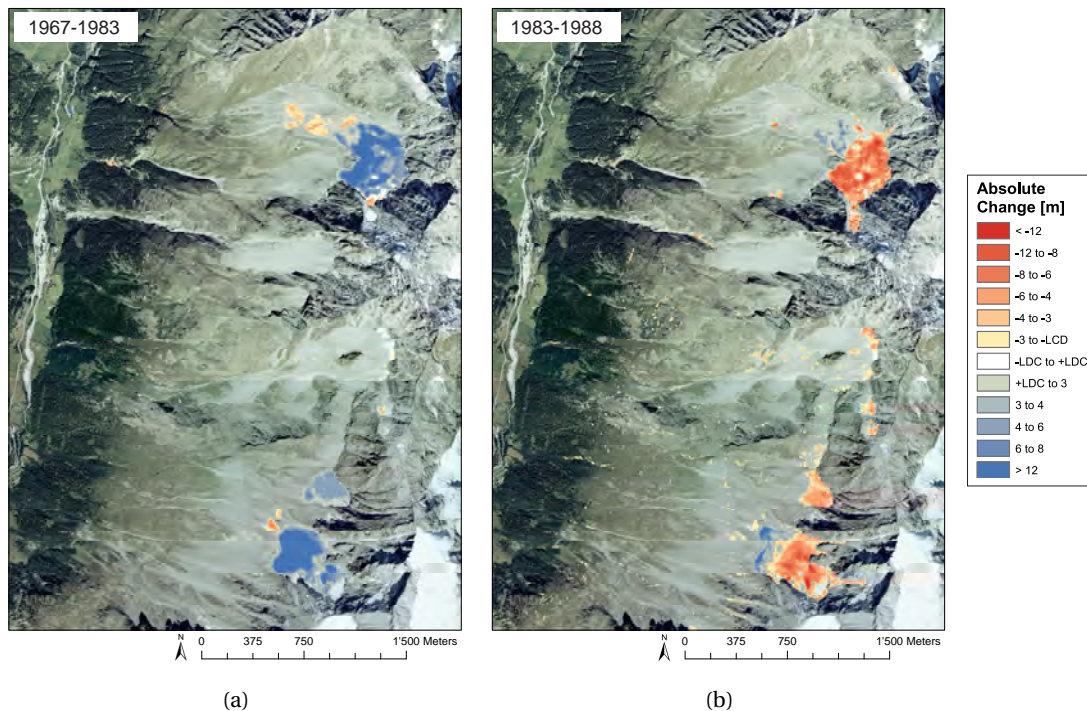
Figure 7.7 – (a) DEM of Difference of cooler and stable temperature period, 1967-1983, LDC 90% = 1.98 m and (b) DEM of Difference of rapid warming period, 1983-1988, LDC 90% = 1.86 m (Orthophoto: Swisstopo 2005).

7.4.3   Rates of surface change

Figure 7.8 shows average volumetric rates of surface change (in $m^3m^{-2}yr^{-1}$) for cooling/stable (blue symbols) and warming periods (red symbols) for every landform on the mountainside. This helps to better identify the dominant pattern for every landform type and link each to the effects of climate forcing. First, rates of change for parts of the landscape associated with glacial processes (i.e., glacier, debris-covered glaciers, moraine deposits) are logically greater than for other landforms, a fact already visible in the DoD (Figures 7.6b and 7.7). Glacial landforms have the greatest rates of gain during colder periods, while their rates of loss under warming are the greatest changes observed. Second, some landforms have enhanced activity during the warming period. Examples are rock glaciers, talus slopes, and rockslides. For these landforms, both rates of gain and loss during warming are greater than changes in the cooler period. Third, for many landforms, rates of gain are greater than losses in the climatically cooler and stable period. Afterward the opposite is observed, with rates of loss becoming considerably larger than rates of gain during the warming that started in the mid-1980s. The clearest examples are talus slopes, rockslides, alluvial fans, moraines, and rock glaciers. Finally, average rates of loss per year during the warming period are comparable to rates of gain during the cooling stage for debris-covered glaciers (0.33 and 0.31 $m^3m^{-2}yr^{-1}$, respectively) but differ for bare ice glaciers (0.46 and 0.21 $m^3m^{-2}yr^{-1}$). Debris-cover glaciers also have higher rates of volumetric gain during warming than loss during cooling, but this appears to be mostly a product of mass displacement rather than cryogenesis or sediment supply.
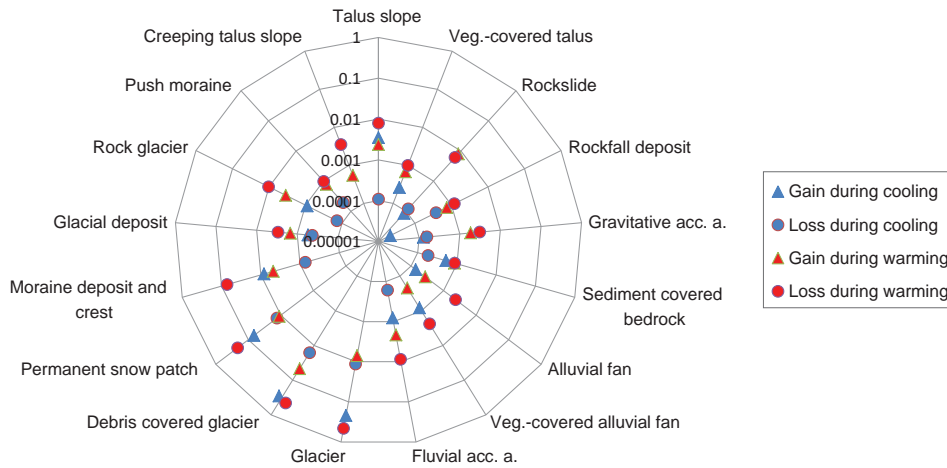
Figure 7.8 – Average yearly volumetric changes for cool/stable and warming periods for different landforms, normalized by their spatial extent [$m^3m^{-2}y^{-1}$]. An absent symbol means no change.

7.4.4 Surface displacements and deformations

Figure 7.9 shows the norms of displacement vectors (horizontal vectors corrected for slope) normalized by number of years for four distinct image pairs. It should be noted how some very active areas such as glaciers and debris-covered glaciers are not highlighted despite being the areas where most consistent movements are expected. This is for two reasons: first, vertical changes in these areas are very high (see Figures 7.6b and 7.7), and thus surface changes are so great that the resulting decorrelation prevents the detection of movement using image correlation analysis. Second, these areas are also likely to feature less ideal contrast because of their snow or ice cover. This is particularly true for the 1977 imagery as the mountainside is partially snow-covered in its upper part.

The surface displacements mapped between 1967 and 1977 (Figure 7.9a) highlight areas where significant elevation changes were not identified by the DoD (see Figure 7.7a). Rock glacier activity is evident with movements of up to 0.6 m/yr for the Tsarmine and La Roussette rock glaciers (B and I in Figures 1 and 6b) but absent or less well defined for others. The large Perroc rockslide (C in Figures 7.1 and 7.6b) also features localized displacements that can reach 0.3-0.4 m/yr. Even though only the lower parts of the glacial and proglacial systems were visible, probable ice-related movements can be identified. In particular, velocities up to 1.75 m/yr are identified in Tsarmine (A in Figures 7.1 and 7.6b). From the period 1977 to
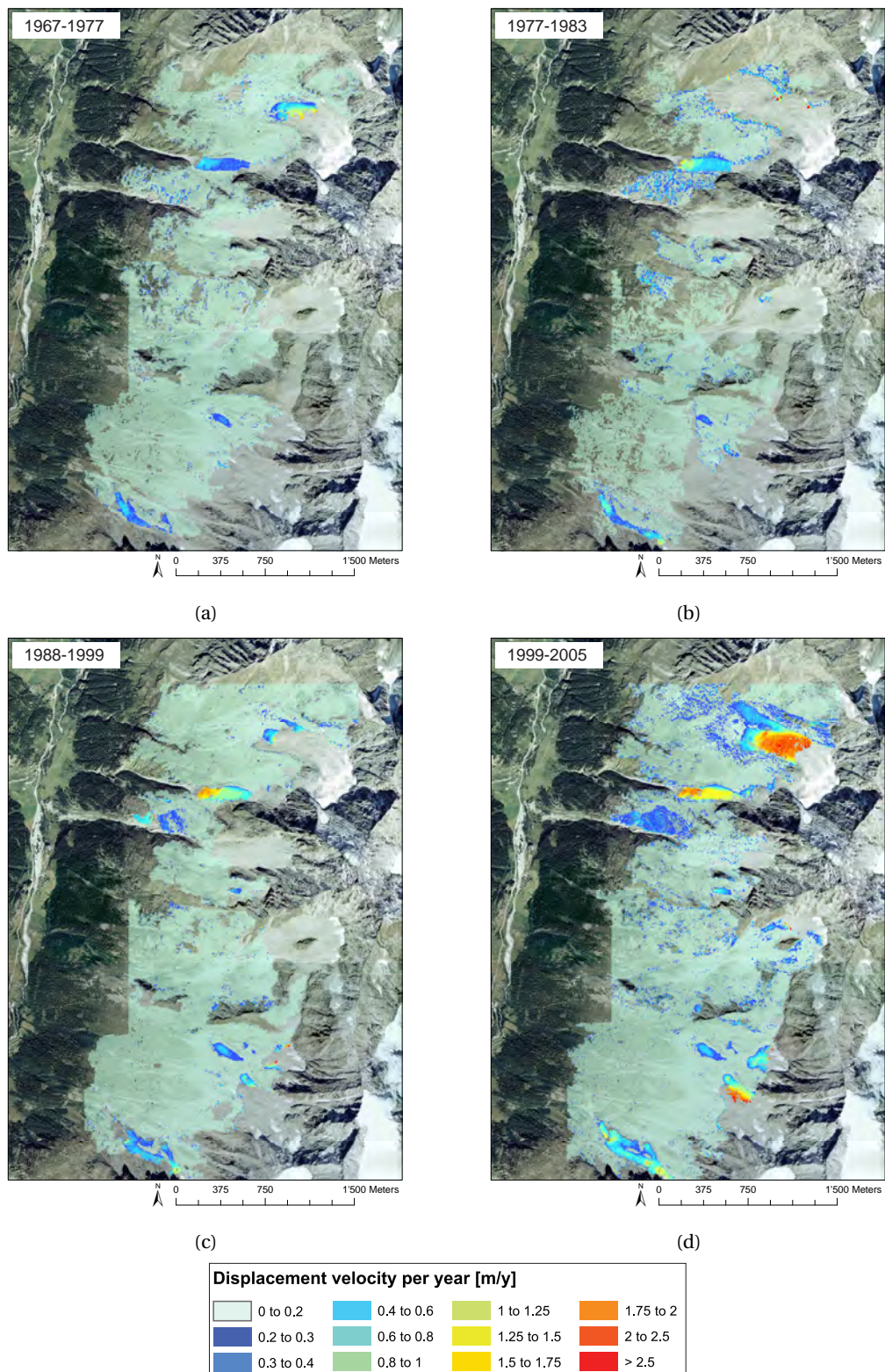
Figure 7.9 – Norm of displacement vectors per year for (a) 1967–1977, (b) 1977–1983, (c) 1988–1999, and (d) 1999–2005 (no data: displacement information not available, orthophoto: Swisstopo 2005).

1983 (Figure 7.9b), the snow cover of the 1977 images, along with the low quality of those of 1983, lead to large data gaps (especially in the northern part of the image) with many scattered, noisy displacements. Nonetheless, creep of the Tsarmine and La Roussette rock glaciers could be identified with a slight acceleration. The large rockslide mentioned earlier appears more active than the previous epoch.

An enhancement of periglacial activity seems to occur between 1988 and 1999 (Figure 7.9c). The Tsarmine rock glacier experienced an acceleration with velocities of up to 0.75-1 m/yr in its upper part and up to 2 m/yr near its front. La Roussette rock glacier also experienced a slight acceleration and has velocities of ~0.5–0.75 m/yr. Displacements on other rock glaciers are also increased and hence now visible. The rock glacier located between the Perroc talus slope and the Genevois basins, west of Dent de Perroc (upper part of the rock glacier called Lé Blâva, E in Figures 7.1 and 7.6b), which appeared stable in terms of elevation changes, reached velocities of ~0.4 m/yr. Movements on the large rockslide are not considerably enhanced with respect to the colder period.

The analysis of displacements between 1999 and 2005 (Figure7.9d) provides more complete results. Generally, greater displacement velocities than previous epochs are evident. The Tsarmine and La Roussette rock glaciers (B and I in Figures 1 and 6b) have increased velocities, up to more than 2 and 1.2 m/yr, respectively, while the rock glacier between Perroc and Genevois reached a velocity of more than 0.7 m/yr at its front. The large Perroc rockslide (C in Figures 7.1 and 7.6b) has a more homogeneous displacement. Its velocity is of the order of ~0.25-0.3 and 0.4 m/yr in its upper and lower parts, respectively. In the lower part, a detachment niche is well identified; it delimits a zone characterized by slightly faster displacements. Movements of debris-covered glacier systems are better highlighted and have high displacement velocities that can reach more than 2.5 m/yr in the middle part of these systems. In Tsarmine (A in Figures 7.1 and 7.6b), the velocities of the push moraine and of the marginal rock glacier are much slower (below 1 m/yr). The same is true for the dead ice in the lower part of La Tsa proglacial forefield (H in Figures 7.1 and 7.6b).

Differencing the norm of the displacement vectors between cold and warm period, represented here by 1967-1977 and 1999-2005 pairs, highlights changes in velocities (Figure 7.10) that are measures of land surface acceleration/deceleration. There is discernible acceleration of the Tsarmine rock glacier (B in Figures 7.1 and 7.6b), where the increase in horizontal velocities reaches 1.5 m/yr (200 to 350% of velocity enhancement). This trend is also important for other rock glaciers; despite incomplete information, the Roussette rock glacier body (I in Figures 7.1 and 7.6b) does not seem to have experienced velocities above 0.8 m/yr (acceleration of 50%), yet in its lower part local peaks with more than a 300% increase in velocity can be observed. The west Perroc reactivation is reflected in a velocity increase of 0.8 m/yr. The same is true for the rock glacier at the margin of the Tsarmine glacier (A in Figures 7.1 and 7.6b), which reactivated and experienced a velocity increase of 0.3-0.4 m/yr. The Perroc rockslide (C in Figures 7.1 and 7.6b) is very active and experienced velocity increases of the order of 0.2-0.3 m/yr. Between 1999 and 2005, higher displacement velocities were also observed on
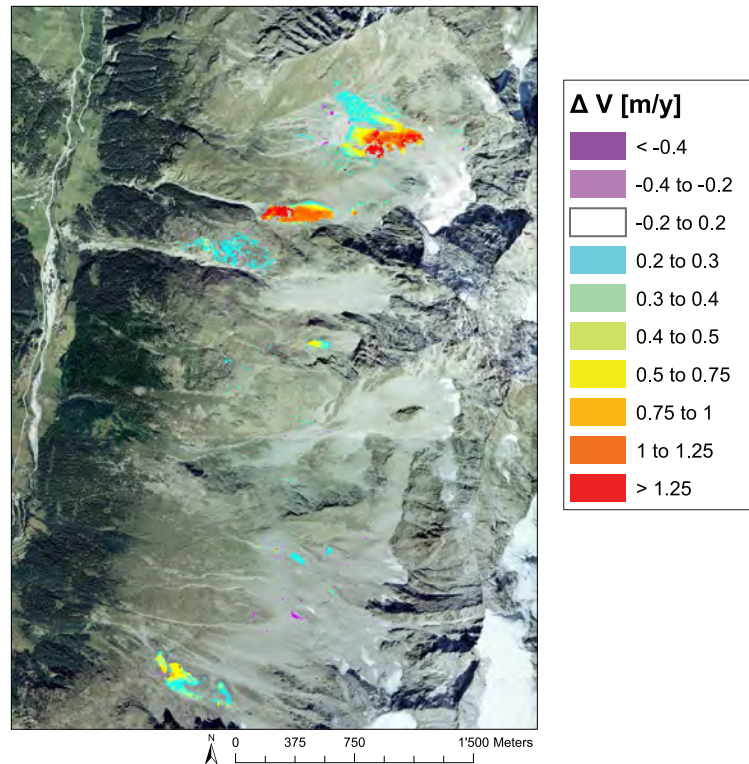
Figure 7.10 – Differences of the norm of displacement vectors between 1967–1977 and 1999–2005: positive values indicate acceleration (orthophoto: Swisstopo 2005).

debris-covered glacier surfaces, where for the identifiable velocity increases can reach 1.5 m/yr (acceleration of 100%). In the lower part of these systems, increments in velocities are limited to 0.2-0.4 m/yr. Decelerations are identified only very locally. The most evident clusters are concentrated on the moraine bastions of Tsarmine and La Tsa glaciers. These decreases in mass movement speed seem more related to single events of gullying or gravitational sliding that occurred during the 1960s and 1970s than a continual process.

Figure 7.11 shows a more detailed view of displacement velocities for the Tsarmine and La Roussette rock glaciers (a) and boxplots of velocities for the three most active rock glaciers in the study area (b). As visible in previous images, these show different velocities under the influence of local conditions. Nonetheless, their median displacements were very similar between 1967 and 1977: 0.23, 0.30, and 0.31 m/yr for the lobe above Lé Blâva, La Roussette, and Tsarmine rock glacier, respectively (B, above E and I in Figures 7.1 and 7.6b). Afterward, despite large velocity differences, the Tsarmine rock glacier and the rock glacier lobe above Lé Blâva have a clear increase in their velocities through time (Figure 7.11b). Median movements for these rock glaciers between 1999 and 2005 are 1.34 and 0.5 m/yr, respectively, corresponding to accelerations of 432% and 217% with respect to the first, cooler period. Acceleration of the La Roussette rock glacier is less evident in the velocity data illustrated in Figure 7.11b, despite it being visible clearly in Figure 7.10. Nevertheless, an increasing trend is still visible
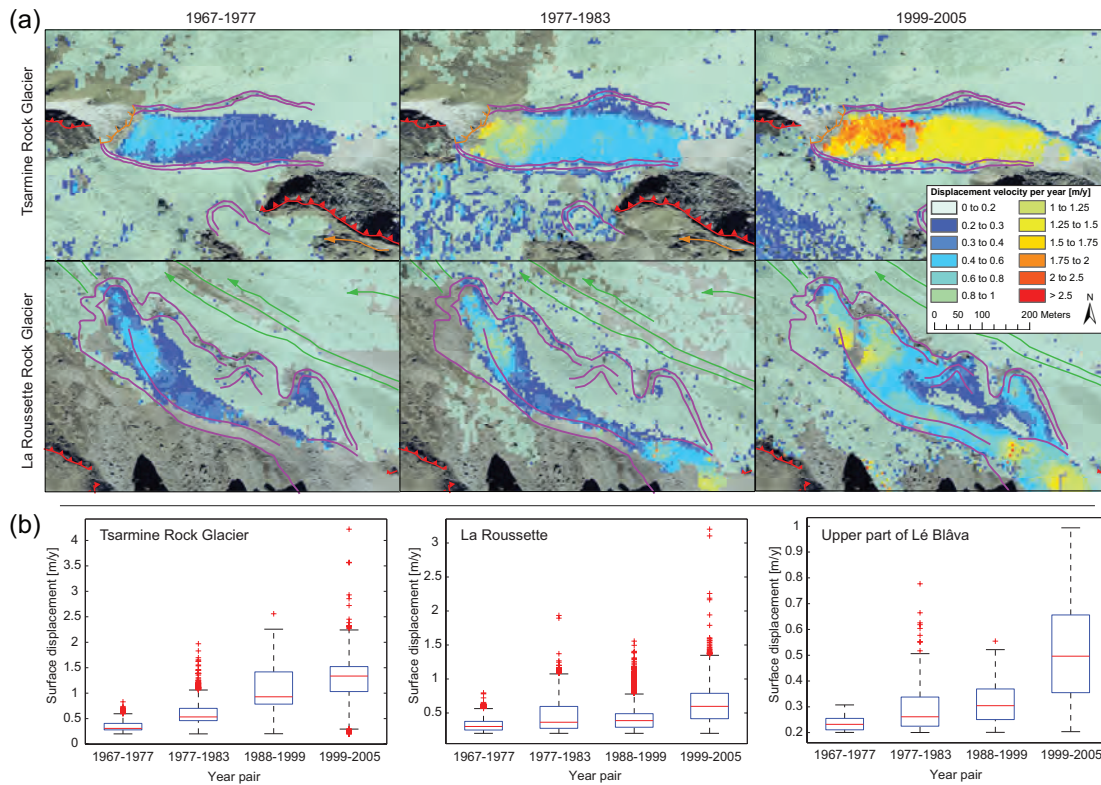
Figure 7.11 – (a) Detail of displacement velocities for the Tsarmine and the La Roussette rock glaciers (orthophoto: Swisstopo 2005). (b) Boxplots of rock glacier surface velocities (Note the different scale of the vertical axes).

and certified by the doubling of median displacement velocities (from 0.3 to 0.6 m/yr) and by the faster outliers occurring between 1967 and 2005.

7.5 Discussion

The analysis of elevation changes between 1967 and 2012 (Figure 7.6b) highlights a general stability of this steep hillslope, and this despite the presence of unconsolidated materials. Nonetheless, warming periods seem to be associated with some detectable increases in both downwasting and surface displacement, something that has been observed in studies of similar environments [Huggel et al., 2010, 2012; Beylich et al., 2011; Fischer et al., 2012]. The most dynamic periods are associated with either or both higher rainfall and snowfall or greater temperatures. The greatest rates of change are spatially delimited and concern mostly glacial and periglacial landforms.

7.5.1 Glacial systems

Surface change during the relatively cold period (1967–1983, Figure 7.7a) shows several meters of elevation gains in the upper parts of glacial zones. This growth in the accumulation area is most likely to be cryogenic. The period 1967-1983 effectively featured favorable climatic conditions for glacial advance. Low temperatures and abundant precipitation and snowcover, from the mid-1970s, possibly translated into larger amounts of unmelted snow at the end of the warm seasons (Figure 7.5b) and hence in glacier growth. Conversely, high-magnitude downwasting occurred in the same areas during the warming period that begins in the 1980s (Figure 7.7b). This period is characterized by a rapid temperature rise (Figure 7.3) and reduced precipitation and lower snow cover (Figure 7.5a). The changes identified demonstrate distinct response to warm and cold periods and to changes in precipitation, an observation confirmed also by volumetric trends (Figure 7.8) especially, but not exclusively, for glaciers and debris-covered glaciers.

The 1967-2012 DoD highlights a dominance of the warming climate conditions compared to the cooler period in the form of the extensive loss of ice volume. This is caused by the longer duration of the warming period, but for the bare ice parts of glaciers it is also a consequence of the difference in average volumetric changes between gain during cooling and loss during warming (0.21 and 0.46 $m^3m^{-2}yr^{-1}$, respectively, Figure 7.8). For debris-covered glaciers, these rates are almost the same (0.31 and 0.33 $m^3m^{-2}yr^{-1}$), a fact that can be attributed to the low thermal conductivity of debris covers [Takeuchi et al., 2000; Lambrech et al., 2011] and to an underestimation of the melting rate during the warming period caused by the effect of ice flux from the accumulation area. Nevertheless, debris-covered glaciers also shrink considerably (see Figure 7.6b), and so the periods 1967 to 1983 and 1983 to 2012 represent climatic conditions either side of a critical threshold (or equilibrium state, Phillips [2009]) for the altitude and aspect of this mountainside. The continuous glacier shrinkage from 1983 to 2012 occurred despite snowcover that was greater than the 1960s. This slight increase was not sufficient to compensate the temperature rise in these systems. Increases in elevation observed by debris-covered glaciers despite this warming are believed to be caused by the complicating effect of ice flux from the accumulation area rather than a changing pattern in the climate forcing reaction.

The case of Tsarmine (A in Figures 7.1 and 7.6b) is particularly interesting because of its heterogeneity and complexity [Lambiel et al., 2004]. In the geomorphological map (Figure 7.6a) the following land surface types are identifiable: bare ice glacier, debris-covered glacier, push moraine, rock glacier, and moraine crests or deposits. Bare ice glaciers experienced cryogenesis (formation of ice from unmelted snow at the end of the warm season) during the 1960s and 1970s and ice ablation afterward, starting from the mid-1980s. Even though surface velocities could not be derived for this area, it could be hypothesized that ice flow is relevant and sufficient to supply ice to the middle part of the system. Effectively, the debris-covered glacial part of the system suggests that it is supplied by ice and sediment produced by rockwalls that are sufficient to counter ice melt. The debris-covered glacier has a high surface velocity

(up to 2.5 m/yr). Distinctions between stable and warming periods can also be made: while both periods feature a flux, there is a surface increase between the two periods (Figure 7.10), of up to 1.5 m/yr. The push moraine and rock glacier are distinguished in the geomorphological map, but this ice-debris mixture area has homogeneous patterns. Significant vertical changes are only visible at long timescales, and rates of downwasting are among the lowest of the Tsarmine system. Substantial surface displacements could not be detected during the cold period, while velocities of 0.3-0.4 m/yr were estimated during the warming period. These velocities are close to those estimated by Kneisel and Kääb [2007] between the 1980s and the mid-1990s (thus the first part of the warming period) for a similar context also in the Swiss Alps. Accordingly, this area seems to accelerate its creep under the influence of warmer conditions. Finally, moraine deposits appear relatively stable from a displacement point of view. In summary, the Tsarmine area is a very active system featuring a coexistence of glacial and periglacial dynamics (i.e., push moraine and rock glacier) but with constant glacial recession over the last three decades.

7.5.2 Rock glaciers

The rates of activity that are visible in the DoDs also can vary within classes of landscape elements. As mentioned in the previous section this is the case for rock glaciers. Only the Tsarmine and La Roussette rock glaciers (B and I in Figure 7.1) have identifiable elevation changes between 1967 and 2012 (Figure 7.6b). These rock glaciers appear to be among the most active parts of the hillslope, and a possible explanation would be a combination of local topographic and subsurface ice conditions [Lambiel et al., 2004; Barboux et al., 2014]. Detectable elevation changes during the last decades (Figure 7.6b) are not homogeneous and of the order of 0.1 m of vertical change per year as observed by Kääb [2002] for a rock glacier in the eastern Swiss Alps. Despite the relatively small magnitude of vertical changes in the DoDs (Figure 7.6b), volume estimations highlight an enhanced activity from the 1960s to present. Both yearly rates of gain and loss during the warming period are higher than the values estimated for the cooling period (Figure 7.8), indicating a clear reaction to a warmer climate.

More interestingly, evaluation of surface displacement shows an acceleration of rock glaciers from 1967 onward. Speedup between the periods 1967-1977 and 1977-1983 may be linked with enhanced precipitation and the greater snow cover (Figures 7.4 and 7.5) that could have caused water infiltration and accelerated creep [Ikeda et al., 2008]. In addition, snow conditions exert a dominant role on ground temperatures by insulating the ground surfaces from the atmosphere during winter [Keller and Gubler, 1993]. Early winter snow falls, coupled with a thick snow cover and late melt, may provoke an increase of mean annual ground surface temperature and rock glacier acceleration [Delaloye et al., 2010; PERMOS, 2013]. The high snow depths of the period 1977-1985 may thus have been responsible for the observed increases in rock glacier velocities. Velocities increased even further after the transition into the warming period. The Tsarmine rock glacier velocities increased from 0.3 to more than 2

m/yr. The very high velocities of recent decades have also been confirmed by differential GPS (dGPS) measurements [Delaloye et al., 2008; PERMOS, 2013] and InSAR data [Lambiel et al., 2008; Barboux et al., 2014]. The trend is the same for La Roussette, where velocities of 0.2-0.5 m/yr (comparable with other studies in Switzerland e.g., Kääb [2002]; Delaloye et al. [2008]) increased to 1.2 m/yr during the warming period.

The velocities of rock glaciers that were otherwise unchanged in terms of detectable elevation changes could also be observed, as for the small rock glacier located above Lé Blâva (E in Figure 7.1), between the Perroc talus slope and the Genevois basins. Its activity is much reduced in respect to the previous examples, and it appeared to be inactive between 1967 and 1977. Despite temperatures still being low, modest displacement is identified at its front between 1977 and 1983, probably due to the input of water caused by enhanced precipitations and melting snow. It experienced a complete reactivation during the warming period with surface velocities up to more than 0.8 m/yr. Another rock glacier located only 500 m west from it is not experiencing the same reactivation. Hence, local conditions appear to exert an important impact upon rock glacier response to cooling and warming [Kirkbride and Brazier, 1995]. However, some rock glaciers did accelerate first under the influence of important water inputs toward the end of the cooler and stable period (1977-1983) and then (1988 onward) under the influence of temperature rise (see Figure 7.11). This supports the hypothesis of a strong influence of climate forcing upon rock glacier velocities (e.g., Kellerer-Pirklbauer and Kaufmann [2012]), which has also been demonstrated in other studies [Roer et al., 2005, 2008; Kääb et al., 2007; Delaloye et al., 2010].

7.5.3 Gravity-driven and fluvial processes

Activity associated with gravity-driven and fluvial landforms in the DoDs is less clear than for glacial and periglacial landforms, because of the smaller magnitude of elevation changes in these areas. With the available resolution of the data and the consequent limits of detection, the activity of some small-scale geomorphic processes cannot be measured. Clear examples are rockfall activity (impossible to observe because of the steepness of rockwalls) and debris flows of small to moderate magnitude. This leads to an underestimation of possible sediment fluxes in the system and, unfortunately, a limit of the use of the archival imagery in this study. Nevertheless, despite leaving weaker signals in the DoDs than ice-related landforms, the analysis of gravitational processes still shows changing patterns through time. In Figure 7.8, the rates of change during the warming period appear generally greater than in the cold period. This is clearly the case for rockslides, where both rates of aggradation and degradation appear to be considerably higher than in the cooler period. Given the location of large rockslides above the lower permafrost limit, a speculative explanation could be related to the presence of permafrost. This hypothesis requires in situ measurements to be confirmed, which are not available at present. The only case of surface displacement change between the 1960s and the 2000s is in terms of the large Perroc rockslide (C), where accelerations of between 0.2 and 0.5 m/yr are observed (Figure 7.10, also detected using InSAR data by Delaloye et al. [2007]).

The rockslide started accelerating in the cold period, probably due to enhanced rainfall and snowmelt input enhancement at the end of the 1970s. Despite less clear signals, it appears that even non-ice-related landforms might respond to climate forcing and accelerate underwetter and warmer climatic conditions, a consideration supported by similar studies [Huggel et al., 2010, 2012; Bennett et al., 2013].

7.5.4 Impacts on sediment flux at landscape scale

Some landforms are found to be sensitive to warming or snow cover and rainfall increases and may lead to locally high sediment flux. Nevertheless, there is evidence in our analysis to suggest that the effects of past climatic conditions upon the landscape has left a heritage in the system that can play a key role in disconnecting zones of high rates of change from the valley bottom. The role of hillslope coupling within the fluvial and torrential systems commonly responsible for sediment transmission downstream has been widely investigated. Various studies (e.g., Harvey [2002]; Heckmann and Schwanghard [2013]) have demonstrated that in most cases only a small percentage of the hillslope is coupled to the channel network because of natural or anthropogenic barriers, leading to abundant hillslope sediment storage. In such cases, the effects of changes in erosion and deposition may be spatially restricted [Harvey, 2001]. Figure 7.12 illustrates the northern part of the study area, where examples of different connectivity settings are found. The Tsarmine glacial system (Figure 7.12, site 1 - A in Figure 7.1), which is showing considerable surface change both vertically and horizontally (see Figures 7.6b and 7.9) and likely being supplied by sediments from the rockwalls located above it, is in a disconnected setting. Effectively, the depression behind the LIA moraine crest prevents sediment transfer down the mountainside despite the large availability of unconsolidated material in the site. Sediment transfer may occur from gully erosion on the moraine bastion, as testified by the presence of debris flow channels. However, recent sediment delivery to the valley bottom is not observed, and associated alluvial fan dynamics are very limited or even absent (Figure 7.12, AF1). This type of disconnection, associated with high sediment availability, is also found for the La Tsa glacier system.

The second state observed is intermediate storage as in the case of the Tsarmine rock glacier (Figure 7.12, site 2 - B in Figures 7.1 and 7.6b). Rock glaciers act as sediment buffers on the hillslope. The role of permafrost is essential in this regard, as ground ice is able to prevent or block the mobilization of unconsolidated sediment. Rock glacier acceleration under warming or wetter climatic conditions could translate into shorter intermediate storage of material. Effectively, the increased velocities of the Tsarmine rock glacier should eventually translate into more sediment delivery to the channel downslope. However, the large boulders delivered to the front of the rock glacier are deposited into a narrow channel with relatively limited water supply and so transport capacity. Extensive boulder deposits are found in the channel, but they do not propagate to the valley bottom. As a result, the alluvial fan below does not receive the sediment supply that is expected given the velocity of the rock glacier (Figure 7.12, AF2). Despite evidence of enhancement of sediment production at the rock glacier front, it can be
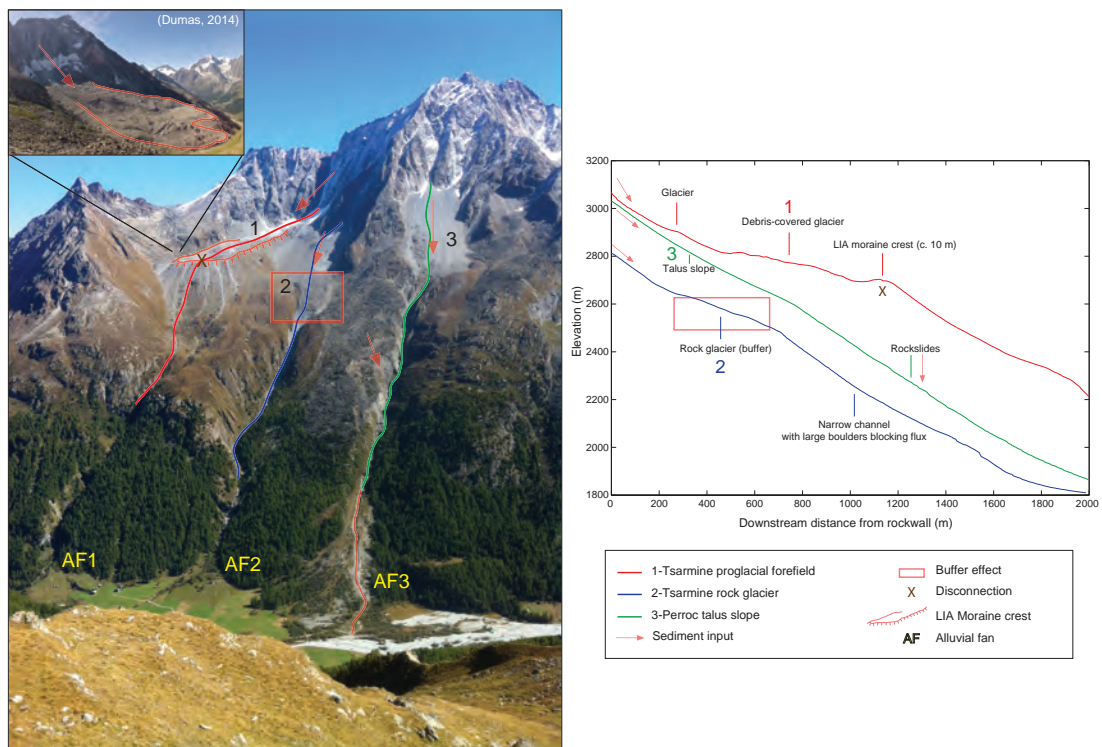
Figure 7.12 – Different connectivity settings in the northern part of the mountainside: disconnection of the Tsarmine glacial system (1), intermediate storage and buffering of the Tsarmine rock glacier (2), and established connectivity of the Perroc talus slope (3). In the lower part it is possible to observe the contrasting conditions of alluvial fans caused by different sediment connectivity.

hypothesized that delivery at the valley bottom may not be strongly affected by climate forcing at the timescales considered. The condition of the La Roussette rock glacier is different: here the disconnection is caused by the fact that its front does not deliver sediments to a channel. It acts as a sediment sink for the wide mountainside topography to its south and effectively insulates any possible upstream increase in sediment flux from propagation through to a channelized system and hence the valley bottom.

Finally, the Perroc talus slope (Figure 7.12, site 3 - D in Figures 7.1 and 7.6b) appears to be characterized by a good, efficient connection. Effectively, the intermediate storage here is the talus slope itself, in a very steep condition that facilitates sediment mobilization by debris flows starting in the overhanging rock couloirs. As a consequence, sediments from rockwalls, the talus slope, and even landslides at the edges of the Perroc rockslide are easily transferred through the channel, aided by a linear, steep, and buffer-free connection. Thus, the largest and apparently most active alluvial fan (Satarma, Figure 7.12, AF3) is associated with the best sediment connectivity and not with large surface changes upslope or the largest sediment availability. Thus, connectivity plays a key role in climatically driven sediment dynamics, an observation that finds support in other contributions [Shroder et al., 2000; Harvey, 2001;

Reynard et al., 2012; Bosson et al., 2014]. In another Swiss case study, Müller et al. [2014] noted that the actual mobilized material at the top of the sediment cascade is much higher than the input in the subsystems throughout the hillslope. Geilhausen et al. [2013] observed that while climate change and enhanced glacier retreat led to an increase in sediment discharge from proglacial zones, downstream sediment fluxes were considerably reduced by the development of proglacial lakes. Accordingly, intermediate storage of loose material exerts a critical control on climate forcing signals in alpine systems [Matsouka, 2008]. This leads to the counter intuitive observation that while landscape response to climatic warming and enhancement in precipitation and snow cover implies a net increase in sediment flux toward the valley bottom, this is not necessarily manifest in the valley bottom itself (e.g., in evident increase in alluvial fan dynamics) because this flux is commonly disconnected for the most reactive parts of the landscape. This is particularly true for small glacier systems, where the rate of paraglacial activity is high but glacier erosion and the geometry of past deposits prevent sediment flux downstream [e.g., Brazier et al. [1998]; Shroder et al. [2000]; Benn et al. [2012]; Bosson et al. [2014]. As Ballantyne [2002] argues, paraglacial system sediment release may be delayed to centuries or even millennia after the beginning of deglaciation. Reflecting wider observations of hillslope buffering of catchment response to external forcing (e.g., Forzoni et al. [2014]), it questions the extent to which decadal-scale, perhaps even centennial-scale, climate forcing can be quantified in valley bottom (e.g., lake) deposits in mountain environments.

7.6   Conclusion

By unlocking the information held in archival aerial imagery, this contribution has been able to associate changes in climate forcing to modifications of alpine geomorphic processes and rates. This was manifest as a distinct landscape response to warm and cold periods and to changes in rates of precipitation and snow cover. From the end of the 1960s to the beginning of the 1980s, despite temperatures still being warmer than during the Little Ice Age, glaciers were able to grow substantially at rates of ~0.3 $m^3m^{-2}yr^{-1}$, while widespread stability was observed for other landforms. The reaction to the rapid warming that followed was fast and seemed to pass a threshold, with a continuous glacial shrinkage observed from the mid-1980s. Estimated melt rates for bare ice glaciers are higher than for their debris-covered parts (0.46 versus 0.33 $m^3m^{-2}yr^{-1}$), because of the insulating role of debris [Takeuchi et al., 2000; Lambrech et al., 2011] and the effect of ice flux from the accumulation zones to the debris-covered parts of the systems. Precipitation and snow cover considerably increased from the mid-1970s and, despite stable and low temperatures, were associated with a general acceleration of surface displacements for different landforms, especially rock glaciers. Moreover, the continuation and accentuation of temperature rise translated into an augmentation of these displacement velocities. Active rock glaciers experienced velocity increases from 0.2-0.3 m/yr to more than 1 m/yr during the period of study, with peaks as high as 2 m/yr. A reactivation of an inactive rock glacier has also been observed. Non-ice-related landforms also appear to accelerate their displacements under wetter and warmer climatic conditions; the most evident examples are

velocity increases of between 0.2 and 0.5 m/yr for a rockslide. Despite some landforms being able to generate an enhanced sediment flux locally, propagation throughout the hillslope is not a direct consequence because of disconnection. Hence, the consequences of climate forcing for sediment dynamics remain highly location specific and sediment delivery under warming and wetter climatic conditions appears to be more dependent on sediment connectivity than on the landform processes themselves. Accordingly, assessing climatic forcing upon sediment transfer rates using valley bottom deposits might be misleading and requires particular care.

Future investigations are necessary to better understand the climate forcing signals observed in this alpine setting. First, surface changes and displacements need to be coupled with additional climatic indicators including the frequency of freeze-thaw cycles, intensity of rainfall events, and data on the magnitude of diurnal temperature amplitudes to strengthen the causal link between climate forcing and geomorphic response. Second, a deeper knowledge of permafrost distribution in the area would be beneficial to explain the observed landform behavior at the decadal scale in response to changing climatic conditions. This could be achieved by *in situ* measurements or modeling approaches. Finally, sediment production rates in the rockwalls represent a key indicator for this type of analysis that could not be derived here and need to be obtained with different approaches.

Acknowledgements

Bibliography

Ballantyne, C. K. (2002). A general model of paraglacial landscape response. *Holocene*, 12(3):371–376.

Ballantyne, C. K., Wilson, P., Gheorghiu, D., and Rodés, A. (2014). Enhanced rock-slope failure following ice-sheet deglaciation: timing and causes. *Earth Surface Processes and Landforms*, 39(7):900–913.

Barboux, C., Delaloye, R., and Lambiel, C. (2014). Inventorying slope movements in an Alpine environment using DInSAR. *Earth Surface Processes and Landforms*, 39(15):2087–2099.

Bayard, D., Stähli, M., Parriaux, H., and Flühler, A. (2005). The influence of seasonally frozen soil on the snowmelt runoff at two Alpine sites in southern Switzerland. *Journal of Hydrology*, 309(1-4):66–84.

Benn, D., Bolch, T., Hands, K., Gulley, J., Luckman, A., Nicholson, L., Quincey, D., Thompson, S., Toumi, R., and Wiseman, S. (2012). Response of debris-covered glaciers in the Mount Everest region to recent warming, and implication for outburst flood hazards. *Earth-Science Reviews*, 114(1-2):156–174.

Bennett, G., Molnar, P., Eisenbeiss, H., and McArdell, B. (2012). Erosional power in the Swiss Alps: characterization of slope failure in the Illgraben. *Earth Surface Processes and Landforms*, 37(15):1627–1640.

Bennett, G., Molnar, P., McArdell, B., Schlunegger, F., and Burlando, P. (2013). Patterns and controls of sediment production, transfer and yield in the Illgraben. *Geomorphology*, 188:68–82.

Beylich, A. A., Lamoreux, S. F., and Decaulne, A. (2011). Developing frameworks for studies on sedimentary fluxes and budgets in changing cold environments. *Quaestiones Geographicae*, 30(1):5–18.

Bosson, J.-b., Deline, P., Bodin, X., Schoeneich, P., Baron, L., Gardent, M., and Lambiel, C. (2014). The influence of ground ice distribution on geomorphic dynamics since the Little Ice Age in proglacial areas of two cirque glacier systems. *Earth Surface Processes and Landforms*, 40(5):666–680.

Bouët, M. (1985). *Climat et météorologie de la Suisse romande*. Payot, Lausanne, 185 p.

Brazier, V., Kirkbride, M., and Owens, I. (1998). The relationship between climate and rock glacier distribution in the Ben Ohau Range, New Zealand. *Geografika Annaler*, 80(3-4):193–207.

Brocklehurst, S. H. and Whipple, K. X. (2002). Glacial erosion and relief production in the Eastern Sierra Nevada, California. *Geomorphology*, 42(1-2):1–24.

Brunsden, D. and Thornes, J. B. (1979). Landscape sensitivity and change. *Transactions of the Institute of British Geographers*, 4(4):463–484.

Capt, M., Bosson, J.-B., Fischer, M., Micheletti, N., and Lambiel, C. (2016). Decadal evolution of a very small heavily debris-covered glacier in an Alpine permafrost environment. *Journal of Glaciology*, doi: 10.1017/jog.2016.56.

Carturan, L., Baldassi, G. A., Bondesan, A., Calligaro, S., and others, . (2013). Current Behaviour and Dynamics of the Lowermost Italian Glacier (Montasio Occidentale, Julian Alps). *Geografiska Annaler: Series A, Physical Geography*, 95(1):79–96.

Chandler, J. H. and Cooper, M. (1988). Monitoring the development of landslides using archival photography and analytical photogrammetry. *Land and Minerals Surveying*, 6(11):576–584.

Committee on Challenges and Opportunities in Earth Surface Processes (2010). *Landscapes on the Edge: New Horizons for Research on Earth's Sciences.* The National Academies Press, Washington D. C.

Davies, M., Hamza, O., and Harris, C. (2001). The effect of rise in mean annual temperature on the stability of rock slopes containing ice-filled discontinuities. *Permafrost and Periglacial Processes*, 12:137–144.

Delaloye, R., Lambiel, C., Lugon, R., Raetzo, H., and Strozzi, T. (2007). Typical ERS InSAR signature of slope movement in a periglacial mountain environment (Swiss Alps). In *Proceedings ENVISAT Symposium.*

Delaloye, R., Perruchoud, E., Avian, M., Kaufmann, V., and others, . (2008). Recent interannual variations of rock glacier creep in the European Alps. In *Proceedings of the Ninth International Conference on Permafrost.*

Delaloye, R., Strozzi, T., Lambiel, C., Mari, S., Stocker, A., Techel, F., and Raetzo, H. (2010). The contribution of InSAR data to the early detection of potentially hazardous active rock glaciers in mountain areas. In *Proceedings ESA Living Planet Symposium.*

Dissart, O. and Jamet, O. (1995). 3D reconstruction of buildings from stereo-images using both monocular analysis and stereomatching: an assessment within the context of cartographic production. In *Proceedings of the Society of Photo-Optical Instrument Engineers.*

Dollar, E. and Rowntree, K. (1995). Hydroclimatic trends, sediment sources and geomorphic response in the Bell River catchment, eastern Cape Drakensberg, South Africa. *South African Geographical Journal*, 77(1)(1):21–32.

Fischer, L., Eisenbeiss, H., Kääb, A., Huggel, C., and Haeberli, W. (2011). Monitoring Topographic Changes in a Periglacial High-mountain Face using High-resolution DTMs, Monte Rosa East Face, Italian Alps. *Permafrost and Periglacial Processes*, 22(2):140–152.

Fischer, L., Huggel, C., Kääb, A., and Haeberli, W. (2012). Slope failures and erosion rates on a glacierized high-mountain face under climatic change. *Earth Surface Processes and Landforms*, 38(8):836–846.

Ford, J. and Bedford, B. L. (1987). The Hydrology of Alaskan Wetlands, U.S.A.: A Review. *Arctic and Alpine Research*, 19(3):209–229.

Forzoni, A., Storms, J., Whittaker, A., and de Jager, G. (2014). Delayed delivery from the sediment factory: modeling the impact of catchment response time to tectonics on sediment flux and fluvio-deltaic stratigraphy. *Earth Surface Processes and Landforms*, 39(5):689–704.

Fryirs, K. (2013). (Dis)Connectivity in catchment sediment cascades: a fresh look at the sediment delivery problem. *Earth Surface Processes and Landforms*, 38(1):30–46.

Geilhausen, M., Morche, D., Otto, J., and Schrott, L. (2013). Sediment discharge from a proglacial zone of a retreating Alpine glacier. *Zeitschrift für Geomorphology*, 57(2):29–53.

Godon, C., Mugnier, J. L., Fallourd, R., Paquette, J. L., Pohl, A., and Buoncristiani, J. F. (2013). The Bossons glacier protects Europe's summit from erosion. *Earth and Planetary Science Letters*, 375:135–147.

Hales, T. C. and Roering, J. J. (2007). Climatic controls on frost cracking and implications for the evolution of bedrock landscapes. *Journal of Geophysical Research*, 112:F02033.

Harvey, A. M. (2001). Coupling between hillslopes and channels in upland fluvial systems: implications for landscape sensitivity, illustrated from the Howgill Fells, northwest England. *Catena*, 42(2-4):225–250.

Harvey, A. M. (2002). Effective timescales of coupling within fluvial systems. *Geomorphology*, 44(3-4):175–201.

Heckmann, T. and Schwanghard, W. (2013). Geomorphic coupling and sediment connectivity in an alpine catchment - Exploring sediment cascades using graph theory. *Geomorphology*, 182:89–103.

Hölzle, M. and Haeberli, W. (1995). Simulating the effects of mean annual air-temperature changes on permafrost distribution and glacier size: an example from the Upper Engadin, Swiss Alps. *Annals of Glaciology*, 21:399–405.

Huggel, C., Clague, J. J., and Korup, O. (2012). Is climate change responsible for changing landslide activity in high mountains? *Earth Surface Processes and Landforms*, 37(1):77–91.

Huggel, C., Salzmann, N., Allen, S., Caplan-Auerbach, J., Fischer, L., Haeberli, W., Larsen, C., Schneider, D., and Wessels, R. (2010). Recent and future warm extreme events and high-mountain slope stability. *Philosophical Transactions of the Royal Society A*, 368(1919):2435–2459.

Hughes, M., McDowell, P., and Marcus, W. (2006). Accuracy assessment of georectified aerial photographs: Implications for measuring lateral channel movement in a GIS. *Geomorphology*, 74(1-4):1–16.

Hunt, J. (2002). Floods in a changing climate: a review. *Philosophical Transactions of the Royal Society of London A*, 360(1796):1531–1543.

Ikeda, A., Matsuoka, N., and Kääb, A. (2008). Fast deformation of perennially frozen debris in a warm rock glacier in the Swiss Alps: An effect of liquid water. *Journal of Geophysical Research*, 113:F01021.

Intergovernmental Panel on Climate Change IPCC (1990). *Climate Change: The IPCC Impacts Assessment*, chapter Seasonal snow cover, ice and permafrost, pages 7.1–7.45. Australian Government Publishing Service: Canberra.

Jomelli, V., Pech, V. P., Chochillon, C., and Brunstein, D. (2004). Geomorphic variations of debris flows and recent climatic change in the French Alps. *Climatic Change*, 64:77–102.

Kääb, A. (2002). Monitoring high-mountain terrain deformation from repeated air- and space borne optical data: examples using digital aerial imagery and ASTER data. *ISPRS Journal of Photogrammetry & Remote Sensing*, 57(1-2):39–52.

Kääb, A., Frauenfelder, R., and Roer, I. (2007). On the response of rockglacier creep to surface temperature increase. *Global and Planetary Change*, 56:172–187.

Kääb, A. and Vollmer, M. (2000). Surface Geometry, Thickness Changes and Flow Fields on Creeping Mountain Permafrost: Automatic Extraction by Digital Image Analysis. *Permafrost and Periglacial Processes*, 11(4):315–326.

Keller, F. and Gubler, H. (1993). Interaction between snow cover and high mountain permafrost murtel/corvatsch, swiss alps. In *Proceedings of the Sixth International Conference on Permafrost*.

Kellerer-Pirklbauer, A. and Kaufmann, V. (2012). About the relationship between rock glacier velocity and climate parameters in Central Austria. *Austrian Journal of Earth Sciences*, 105(2):94–112.

Kirkbride, M. P. and Brazier, V. (1995). On the sensitivity of Holocene talus-derived rock glaciers to climate change in the Ben Ohau Range, Southern Alps, New Zealand. *Journal of Quaternary Science*, 10(4):353–365.

Kneisel, C. and Kääb, A. (2007). Mountain permafrost dynamics within a recently exposed glacier forefield inferred by a combined geomorphological, geophysical and photogrammetrical approach. *Earth Surface Processes and Landforms*, 32(12):1797–1810.

Knox, J. C. (1999). *Fluvial Processes and Environmental Change*, chapter Long-term episodic changes in magnitudes and frequencies of floods in the Upper Mississippi River Valley, pages 255–282. John Wiley and Sons, New York.

Korup, O. (2004). Landslide-induced river channel avulsions in mountain catchments of southwest New Zealand. *Geomorphology*, 63(1-2):57–80.

Kundzewicz, Z. W., Mata, L. J., Arnell, N. W. Döll, P., Kabat, P., Jimenez, B., Miller, K. A., Oki, T., Sen, Z., and Shiklomanov, I. A. (2007). *Climate Change 2007: Impacts, Adaptation and Vulnerability. Contribuition of Working Group II to the Fourth Assessment Report of the Intergovernamental Panel on Climate Change*, chapter Freshwater ressources and their management. Cambridge University Press, Cambridge, UK.

Lambiel, C., Delaloye, R., Strozzi, T., Lugon, R., and Raetzo, H. (2008). ERS InSAR for assessing rock glacier activity. In *Proceedings of the Ninth International Conference on Permafrost*.

Lambiel, C., Maillard, B., Kummert, M., and Reynard, E. (2016). Geomorphological Map of the Hérens Valley (Swiss Alps). *Journal of Maps*, 12(1):160–172.

Lambiel, C. and Reynard, E. (2001). Regional modelling of present, past and future potential distribution of discontinuous permafrost based on a rock glacier inventory in the Bagnes-Hérémence area (Western Swiss Alps). *Norwegian Journal of Geography*, 55(4):219–223.

Lambiel, C., Reynard, E., G., C., and Lugon, R. (2004). Distribution du pergélisol dans un versant instable, le cas de Tsarmine (Arolla, Evolène, VS). *Bulletin de la Murithienne*, 122:89–102.

Lambrech, A., Mayer, C., Hagg, W., Popovnin, V., Rezepkin, A., Lomidze, N., and Svanadze, D. (2011). A comparison of glacier melt on debris-covered glaciers in the northern and southern Caucasus. *Cryosphere*, 5:525–538.

Lane, S. N., James, T. D., and Crowell, M. D. (2000). Application of digital photogrammetry to complex topography for geomorphological research. *The Photogrammetric Record*, 16(95):793–821.

Lane, S. N., Tayefi, V., Reid, S. C., Yu, D., and Hardy, R. J. (2007). Interactions between sediment delivery, channel change, climate change and flood risk in a temperate upland environment. *Earth Surface Processes and Landforms*, 32(3):429–446.

Lane, S. N., Westaway, R. M., and Murray Hicks, D. (2003). Estimation of erosion and deposition volumes in a large, gravel-bed, braided river using synoptic remote sensing. *Earth Surface Processes and Landforms*, 28(3):249–271.

Lane, S. N., Widdison, P. E., Thomas, R. E., Ashworth, P. J., Best, J. L., Lunt, I. A., Sambrook Smith, G. H., and J., S. C. (2010). Quantification of braided river channel change using archival digital image analysis. *Earth Surface Processes and Landforms*, 35(8):971–985.

Matsouka, N. (2008). Frost weathering and rockwall erosion in the southeastern Swiss Alps: long-term (1994-2006) observations. *Geomorphology*, 99(1-4):353–368.

MeteoSwiss (2014). Climate Today: Trends in Switzerland. Technical report, Federal Office of Meteorology and Climatology Meteoswiss, Zürich http://www.meteoswiss.admin.ch/home/climate/present-day/climate-trends.html [Accessed; 1st December 2014].

Micheletti, N., Chandler, J. H., and Lane, S. N. (2015). Application of archival aerial photogrammetry to quantify climate forcing of alpine landscapes. *The Photogrammetric Record*, 30(150):143–165.

Montgomery, D. R. and Stover, S. C. (2001). Channel change and flooding, Skokomish River, Washington. *Journal of Hydrology*, 243(3-4):272–286.

Müller, J., Gärtner-Roer, I., Kenner, R., Thee, P., and Morche, D. (2014). Sediment storage and transfer on a periglacial mountain slope (Corvatsch, Switzerland). *Geomorphology*, 218:35–44.

Oliva, M. and Ruiz-Fernandez, J. (2015). Coupling patterns between para-glacial and permafrost degradation responses in Antarctica. *Earth Surface Processes and Landforms*, 40(9):1227–1238.

Pelto, M. S. and Hedlund, C. (2001). Terminus behavior and response time of North Cascade glaciers, Washington, USA. *Journal of Glaciology*, 47:497–506.

PERMOS (2013). Permafrost in Switzerland 2008/2009 and 2009/2010. Noetzli, J., Naegeli, B., and Vonder Muehll, D. (eds.). *Glaciological Report (Permafrost) No. 10/11 of the Cryospheric Commission of the Swiss Academy of Sciences*, :80.

Phillips, J. D. (2003). Sources of nonlinearity and complexity in geomorphic systems. *Progress in Physical Geography*, 27(1):1–23.

Phillips, J. D. (2009). Changes, perturbations, and responses in geomorphic systems. *Progress in Physical Geography*, 33(1):17–30.

Reynard, E., Lambiel, C., and Lane, S. N. (2012). Climate change and integrated analysis of mountain geomorphological systems. *Geographica Helvetica*, 1-2:5–14.

Roer, I., Haeberli, W., Avian, M., Kaufmann, V., Delaloye, R., Lambiel, C., and Kääb, A. (2008). Observations and considerations on destabilizing active rock glaciers in the European Alps. In *Proceedings of the Ninth International Conference on Permafrost*.

Roer, I., Kääb, A., and Dikau, R. (2005). Rockglacier kinematics derived from small-scale aerial photography and digital airborne pushbroom imagery. *Zeitschrift für Geomorphology*, 49:73–87.

Rumsby, B. T. and Macklin, M. G. (1994). Channel and floodplain response to recent abrupt climate change: The Tyne basin, northern England. *Earth Surface Processes and Landforms*, 19(6):499–515.

Schaefli, B., Hingray, B., Niggli, M., and Musy, A. (2005). A conceptual glacio-hydrological model for high mountainous catchments. *Hydrology and Earth System Sciences*, 9:95–109.

Schaefli, B. and Huss, M. (2011). Integrating point glacier mass balance observations into hydrologic model identification. *Hydrology and Earth System Sciences*, 15:1227–1241.

Schwab, M., Rieke-Zapp, D., Scheider, H., Liniger, M., and Schlunegger, F. (2008). Landsliding and sediment flux in the Central Swiss Alps: A photogrammetric study of the Schimbrig landslide, Entlebuch. *Geomorphology*, 97(3-4):392–406.

Shroder, J. F. ad Bishop, M. P., Copland, L., and Sloan, V. F. (2000). Debris-covered Glaciers and Rock Glaciers in the Nanga Parbat Himalaya, Pakistan. *Geografika Annaler: Serie A, Physical Geography*, 82(1):17–31.

Staines, K. E. H., Carrivick, J. L., Tweed, F. S., Evans, A. J., Russell, A. J., Johannesson, T., and Roberts, M. (2015). A multi-dimensional analysis of pro-glacial landscape change at Sólheimajökull, southern Iceland. *Earth Surface Processes and Landforms*, 40(6):809–822.

Takeuchi, Y., Kayastha, R. B., and Nakawo, M. (2000). Characteristics of ablation and heat balance in debris-free and debris-covered areas on Khumbu Glacier, Nepal Himalayas, in the pre-monsoon season. In *Debris-Covered Glaciers*.

Thomas, M. F. (2001). Landscape sensitivity in time and space - an introduction. *Catena*, 42(2-4):83–98.

Tobin, C., Nicotina, L., Parlange, M. B., and Berne, A. Rinaldo, A. (2011). Improved interpolation of meteorological forcings for hydrologic applications in a Swiss Alpine region. *Journal of Hydrology*, 401:77–89.

Vacher, P., Dumoulin, S., Morestin, F., and Mguil-Touchal, S. (1999). Bidimensional strain measurement using digital images. *Proceedings of the Institution of Mechanical Engineers*, 213(8):811–817.

VAW Laboratory of Hydraulics, H. and Glaciology (2013). Glaciological reports (1881-2015). "The Swiss Glaciers", Yearbooks of the Cryospheric Commission of the Swiss Academy of Sciences (SCNAT) . Technical report, ETH Zürich (http://glaciology.ethz.ch/swiss-glaciers).

Walstra, J., Dixon, N., and Chandler, J. H. (2007). Historical aerial photographs for landslide assessment: two case histories. *Quarterly Journal of Engineering Geology and Hydrogeology*, 40(4):315–332.

Wangensteen, B., Gudmundsson, A. Eiken, T., Kääb, A., Farbrot, H., and Etzelmüller, B. (2006). Surface displacements and surface age estimates for creeping slope landforms in Northern and Eastern Iceland using digital photogrammetry. *Geomorphology*, 80(1-2):59–79.

Warner, R. F. (1987). *River channel changes, environment and process*, chapter Spatial adjustment to temporal variations in flood regime in some Australian Rivers, pages 14–40. Basil Blackwell, Oxford.

8 Water yield and sediment export in small, partially glaciated Alpine watersheds in a warming climate

Natan Micheletti, Stuart N. Lane

Context

This contribution deepens the findings of Chapter 7 on climate forcing of Alpine landscapes by exploring water yield and sediment exports in two partially glaciated watersheds. Equivalently, archival imagery is used to reconstruct surface change at decadal scale. Furthermore, we employ a long term record, beginning in the early 1960s, of sediment export based upon the flushing from hydroelectric power intakes. Results unveil enhancement of sediment export, possibly caused by water yield increase by means of glacier retreat and snowmelt contributions. However, the flows in the watersheds appear in supply-limited conditions, suggesting a key role of the ineffectiveness of the sediment cascade. Crucially, extreme events seem to be necessary to overcome transport limitation and permit sediment delivery at the outlets.

In the context of this thesis, this piece of research represents a fundamental contribution to our understanding of the dynamics of Alpine watersheds in the face of climate warming.

Chapter 8. Water yield and sediment export in small, partially glaciated Alpine watersheds in a warming climate

Abstract

Climate change is expected to modify the hydrological and geomorphological dynamics of mountain watersheds significantly, so impacting on downstream water yield and sediment supply. However, such watersheds are often poorly instrumented, making it difficult to link recent and rapid climate change to landscape response. Here we combine unique records of river flow and sediment export, with historical archival imagery to test the hypothesis that climate warming has substantially increased both water yield and sediment export from small Alpine watersheds ($< 3 \text{ km}^2$) characterized by small ($< 0.5 \text{ km}^2$ surface) glaciers. To examine ice and landform response to climate change, we apply archival digital photogrammetry to historical aerial imagery available from 1967 to present. We use the resulting data on ice loss, in combination with reliable records of stream flow from hydroelectric power intakes and climate data to approximate a water budget and to determine the evolution of different contributions to river flow. We use the stream flow records to estimate volumetric sediment transport capacity and compare this with the volumes of sand and gravel exported from the watersheds, quantified from records of intake flushing. The data show clearly that climate forcing since the early 1980s has been accompanied by a net increase in both water yield and sediment transport capacity, and we attribute these as signals of reduced snow accumulation and glacier recession. However, sediment export has not responded in the same way and we attribute this to limits on sediment delivery to streams because of poor rockwall-hillslope-channel connectivity. However, we do find that extreme climate conditions can be seen in sediment export data suggesting that these, rather than mean climate warming, may dominate watershed response.

Keywords: water yield; sediment export; climate change; sediment connectivity; hydroelectric power infrastructures; archival photogrammetry

8.1   Introduction

Under rapid glacier recession [Knight and Harrison, 2009; Bolch et al., 2012; Fischer et al., 2014] and the significant modification of the associated flow regimes [Jasper et al., 2004; Huss et al., 2008; Farinotti et al., 2012], hydrological and geomorphological dynamics in Alpine landscapes may be highly sensitive to climate warming. The consequences of recent temperature increases and shifts in precipitation patterns on the hydrological regimes of high mountain watersheds have been investigated (e.g. Stahl et al. [2008]; Weber et al. [2010]; Finger et al. [2012]). They suggest that watersheds with a high degree of glaciation are likely to experience an increase in annual runoff as an initial response to rapid climate warming due to ice melt, followed by an evolution to greater precipitation dependence as the percentage of the watershed that is ice occupied decreases. There have been fewer attempts to quantify what these changes might mean for sediment production and export, partly because such data are rarely available at the decadal timescale, but with some exceptions [Raymond Pralong et al., 2015; Lane et al., 2016].

Yet, Alpine watersheds undergoing rapid glacier recession and permafrost degradation may also have substantially different rates of sediment production and transfer. Glacier recession may: (1) increase the length of proglacial stream able to erode laterally [Leggat et al., 2015; Lane et al., 2016]; (2) increase downstream sediment flux rates because streams transport sediment more rapidly than glaciers [Østrem, 1975; Hunter et al., 1996; Lane et al., 1996; Orwin and Smart, 2004; Morche et al., 2012; Geilhausen et al., 2013; Baewert and Morche, 2014]; and (3) lead to debuttressing of valley sidewalls [Porter et al., 2010] and the headward extension of sidewall tributaries (e.g. Schiefer and Gilbert [2008]), and hence better hillslope to proglacial stream connectivity. Thus, the transition from glacial to paraglacial conditions should increase sediment export [Knight and Harrison, 2009; Slaymaker, 2009]. Alpine watersheds may also have extensive permafrost cover and permafrost decay may increase sediment production rates (e.g. Kääb et al. [2007]; Harris et al. [2009]; Sass and Oberlechner [2012]; Deline et al. [2015]). Taken together, these processes imply that at least at first, in response to rapid warming, Alpine watersheds are likely to increase sediment export [Warburton, 1990; Huggel et al., 2010; Keiler et al., 2010; Bennett et al., 2013; Geilhausen et al., 2013; Micheletti et al., 2015b]. This has been shown by Lane et al. (2016) for the case of rapid retreat of a valley glacier. However, there are few other studies of this effect, not least because of the lack of reliable quantitative data on sediment export. More importantly, Lane et al. [2016] did not consider the effects of recession of smaller, hillslope attached glaciers. These are likely to involve different responses to valley glaciers because of greater topographic relief, a strong influence of glacial landform history (e.g. moraines), a stronger rock wall influence on sediment supply and on levels of snow accumulation (e.g. by avalanches), and generally reduced glacier dynamics [Kuhn, 1995; Grunewald and Scheithauer, 2010; Bosson et al., 2015; Capt et al., 2016].

Thus, the aim of this paper is to quantify the relationships between the evolution in annual water yield and coarse sediment flux from small partially glaciated Alpine watersheds and climate forcing at the decadal scale. Specifically, we hypothesize that: (1) under rapid glacier recession, and notwithstanding possible changes in precipitation and snowmelt conditions, climate warming should lead to increases in annual water yield; (2) as a consequence, and because river flows in glaciated watersheds are commonly close to the threshold for sediment transport during summer months, an increase in the sediment transport capacity of proglacial streams should occur; and (3) an increase in watershed sediment export should follow. Undertaking the latter is a particular challenge because it is extremely difficult to measure coarse sediment transport and we have almost no decadal-scale monitoring systems in Alpine glaciated watersheds designed for this purpose. In this paper, we make use of unique datasets provided by hydroelectric power intakes, which need to be flushed of sediment regularly, to construct annual to decadal scale sediment export. These data are combined with the quantitative analysis of historical aerial imagery based upon digital photogrammetry and climatic and meteorological data to address the three hypotheses above.

8.2   Methodology

The case studies for this research are two small and partially glaciated watersheds located in Arolla, in the Hérens Valley, in the South-western part of the Swiss Alps: the Douves Blanches and Bertol watersheds (Figure 8.1). These watersheds were chosen because as a result of hydroelectric power regulation since the 1960s, and because of strict regulatory requirements, they have an extremely reliable record of streamflow as well as, through the need to flush the associated water intakes, a record of sediment export from each watershed. The overall methodological approach is centred on the fact that, through the analysis of hydroelectric power data, it is possible to estimate with high confidence annual water yield and sediment export from a watershed. Coupling the evolution of these data with climatic indicators and meteorological extremes might unveil a possible correlation between sediment export at the intake and temperature and precipitation forcing. More specifically, high frequency, heavy rainfall events are suspected to play a critical role in starting sediment mobilization.

However, such correlation needs to be accompanied by studies of the geomorphic processes occurring within individual watersheds, which conditions such climate-export linkage. Thus, we also analyze digital elevation data, historically and specially flown. Unlocking the information contained in archival aerial imagery, commonly acquired from national agencies since the 1950s, represents a unique opportunity to derive data on past landscape history and erosion and deposition within a watershed. It can also provide detailed measurement of glacier dynamics that, coupled with the previously-mentioned climatic data, can lead to insights on the contribution to stream flow by different sources, and its alteration in time. The detailed runoff measurements available can be linked to volumes of sediment export, notably using estimations of flow transport capacity, to verify if the proglacial streams in the area are transport-limited or supply-limited, hence allowing a deeper interpretation of the sensitivity of geomorphic dynamics to climate forcing. Finally, by obtaining a specially-flown high resolution DEM, quantitative analysis of within watershed connectivity, which may impact on sediment flux and hence sediment export, is possible.

8.2.1   Watershed characteristics

The two study watersheds are located in lateral, suspended valleys with a watershed area of 1.01 and 2.51 km^2 respectively (Figure 8.2). They both contain small glacial systems and an assemblage of landforms typical of Alpine mountain watersheds. In addition to glaciers, of particular interest for this study are the widely present sediment sources and stores: rockwalls (most likely in a permafrost state at this altitude and orientation [PERMOS, 2009]), various sites prone to form debris-flows, large amounts of loose sediment in steep talus slopes and in proglacial areas, landforms related to past glaciation (notably moraines) and, in the case of Bertol, rock glaciers. The two watersheds share their highest peak, the Pointes des Douves Blanches (3642 m a.s.l.), and are both limited in their lower part by intakes for water retention at 2400 m a.s.l., setting the elevation range of the study area at 1200 m. Reflecting the availability of the data at our disposal, the period of study is from the end of the 1960s to 2014.
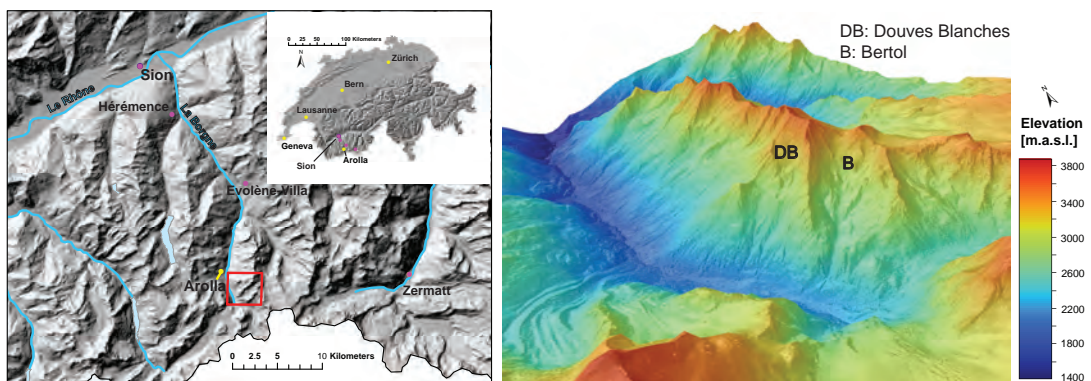
Figure 8.1 – The Douves Blanches and Bertol case studies in Arolla, Hérens Valley, Switzerland (Relief shaded and river data: Swisstopo). The purple dots indicate meteorological stations near the sites of study.
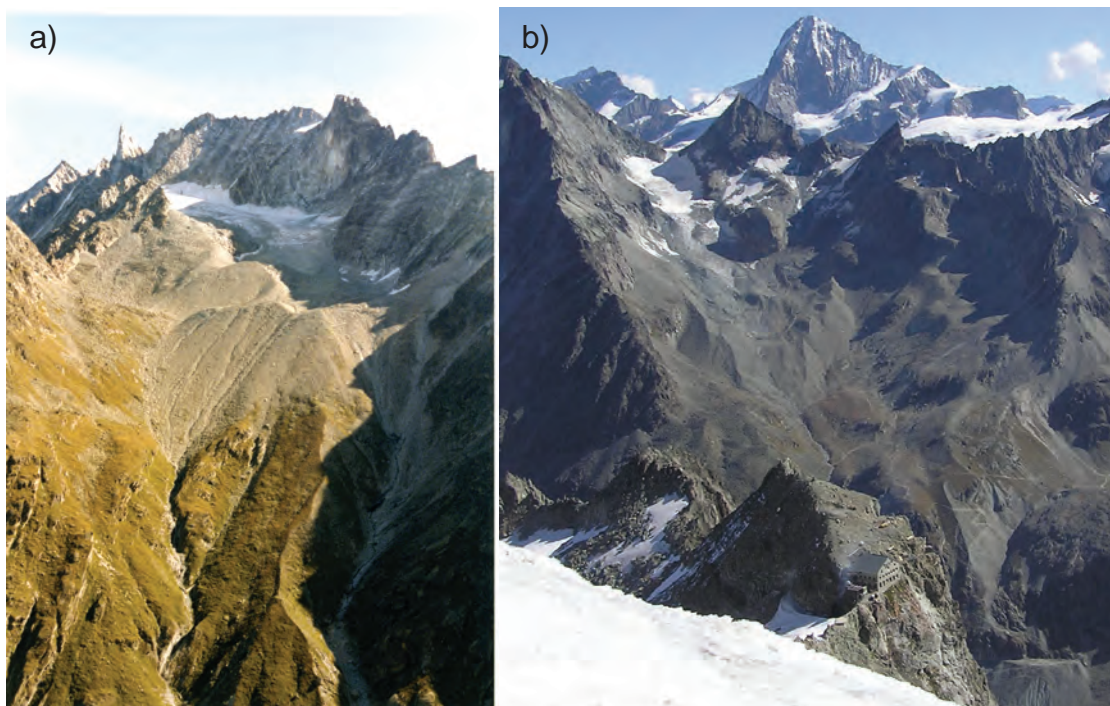
Figure 8.2 – Photograph of the Douves Blanches watershed and its steep channel, with water flow interrupted by water intakes visible on the lower right corner (a, Bezinge 1991), and of the Bertol watershed with the intake not visible because it is located behind the Vignette hut (b, http://www.chamonix-guides.com).

8.2.2 Climate and meteorological data

A detailed description of the climatic conditions that affected the region during the last 50 years is provided by Micheletti et al. [2015b]. Mean Annual Air Temperature (MAAT) data for Sion (24 km from Arolla) suggest two distinct periods in relation to temperature (Figure 8.3).

159
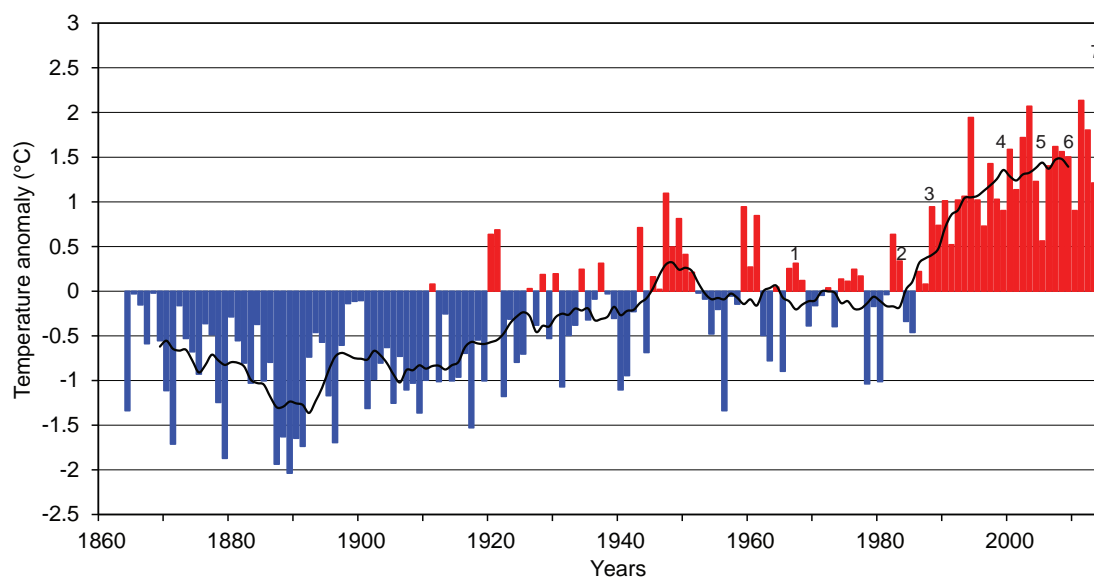
Figure 8.3 – Mean Annual Air Temperature (MAAT) in Sion (24 km from Arolla) between 1864 and 2014 as deviation from the reference mean established between 1961 and 1990, with the 10 year moving average. The numbers signal the years with available aerial imagery. Data: Swiss Federal Office of Meteorology and Climatology MeteoSwiss (www.meteoswiss.admin.ch).

During the 1960s and up to the early 1980s, temperature was relatively steady and slightly cooler than the previous decade. This was followed by rapid warming from the mid-1980s to present. To identify the hottest years, the 15% highest values of MAAT have been identified. With the exception of 1994, all occur since 2000.

Annual rainfall data from nearby stations show a decrease of precipitation between the end of the 1960s and the beginning of the 1970s, followed by a considerable increase in the second part of the 1970s (Figure 8.4). From the 1980s, after a modest decrease, annual precipitation has remained relatively stable, with a 30 year mean of 730 mm per year. Of particular interest are the two meteorological stations located nearest to the watersheds. In Hérémence, c. 15 km north of the watersheds at 1238 m a.s.l., a rain gauge measured annual rainfall for the whole period of interest. The Evolène-Villa meteorological station (1826 m a.s.l.) is only 9 km north of the watersheds and hence likely to be more representative of their conditions; its data are available from 1987. The comparison between Hérémence and Evolène-Villa annual rainfall data shows that an elevation-based precipitation gradient is not present. Rather, contrariwise, it is in Evolène-Villa that lower values of annual precipitation are recorded (see also Figure 8.4), although the difference is very small (-39±76 mm per year). The absence of an elevation-based gradient is likely to be explained by the sheltering from the mean atmospheric disturbances and rain-bearing systems provided by the Alpine barrier to the upper part of the Hérens valley [Lambiel et al., 2016].
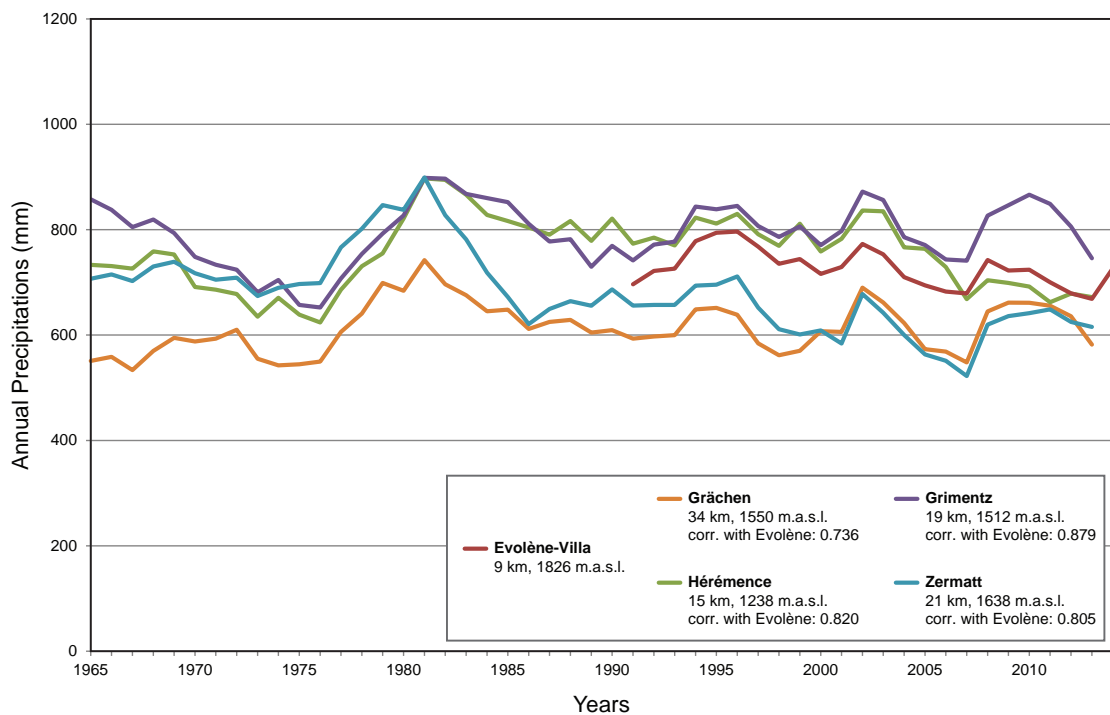
Figure 8.4 – Annual precipitation for meteorological stations located near Arolla (5 year moving average). In the legend, altitude and distance from Arolla and the correlation 1987-2014 with Evolène-Villa are shown. Data: Swiss Federal Office of Meteorology and Climatology MeteoSwiss (www.meteoswiss.admin.ch).

To identify the most important rainstorms in the area, we isolated single events from the Evolène-Villa timeseries on the basis of 72 hours precipitation totals. As with temperature, we considered the highest 15% of these as extreme events; these occurred in 4 years (February 1990, December 1991, September 1993, October 2000). Given their months of occurrence, at least half of them can be considered rain-on-snow events, thus potentially of high impact. However, data in Evolène-Villa only cover the 1987-2014 period and so we also considered data for Hérémence, given their similarity. By applying the same 15% criteria to 72 hours precipitation totals, the most intense rainstorms are identified (November 1968, December 1981, November 1983, May 1985, February 1990, December 1991, October 2000). Rainstorms identified in Héremence coincide with those in Evolène-Villa when data overlap, which is encouraging for their representativeness.

General information about snow cover in the area is available in Micheletti et al. [2015b] in the form of basic snow depth modelling. For the elevation concerned, a progressive decline in snow depth at the end of the accumulation season (31 March) is observed from the early 1980s, while permanent snow cover at the end of the ablation season is present only between the mid-1970s and the mid-1980s (30 September, see Figure 5 in Micheletti et al. [2015b] for details).

8.2.3 Archival aerial photogrammetry

High resolution (1m) digital elevation models (DEMs) for seven dates were generated for the Douves Blanches and Bertol watersheds following methods presented in Micheletti et al. [2015a,b]. Aerial photographs were acquired by the Swiss Federal Office of Topography (Swisstopo, www.swisstopo.admin.ch) and by Flotron AG (www.flotron.ch) and were provided with the corresponding camera calibration certificates. Swisstopo used a photogrammetric-quality device to scan their images (23 cm x 23 cm) at a resolution of 14 μm (1814 dpi). The Flotron images comprised 14,430 x 9,420 pixels with a 7.2 μm resolution. The ground control points (GCPs) necessary for photogrammetric restitution were collected by the authors using two Leica System 500 differential GPS units and were corrected using Automated GNSS Network for Switzerland (AGNES) data. The digital photogrammetry tasks and the necessary post-processing operations were performed on ERDAS IMAGINE 2014, Matlab 2013 and ESRI ArcGIS 10.1. To perform a quantitative comparison, DEMs of Difference (DoD) were computed by subtracting pairs of DEMs of different years. To ensure that the observed differences comprised real morphological change and not random errors, the error propagation proposed by Lane et al. [2003] was adopted. The quality of the DEMs was evaluated using the unused dGPS measurements (as in Lane et al. [2000]) and was bias corrected. The Limit of Detection of change (LDC) with a confidence limit of 90% was then estimated, and was between ±0.75 m and ±1.45 m according to the DEMs being compared. The analysis allows the identification and quantification of significant elevation change for every epoch. Details of the aerial photographs, the derived DEMs quality and error propagation are presented in Table 7.1. A full description of the data analysis procedure is available in Micheletti et al. [2015a,b] for a different study site.

Table 8.1 – Characteristics of the aerial imagery available from Swisstopo (1967-2009) and Flotron AG (2014), photogrammetric triangulation performance [Total Image Unit Weight] and DEM precision and accuracy assessment using dGPS survey data [m].

Date	Scale	Camera Type	Emulsion	Δ TIUW RMSE	μ_{DEM}	σ_{DEM}
1967/09	1:15,700	Frame	BW	0.349	0.42	±0.57
1983/09	1:20,900	Frame	BW	0.284	0.44	±0.67
1988/09	1:22,200	Frame	BW	0.327	0.24	±0.58
1999/09	1:26,000	Frame	RGB	0.204	0.23	±0.36
2005/08	1:24,000	Frame	RGB	0.260	0.37	±0.33
2009/09	1:13,000	Frame	BW	0.245	0.23	±0.35
2014/10	1:5,200	Digital	RGB-NIR	0.179	0.08	±0.31

8.2.4 Long term records of hydroelectric power intake activity

The Douves Blanches and Bertol watersheds are part of the hydroelectric power scheme managed by the Grand Dixence SA company. At the outlet of each watershed, an intake structure retains all water (and sediments) leaving the system (there is no minimum flow

requirement associated with this concession). These intakes are called Douves Blanches and Upper Bertol respectively [Bezinge et al., 1989]. The water collected is transferred to a retention lake in an adjacent valley, the Lac des Dix, which has a storage capacity of 400 million m^3 [Raymond Pralong et al., 2015]. The two watersheds investigated contribute a mean annual runoff volume (1967-2014) of 1.15 million and 3.04 million m^3, which corresponds to a runoff per unit area of 1190 mm per year. In order to maintain hydraulic efficiency, sediment has to be separated from the water before the transfer. Thus, the intakes are designed to trap the solid charge in the sand and coarser fractions (see Bezinge et al. [1989] for details). Once full, the intakes are systematically flushed (purged) in order to evacuate the sediments [Morris and Fan, 1998; Raymond Pralong et al., 2015].

Hydroexploitation SA operates the Douves Blanches and Upper Bertol intakes on behalf of Alpiq SA and Grande Dixence SA, and provided continuous 15 minutes resolution flow records from the end of the 1960s. Given the strict regulatory requirements that the company must satisfy, the measurement uncertainty in these timeseries is negligible. During a purge, water is no longer taken in and instead used to flush the intake. This diverts water away from the discharge recorder and is manifest as a sudden drawdown in the flow record lasting for between 30 minutes and one hour. Following Bezinge et al. [1989] and Lane et al. [2016], each intake opening was manually identified so to reconstruct the number of purges that occurred each year. Periods of purge were removed and replaced by linear interpolation using values either side of the purge (see Lane et al. [2016]). The fact that purges generally occur in periods of high glacial runoff makes them easy to identify, aiding this process. Figure 8.5 illustrates an example of hydrograph prior (a) and after (b) purge removal for the Douves Blanches watershed. Although the Douves Blanches watershed is c. 29% glaciated, the flow regime is classed as *Glacial-nival (type a)* following Weingartner and Aschwanden [1994] (see also Gabbud and Lane [2016]); a first peak due to snowmelt is normal before the 1 June in any hydrological year. Flow is then sustained by glacier melt until its highest values in late July and early August. The Bertol watershed has similar patterns, and has also a *Glacial-nival (type a)* regime with 19% of its surface being glaciated (Gabbud and Lane [2016], Table 1).

The frequency of the flushing operation, associated with estimates of the mean of material evacuated in each purge and its uncertainty, have commonly been used to estimate sediment transport volumes (e.g. Wold and Østrem [1979]; Bezinge et al. [1989]; Lane [1997]; Raymond Pralong et al. [2015]; Lane et al. [2016]). In our case, Bezinge et al. [1989] estimated the mean volume of material evacuated with each purge based on the design volume of the associated sediment traps of 20 m^3 for Douves Blanches and 15 m^3 for Upper Bertol. However, these values need to be corrected for packing density effects. Field investigations for two intakes in the region provided end member estimations of 1.300 and 1.630 tonnes per m^3 respectively [Bezinge et al., 1989]. These two packing densities are adopted as end members in evaluations of sediment export volumes to correct for filling effects, in conjunction with estimated sediment density (2,650 kg/m^3, Lane et al. [2016]). Both water intakes are equipped with single traps for sediment and so distinguishing the proportions of fine (suspended) and coarse (bedload) material is not possible. However, these traps do retain all the sediment
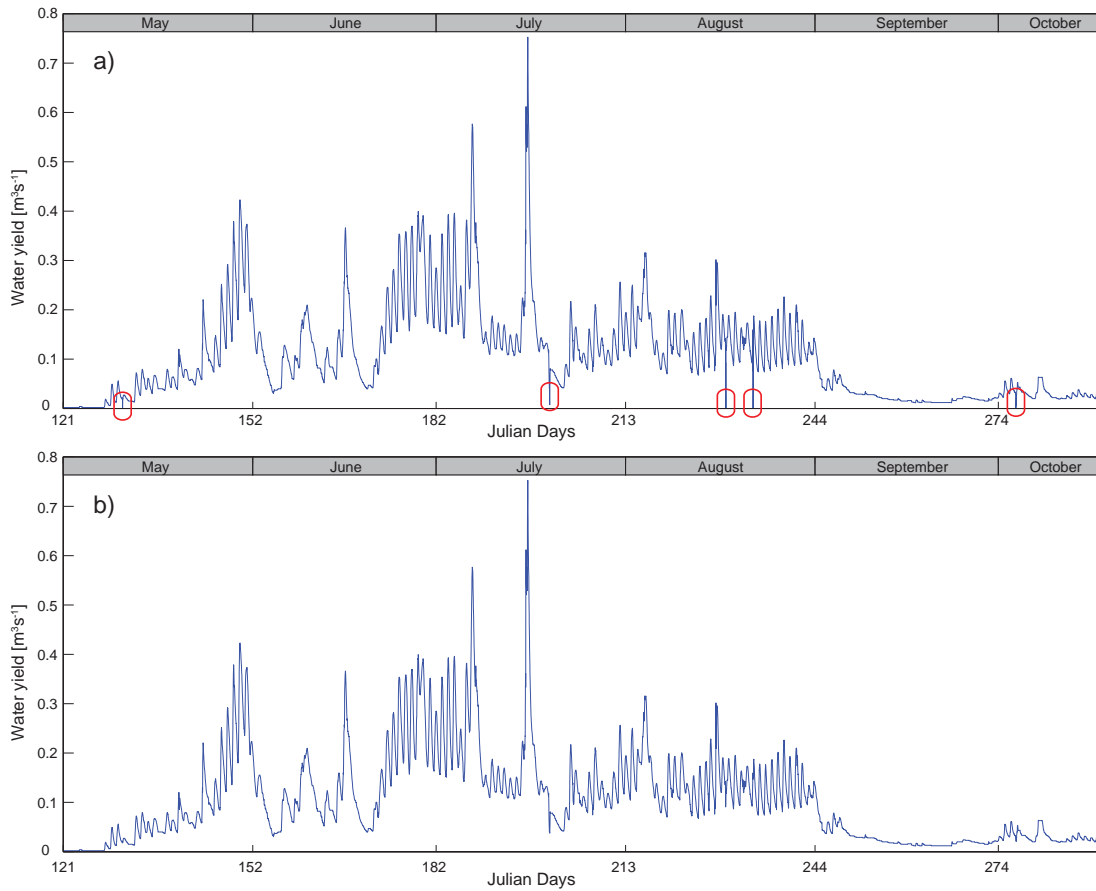
Figure 8.5 – Example of data provided by Hydroexploitation SA illustrating hydrographs (a) prior and (b) after purge removal (Douves Blanches intake, year 2001, five purges identified).

except the washload that is, only particles finer than sand are not trapped.

8.2.5   Contribution to water yield at the intakes

The stream flow allowed us to quantify annual water yield and also provided the input into our estimates of sediment transport capacity. However, in order to link the changing volume of ice in the watersheds to the water yield it was necessary to consider other water inputs. A basic water balance equation for Alpine watersheds was used:

$$Q = P + \Delta_{ICE} + \Delta_{SNOW} + \Delta_{PF} - E - I \tag{8.1}$$

where Q is runoff (or water yield) at the intake, P is rainfall, Δ_{ICE} is water equivalent of icemelt, Δ_{SNOW} is the snow budget (water equivalent of snowfall - snowpack at the end of the ablation period), Δ_{PF} is water flow from permafrost-related landforms (e.g. rock glaciers), E is evapotranspiration and I is water infiltration. The annual yield of water Q should be knowable

with a reasonable level of confidence from integration through time of the hydrological records (e.g. Figure 8.5). However, initial inspection of the Bertol data gave us some cause for concern: between 1968 and 1985 the values of water yield were unrealistically high when expressed as runoff per unit area per year, in comparison with other years of Bertol data and comparison with Douves Blanches (Figure 8.6). To address this problem we determined the average Bertol to Douves Blanches runoff ratio for the period 1986-2014 and applied this to the Douves Blanches data for 1968-1985 to estimate the Bertol data. We attribute the error to instrument calibration and note that it should not impact the purge record, only the runoff record. Assessment of the fit (i.e. the mean ratio of the calculated Bertol record as compared with the measured Bertol record) suggested a mean error in water yield of -0.03 million of m^3yr^{-1}.
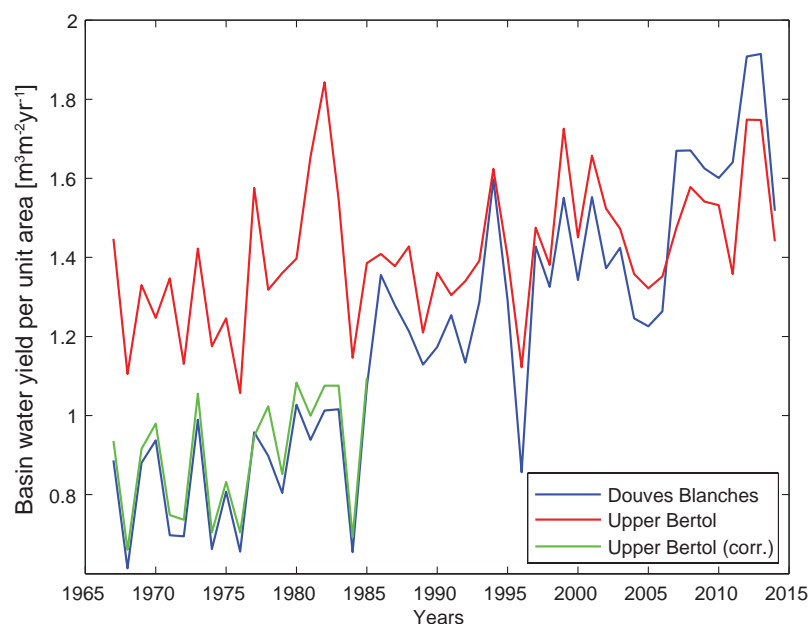
Figure 8.6 – Unrealistic annual water yield per unit area registered until 1985 at the Upper Bertol intake and comparison with Douves Blanches data. The green line represents the corrected water yield for the period 1967-1985.

It is possible to derive ice melt (Δ_{ICE}) directly. Following Micheletti et al. [2015b], we identified glacier and debris-covered glacier surfaces from a geomorphological map and computed volumes of change from DoDs. This operation is considered reliable because the data for the DEMs is systematically acquired at the end of the summer, hence comparable (Table 7.1). To estimate the uncertainty in ice melt volume calculations, we multiplied the Limit of Detection of change (LDC) for a single pixel (1m x 1m, hence $1m^2$) with a confidence limit of 90% with the area of extent occupied by glaciers and debris-covered glaciers. To account for the different density of ice and water, the conversion factor of 850±60 kgm^{-3} proposed by Huss [2013] is used for ice volume calculations.

The estimation of rainfall contribution (P) is accounted using precipitation data from the

closest station to the study site that include the whole period of study (Hérémence, 15 km from Arolla, Figure 8.4). The comparison with Evolène-Villa, which theoretically represents the most representative site available, shows that an elevation-based precipitation gradient is not present, and that annual totals are very similar. Accordingly, Hérémence can be used as an appropriate proxy for annual precipitations in the watersheds. The amounts of rainfall for each period are multiplied by the surface of each watershed to derive the volume of water that entered the watersheds this way. To account for uncertainty, we employ the standard deviation of the discrepancy between Evolène-Villa and Hérémence annual precipitation (± 76 mm, see 8.2.2) and we multiplied it with the area of the watersheds.

The estimation of volumes of water for the other terms in Equation 8.1 is subject to large uncertainty and would require speculation with the data at our disposal. Thus, we employ the two adequately well known water sources (precipitation and ice-melt) and observe the decadal-scale evolution of their contribution to water yield. We assume that over the time period of this study evapotranspiration and water infiltration is not significantly changing at the scale of investigation. There is almost no vegetation cover in either basin. Given the lack of soil to store water, evaporation is likely to be limited by water availability rather than temperature. This leaves the contribution of snowmelt and runoff from permafrost-related landforms which is assumed to fill the discrepancy between Q and the sum of P and Δ_{ICE} (with their related uncertainties). Despite the relatively severe assumptions we make in this analysis, as well as uncertainties in some of the data sources, this approach is deemed appropriate for investigating the evolution of the relative contribution of ice melt to river flow during the period of study.

8.2.6   Estimation of river sediment transport capacity

Changes in water yield should translate into changes in river sediment transport capacity. Thus, a primary interest in this work is whether or not sediment export tracks this changing transport capacity. If it does, then we can conclude that sediment export is currently limited by stream sediment transport capacity. If the transport capacity calculation is correct, where capacity is greater than export, the river should either erode or coarser its bed: that is, the grain size used in the capacity calculation should coarsen. We do not represent this dynamic process in the analysis, but rather use the capacity-export discrepancy as a measure of sediment supply limitation. The testing of this model has been based upon a large number of transport-limited sites [Nitsche et al., 2011] and so we take the model as being reliable for the application. That said, estimating sediment transport capacity is highly uncertain. Thus, our aim is not to obtain precise estimates of sediment transport capacity but rather to transform our discharge time series into a variable that can represent the variability in sediment transport capacity and then to relate this to changes in sediment export. Such a transformation is needed because sediment transport is a threshold-dependent process and water yield should not be linearly nor directly related to sediment export.

To estimate sediment transport capacity, we developed an approach evaluated for instrumented Swiss watersheds by Nitsche et al. [2011]. Its application to this kind of watershed is explained in detail in Lane et al. [2016] and only a summary is provided here. It follows Ferguson [2007] in estimating the relationship between discharge, water level and velocity, and hence shear stress; and Rickenmann and Recking [2011] in dividing available shear stress into that lost to resistance and that which can be used to transport sediment. The result is an estimate of the volumetric transport rate per unit channel width. The model was applied using the corrected flow data presented in Section 8.2.4. To run the model, the geometry of the channel and its slope were derived from the 2014 DEM. In Bertol, channel slope is measured as 0.302. Douves Blanches has an even steeper condition because it corresponds to a torrential system below a Little Ice Age moraine crest (see Figure 8.2), and is measured from the DEM at 0.633. In the absence of grain size data (notably for Douves Blanches, which is difficult and dangerous to access), the regression equations proposed by Raymond Pralong et al. [2015], calibrated for Swiss Alpine watersheds in the region, were used. In Bertol, it was estimated that $D_{50} = 0.075$ m and $D_{84} = 0.243$ m, while in Douves Blanches $D_{50} = 0.092$ m and $D_{84} = 0.319$ m. Although these values are evidently uncertain, they are realistic given the watershed appearance and slope and it is reasonable to assume that they are representative of the bed grain size through time.

Volumetric transport rates were integrated to obtain the annual volumetric transport capacity. As in Lane et al. [2016], a calibration on the sediment flushing estimates was not performed as it is believed that release volumes are dependent not only on transport capacity, but also on sediment supply, which is in turn controlled by connectivity and efficiency of the sediment cascade. For Bertol, given the need to scale the flow for data before 1986, we only apply the model from 1986.

8.2.7 Within-watershed connectivity

In order to attempt to understand the relative balance of modelled transport capacity and sediment export we also aimed to identify the extent to which upstream sources of sediment were connected to the stream channel. It is well known that sediment flux at watershed outlets can be reduced or damped because of the presence of barriers or obstacles created by topographic complexity or surface roughness (e.g. Caine and Swanson [1989]; Harvey [2002]; Heckmann and Schwanghard [2013]; Micheletti et al. [2015b]). The coupling between sediment source areas and the stream network can be of fundamental importance in controlling if and how sediment transport capacity is actually realized and solid charge is delivered downstream, in our case to the water intakes. In order to investigate this aspect and assess spatial patterns of sediment connectivity, we compute a Connectivity Index (CI) based on the approach of Borselli et al. [2008], following Cavalli et al. [2013]. This geomorphometric index has been widely used in geomorphological studies (e.g. Foerster et al. [2014]; Heiser et al. [2015]). The toolbox developed by Cavalli et al. [2013] and freely available at www.sedalp.eu was adopted. The latter is designed for ESRI ArcGIS 10.1 and requires the use of the Tarboton TauDEM

functions (hydrology.usu.edu/taudem). Here, the most recent DEM available, with filled pits, was used as input. The CI can be computed with the consideration of a weighting factor, introduced by Borselli et al. [2008] to model the impedance to runoff and sediment fluxes due to properties of the local land use and soil surface. In our case, this impedance is mainly defined by apparent roughness, e.g. the difference between a smooth surface or a field of boulders in allowing mass fluxes. Accordingly, we computed a Roughness Index as described in Cavalli and Marchi [2008] that is, by calculating the standard-deviation (5x5 pixels) of the residual topography (defined as the difference between the original DEM and an averaged DEM using a 5x5 pixel moving window). The CI is computed by evaluating the connection with respect to one or multiple targets. In this study we are considering sediment export, hence the targets were set to be the watersheds outlets (the water intakes). In addition, in Douves Blanches the steep rockwalls have been masked out to avoid misleading interpretation, as we consider that material sourced in these zones is most probably likely to reach the base of their slopes and hence the analysis of the Connectivity Index is not justified for that area. Since the Connectivity Index is defined in the range of $[-\infty, +\infty]$ [Cavalli et al., 2013], the result is presented relatively in terms of high or low index, where high values represent higher connectivity.

8.3 Results

8.3.1 Surface change and a distinct response to temperature forcing

The DEM of difference (DoD) between 1967 and 2014 (Figure 8.7, a) shows the changes in elevation within the two studied watersheds over a five decade period, with a current geomorphological map (b) to attribute these changes to different landforms, in particular to glacier cover. The warming climate conditions strongly affected glacier evolution (Figure 8.7a), as demonstrated by the extensive lowering of surface that affected glacial landforms. In the Douves Blanches watershed, erosion is also detected in various parts outside the glacier boundaries in the Southern part of the watershed. These zones may be sources of solid material and supply sediment downstream by fluvial transport or debris-flows events. Similar patterns are visible in the Bertol watershed as well, on the right bank of the river. At this temporal scale of analysis, the activity of the rock glacier in the Southern part of the watershed is clearly visible, while no significant elevation change is observed for the other rock glacier in the watershed (see geomorphological map, Figure 8.7b). The active rock glacier may have lost mass because of core-ice melting, and at the same time provoked an increase of elevation at its lobes' fronts because of rock glacier advance and sediment delivery. Above the rock glacier, surprisingly high surface lowering rates are observed for a talus slope. This may be evidence of permafrost decay and matches examples described for sites of similar elevation and orientation [PERMOS, 2009].

Figure 8.8 shows sequential DEMs of Difference (DoDs) of the area. The patterns observed during the two distinct temperature-forcing periods are opposed. Elevation gains of several
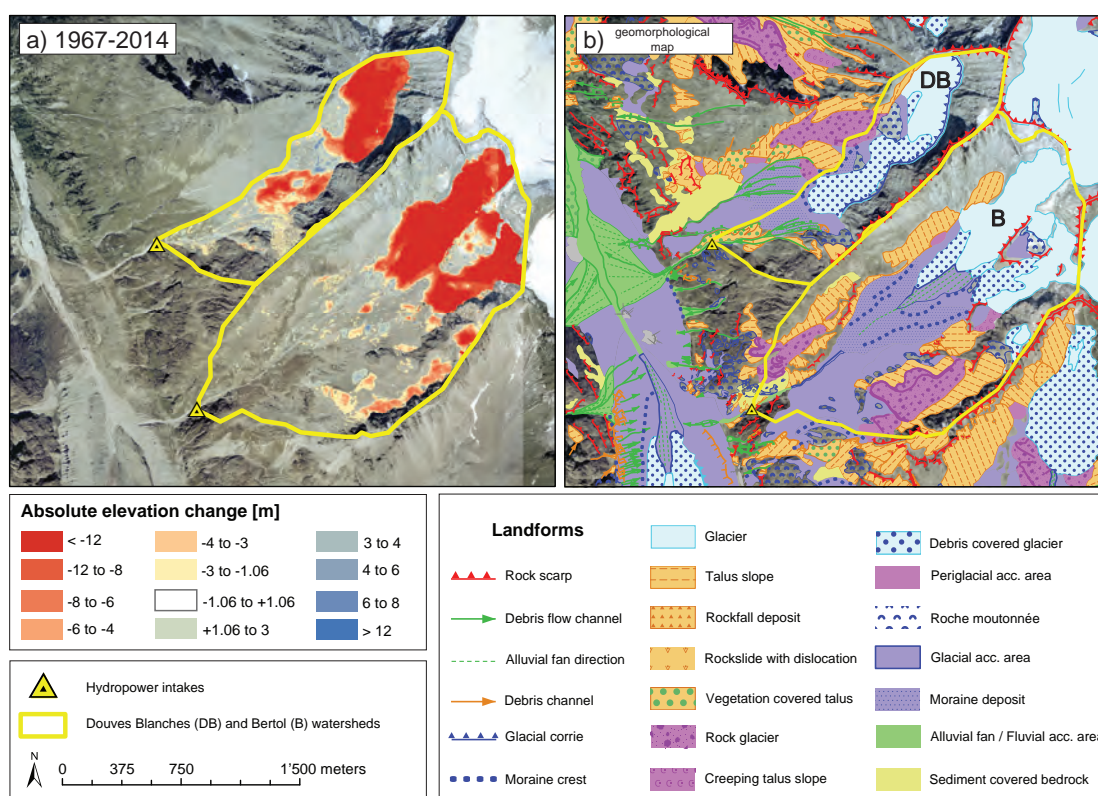
Figure 8.7 – (a) DEMs of Difference (elevation changes) of a five decade period and (b) geo-morphological map of the Douves Blanches and Bertol watersheds [Lambiel et al., 2016]. The limit of detection of elevation change is set at the 90% confidence limit (see Table 8.1).

meters are observed in glacier and debris-covered glacier surfaces between 1967 and 1983 (Figure 8.8a). It appears that the cooler climatic conditions of these years were favourable for glacier advance in both watersheds. This glacial growth was possible despite temperatures still being warmer than the Little Ice Age and is consistent with observations on similar small glaciers in this region [VAW Laboratory of Hydraulics and Glaciology, 2013; Micheletti et al., 2015b]. Traces of erosion and deposition are also observed for non-glacier landforms during this cooler period. The most evident examples are gully erosion in the lower part of the Douves Blanches watershed and elevation changes on a rock glacier / talus slope area in the Southern part of the Bertol watershed. The 1983-1988 DoD (Figure 8.8b) shows extensive low magnitude erosion patches, possibly resulting from the abrupt transition from cooler to warming periods. Of particular interest is localized gully erosion and surface lowering in permafrost-affected areas. The elevation changes that occurred from 1988 (Figure 8.8c-8.8f) are well representative of the reversed tendency that started in the mid-1980s. Considerable elevation loss affected glaciers and debris-covered glaciers, observable in all recent DoDs, and this can be attributed to the role of temperature forcing. Thus, the periods 1967 to the mid-1980s and the mid-1980s to 2014 represent climatic conditions either side of a critical state (see Phillips [2009]) for these glaciers, something that has been observed for many glaciers in the Swiss Alps [Haeberli and

Beniston, 1998; Huss, 2012; Vaughan et al., 2013; Huss et al., 2015] and in the same valley [Micheletti et al., 2015b; Capt et al., 2016]. For the warming period (1983-2014), mean glacier surface losses of 1.10 m³m⁻²yr⁻¹ for Douves Blanches and 1.30 m³m⁻²yr⁻¹ for Bertol were estimated. During the warming period, the DoDs suggest elevation changes for non-glacier areas as well. Scattered zones of deposition are occasionally visible, in particular in Southern Bertol at the base of rockwalls, near the glacier snout and in proximity to the large rock glacier in that area. These could be indications of sediment production and delivery by permafrost degradation in rockwalls, erosion and transport of morainic material, or processes associated with rock glaciers. While these processes seem representative of the mid-1980s to the present period, their low magnitude associated with DEM uncertainty make them visible only in some maps. We are also assuming that geomorphic changes are manifest as surface changes and not changes in lateral flux that lead to only a small surface expression. It is important to note how, despite signs of extensive increase and decrease in thickness during the period of study, the snouts of the Douves Blanches and Bertol glaciers did not modify significantly their positions, an outcome in strong contrast with observations for other glaciers in the valley (e.g. Lane et al. [2016]). Their small size and the extensive debris-cover, acting as insulating layer [Lambrecht et al., 2011; Capt et al., 2016], may be the cause.
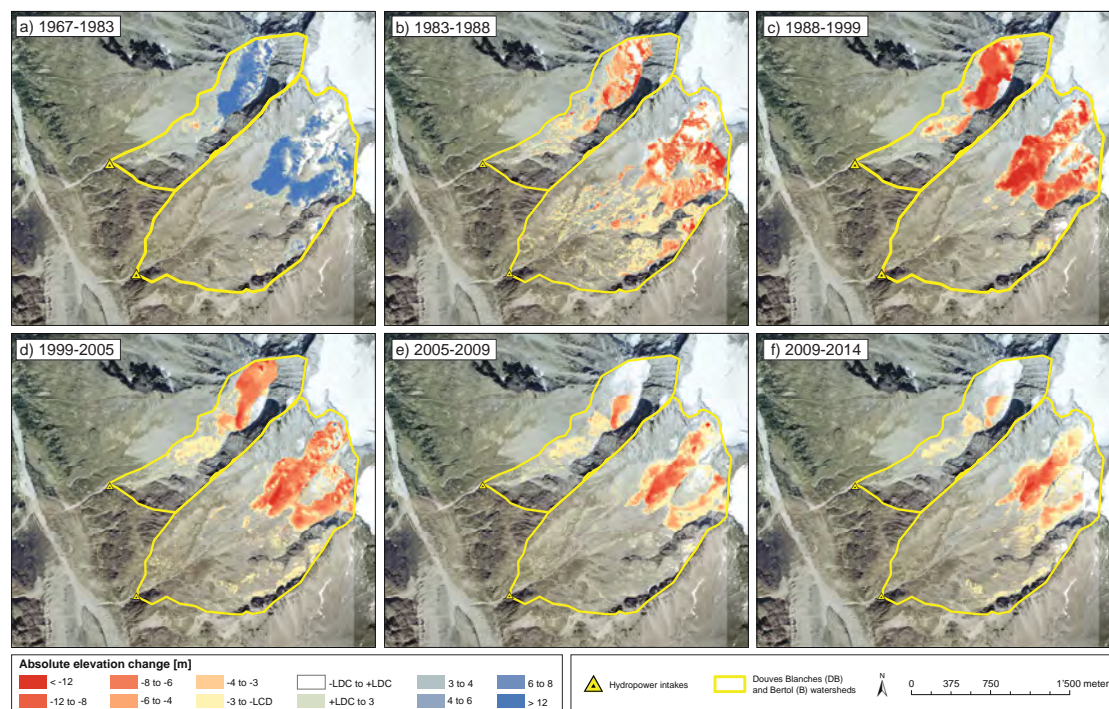

Figure 8.8 – Sequential DEMs of Difference (elevation changes) for the Douves Blanches and Bertol watersheds. Limit of detection of change between 1.06 m and 1.44 m at the 90% confidence limit (see Table 8.1).

8.3.2 Evolution of water yield and sediment export

Figure 8.9 shows the number of flushing events per year since 1967 at the Douves Blanches and Upper Bertol hydroelectric power intakes. Also shown is the annual water yield based on data for both sites from 1985, and on data for Douves Blanches and by scaled Douves Blanches data for Bertol to 1985. Watershed water yield between 0.6 and 1 million of m^3yr^{-1} was registered in Douves Blanches until the mid-1980s (Figure 8.9a). Despite an increase in precipitation from the mid-1970s, water yield appears relatively stable and affected only by inter-annual variability during the cold period. From 1985, annual water yield in the Douves Blanches starts to rise progressively to reach almost 2 million m^3yr^{-1} most recently (2012 and 2013). Considering the coincidence between the beginning of temperature warming (see Figure 8.3) and this rise, it is justified to hypothesize a causal link between water yield and temperature forcing. The total number of flushing events per year (purges) is representative of annual quantities of exported sediments (see Section 8.2.4). Between 1967 and 1990, it was never necessary to flush sediments out of the Douves Blanches water intake more than four times per year. A change in sediment export behaviour follows the transition between cooler and warming periods, albeit delayed by a few years, as it is clear only from 1991 (and following one of the most intense rainfall events that occurred in 1990). From 1991, a substantial inter-annual variability in flushing frequency is observed, but more than half of the years considered registered more purges than the maximum observed prior to 1991 and a general upward trend is visible. The highest number of purge events occurred in 2014 (the last observation), a year with one of the highest mean annual air temperature values. Thus, while the warmer period led to a clear rise in water yield, it also led to an increase in the inter-annual variability in sediment export, and hence in the 5 year running mean of sediment export.
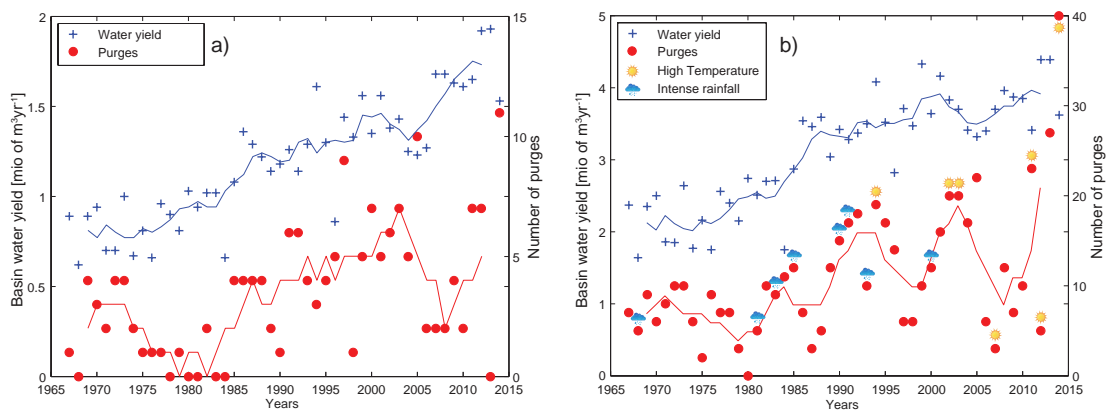
Figure 8.9 – Annual water yield and number of purges at the (a) Douves Blanches and (b) Upper Bertol intakes, also showing the years with the heaviest rainfall events in Evolène-Villa and Héremence and highest temperatures in Sion (Figure 8.3). The lines represent the 5 year running mean.

The evolution of water yield at the Upper Bertol intake (Figure 8.9, b) follows a trend similar to that in the Douves Blanches watershed from 1985, when the yield becomes based on direct

measurement rather than scaled from Douves Blanches data. Larger volumes of water were produced every year from the second part of the 1980s until present, and they were all higher than the 1967-1985 maximum with a sole exception (1996). Again, there is a clear association with the strong temperature forcing that started in the mid-1980s. The need to flush the intake of sediment seems to increase from 1990 in a similar way to Douves Blanches. However, there is less inter-annual variability. There are three examples of where years with more purges are preceded by or correspond to period of large rainstorms or elevated temperatures. The 1990-1995 period featured the first considerable increase in purge frequency with three of the four strongest precipitation events over 72 hours in the area (Evolène-Villa data, Figure 8.9, b). At the beginning of the 2000s the number of purges per year also increased. This followed the exceptionally severe precipitation of October 2000 (the highest recorded in Evolène-Villa with 128 mm in 3 days). Note that 2002 and 2003 are years of very high MAAT (Figure 8.3). Finally, the three highest scores of flushing events per year are registered between 2011 and 2014. These 4 years featured half of the hottest six years (2011, 2012, 2014). In between these peaks in the number of purges per year, lower values are observed, similar to Douves Blanches. Despite the high variability, 16 out of 25 years from 1990 experienced more flushing events than any year between 1967 and 1989.

Extreme precipitation and temperature events seem to be important earlier in the record during the cooler period as well, although to a lesser extent. For instance, for both watersheds, the intense rainfall events observed in 1968 and at the beginning of the 1980s did not influence water yield in an appreciable way. Nevertheless, the rising number of purges from 1980 to 1995 are not only associated with rising mean annual air temperature (Figure 8.3), but also with a cluster of intense rainfall events. Despite the warmer temperature being maintained after 1995, the sediment export falls between 1995 and 2000, and is only rising again after a major event in 2000. Again, export falls from 2005 and is only rising in more recent years. Thus, the hypothesis that arises from these observations is that the combination of high temperature (sediment production), water yield and intense rainfall events (energy for sediment transport) exert an influence on solid material delivery to the intakes, and thus on the frequency of the flushing operations. Intense rainfall events can have an appreciable effect even if production is generally lower during cooler conditions and total annual water yield is not particularly high. Finally, the last decade shows the progressive rise of export despite no intense rainfall events occurred. Similar trends are observed for an adjacent valley glacier [Lane et al., 2016] and may reflect a systematic shift in basin connectivity. Sediment export records for the two watersheds are significantly (if not highly) correlated (r = 0.552; p < 0.001), suggesting that they might both respond partly to a common, external forcing.

8.3.3   Water yield and contribution to river flow

Figure 8.10 illustrates the evolution of annual water yield (similar to Figure 8.9, but aggregated per period of available imagery). Douves Blanches (Figure 8.10a) has one less period because its glacier was not represented entirely in the 2009 DEM (see Figure 8.8e and 8.8f). As noted

in the previous section, annual water yield increases through time for both watersheds and almost doubled in the most recent period in comparison with 1967-1983. Whilst absolute amounts of precipitation remained to a certain extent constant during the last five decades, their relative contribution to yield diminished from more than 80% for both watersheds to less than 50% most recently. That is, the rising water yield is associated not with precipitation but rather loss of ice-stored water and other sources. Whilst it could not be quantified, it could be hypothesized that a considerable contribution is provided by snowmelt. With enhanced temperatures from the second part of the 1980s, a transition from snow transformation into glacier ice (hence contributing to glacier growth) to snow melt and rising water yield occurred. At the same, time loss from the ice store also became important notably between 1983 and 2005. Taken together, there is a dual impact on glacier mass balance: reduced accumulation and increased ablation. Given the small size of these glaciers, it is perhaps not surprising that since 2005, and notably for the smaller Douves Blanches system, the ice melt contribution has begun to diminish, although we cannot yet be sure that this is sufficient to allow it to be identified in a slowing increase, or even a decrease of water yield. Finally, a source that could not be evaluated concerns permafrost-related water yield. Surface lowering due to permafrost degradation may be visible in some rock glaciers and talus slopes in Bertol (see Figures 8.7 and 8.8), but it could not be quantified because changes could equally be caused by erosion of sediment. The unquantified contributions appear to be increasing and explain half of the water yield in the most recent years. They only partially compensate the uncertainty inherent to the other runoff components.

8.3.4 Sediment export and its relation to transport capacity

Section 8.3.2 illustrated how annual water yield and the number of flushing operations per year have generally increased since the end of the 1980s in the Douves Blanches watershed and, more systematically, in the Bertol watershed. There appeared to be some temperature and extreme event association, but to investigate this more fully, we compare the purge records with modelled sediment transport capacity. Figure 8.11 shows the results for the Douves Blanches watershed. Unsurprisingly, annual water yield and volumetric transport capacity both increase through time, suggesting that water yield partly controls the rate of sediment export. In addition, the two indicators are strongly correlated (Figure 8.11a, r = 0.963; p < 0.001). Transport capacity is also significantly correlated with sediment export but the correlation is much lower (r = 0.323; p < 0.05). Whilst they both follow a common temporal trend (they both seem increase through time, Figure 8.11b), estimated sediment export is two orders of magnitude lower than modelled transport capacity. Given the low correlation, and notwithstanding the high uncertainty in the absolute values of the modelled sediment transport capacity, it appears that there is supply limitation in the Douves Blanches watershed. Further, if we observe the years with highest estimated sediment export, they are often followed by years with exceptionally low ones, and this despite high transport capacity. The highest sediment export occurred in 2014 and so our observation cannot be verified on that date, but the second highest export (2005, between 100 and 120 m^3yr^{-1}), was followed
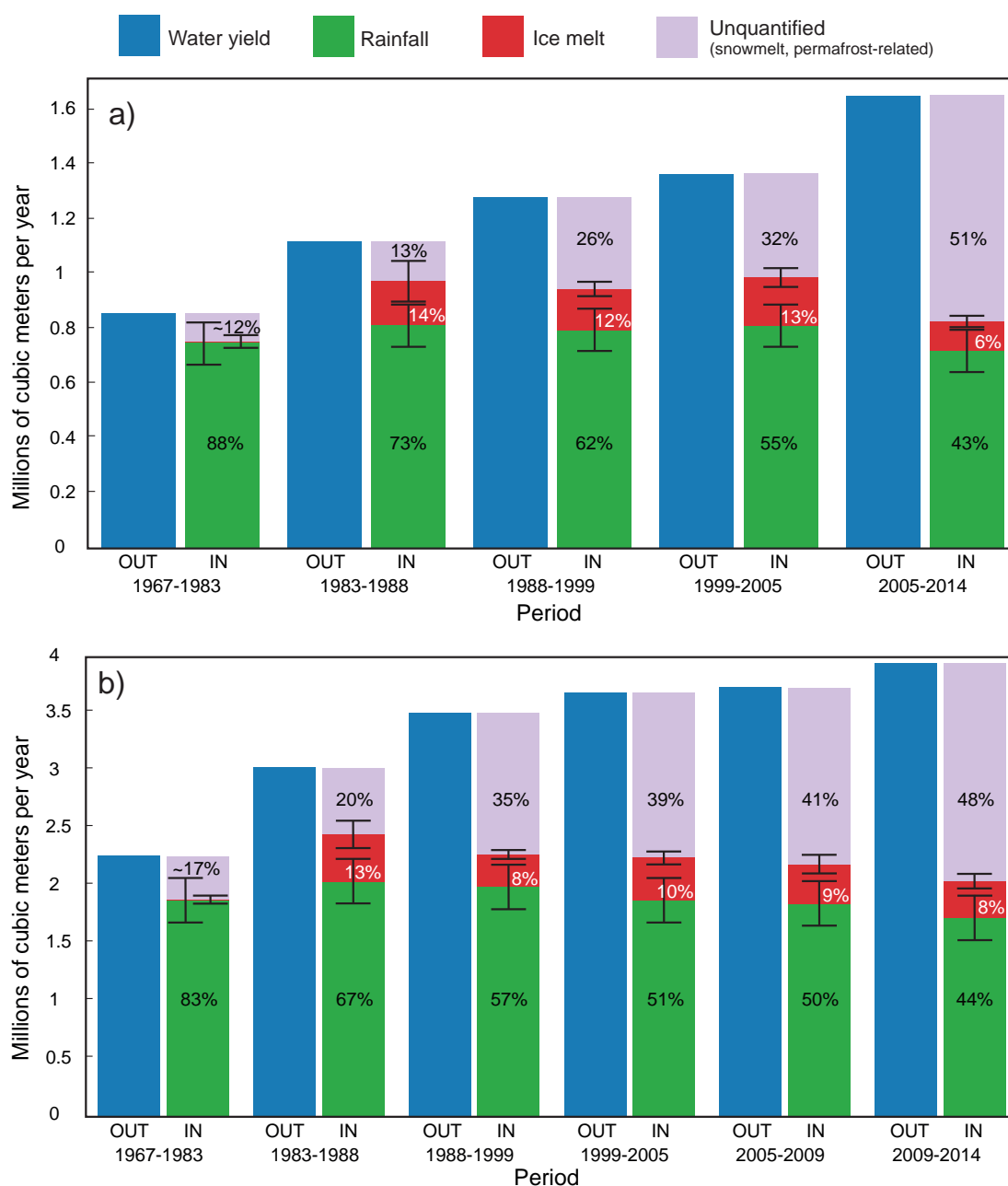
Figure 8.10 – Approximation of annual water yield and contribution to river flow from rainfall and icemelt at the (a) Douves Blanches and (b) Upper Bertol intakes. Unquantified water contributions includes snowmelt and thaw in permafrost-related landforms.

by five years of low exported volumes. The same was true for the third ranked, 1997, which was followed by a year of exceptionally low export. This effect could be observed to a lesser extent for other years as well. Field observations of the authors suggest that a crucial variable may be the occurrence of debris-flow events, which are necessary to deliver sediment to the channel for export and reflected in the possible association with extreme rainfall events

described above. In the absence of such events, exhaustion effects can develop. It is not possible to distinguish if the increase of annual sediment export in the Douves Blanches watershed is related to enhanced sediment production induced by climate change, higher volumetric transport capacity available to mobilize stored material and to deliver it to the channel network or, as is probably the case, both.
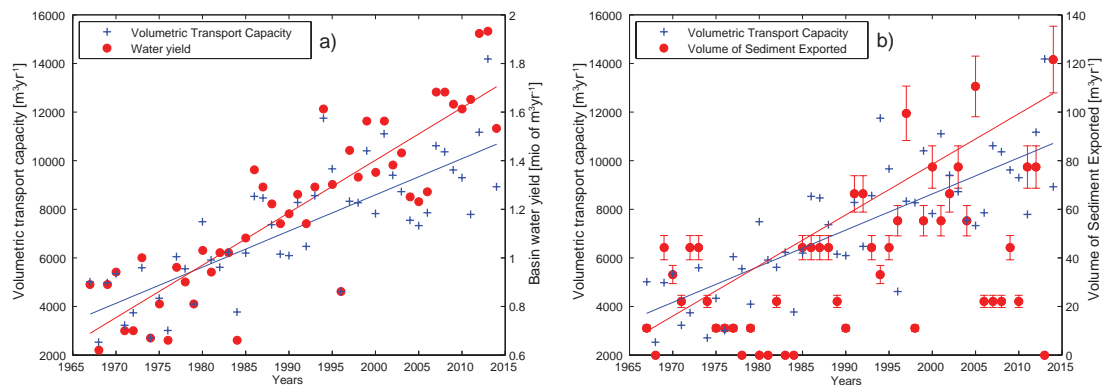

Figure 8.11 – Modelled sediment transport capacity following Nitsche et al. [2011] and its relation with (a) watershed water yield and (b) volume of exported sediment (with packing density uncertainties) for the Douves Blanches watershed.

In the Bertol watershed (Figure 8.12a), annual water yield and volumetric transport capacity integrated through each year progressively increase between the end of the 1960s and 2014. These two indicators are strongly correlated (r = 0.927; p < 0.001). However, unlike for Douves Blanches, the estimated volume of sediment exported is almost completely unrelated to volumetric transport capacity (Figure 8.12b, r = 0.039; p > 0.05), and seems to oscillate between periods of high export and of low delivery. Effectively, and as the exported volume is linearly related to the number of purges in Figure 8.9b, after small peaks at the beginning of the 1970s and 1980s, it peaks at the first years of the 1990s, the first years of the 2000s and again in most recent years. During the late 1970s, 1980s, 1990s and 2000s lower amounts are exported, and this despite volumetric transport capacity being even higher than in the periods of more important sediment export. As in the Douves Blanches watershed, estimations of sediment transport capacity are orders of magnitude higher than the measured export. These results demonstrate again that sediment delivery at the outlet is likely to be less dependent on the capacity of the river to transport sediment, and more dependent on sediment delivery. Field observations show that large amounts of unconsolidated material are available in the system, yet these appear to be unable to leave the watershed. We hypothesize that this is due to topographic complexity and hillslope surface roughness, that translate into the ineffectiveness of the sediment cascade and/or poor within-channel connectivity upstream. The coincidence of sediment export peaks and climatic extremes sustain this interpretation. High temperature and intense precipitation potentially enhance the efficiency of the sediment cascade, notably allowing debris-flows to move talus sediments further downslope, so supplying solid charge to the (efficient) channel network outlet. We explore sediment connectivity in the next section.
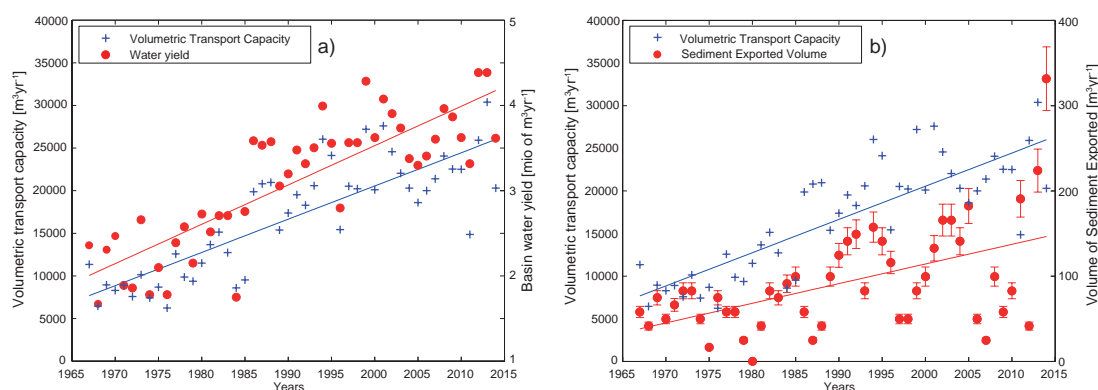
Figure 8.12 – Modelled sediment transport capacity following Nitsche et al. [2011] and its relation with (a) watershed water yield and (b) volume of exported sediment (with packing density uncertainties) for the Bertol watershed.

8.3.5 Sediment connectivity within the watersheds

In both the Douves Blanches and the Bertol watersheds, the estimated volumetric sediment transport capacity was substantially higher than measured sediment export, suggesting that sediment transport could be limited by supply and notably the efficiency of the sediment transport cascade. To investigate the coupling between sediment source areas and the fluvial and torrential network, the Connectivity Index proposed by Borselli et al. [2008] and Cavalli et al. [2013] was calculated (Figure 8.13). For the Douves Blanches watershed, it suggests that the watershed divides quite clearly into a more connected zone and a less connected zone. The glacierized part of the watershed is disconnected because of the barrier represented by the LIA moraine crest (see Figure 8.2), in a context similar to that described in Micheletti et al. [2015b] for another watershed in the region. The rockwalls (with probable permafrost presence, PERMOS [2009]) are likely to supply large amounts of sediment, yet these remain stored in the proglacial area, hence a signal of enhancement of sediment production induced by climate forcing would not be visible in the purge records. The increased sediment export (see Figure 8.9, a) has to be attributed to the lower, very steep area, where connectivity is better established. Field evidence indicates that the driving processes for sediment delivery are erosion of morainic material and debris-flow events. The latter may be increasing in frequency through sediment release from decaying permafrost sites under the influence of air temperature [Huggel et al., 2012]. In the present case, a possible source would be the northwest-facing rockwalls that allegedly feature permafrost [PERMOS, 2009]. Hence, the joint effect of water yield (and thus transport capacity) increase and of rapid climate warming might explain why sediment export rates have grown since the 1990s in the Douves Blanches watershed. Nonetheless, the generalization of these dynamics requires care, as the response of hillslope sediment transfer can vary even within a single massif (e.g. Jomelli et al. [2007]).

In the Bertol watershed, very high values are concentrated within the main streams. Evident disconnections are detected in the lower part of the watershed, were rock glaciers are located
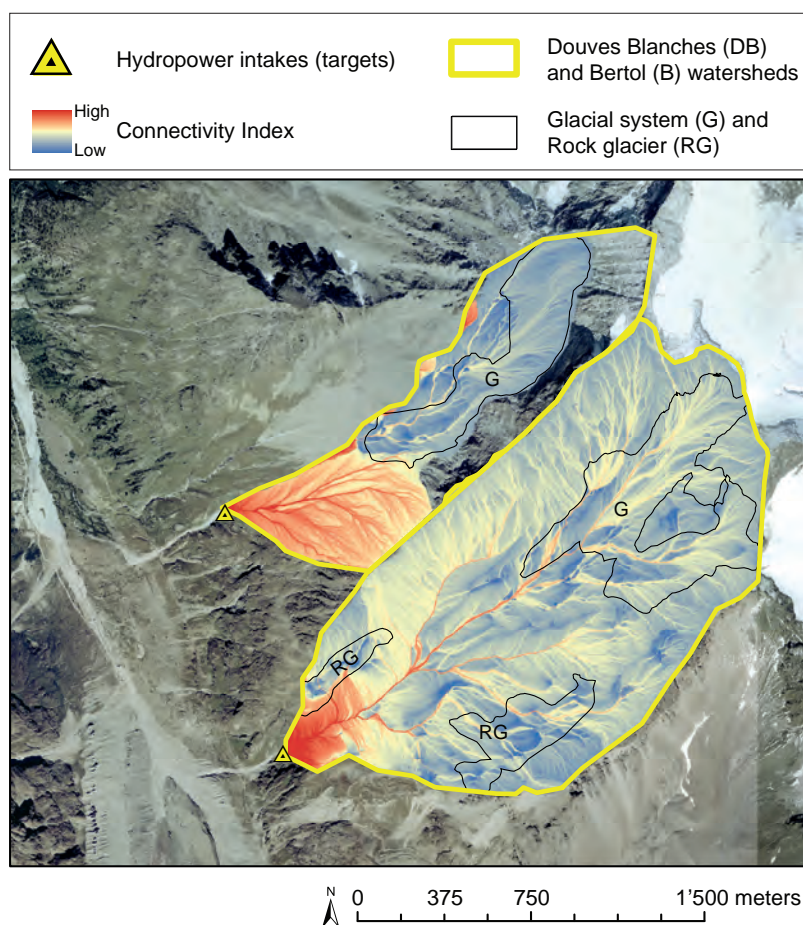
Figure 8.13 – Connectivity Index in the Douves Blanches and Bertol watersheds computed following Borselli et al. [2008] and Cavalli et al. [2013].

(see Figure 8.7b). This is particularly relevant for the Southern part of the watershed, where permafrost dynamics were identified (see Section 8.3.1). In that area, only small channels have high connectivity, and landforms that potentially produce high amounts of sediments are disconnected from the drainage system. The front of the rock glacier nearest the water intake seems well connected, but the rock glacier does not appear to be very active (see the absence of change in Figure 8.7a). On the glacier surface and in the proglacial area various low connectivity (blue) spots are present. These are likely to act as sediment sinks, potentially trapping loose material. As a result, the rockwall-hillslope-channel-outlet sediment transfer might be inefficient. These results are coherent with the low correlation found between stream transport capacity and estimated sediment exports. Coarse material is presumably rarely transported and delivered to the drainage system in most of the catchment. Accordingly, sediment delivery at the water intake appears mostly controlled by extreme events as: (i) high temperatures potentially enhancing sediment production [Huggel et al., 2012; Bennett et al., 2013], and (ii) intense rainfall events, both eroding and mobilizing sediments on hillslopes [Stoffel and Huggel, 2012], as demonstrated by their coincidence in Figure 8.9b.

8.4   Discussion

The last five decades history of the Douves Blanches and Bertol watersheds suggests that, in the face of rapid climate warming, the hydrological and geomorphological dynamics of small and partially glaciated Alpine watersheds are changing. The change began with the considerable increase in temperature in the second part of the 1980s. In the first instance, a transition from a phase of glacier growth (1960s-1980s) to continuous glacier recession (mid-1980s-ongoing) occurred. Similar findings have been reported elsewhere. For instance, Huss [2012] estimated a decadal mean mass balance of +0.11 m w.e. yr^{-1} between 1970 and 1980, followed by respectively -0.40, -0.68 and -0.99 m w.e. yr^{-1} in the following three decades. Another consequence of temperature rise has been the modification of contribution to the river flow. Whereas precipitation was the widely dominant water source for streams until the mid-1980s, its relative contribution then started decreasing, although its absolute input remained stable. The explanation lies in the rising contribution of other sources, notably ice melt and the unquantified snowmelt, and it is most likely that the snowpack no longer contributes to glacier growth but becomes a subsidy of water yield and that additional contributions come from thawing of permafrost-related landforms. These changes have caused water yield to almost double in the studied watersheds through the last five decades. An increase in annual runoff in similar watersheds is a frequent outcome of rapid climate warming [Huss et al., 2008; Farinotti et al., 2012].

The records of sediment export that we make use of in this paper are extremely rare and allow us to get a decadal scale estimate of the extent to which watersheds that are being forced by rapid warming lead to significant sediment export. The increase in the frequency of sediment flushing at the watershed outlets from 1990 did suggest that contemporary sediment yield was rising. At least some of this could be related to rising sediment transport capacity associated with the rising water yield. But, it did not explain the pattern completely and there was substantial additional variability, suggesting processes other than the ability of the stream to transport sediment may be important. First, it should be noted that, under the influence of higher air temperatures, sediment production may be enhanced, as documented in other studies [Kääb et al., 2007; Knight and Harrison, 2009; Huggel et al., 2012; Bennett et al., 2013; Lane et al., 2016]. There is some evidence that as the warming begins in the mid-1980s, sediment export increases, manifest as a clear wave form in Bertol until the late 1990s, and possibly in the same way in Douves Blanches, but where there is much more variability. Second, identifying the effects of warming on sediment export was difficult because of a buffering effect in the sediment cascade associated with connectivity [Heckmann and Schwanghard, 2013; Bennett et al., 2014; Messenzehl et al., 2014; Micheletti et al., 2015b; Lane et al., 2016]. Albeit manifest in different ways, in both watersheds, we argue that topography complexity and surface roughness play a fundamental role in controlling this buffering effect. In Douves Blanches, the vast majority of the watersheds (including the allegedly frozen rockwalls) are disconnected from the outlet by a LIA moraine crest in a comparable way to that described by Micheletti et al. [2015b] for a glacier a few km to the North. In Bertol, disconnected areas, sediment

sinks and rough surfaces impeded sediment delivery to the proglacial river. Hence, while the climate forcing of sediment export is partially visible at the water intakes, the sediment export records may under-estimate the actual levels of material mobilization upstream in response to climate forcing. Conversely, the ineffectiveness of rockwall-hillslope-channel-outlet connectivity may reduce the extent to which climate forcing of landscape response can be detected in valley-bottom sediment delivery and deposits. This implies that landscape sensitivity to climate forcing and the propagation of change are related to connectivity (see Brunsden and Thornes [1979]). Given that we study sediment export from two adjacent watersheds with different controls on connectivity (Figure 8.13) and different sediment export records (Figure 8.9) generalizing climate forcing impacts on sediment dynamics needs to pay careful attention to the geomorphic functioning of the watershed being considered, and its context in the landscape. For example, in a study of a valley glacier in the region, Lane et al. [2016] describe how sediment delivery downstream is enhanced with glacier recession because of the replacement of slow glacier surface sediment transport with more rapid fluvial transport and because of the evolution of sediment connectivity. As shown in Section 8.3.1, the snout of both Douves Blanches and Bertol glaciers did not change position significantly during the period of study, and they are situated in steeper watersheds. Thus, we argue that glacier recession is not relevant in these smaller and steeper watersheds because of the absence of valley sidewall debuttressing and of large areas where braided rivers can develop and access and mobilize sediment. Rather, increasing sediment export is a function of extreme events that can overcome the poor level of coupling to stream channels and the associated low levels of connectivity in the sediment cascade. Low rates of glacier recession are sustained by the insulating effect of a heavily debris mantle [Lambrecht et al., 2011; Capt et al., 2016] and glacier confinement in a relatively colder zone (their snout is located at 2850 and 2830 m a.s.l., a few hundred meters higher than the Haut Glacier d'Arolla studied by Lane et al. [2016]).

Third, there was some evidence of the importance of extreme storms as a control on erosion and delivering sediments from hillslopes to the stream [Stoffel and Huggel, 2012]. The evidence was clearest in the Bertol watershed (Figure 8.9b), even though not every extreme precipitation event or warm year resulted in high volumes of exported sediment. We suggest that extreme events are necessary to overcome transport-limitation in the hillslope sediment system given that the proglacial streams of both watersheds are efficient in transporting sediments once delivered. These considerations are supported by the relatively low volumes of sediment export observed at the water intakes, but highlight the difficulty in predicting future behaviour of sediment yield in Alpine watersheds advanced by Raymond Pralong et al. [2015] without reference to within-watershed processes.

By reason of the considerations above, formulating scenarios for future sediment export for these small, partially glaciated watersheds is challenging. Water yield is likely to increase further, at least until it becomes limited by available ice to melt, and with it sediment transport capacity in the drainage network. Farinotti et al. [2012] foresee that maximum annual runoff in Alpine watersheds is going to be reached by 2050, followed by a tendency to decreasing and/or more variable water yield, although it is still unclear how this timing applies to small, heavily

debris-covered glaciers. Nevertheless, as demonstrated in this research, the controlling factor on future sediment export would more likely be the actual efficiency of the rockwall-hillslope-channel cascade. Whilst we expect an increase in sediment production within the watersheds in particular by mean of the decay of permafrost, most of the material is unlikely to leave the basin because of poor connectivity. As a consequence, the volumes of material produced and mobilized under the effect of climate forcing are going to be much higher than the actual delivery at the valley bottom. On the other hand, heavy rainfall events and debris-flows play a fundamental role in sediment export and are likely to produce years of very high delivery at the outlets, requiring an increase in the frequency of flushing operations in the water intakes. Thus, we would expect an extremely high interannual variability in sediment export in the future, similar to what observed for the period 2000-2014 (Figure 8.9).

More critically, investigating landscape dynamics in small watersheds over the timescales of decades is challenging because of the difficulty of collecting high quality observations. The present contribution benefits from the coupling of archival imagery, long term records of operation in hydroelectric power water intakes and climatic and meteorological data from stations located in proximity of the study area. Despite the good quality of these data, a number of uncertainties and limitations arise. Photogrammetrically-derived DEMs and the associated estimates of surface change could not account for rockfall activity (impossible to observe from aerial imagery because of the steepness of the rockwalls) and low magnitude erosion and deposition patterns. Hydropower intakes records are generally of good quality in the cases studied here because they have to meet regulatory requirements, but unrealistic water yields were observed prior to 1985 for one watershed. Other aspects not treated here include the relative contribution of sediment from glacial and proglacial areas and the role of seasonality. We would expect sediment delivery from the proglacial area during the snowmelt period and in case of intense rainfall events, and from glaciated areas during the glacier melting period in the summer, because of the crucial role of runoff generation processes on sediment supply and temporal availability [Mao et al., 2014]. Other studies found that the suspended sediment supply is approximately equally divided between snowmelt season and glacier melting [Mao and Carrillo, 2015]. However, our data do not allow seasonality effects to be identified. Modelling transport capacity following Nitsche et al. [2011] incorporates a number of assumptions and the predictions obtained can only be used indicatively. Finally, estimating the contribution of rainfall and ice melt to river flow was tentative, as it required a number of assumptions, estimations and boundary conditions to be accepted and these types of analysis are naturally challenging. Nonetheless, and in spite a number of processes remaining unquantified, the general trend of the last five decades in these watersheds could be observed.

Future developments to better understand how these small partially glaciated Alpine watersheds react to ongoing climatic change are required. First, additional data need to be collected within the watersheds, including grain size estimations, the location of their deposits, permafrost presence/degradation and sediment production patterns. Collecting such information is challenging because of the steep and dangerous nature of the sites, but much

may be done using remote sensing methods, especially terrestrial laser scanning and the emerging drone technologies. Second, coupling our knowledge of the 1960s-to-present evolution of these landscape with Regional Climate Models (RCMs) is necessary to deepen our understanding on how sediment flux may be affected by climate change in the next decades. Whilst there are important contributions to this subject (e.g. Raymond Pralong et al. [2015]), it could be argued that at present we do not sufficiently understand the impacts of climate change on geomorphological systems or their sensitivity to such changes [Knight and Harrison, 2009], as demonstrated by the complex patterns unveiled in this research.

8.5 Conclusions

The impacts of last five decades climate forcing on landscape dynamics in small, partially glaciated Alpine watersheds has been investigated using archival aerial imagery and long-term records from hydroelectric power infrastructure. Photogrammetrically derived DEMs allowed the identification of significant surface change within the watershed. These observations are coupled with geomorphological maps to identify the spatial assemblage of landforms present within the watersheds. Data from water intakes provided estimations of annual water flow, while the frequency of sediment flushing operations (the so-called purges) were used to estimate volumes of sediment leaving the system. Extant climate data from meteorological stations located near the area of study permitted the interpretation of results in the matter of climate forcing.

A transition from a cooler and stable period to a context of rapid temperature warming occurred in the mid-1980s and provoked a shift in glacier dynamics, from glacial advance to recession. The related enhanced snowmelt and ice melt contribution induced an increase in annual water yield for the studied watersheds. The frequency of purging events, and hence sediment export, increased, although years of low sediment export are still observed. Climatic conditions favourable for sediment production and mobilization (high temperatures and extreme rainfall events) are related to peaks in sediment flushing. The fact that the modelled annual transport capacity of streams was much greater than rates of export suggests that these flows are in supply-limited conditions. A key role is attributed to the ineffectiveness of the sediment cascade, with several consequences. First, sediment delivery downstream might be associated more with single events such as rockfalls or debris-flows that occurred when certain conditions or triggering points are met, and when sediment connection can be assured. These occurrences might help mobilize the wide amounts of sediments available in the system (historically or for minor, recent events). Second, ineffectual connectivity means that climate forcing of sediment dynamics is only partially manifest at watershed outlets, and by implication in deposits downstream. Thus, identifying watershed response to climate forcing from sediment deposits may be a challenge. Finally, coupling of these considerations highlights the difficulty in observing, understanding, modelling and predicting future sediment yield in these landscapes, despite these questions being of fundamental importance because of the significant impact that sediment transport has on hydroelectric

power infrastructure.

Acknowledgements

Bibliography

Baewert, H. and Morche, D. (2014). Coarse sediment dynamics in a proglacial fluvial system (Fagge River, Tyrol). *Geomorphology*, 218:88–97.

Bennett, G., Molnar, P., McArdell, B., and Burlando, P. (2014). A probabilistic sediment cascade model of sediment production, transfer and yield in the Illgraben. *Water Resources Research*, 50:1225–1244.

Bennett, G., Molnar, P., McArdell, B., Schlunegger, F., and Burlando, P. (2013). Patterns and controls of sediment production, transfer and yield in the Illgraben. *Geomorphology*, 188:68–82.

Bezinge, A., Clark, M. J., Gurnell, A. M., and Warburton, J. (1989). The management of sediment transported by glacial melt-water streams and its significance for the estimation of sediment yield. *Annals of Glaciology*, 13:1–5.

Bolch, T., Kulkarni, A., Kääb, A., Huggel, C., Paul, F., Cogley, J. G., Frey, H., Kargel, J. S., Fujita, K., Scheel, M., Bajracharya, S., and Stoffel, M. (2012). The State and Fate of Himalayan Glaciers. *Science*, 336:310–314.

Borselli, L., Cassi, P., and Torri, D. (2008). Prolegomena to sediment and flow connectivity in the landscape: a GIS and field numerical assessment. *Catena*, 75:268–277.

Bosson, J.-B., Deline, P., Bodin, X., Schoeneich, P., Baron, L., Gardent, M., and Lambiel, C. (2015). The influence of ground ice distribution on geomorphic dynamics since the Little Ice Age in proglacial areas of two cirque glacier systems. *Earth Surface Processes and Landforms*, 40:666–680.

Brunsden, D. and Thornes, J. B. (1979). Landscape sensitivity and change. *Transactions of the Institute of British Geographers*, 4(4):463–484.

Caine, N. and Swanson, S. (1989). Geomorphic coupling of hillslope and channel systems in two small mountain basins. *Zeitschrift für Geomorphologie*, 33:189–203.

Capt, M., Bosson, J.-B., Fischer, M., Micheletti, N., and Lambiel, C. (2016). Decadal evolution of a very small heavily debris-covered glacier in an Alpine permafrost environment. *Journal of Glaciology*, doi: 10.1017/jog.2016.56.

Cavalli, M. and Marchi, L. (2008). Characterisation of the surface morphology of an alpine alluvial fan using airborne LiDAR. *Natural Hazards and Earth System Science*, 8:323–333.

Cavalli, M., Trevisani, S., Comiti, F., and Marchi, L. (2013). Geomorphometric assessment of spatial sediment connectivity in small Alpine catchments. *Geomorphology*, 188:31–41.

Deline, P., Gruber, S., and others, . (2015). *Snow and ice-related hazards, risks, and disasters*, chapter Ice Loss and Slope Stability in High-Mountain Regions, pages 521–561. Academic Press: San Diego.

Chapter 8. Water yield and sediment export in small, partially glaciated Alpine watersheds in a warming climate

Farinotti, D., Usselmann, S., Huss, M., Bauder, A., and Funk, M. (2012). Runoff evolution in the Swiss Alps: projections for selected high-alpine catchments based on ENSEMBLES scenarios. *Hydrological Processes*, 26:1909–1924.

Ferguson, R. I. (2007). Flow resistance equations for gravel- and bouler-bed stream. *Water Resources Research*, 43:W05427.

Finger, D., Heinrich, G., Gobiet, A., and Bauder, A. (2012). Projections of future water resources and their uncertainty in a glacierized catchment in the Swiss Alps and the subsequent effects on hydropower production during the 21st century. *Water Resources Research*, 48:W02521.

Fischer, M., Huss, M., and Hoelzle, M. (2014). Surface elevation and mass changes of all Swiss glaciers 1980-2010. *The Cryosphere Discuss.*, 8:4581–4617.

Foerster, S., Wilczok, C., and Brosinsky, A. (2014). Assessment of sediment connectivity from vegetation cover and topography using remotely sensed data in a dryland catchment in the Spanish Pyrenees. *Journal of Soils and Sediments*, 14:1982–2000.

Gabbud, C. and Lane, S. N. (2016). Ecosystem impacts of Alpine water intakes for hydropower: the challenge of sediment management. *WIREs Water*, 3:41–61.

Geilhausen, M., Morche, D., Otto, J.-C., and Schrott, L. (2013). Sediment discharge from the proglacial zone of a retreating Alpine glacier. *Zeitschrift für Geomorphologie*, 57:29–53.

Grunewald, K. and Scheithauer, J. (2010). Europe's southernmost glaciers: response and adaptation to climate change. *Journal of Glaciology*, 56:129–142.

Haeberli, W. and Beniston, M. (1998). Climate Change and its Impacts on Glaciers and Permafrost in the Alps. *Ambio*, 27:258–265.

Harris, C., Arenson, L. U., and others, . (2009). Permafrost and climate in Europe: Monitoring and modelling thermal, geomorphological and geotechnical responses. *Earth-Science Reviews*, 92:117–171.

Harvey, A. M. (2002). Effective timescales of coupling within fluvial systems. *Geomorphology*, 44:175–201.

Heckmann, T. and Schwanghard, W. (2013). Geomorphic coupling and sediment connectivity in an alpine catchment - Exploring sediment cascades using graph theory. *Geomorphology*, 182:89–103.

Heiser, M., Scheidl, C., Eisl, J., Spangl, B., and Hübl, J. (2015). Process type identification in torrential catchments in the eastern Alps. *Geomorphology*, 232:239–247.

Huggel, C., Clague, J. J., and Korup, O. (2012). Is climate change responsible for changing landslide activity in high mountains? *Earth Surface Processes and Landforms*, 37:77–91.

Huggel, C., Salzmann, N., Allen, S., Caplan-Auerbach, J., Fischer, L., Haeberli, W., Larsen, C., Schneider, D., and Wessels, R. (2010). Recent and future warm extreme events and high-mountain slope stability. *Philosophical Transactions of the Royal Society A*, 368:2435–2459.

Hunter, L. E., Powell, R. D., and Lawson, D. E. (1996). Flux of debris transported by ice at three Alaskan tidewater glaciers. *Journal of Gla*, 42:123–135.

Huss, M. (2012). Extrapolating glacier mass balance to the mountain-range scale: the European Alps 1900−2100. *The Cryosphere*, 6:713–727.

Huss, M. (2013). Density assumptions for converting geodetic glacier volume change to mass change. *The Cryosphere*, 7:877–887.

Huss, M., Dhulst, L., and Bauder, A. (2015). New long-term mass balance series for the Swiss Alps. *Journal of Glaciology*, 61:551–562.

Huss, M., Farinotti, D., Bauder, A., and Funk, M. (2008). Modelling runoff from highly glaciated alpine drainage basins in a changing climate. *Hydrological Processes*, 22:3888–3902.

Jasper, K., P., C., Gyalistras, D., and Fuhrer, J. (2004). Differential impacts of climate change on the hydrology of two alpine river basins. *Climate Research*, 26:113–129.

Jomelli, V., Brunstein, D., Grancher, D., and P., P. (2007). Is the response of hill slope debris flows to recent climate change univocal? A case study in the Massif des Ecrins (French Alps). *Climate Change*, 85:119–137.

Kääb, A., Chiarle, M., Raup, C. S., and Schneider, C. (2007). Climate change impacts on mountain glaciers and permafrost. *Global and Planetary Change*, 56:7–9.

Keiler, M., Knight, J., and Harrison, S. (2010). Climate change and geomorphological hazards in the eastern European Alps. *Philosophical Transactions of the Royal Society A*, 368:2461–2479.

Knight, J. and Harrison, S. (2009). Sediment and future climate. *Nature Geoscience*, 2:230.

Kuhn, M. (1995). The mass balance of very small glaciers. *Zeitschrift für Gletscherkunde und Glazialgeologie*, 31:171–179.

Lambiel, C., Maillard, B., Kummert, M., and Reynard, E. (2016). Geomorphological Map of the Hérens Valley (Swiss Alps). *Journal of Maps*, 12:160–172.

Lambrecht, A., Mayer, C., Hagg, W., Popovnin, V., Rezepking, A., Lomidze, N., and Svanadze, D. (2011). A comparison of glacier melt on debris-covered glaciers in the northern and southern Caucasus. *The Cryosphere*, 5:525–538.

Lane, S. N. (1997). The reconstruction of bed material yield and supply histories in gravel-bed streams. *Catena*, 30:183–196.

Lane, S. N., Bakker, M., Gabbud, C., Micheletti, N., and J.-N., S. (2016). Sediment export, transient landscape response and catchment-scale connectivity following rapid climate warming and Alpine glacier recession. *Geomorphology*, doi:10.1016/j.geomorph.2016.02.015.

Lane, S. N., James, T. D., and Crowell, M. D. (2000). Application of digital photogrammetry to complex topography for geomorphological research. *The Photogrammetric Record*, 16(95):793–821.

Lane, S. N., Richards, K. S., and Chandler, J. H. (1996). Discharge and sediment supply controls on erosion and deposition in a dynamic alluvial channel. *Geomorphology*, 15:1–15.

Lane, S. N., Westaway, R. M., and Murray Hicks, D. (2003). Estimation of erosion and deposition volumes in a large, gravel-bed, braided river using synoptic remote sensing. *Earth Surface Processes and Landforms*, 28:249–271.

Leggat, M. S., Owens, P. N., Stott, T. A., Forrester, B. J., Déry, S. J., and Menounos, B. (2015). Hydro-meteorological drivers and sources of suspended sediment flux in the pro-glacial zone of the retreating Castle Creek Glacier, Cariboo Mountains, British Columbia, Canada. *Earth Surface Processes and Landforms*, 40:1542–1559.

Mao, L. and Carrillo, R. (2015). Temporal dynamics of suspended sediment transport in a glacierized Andean basin. *Geomorphology*, doi:10.1016/j.geomorph.2016.02.003.

Mao, L., Dell'Agnese, A., Huincache, C., Penna, D., Engel, M., Niedrist, G., and Comiti, F. (2014). Bedload hysteresis in a glacier-fed mountain river. *Earth Surface Processes and Landforms*, 39:964–976.

Messenzehl, K., Hoffmann, T., and Dikau, R. (2014). Sediment connectivity in the high-alpine valley of Val Müschauns, Swiss National Park - linking geomorphic field mapping with geomorphometric modelling. *Geomorphology*, 221:215–229.

Micheletti, N., Chandler, J. H., and Lane, S. N. (2015a). Application of archival aerial photogrammetry to quantify climate forcing of Alpine landscapes. *The Photogrammetric Record*, 30:150:143–165.

Micheletti, N., Chandler, J. H., and Lane, S. N. (2015b). Investigating decadal-scale geomorphic dynamics in an alpine mountain setting. *Journal of Geophysical Research: Earth Surface*, 120:2155–2175.

Morche, D., Haas, F., Baewert, H., Heckmann, T., Schmidt, K.-H., and Becht, M. (2012). *Erosion and Sediment Yields in the Chaging Environment*, chapter Sediment transport in the proglacial Fagge River (Kaunertal/Austria, pages 72–80. IAHS Special Publication, 356, Wallingford, U.K.

Morris, G. L. and Fan, J. (1998). *Reservoir Sedimentation Handbook*. McGraw-Hill Book Co., New York.

Nitsche, M., Rickenmann, D., Turowski, J. M., Badoux, A., and Kirchner, J. W. (2011). Evaluation of bedload transport predictions using flow resistance equations to account for macro-roughness in steep mountain streams. *Water Resources Research*, 47:WR010645.

Orwin, J. F. and Smart, C. C. (2004). Short-term spatial and temporal patterns of suspended sediment transfer in proglacial channels, Small River Glacier, Canada. *Hydrological Processes*, 18:1521–1542.

Østrem, G. (1975). *Glaciofluvial and glaciolacustrine sedimentation*, chapter Sediment transport in glacial meltwater streams, pages 101–122. Society of Economic Paleontologists and Mineralogists.

PERMOS (2009). Permafrost in Switzerland 2004/2005 and 2005/2006. Noetzli, J., Naegeli, B., and Vonder Muehll, D. (eds.). *Glaciological Report (Permafrost) No. 6/7 of the Cryospheric Commission of the Swiss Academy of Sciences*, :100.

Phillips, J. (2009). Changes, perturbations, and responses in geomorphic systems. *Progress in Physical Geography*, 33:17–30.

Porter, P. R., Vatne, G., NG, F., and Irvine-Fynn, T. D. L. (2010). Ice-marginal sediment delivery to the surface of an high-Artic glacier: Austre Brøggerbreen, Svalbard. *Geografiska Annaler*, 92(4):437–449.

Raymond Pralong, M., Turowski, J. M., Rickenmann, D., and Zappa, M. (2015). Climate change impacts on bedload transport in alpine drainage basins with hydropower exploitation. *Earth Surface Processes and Landforms*, 40:12:1587–1599.

Rickenmann, D. and Recking, A. (2011). Evaluation of flow resistance equations using a large field data base. *Water Resources Research*, 47:W07538.

Sass, O. and Oberlechner, M. (2012). Is climate change causing increased rockfall frequency in Austria? *Natural Hazards and Earth System Science*, 12:3209–3216.

Schiefer, E. and Gilbert, R. (2008). Proglacial sediment trapping in recently formed Silt Lake, Upper Lillooet Valley, Coast Mountain, British Columbia. *Earth Surface Processes and Landforms*, 33:1542–1556.

Slaymaker, O. (2009). Proglacial, periglacial or paraglacial? *Geological Society, London, Special Publications*, 320:71–84.

Stahl, K., Moore, R. D., Shea, J. M., Hutchinson, D., and Cannon, A. J. (2008). Coupled modelling of glacier and streamflow response to future climate scenarios. *Water Resources Research*, 44:W02422.

Stoffel, M. and Huggel, C. (2012). Effects of climate change on mass movements in mountain environments. *Progress in Physical Geography*, 36:421–439.

Vaughan, D., Cosimo, J., and others, . (2013). *Climate Change 2013: The Physical Science Basis. Contribution of Working Group I to the Fifth Assessment Report of the Intergovernmental Panel on Climate Change*, chapter Observations: Cryosphere, pages 317–382. Cambridge University Press.

VAW Laboratory of Hydraulics, H. and Glaciology (2013). Glaciological reports (1881-2015). "The Swiss Glaciers", Yearbooks of the Cryospheric Commission of the Swiss Academy of Sciences (SCNAT) . Technical report, ETH Zürich (http://glaciology.ethz.ch/swiss-glaciers).

Warburton, J. (1990). An alpine proglacial fluvial sediment budget. *Geografiska Annaler*, 72:261–272.

Weber, M., Braun, L., Mauser, W., and Prasch, M. (2010). Contribution of rain, snow and icemelt in the upper Danube discharge today and in the future. *Geografia Fisica e Dinamica Quaternaria*, 33:221–230.

Weingartner, R. and Aschwanden, H. (1994). Quantification des débits des cours d'eau des Alpes suisses et des influences anthropiques qui les affectent. *Revue de géographie alpine*, 82:45–57.

Wold, B. and Østrem, G. (1979). Subglacial constructions and investigations at Bondhusbreen, Norway. *Journal of Glaciology*, 23:363–379.

Conclusion Part IV

9 | Conclusions

9.1 Remote sensing methods for the investigation of the geomorphic dynamics of Alpine landscapes

As mentioned more than once along the chapters of this thesis, remote sensing techniques have greatly contributed in the field of geomorphology by serving as a valuable resource to obtain spatially extensive topographic datasets, especially in areas difficult to access. This thesis endorsed the potential of photogrammetric methods and laser scanning techniques for investigating the geomorphic dynamics of an Alpine site. Whilst several cases of application of these approaches in the field of geomorphology exist (e.g. Chandler and Brunsden [1995]; Kääb and Vollmer [2000]; Lane et al. [2000]; Heritage and Hetherington [2007]; Kneisel and Kääb [2007]; Alho et al. [2009]; Bennett et al. [2013]; Deems et al. [2013]; Abellan et al. [2014]; Gabbud et al. [2015, 2016]), it is also true that: (i) their use is challenging in Alpine environments with steep slopes and large elevation differences, and (ii) the motivation of geomorphologists is not the method itself but the data that the method can provide. Thus, geomorphologists are constantly seeking innovative data acquisition methods and processing procedures that might reduce financial costs, relax or even remove acquisition constrains, speed up data processing, reduce the computational burden, etc. This work contributed to this goal as a primary thesis aim. In addition, this thesis represented a step further towards the understanding of the impacts and consequences of climate change on geomorphic dynamics in mountain regions. In this concluding chapter, the major contributions of the thesis are summarized under these two headings and remaining research questions are presented.

9.1.1 Remote sensing methods for Alpine research

Archives of aerial photographs represent a unique opportunity for obtaining spatially extensive and quantitative information on past landscapes. In Chapter 3 we addressed the challenge of working with archival imagery in Alpine environments, by reason of topographic complexity (including occlusions and large elevation ranges), sub-optimal quality and varying scale of

imagery, and the difficulties of establishing ground control. Chapter 3 also presented means to overcome these challenges. The complete workflow proposed included techniques to establish appropriate control, caveats to accomplish each step of the photogrammetric analysis and a conservative error propagation approach. Results suggested a height precision close to theoretical expectations [Fryer et al., 1994] that is, of ± 1 to ± 3 parts per 10000 of the flying height. By following the procedure suggested in Chapter 3, it is possible to employ archival imagery to obtain high-quality DEMs and orthophoto-images suitable for geomorphological research.

The popularity of Structure-from-Motion photogrammetry for geoscience applications is due to its ability to rapidly generate three-dimensional data with minimal financial cost and expertise. Developments even include low cost, sometimes free, internet-based processing systems, where images can be uploaded and processed to derive three-dimensional data in only a few minutes. The ease of sensor distortion modelling in SfM approaches permits the use of consumer grade digital cameras, including the near ubiquitous smartphones. Taken together, these two developments offer the possibility of near instantaneous acquisition of 3D data, based upon the analysis of smartphone-acquired images submitted using wireless communication systems. In Chapter 4 we assessed how far SfM can be taken in terms of enabling exceptionally low cost, rapid and easy digital terrain model acquisition for geomorphological applications. Straightforward SfM approaches using basic smartphone imaging technology and partially and fully automated data-processing resources provided very satisfying outcomes for both close and intermediate ranges of applications. The quality of results appears to be strictly related to the quality and the scale of the photograph and to image geometry. However, and despite the emergence of automated calibration and matching routines, recognition of traditional photogrammetric principles remains critical for successful application using SfM. In this regard, Chapter 4 and its related guidelines paper [Micheletti et al., 2015] offer tips and caveats for profitably exploiting SfM photogrammetry.

Major software corporations (Google, Microsoft, Autodesk) are giving particular attention to historical and recent developments in both photogrammetry and computer vision, and this will lead to further radical and rapid improvements in SfM algorithms in the near future, including highly automated routines. The latter, associated with the rise in popularity of Unmanned Aerial Vehicles (UAVs, or drones) as imagery acquisition alternatives, are making SfM photogrammetry more and more accessible to non-expert users. SfM approaches are already substituting the routinely used laser scanning techniques for DEM collection, and it should be expected that they become the dominant choice for high-resolution topographic surveying in the Earth sciences.

Often compared to SfM methods in recent times, terrestrial laser scanning (TLS) has been one of the most successful method for three-dimensional data collection in the geosciences. However, most existing TLS operate at wavelengths highly absorbed by snow and ice, and this strongly limits their application in the field of glaciology. A new generations of TLS systems employing wavelengths in the near-infrared now allows long-range scanning of icy and snowy

surfaces. In Gabbud et al. [2015] we tested these technical developments for the monitoring of a glacier surface at the seasonal and daily scales. At the seasonal scale, spatial patterns of surface melt were quantified and appeared to be controlled by both aspect and debris cover. At the daily scale, evidence highlightde the effects of differential debris cover (ogive-related) on ablation patterns. Moreover, an alleged hydraulic jacking of the glacier associated with short-term water pressure rise has been observed.

Traditionally, a major challenge for TLS applications is the burden of managing the large number of points acquired, the handling of the effects of occlusions or spatially-variable point densities, and the common practice of interpolating point clouds to regular raster grids or triangulated irregular network, with several consequences for the subsequent quantitative estimations. Because of these reasons, being able to perform calculations directly on point clouds would be profitable. In Chapter 5 we proposed a semi-automatic clustering approach for point cloud analysis based on the Density-Based Scan Algorithm with Noise (DBSCAN). The latter permits the accurate detection and mapping of erosion and deposition features directly from two co-registered point clouds of the same area, without the need to thin or to interpolate the original three-dimensional datasets. Accordingly, realistic volumetric features (depending only on the actual data available) are extracted. The proposed approach is suitable for any type of point clouds.

9.1.2   Recent climate forcing and geomorphic dynamics in Alpine landscape

The scientific community is making great efforts to better understand, relate and quantify the consequences of anthropological-driven climate change for the Earth system, but scientific knowledge remains incomplete in some domains. In particular, little is known about the expected impacts on geomorphic dynamics in mountain watersheds, notably regarding sediment production and transfer. This thesis concentrated on this issues, and permits to draw some considerations on this topic.

Although anthropological-driven climate change appears to have accelerated during recent decades (see Figures 7.3 and 8.3), the analysis of DEMs between the 1960s and present day highlights a general stability of non-glacial or periglacial areas of the steep hillslopes in the case study chosen here (Figures 7.6 and 8.7), and this despite the ample availability of unconsolidated material characteristic of these environments. Surface changes appear confined to specific areas of the landscape and the greatest rates of change concern mostly glacial and periglacial landforms. Nonetheless, a distinct landscape response to warm and cold periods and to changes in rates of precipitation and snow cover is observed (Figures 7.7 and 8.8). Warming periods seem to be associated with some detectable increases in downwasting. However, subsequent image analysis showed that in zones where there was low or even non-significant surface elevation change, there could be significant lateral surface displacement (e.g. rock glaciers, Figure 7.9,7.11 and 9.1). These also seemed to be sensitive to climate, with rock glaciers acceleration during warmer periods. This work emphasizes the importance of not only focusing on surface change in evaluating climate change impacts on landscapes.
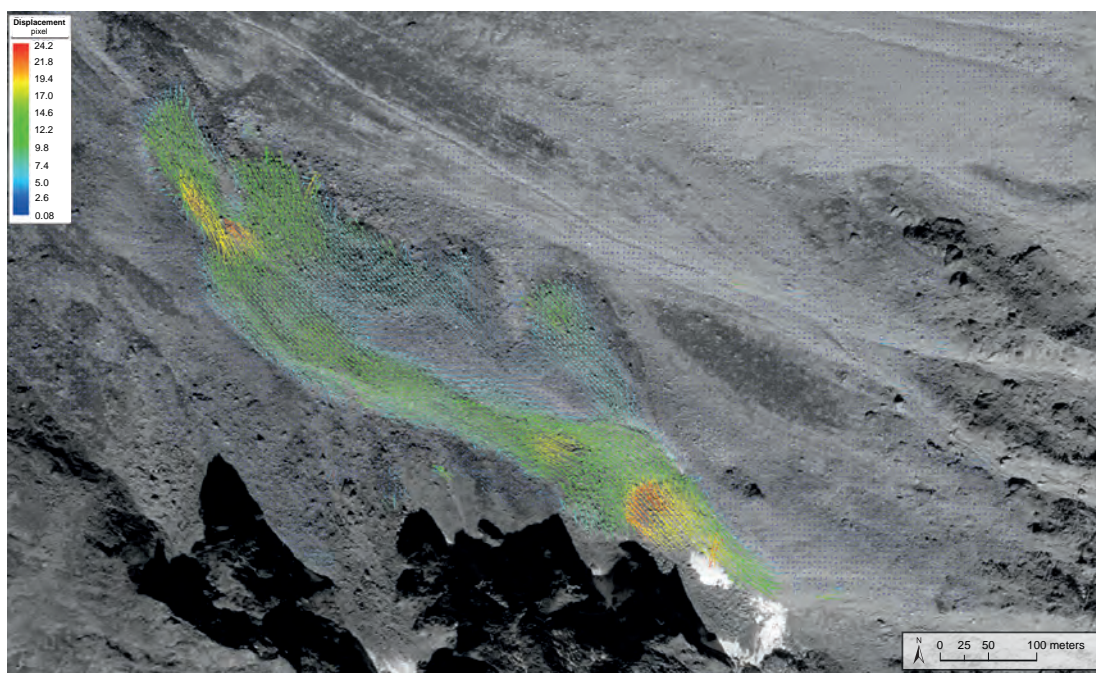
Figure 9.1 – Vectors of surface displacement for the La Roussette rock glacier between 1999 and 2005 (pixel size: 0.35 m x 0.35 m).

Glaciers are the elements of the landscape featuring the highest absolute sensitivity that is, they undergo the topmost magnitude of change at the temporal scale considered. Our results demonstrated that low temperatures and abundant precipitation and snow cover from the mid-1970s translated into large amounts of unmelted snow at the end of warm seasons (Figure 7.5b), and to positive mass balances for many glaciers in the area. This pattern has been generally observed for the vast majority of glaciers in Switzerland [Haeberli and Beniston, 1998]. Nevertheless, we observed that not all glaciers in the region have grown during this cooler period; the Haut Glacier d'Arolla has been in constant recession since the 1960s (Figure 9.2, Gabbud et al. [2016]).

Another consequence of temperature rise has been the modification of the hydrological dynamics of proglacial streams. The absolute input of precipitation has not considerably changed in the last five decades (Figures 7.4 and 8.4). However, whilst precipitation was the widely dominant water source for these streams until the mid-1980s, its relative contribution started decreasing because of the rising input provided by ice melt (glacial shrinkage) and snowmelt (Figure 8.10). These changes caused water yield to almost double through the last 50 years in the Douve Blanche and Bertol watersheds (Figures 8.9 and 8.10) and to increase by c. 50% downstream of the Haut Glacier d'Arolla snout (see Figure 3 in Lane et al. [2016]). This increase is a frequent outcome of rapid air temperature rise in streams regulated by glacial-nival flow regimes [Huss et al., 2008; Farinotti et al., 2012].

We engaged further with data from the hydroelectric power system by analysing the frequency
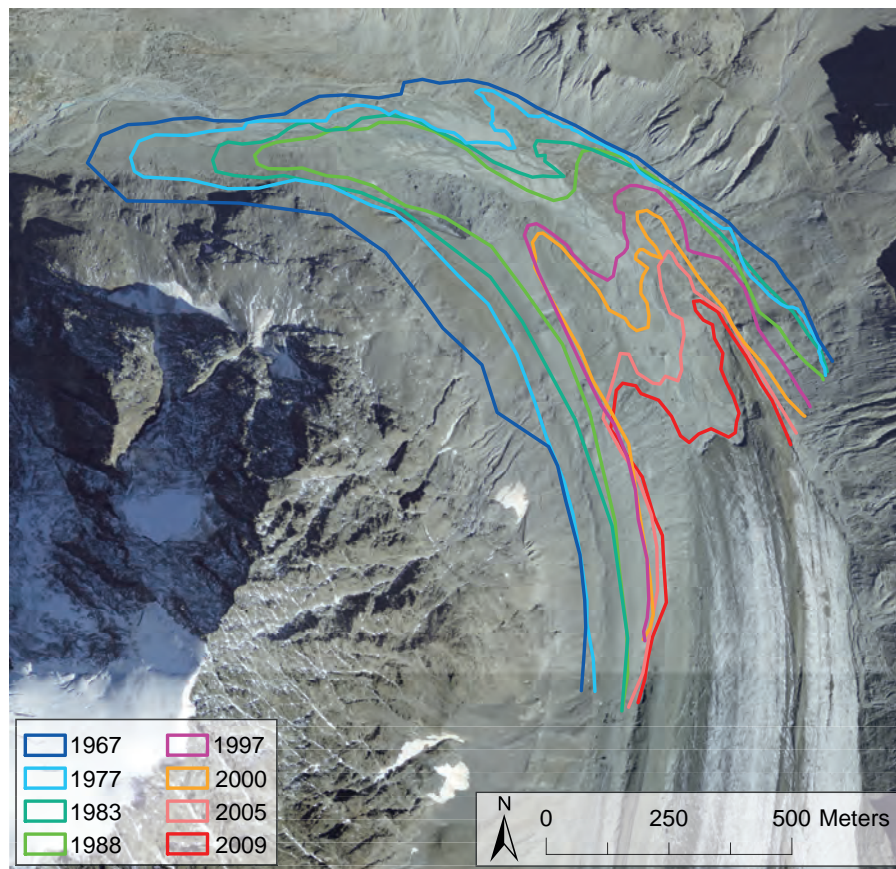
Figure 9.2 – Haut Glacier d'Arolla stages since 1967, originally published in Gabbud et al. [2016] (modified, Orthophoto: Swisstopo 2010).

of sediment flushing at the watershed outlets, which are equipped with water intake structures. We observed that an increase in the frequency of these events occurred, and this can be taken as a proxy for enhancement of sediment export. At least some of this could be related to intensification of sediment production under the influence of warmer air temperatures [Kääb et al., 2007; Knight and Harrison, 2009; Huggel et al., 2012; Bennett et al., 2013] and rising transport capacity associated with increase in water yield (Figures 8.11 and 8.12). However, substantial variability remains for all the watersheds considered (Figure 8.9 and Figure 4 in Lane et al. [2016]), suggesting that other factors ought to be relevant. Evidence from the analysis of topographic complexity shows that disconnected areas and rough surfaces possibly caused the delivery into the proglacial streams to be impeded (Figure 8.13). As a consequence, the sediment export records may under-estimate the actual levels of upstream response to climate forcing. Furthermore, we observed an explicit coincidence between extreme events (i.e. heavy rainfall events, thunderstorms and persistent precipitation) and peaks of sediment export in the Douve Blanche and Bertol watersheds (Figure 8.9), suggesting that these events are necessary to overcome the transport-limitation condition of slopes within of basins and to deliver sediment to the transport-efficient but supply-limited proglacial channels. Despite the

high magnitudes of geomorphic changes are observed in these basins, relatively low volumes of sediment exports are observed at the water intakes (magnitudes less than the estimated sediment transport capacity, Figures 8.11 and 8.12). This sustains the interpretations above. Various studies demonstrated that in most cases only a reduced part of the hillslope is coupled to the channel network by reason of natural or anthropogenic barriers, leading to abundant hillslope sediment storage [Harvey, 2002; Heckmann and Schwanghard, 2013]). Consequently, the effect of changes in erosion and deposition may be spatially restricted (see also Harvey [2001]). In the region of study, Little Ice Age moraine crests contributed in many occasion to cause disconnection of rockwalls and glacial and proglacial systems from the rest of the hillslope and the valley bottom (e.g. Figure 7.12). We observed that rock glaciers act as intermediate storage units, buffering the sediment transfer throughout the hillslope. However, rock glacier acceleration under warming climatic conditions could translate into shorter intermediate storage of material. Furthermore, it has been found that, especially during remarkably hot summers, rock glaciers produce several hundreds of cubic meters of sediment at their front (Chapter 5). This material is released downstream, but its propagation depends mainly on topography. Often, and as in the case of Tsarmine (see Chapters 5 and 7), the material does not propagate far as it becomes blocked in narrow channels because of its coarse nature combined with relatively limited water supply. As a consequence, and as evidence shows, although sediment production at a rock glacier front may be enhanced under warmer climatic conditions, delivery to the valley bottom may not be strongly affected at the timescales of decades. On the other hand, by reason of the fundamental role of disconnections and buffers, zones of highest sediment delivery at the valley bottom may be mostly associated with the best sediment connectivity and not with the largest surface changes upslope or the greatest sediment availability. In that sense, as also noted by Müller et al. [2014], the actual mobilized material at the top of the sediment cascade is much higher than the actual delivery to alpine valley bottoms. These observations somehow challenge the alarmist conception of a geomorphological crisis of Alpine systems at decadal scale (e.g. Mercier [2008]), in contempt of observed permafrost degradation, rapid glacier recession and acceleration in sediment production and transport rates (e.g. Jomelli et al. [2004]; Roer et al. [2008]; Huggel et al. [2010, 2012]; Bennett et al. [2013]). In fact, whilst climate change naturally leads to paraglacial and paraperiglacial geomorphological adjustment [Mercier, 2008; Scapozza, 2013], the Little Ice Age and the 20th century cooling period (1950s-1980s) to which we compare our present process observations may have been a brief pause in the Holocene paraglacial adjustment, and paraglacial sediment fluxes may be slowed with associated sediment export occurring centuries or even millennia after the beginning of deglaciation [Ballantyne, 2002] and this adjustment can be prolonged for several centuries or millenniums in areas of sediment storage as in Alpine regions [Cossart and Fort, 2008; Mercier, 2008]. Nonetheless, the present trends in greenhouse-gas and aerosol emissions are now moving the Earth system into a regime in terms of multi-decadal rates of change that are unprecedented in the last thousands of years [Smith et al., 2015]; anthropogenically driven climate changes are indeed altering the natural course of the climatic variability of the Holocene. Although the consequences of recent climate change are visible, we might still have to wait to see how ongoing rapid climate change

will play out for Alpine environments. The extent of paraglacial process acceleration is likely going to depend on future human activities and greenhouse-gas emissions.

In conclusion, the geomorphic dynamics in mountain watersheds appear to be impacted by recent climate change, mostly by reason of their dependence upon ice and permafrost conditions. Nevertheless, sediment fluxes are more confined and climate change impacts are consequently not easily propagating through the sediment cascade of high mountain systems. On the one hand, these processes are likely to be part of the Holocene paraglacial adjustment of these mountain regions, and sediment signals may be delayed for many centuries or even millennia. On the other hand, the role of anthropogenic activities in accelerating and exacerbating the current climate warming may accelerate it.

9.1.3   Summary of the main contributions of the thesis

The main contribution of the thesis can be summarized as follows:

- The development of a workflow to overcome the challenges often encountered by geomorphologists working with (archival) aerial photogrammetry in steep and complex terrain (Chapter 3).

- Demonstration that it is possible to acquire high-resolution topographic and terrain data using hand-held smartphone technology coupled with Structure-from-Motion internet-based processing systems (Chapter 4).

- The promotion of a 3-D clustering approach for feature detection directly from point clouds (Chapter 5) obtained for steep mountain sides.

- A contribution to our understanding of the response of high mountain geomorphic systems to recent climate change, in particular:

  - Quantification of the geomorphic dynamics of a whole alpine mountainside and of the individual elements that compose it (Chapter 7)

  - Demonstration of the role of hydrological dynamics and sediment connectivity in the response to climate change of glaciated basin (Chapter 8)

9.2   Future research

9.2.1   Remote sensing methods for Alpine research

In this thesis we concentrated on photogrammetric approaches and terrestrial laser scanning for Alpine research. Whilst their application proved successful and the results were satisfying, the use of these technologies encompasses some issues. Whilst a major problem with LiDAR devices is their high financial cost, in high mountain the angle of incidence of the laser pulse

and the shade effect caused by complex topography are also problematic. Commissioned photography (i.e. aerial imagery) are also very expensive, and it is not always possible to control when the data can be acquired. A great opportunity to reduce the cost of data acquisition while increasing its frequency is represented by Unmanned Aerial Vehicles (UAVs), which are becoming the more and more popular, efficient and reliable. UAV-collected imagery processed using SfM-MVS is becoming a primer approach to monitor landforms and landscapes following the developments reviewed by Smith et al. [2015] (e.g. improvements in on-board GPS systems, in image stability, etc.). In the context of this thesis, it would be interesting to collect aerial imagery using drone devices to obtain extremely high resolution DEM and orthophotographs, to detect geomorphic changes and surface displacements over short terms.

Whilst UAVs represent a primary resource for future landscape and landform monitoring, it would be profitable to develop and implement methods to make a better use of the wide archives of historical imagery. As mentioned earlier (see Chapter 3), working in high mountain regions might complicate the photogrammetric restitution and stereo-matching results could still feature a relatively coarse resolution in some areas. A possible way to address this issue is to perform a stochastic downscaling of digital elevation models. LiDAR and UAVs approach allow the acquisition of very high resolution altimetric data, but only within reduced spatial extents. Nonetheless, this data could be used in specific algorithms, e.g. harnessing a multiple-point geostatistical simulation, to downscale the coarse, historical 3D data to higher resolution (e.g. Rasera et al. [2016]).

Another extension of this thesis could be the improvement of the change detection methodology to produce more robust and spatially variable estimation of historical DEM uncertainties. Propagating these uncertainties would likely lead to estimates of geomorphic changes of higher quality, as shown for the DBSCAN application in Chapter 5. In this regard, two possible approaches for regular grids have been proposed by Wheaton et al. [2010]: one based on a fuzzy interference system and one relying on the spatial coherence of erosion and deposition units to modify DEM uncertainty. The application of these (or similar) calculations could significantly improve the quality or reinforce the confidence of the volumetric changes and the DEMs of Difference presented in Chapters 7 and 8.

Finally, aerial photogrammetry is not able to successfully reproduce near vertical landforms (e.g. rockwalls), and thus surface changes in these areas could not be estimated with this technique. Accordingly, it would prove useful to test methods for highly oblique monitoring. If one possibility is represented by the use of TLS devices (e.g. Heckmann et al. [2012]; Abellan et al. [2014]; Tonini and Abellan [2014]), UAVs serve as a cheap and practical alternative.

9.2.2 Recent evolution of Alpine landscapes

The possible extensions of the investigations presented in this thesis are numerous. They are mostly targeted at understanding in depth how the elements of mountain geomorphic systems are evolving and how they couple together in the systemic, holistic ensemble that they form.

First, some efforts should be put into quantifying sediment production rates at the top of the cascade, i.e. the rockwalls. Effectively, sediment production from rockfall events are a primary input and a first-order geomorphic agent in mountain systems. Whilst it was not possible to retrieve insights in this regard from aerial photographs by reason of their near-vertical characteristics, TLS data could be employed to perform a detailed monitoring of rockfall events (e.g. Heckmann et al. [2012]). However, this would require long term monitoring to assess sediment production rates confidently so as to determine their relation to climate warming. Useful information could also be obtained by measuring/modelling of MARST (Mean Annual Rock Surface Temperature) and of the frequency of freeze-thaw cycles (e.g. Magnin et al. [2015]). These could help us identify the location of the frost-cracking window [Hales and Roering, 2007, 2009] and infer if, where and when enhancement of sediment production by ice segregation is to expect. These processes are very likely to play a fundamental role in terms of input of material at the upper part of the sediment cascade. Effectively, as shown in recent studies (e.g. Messenzehl et al. [2016]), regional-scale rockfall activity is mostly driven by topo-climatic (strictly permafrost-related) and paraglacial (adjustment following the last glaciation maximum) factors.

A related topic regards ground temperatures. A deeper knowledge of permafrost distribution in the Alps would be beneficial to explain the observed surface changes and to infer areas prone to a stronger response to changing climatic conditions. However, by reason of the complexity of the micro-scale processes responsible for controlling permafrost presence, this task is very challenging and requires innovative modelling approaches. Numerous models exist for permafrost mapping, but none is able to predict the occurrence of permafrost at the very local scale. One solution would be to harness machine learning (ML) methods, which have the advantage of inferring functional dependencies between permafrost and its explaining controlling factors by deriving them directly from labelled training data (pixels of permafrost absence and presence) with the purpose of predicting permafrost occurrence where the latter is unknown [Deluigi and Lambiel, 2013]. ML techniques can be coupled with feature selection algorithms or have an embedded ability to provide measures of the variable importance. This allows the identification of the statistical contribution of each controlling factor without recurring to complex physical models.

If monitoring rockfall activity could provide an insight on sediment input for Alpine systems, analysing tree-rings at the valley bottom could contribute to the reconstruction of past delivery from the mountainsides. Effectively, dendrochronology could be employed to date collisions between solid charge (e.g. debris-flow material) and trees, thus estimating the frequency of substantial sediment delivery and its change over time [Stoffel et al., 2010]. To this regard, a field campaign has been carried out on the Satarma alluvial fan (see Figures 4.5 and 7.12), various trees in its channels and paleochannels were cored, and the tree-rings analysis was performed using a state-of-the-art microscopy. Hopefully this ongoing research is going to allow us to identify and to date major debris-flows events, to correlate them to climatic extremes and/or to see if a substantial change in event frequency follows transitions from cold to warming periods or changes in precipitation and/or snow cover in the 20th century.

Finally, the rather simplistic connectivity analysis proposed in this thesis needs to be improved to consider the possible vectors for sediment transfer and their routing. Preliminary attempts in that regard have been made and provided encouraging results. In particular, we are aiming at following a graph theory approach (see Heckmann and Schwanghard [2013]; Heckmann et al. [2015]), where different geomorphological processes responsible for sediment transport are simulated and coupled as start and target nodes. More specifically, the work will assess sediment connectivity by considering: (1) potential rockfall trajectories, (2) modelled debris-flow pathways and erosional and depositional parts, and (3) the sediment contributing area (SCA) as the area contiguously steep adjacent to the channel network. The ultimate objective would be the comparison of the several sub-catchments of the Arolla valley in terms of sediment connectivity to infer how climate forcing signals could propagate through the landscape. Moreover, we hope to be able to develop scenarios of future connectivity related to the magnitude and frequency and/or to changing initiation of rockfall and debris-flow events.

The possible findings from the approach detailed above could represent the basis for a more ambitious modelling of sediment transfer in high mountain landscapes in the context of a changing climate. The objective could be the formulation of a couple system model (e.g. see Heckmann et al. [2015]), using insights from the connectivity analysis above to qualify the relations between different elements of the landscape. Hopefully, it would be possible to model the effect of exogenous forces and endogenous processes for single sediment transfer mechanisms in a coupled framework, where a transmission function could manage how material moves through the different elements of the sediment cascade. Once that the coupled system model has been calibrated, it could be possible to include the use of Regional Climate Models (RCMs) to predict sediment transport in Alpine landscapes in the future, e.g. in the second part of the 21th century considering different emissions scenarios.

Bibliography

Abellan, A., Oppikofer, T., Jaboyedoff, M., Rosser, N. J., Lim, M., and Lato, M. J. (2014). Terrestrial laser scanning of rock slope instabilities. *Earth Surface Processes and Landforms*, 39(1):80–97.

Alho, P., Kukko, A., Hyyppa, H., Kaartinen, H., Hyyppa, J., and Jaakkola, A. (2009). Application fo boat-based laser scanning for river survey. *Earth Surface Processes and Landforms*, 34(13):1831–1838.

Ballantyne, C. K. (2002). A general model of paraglacial landscape response. *Holocene*, 12(3):371–376.

Bennett, G., Molnar, P., McArdell, B., Schlunegger, F., and Burlando, P. (2013). Patterns and controls of sediment production, transfer and yield in the Illgraben. *Geomorphology*, 188:68–82.

Chandler, J. H. and Brunsden, D. (1995). Steady state behaviour of the Black Ven mudslide: the application of archival analytical photogrammetry to studies of landform change. *Earth Surface Processes and Landforms*, 20(3):255–275.

Cossart, E. and Fort, M. (2008). Sediment release and storage in early deglaciated areas: Towards an application of the exhaustion model from the case of Massif des Écrins (French Alps) since the Little Ice Age. *Norsk Geografisk Tidsskrift - Norwegian Journal of Geography*, 62(2):115–131.

Deems, J., Painter, T., and Finnegan, D. (2013). LiDAR measurement of snow depth: a review. *Journal of Glaciology*, 59(215):467–479.

Deluigi, N. and Lambiel, C. (2013). Permal: a machine learning approach for alpine permafrost distribution modeling. in: Graf, c.(ed). *Mattertal - ein Tal in Bewegung. Jahrestagung der Schweizerischen Geomorphologischen Gesellschaft*, 29. Juni - 1. Juli 2011. St.Niklaus, Birmensdorf, Eidg. Forschungsanstalt WSL, 47-62:47–62.

Farinotti, D., Usselmann, S., Huss, M., Bauder, A., and Funk, M. (2012). Runoff evolution in the Swiss Alps: projections for selected high-alpine catchments based on ENSEMBLES scenarios. *Hydrological Processes*, 26:1909–1924.

Fryer, J. G., Chandler, J. H., and Cooper, M. A. R. (1994). On the accuracy of heighting from aerial photographs and maps: implications to process modellers. *Earth Surface Processes and Landforms*, 19(6):577–583.

Gabbud, C., Micheletti, N., and Lane, S. N. (2015). Lidar measurement of surface melt for a temperate Alpine glacier at the seasonal and hourly scale. *Journal of Glaciology*, 61(229):963–974.

Gabbud, C., Micheletti, N., and Lane, S. N. (2016). Response of a temperate Alpine valley glacier to climate change at the decadal scale. *Geografiska Annaler: Series A, Physical Geography*, 98(1):81–95.

Haeberli, W. and Beniston, M. (1998). Climate Change and its Imapcts on Glaciers and Permafrost in the Alps. *Ambio*, 27:258–265.

Hales, T. C. and Roering, J. J. (2007). Climatic controls on frost cracking and implications for the evolution of bedrock landscapes. *Journal of Geophysical Research*, 112:F02033.

Hales, T. C. and Roering, J. J. (2009). A frost "buzzsaw" mechanism for erosion of the eastern Southern Alps, New Zealand. *Geomorphology*, 107(3-4):241–253.

Harvey, A. M. (2001). Coupling between hillslopes and channels in upland fluvial systems: implications for landscape sensitivity, illustrated from the Howgill Fells, northwest England. *Catena*, 42(2-4):225–250.

Harvey, A. M. (2002). Effective timescales of coupling within fluvial systems. *Geomorphology*, 44(3-4):175–201.

Heckmann, T., Bimböse, M., Krautblatter, M., Haas, F., Becht, M., and Morche, D. (2012). From geotechnical analysis to quantification and modelling using LiDAR data: a study on rockfall in the Reintal catchment, Bavarian Alps, Germany. *Earth Surface Processes and Landforms*, 37(1):119–133.

Heckmann, T. and Schwanghard, W. (2013). Geomorphic coupling and sediment connectivity in an alpine catchment - Exploring sediment cascades using graph theory. *Geomorphology*, 182:89–103.

Heckmann, T., Schwanghard, W., and Phillips, J. D. (2015). Graph theory - Recent developments of its application in geomorphology. *Geomorphology*, 243:130–146.

Heritage, G. and Hetherington, D. (2007). Towards a protocol for laser scanning in fluvial geomorphology. *Earth Surface Processes and Landforms*, 32(1):66–74.

Huggel, C., Clague, J. J., and Korup, O. (2012). Is climate change responsible for changing landslide activity in high mountains? *Earth Surface Processes and Landforms*, 37(1):77–91.

Huggel, C., Salzmann, N., Allen, S., Caplan-Auerbach, J., Fischer, L., Haeberli, W., Larsen, C., Schneider, D., and Wessels, R. (2010). Recent and future warm extreme events and high-mountain slope stability. *Philosophical Transactions of the Royal Society A*, 368(1919):2435–2459.

Huss, M., Farinotti, D., Bauder, A., and Funk, M. (2008). Modelling runoff from highly glaciated alpine drainage basins in a changing climate. *Hydrological Processes*, 22:3888–3902.

Jomelli, V., Pech, V. P., Chochillon, C., and Brunstein, D. (2004). Geomorphic variations of debris flows and recent climatic change in the French Alps. *Climatic Change*, 64:77–102.

Kääb, A., Chiarle, M., Raup, C. S., and Schneider, C. (2007). Climate change impacts on mountain glaciers and permafrost. *Global and Planetary Change*, 56:7–9.

Kääb, A. and Vollmer, M. (2000). Surface Geometry, Thickness Changes and Flow Fields on Creeping Mountain Permafrost: Automatic Extraction by Digital Image Analysis. *Permafrost and Periglacial Processes*, 11(4):315–326.

Kneisel, C. and Kääb, A. (2007). Mountain permafrost dynamics within a recently exposed glacier forefield inferred by a combined geomorphological, geophysical and photogrammetrical approach. *Earth Surface Processes and Landforms*, 32(12):1797–1810.

Knight, J. and Harrison, S. (2009). Sediment and future climate. *Nature Geoscience*, 2:230.

Lane, S. N., Bakker, M., Gabbud, C., Micheletti, N., and J.-N., S. (2016). Sediment export, transient landscape response and catchment-scale connectivity following rapid climate warming and Alpine glacier recession. *Geomorphology*, doi:10.1016/j.geomorph.2016.02.015.

Lane, S. N., James, T. D., and Crowell, M. D. (2000). Application of digital photogrammetry to complex topography for geomorphological research. *The Photogrammetric Record*, 16(95):793–821.

Magnin, F., Deline, P., Ravanel, L., Noetzli, J., and Pogliotti, P. (2015). Thermal characteristics of permafrost in the steep alpine rock walls of the Aiguille du Midi (Mont Blanc Massif, 3842 m a.s.l). *The Cryosphere*, 9:109–121.

Mercier, D. (2008). Paraglacial and paraperiglacial landsystems: concepts, temporal scales and spatial distribution. *Géomorphologie*, 4:223–234.

Messenzehl, K., Meyer, H., Otto, J.-C., Hoffmann, T., and Dikau, R. (2016). Regional-scale controls on the spatial activity of rockfalls (Turtmann Valley, Swiss Alps) - A multivariate modeling approach. *Geomorphology*, doi:10.1016/j.geomorph.2016.01.008.

Micheletti, N., Chandler, J. H., and Lane, S. N. (2015). Structure from Motion (SfM) Photogrammetry. *Geomorphological Techniques*, Chap. 2:Sec. 2.2.

Müller, J., Gärtner-Roer, I., Kenner, R., Thee, P., and Morche, D. (2014). Sediment storage and transfer on a periglacial mountain slope (Corvatsch, Switzerland). *Geomorphology*, 218:35–44.

Rasera, L. G., Mariethoz, G., and Lane, S. N. (2016). Stochastic Downscaling of Digital Elevation Models. In *Geophysical Research Abstracts, Vol. 18, EGU General Assembly 2016*.

Roer, I., Haeberli, W., Avian, M., Kaufmann, V., Delaloye, R., Lambiel, C., and Kääb, A. (2008). Observations and considerations on destabilizing active rock glaciers in the European Alps. In *Proceedings of the Ninth International Conference on Permafrost*.

Scapozza, C. (2013). *Stratigraphie, morphodynamique, paléoenvironnements des terrains sédimentaires meubles à forte déclivité du domaine périglaciaire alpin.* Institut de géographie-Université de Lausanne.

Smith, M. W., Carrivick, J. L., and Quincey, D. J. (2015). Structure from motion photogrammetry in physical geography. *Progress in Physical Geography*, doi: 10.1177/0309133315615805.

Stoffel, M., Bollschweiler, M., Butler, D., and Luckman, B. (2010). *Tree Rings and Natural Hazards: A State-of-the-Art.* Springer Science+Business Media B. V.

Tonini, M. and Abellan, A. (2014). Rockfall detection from terrestrial LiDAR point clouds: A clustering approach using R. *Journal of Spatial Information Science*, 8:95–110.

Wheaton, J. M., Brasington, J., Darby, S. E., and Sear, D. A. (2010). Accounting for uncertainty in DEMs from repeat topographic surveys: improved sediment budgets. *Earth Surface Processes and Landforms*, 35(2):136–156.